Methodology for shot-peening induced intragranular residual stress prediction

Simon Breumier

N° d'ordre NNT: 2021LYSEM008

THESE de DOCTORAT DE L'UNIVERSITE DE LYON

opérée au sein de

l'Ecole des Mines de Saint-Etienne

délivrée en partenariat international avec

ECOLE POLYTECHNIQUE DE MONTREAL

Ecole Doctorale N° 488

Sciences, Ingénierie, Santé

Spécialité de doctorat : Génie matériaux

Soutenue publiquement à huis close le 25/01/2021 par:

SIMON BREUMIER

Methodology for shot-peening induced intragranular residual stress prediction

---

Devant le jury composé de :

Sylvain Turenne, Professeur, Ecole Polytechnique de Montréal	President
Samuel Forest, Directeur de Recherche CNRS, MINES ParisTech	Rapporteur
Thomas Pardoen, Professeur, EPL, Louvain-la-Neuve (IMMC)	Rapporteur
Pascale Kanouté, Ingénieur de Recherche, ONERA	Examinateur
Guillaume Kermouche, Professeur, Ecole des Mines de Saint-Etienne	Directeur de thèse
Martin Lévesque, Professeur, Ecole Polytechnique de Montréal	Co-directeur de thèse
Aurélien Villani, Maître-Assistant, Ecole des Mines de Saint-Etienne	Co-encadrant

Dedication

Aux rencontres qui m'ont construit.

Acknowledgements

Je voudrais avant tout remercier Sylvain Turenne, Thomas Pardoen, Samuel Forest et Pascale Kanouté pour avoir accepté d'évaluer mon travail, pour m'avoir offert un beau débat scientifique lors de ma soutenance ainsi que pour les quelques échanges que nous avons pu (avec certains) avoir au cours de ma thèse. Je pense que la discussion et l'échange sont le cœur d'une pensée scientifique qui se développe et chacune de ces interactions m'a permis de grandir, de prendre de la distance, de positiver et d'avancer.

Merci à Guillaume Kermouche et Martin Lévesque pour avoir monté ce sujet avec moi. Mais aussi pour m'avoir écouté, supporté et soutenu pendant 3 ans. Pour m'avoir challengé à chaque réunion. Pour avoir encadré mon côté effusif et, bien des fois, balayé mon pessimisme et m'avoir remis sur les rails de l'enthousiasme.

Merci à Aurélien pour tout ce que tu m'as appris et pour avoir supporté mon flot de questions ainsi qu'à Claire Maurice pour m'avoir transmis une partie de ton savoir sur l'EBSD.

Merci à Fabrice Richard pour cette belle collaboration sur les indices d'identifiabilité, à Cécile Langlade pour avoir pris le temps de faire avec nous des essais de micropercussion, à Jérome Vétel, Etienne Robert et Olivier Jobin pour leur aide avec les caméras hautes-vitesses, à Gaylord pour nos discussions et son aide en micromécanique haute vitesse. Mais aussi à tous les autres chercheurs que j'ai rencontrés en conférences pour la prise de distance qu'ils m'ont apportée.

Merci à toutes l'équipe de Safrantech et en particulier à Frédéric Adamski, Jawad Badreddine, Mikael Podgorski, Daniel Galy et toute l'équipe du labo pour m'avoir accueilli pendant 4 semaines pour cette belle collaboration, et pour avoir donné un côté plus appliqué à une

thèse qui devenait si fondamentale.

Merci à tous les gens du labo de Saint-Etienne and from Montréal. Merci à Maryline et Sergio pour leur soutien, leur bonne humeur et leur temps. Merci à Gilles pour nos débats kubrickien et pour son enseignement de maître. Many thanks to Kambiz, as well as Thierry Lafrance and Francis Trudeau-Lalonde for their help in the lab and with the cannon.

In English comme en Français, thanks to all the teachers/permanent, Ph.D., postdoctoral and master students I've met, discussed, and had fun (beers and so on) with. Merci à Alixe, Margaux, Justin, Jolan, Julien, Nicolas, Maxime Dumas pour leurs accueils renouvelés à Saint-Etienne, les débats, les ballades dans le Pilat et les cafés. Many thanks to Maxime Paques, Vlad, Wassime, Olivier, Lingyu, Mohammadreza, Pierre, Abouthaina, Khouloud, Mohit, Ilyass... for making the A116 such an awesome office. Dédicace spéciale à Juliette, Isa, Mathilde, Jean and Clément pour m'avoir rendu mon chien.

Merci aux Chouettes et Hiboux des Yacks du Pilat, étoile montante de la scène de métal stéphanoise, ainsi qu'à Franck et Cécile pour leur aide précieuse qui a grandement facilité les nombreux déménagements qu'une cotutelle internationale implique, ainsi qu'à Sam et Cat pour leur aide.

Merci à Claire pour ton inconditionnel soutien et pour avoir tenu la distance. Enfin, merci à mes parents, ma sœur et ma famille pour m'avoir poussé vers la science et de nombreuses fois remis face à la réalité.

Résumé

Le grenaillage est un traitement mécanique des surfaces qui consiste à projeter des billes à très haute vitesse à la surface d'une pièce. Ce traitement est utilisé depuis plus d'une soixantaine d'année dans l'industrie pour améliorer la durée de vie en fatigue des matériaux par l'introduction de contraintes résiduelles de compression et de gradients de duretés en sous surface. Le procédé a longtemps été simplement considéré comme bénéfique sans réelle quantification des bénéfices apportés sur la durée de vie en fatigue et les évolutions de microstructures. En effet, modéliser le procédé a longtemps été un verrou car cela implique de simuler un grand nombre d'impacts, de reproduire avec précision la cinétique des billes et de prendre en compte un certain nombre de non-linéarités dues au contact et aux déformations plastiques. Cependant les avancées de ces dix dernières années ont permis le développement de modèles pouvant prédire avec précision le profil moyen de contraintes résiduelles en profondeur ainsi que les gradients d'écrouissage résultants.

Peu d'études ont cependant tenté de prédire les contraintes résiduelles et l'écrouissage induits à l'échelle d'un grain. Les variations intragranulaires des contraintes ont pourtant une influence sur la durée de vie à grand nombre de cycle d'un matériau. Par ailleurs l'écrouissage local constitue une donnée cruciale pour certains modèles de prédiction de durée de vie en fatigue. Les verrous principaux à lever pour effectuer de telles prédictions sont l'identification précise de modèles de plasticité cristalline à l'échelle de la surface et dans les conditions du procédé, ainsi que le développement de méthodes expérimentales de validation des modèles développés.

L'objectif de cette thèse est de développer une méthodologie pour la prédiction des contraintes

résiduelles et de l'écrouissage intragranulaire à l'aide de modèles de plasticité cristalline par éléments finis et de validations expérimentales.

Des essais d'indentation sphérique sur des monocristaux de cuivre sont présentés afin d'estimer le champ de contrainte induit en sous surface expérimentalement et numériquement. Les résultats révèlent que l'anisotropie de la plasticité cristalline peut induire des contraintes résiduelles de tension en sous surface. La comparaison des champs numériques et expérimentaux confirme aussi la possibilité de comparer des champs de contraintes estimés par EBSD à haute résolution à ceux prédits par des modèles de plasticité cristalline de façon suffisament quantitative pour permettre la validation de modèle.

Les évolutions microstructurales induites par le grenaillage d'un coin sont ensuite étudiées par des estimations EBSD de densités de dislocations géométriquement nécessaires à l'aide de nouvelles méthodes d'indexation alternatives. Les différences d'écrouissage relevées démontrent l'importance de modéliser le procédé à l'échelle du grain.

Une méthodologie pour l'identification de loi de plasticité cristalline à haute vitesse basée sur des essais de microcompression est détaillée. Une attention particulière à été portée sur le caractère bien posé du problème d'identification, à l'aide d'indice d'identifiabilités. Un canon a grenailler capable de projeter des billes isolées avec une large gamme de vitesse et une haute précision a été développé pour valider le modèle. Un code a été implémenté pour estimer la trajectoire de la bille en trois dimensions avec une précision de 200 μm pour servir d'entré aux modèles éléments finis. La validation du modèle précédent est effectuée par comparaison du déplacement de la bille, de la topologie de l'empreinte d'impact et du champ de désorientation sous l'empreinte estimés expérimentalement et numériquement.

Enfin la possibilité d'utiliser le déplacement de la bille et le champ de contraintes résiduelles induit par un impact est explorée par une étude d'identifiabilité détaillée. Ces travaux offrent de nouveaux outils et méthodologies pour l'identification de paramètres et la validation de modèles à l'échelle du grain et à haute vitesse.

Abstract

Shot peening is a mechanical surface treatment which consist in projecting several spherical particles onto a material's surface. The process have been widely used in the industry over more than sixty years to enhance material's fatigue properties by introduction of subsurface compressive stresses and hardening gradients. It has been long used as a 'nice to have' without any quantification of its benefits as its modeling involved a large number of impacts, complex shot kinematics and non linearities induced by contact and plastic deformations. Nonetheless, advances over the past twenty years provided models that successfully reproduced experimentally measured average residual stress profiles and hardening gradients.

However, only few attempts to predict the residual stress and hardening variations at the grain scale have yet been reported. Intragranular stress variations could influence a structure high cycle fatigue behaviour and local hardening could be a crucial input for fatigue life predictions models. The main barriers to achieve such predictions are mainly the difficulty to identify accurate crystal plasticity models in the process conditions as well as defining relevant validation procedures to assess the ability of the models to predict residual stress variations.

The objective of this thesis is to develop a methodology for shot peening induced intragranular residual stress and hardening prediction using crystal plasticity finite element simulations and experimental validations.

Indentation on single crystal copper are first presented to assess the residual stress variations in a single grain under the indent both experimentally and numerically. The results reveal that crystal plasticity anisotropy could induce subsurface tensile residual stresses under a

spherical contact. It also demonstrates that experimental residual stress fields estimated by high angular resolution electron backscattered diffraction could be quantitatively compared to finite element models. This finding makes it a relevant tool for constitutive behaviour validation.

The microstructural evolutions induced by shot peening of a corner are investigated using electron backscatter diffraction geometrically necessary dislocation estimations with recently developed alternative indexation methods. The differences in hardening gradient close to the corner compared with a reference shot peened material evidences that accurately predict microstructural evolutions induced by the process at the grain scale is necessary to predict the induced hardening distribution. These works provides new evidences of the relevance of modeling the process at the crystal scale.

A methodology for identification of crystal plasticity parameters at high strain rates using micropillar compression is then detailed. Particular attention is paid to the identification problem well-posedness using identifiability indicators provided by the literature. A shot-peening canon that can propel single shot over a wide velocity range with high aiming precision is developed. An in-house code that can estimate the shot trajectory within 200 μm is implemented to provide input for finite element analyses. The setup is used for validation of the previously identified model by comparison of the shot displacement impact dent topography and in-depth crystal misorientation field.

Finally, the possibility to use the shot displacement curve and residual stress field under the dent produced by the setup is investigated through a detailed identifiability analyses. These works provide new tools and methodologies for crystal plasticity parameters identification and validation at the grain scale and at high strain rates.

Table of contents

List of tables

List of figures

List of symbols and acronyms

SP	Shot Peening
HCF	High Cycle Fatigue
LCF	Low Cycle Fatigue
FEM	Finite Element Model
FEA	Finite Element Analysis
XRD	X-Ray Diffraction
CPFE	Crystal Plasticity Finite Element
RVE	Representative Volume Element
FCC	Face Centered Cubic
BCC	Body Centered Cubic
GND	Geometrically Necessary Dislocations
SSD	Statistically Stored Dislocations
EBSD	Electron BackScattered Diffraction
HR-EBSD	High Resolution Electron BackScattered Diffraction
TEM	Transmission Electron Microscopy
DIC	Digital Image Correlation
DEM	Discrete Element Modeling
DDD	Discrete Dislocation Dynamic
SEM	Scanning Electron Microscope
FIB	Focused Ion Beam
CCD	Charge-Coupled Device
PC	Pattern Center

ZOI	Zone of Interest
ROI	Region of Interest
NLPAR	Non-Local Pattern Averaging Reindexing
AFM	Atomic Force Microscopy
SHPB	Split Hopkinson Pressure Bar
IPF	Inverse Pole Figure
LSP	Laser Schock Peening
KAM	Kernel Average Misorientation
DI	Dictionary Indexing
CSM	Continuous Stiffness Measurement
SMAT	Surface Mechanical Attrition treatment
FEMU	Finite Element Model Updating
CoR	Coefficient of Restitution

List of Appendices

CHAPTER 1

Introduction

Fatigue crack initiation on structural parts is known to be mainly driven by the part's surface properties. Such properties are therefore often improved using surface mechanical or chemical treatments in the industry [4]. Shot-Peening (SP) is a surface mechanical treatment that consists in propelling hard particles, called shot ($\approx$ 0.1 to 2 mm diameter) onto a ductile metallic surface, at high velocity. The process (i) induces subsurface residual compressive stresses [5] and, in some cases, (ii) increases subsurface hardness due to subsurface microstructural evolutions [6]. These effects increase fatigue life and wear resistance, which led to the widespread use of the process in the industry.

SP also increases surface roughness, which could be a critical fatigue parameter, especially in the Low Cycle Fatigue (LCF) regime [7]. Authors have therefore devised modeling strategies to predict the resulting effects the process has in terms of fatigue life [8, 9]. Also, fatigue life prediction models usually require residual stresses, roughness and hardening, among other parameters. To that end, authors [10–14] have developed dynamic Finite Element Models (FEMs) to predict peening induced roughness, residual stresses and hardening where the media is explicitly represented. These models mostly dealt with macroscopic quantities and very few authors attempted to simulate residual and hardening fields at the grains scale.

Intra-granular (also called "Type II") residual stresses influence structure's High Cycle Fatigue (HCF) behaviour. Type II tensile stresses favor early stage plasticity, crack initiation and drives crack propagation paths [15, 16]. It also influences macroscopic residual stresses

stability over the load cycles [17]. Also, local hardening could be a precious input for fatigue lifetime prediction models, which usually require knowledge of the material loading history.

Crystal Plasticity Finite Element(CPFE) simulations could provide accurate intragranular residual stresses and hardening predictions. Recent works studied the initial microstructure influence on SP induced residual stress fields and geometrically necessary dislocation density [18, 19] using such simulations. However, the predictions were not compared against experimental residual stresses evaluation, as such experimental assessment remains a challenge. Advances in High-Resolution Electron BackScattered diffraction (HR-EBSD) unlocks the possibility to obtain residual stress variation under single impacts to validate such model.

Also most of the aforementioned studies used CPFE models with coefficients identified either using low strain rate fatigue tests or high strain rate Split Hopkinson Pressure bar tests. The strain rate used for identification were therefore below those involved by the process (up to 6.10^5 s^{-1} [20]). Furthermore, as shot-peening involves mainly local surface deformations, the material constitutive behaviour used for modeling should be identified using local test procedures with similar deformation mechanisms. An identification methology using local tests in shot peening conditions therefore has to be developed. The identified parameters should then be validated considering the quantity of interest, *e.g.* the residual stress field under one or several impacts performed in controlled conditions.

This research projects aims at **developing a methodology for SP-induced intra-granular residual stress and hardening prediction using crystal plasticity finite element simulations, and its experimental validations**. The main objectives of the projects were **(i)** to assess the relevance to model the process at the crystal scale, **(ii)** develop a methodology for identification of the CPFE parameters in the process conditions at the crystal scale using a variety of experimental observations and **(iii)** provide tools to validate the identified parameters in the process conditions.

This document is organized as follows:

- In **Chapter 2**, the literature related to the project is summarized and tools to understand the presented work are provided. The shot peening process is presented with a particular focus on residual stresses and modeling. A general introduction to crystal plasticity at low and high strain rate is provided. Tools for mechanical surface properties and microstructural state caracterization at the grain scale, that could be useful for the project, are then developed. Methodologies and important considerations for constitutive parameter indentification are also detailed.

- In **Chapter 3**, the effect of crystal orientation on spherical indentation induced residual

stress fields explored during the project and published in Materials & Design [21] is presented. The objective of the chapter is to assess the relevance to model the process at the grain scale and to use HR-EBSD as a validation tool for constitutive behaviour validation.

- In **Chapter 4**, the result of a study performed in collaboration with Safrantech on the microstructural characterization of the bulge induced by shot-peening of a sharp corner submitted in Materials Science and Engineering: A [22] is developed. This study further emphasizes the importance to account for microstructural evolution at the grain scale to model the process, especially when treating non linear geometries.

- In **Chapter 5**, an identification methodology of crystal plasticity strain rate dependent constitutive parameters using high strain rate micropillar compression that was published in Materials & Design [23] is developed. The work lays the first basis for CPFE constitutive parameters in the process condition at the surface scale.

- In **Chapter 6**, the shot peening test rig canon developed during the project to propel a single shot under controlled conditions is presented. The methodology developed in this work to extract the shot trajectory to be used as simulation input, as well as two different applications of the test rig, are presented. This work was submitted in Strains [24].

- In **Chapter 7**, the possibility to use experimental output produced by the canon such as the displacement curve and the residual stress field under an impact for constitutive parameters inverse identification is investigated through an identifiability analysis. This work was submitted in the Journal of Theoretical, Computational and Applied Mechanics [24]

CHAPTER 2

Literature review

2.1 Shot peening

2.1.1 Generalities

Shot peening is a surface mechanical treatment which consists in projecting hard ceramic or metallic shot onto a material surface at high velocity. It is widely used to enhance material's fatigue life by subsurface hardening [6] and compressive residual stresses introduction [5].

Several process parameters can be varied to optimize the SP-induced surface properties (Figure 2.1) [25]: shot characteristics (material properties, hardness HV, diameter d), shot velocities v (between 50 and 100 m.s^{-1} [26]), impact angles ω and the exposition time t_{exp}.

Two sets of parameters are used to characterize the process induced surface properties:

- The **surface coverage**, which is the impacted surface ratio. Coverages over 100% are usually measured as multiples of the SP time required to reach 100%.
- The **Almen intensity**, which is defined as the residual arc height of a relaxed beam after SP.

Residual stresses result from the residual elastic strains constrained by the impact-induced plastic deformations. Shot induce subsurface inhomogeneous plastic strains during SP. To ensure strain continuity, the material in the surrounding plastic zone must deform elastically, which produces residual stresses that should satisfy equilibrium. As residual elastic strains counter a shot-induced plastic stretch, SP induces global subsurface residual compressive stresses (see Figure 2.2).

The literature provides a wealth of experimental [7, 27–30] and numerical studies [31–34],

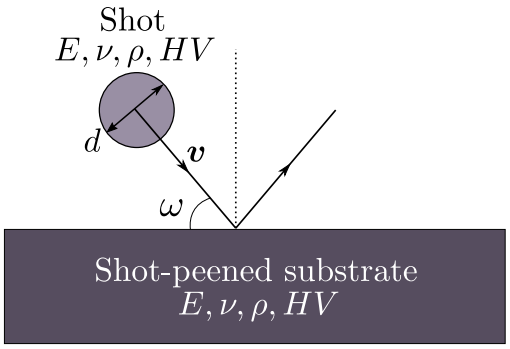

Figure 2.1 Process parameters used for conventional SP. E, ν, ρ, HV are respectively the shot or the material Young's modulus, Poisson's ratio, density and hardness. d, v and ω are the shot diameter, velocity and impact angle [25].

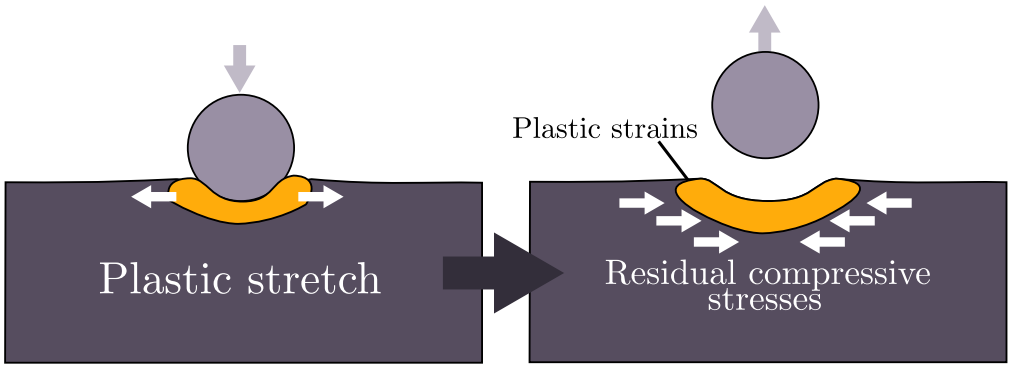

Figure 2.2 Mechanism leading to compressive residual stresses resulting from residual elastic strains constrained by the impact-induced plastic deformations. The orange zone represents shot-induced plastically strained zone. SP induces subsurface plastic-stretch which is countered by residual elastic strains. Such mechanism induces global subsurface residual compressive stresses

using respectively X-Ray diffraction (XRD) residual stress measurement methods (such as the $\sin^2\psi$ method) and Finite Element Analyses (FEA), to estimate the averaged residual stress profiles. Classical residual stress profiles obtained with these methods are presented in Figure 2.3. Compressive residual stresses are generally found for depth varying from a few hundreds micrometres to few millimetres. Tensile stresses are usually found in the bulk beneath the compressive zone, as it ensures the sample's global mechanical equilibrium.

The deformation mechanisms leading to such stresses have also extensively been studied. For isotropic materials, Wohlfahrt [35] suggested that the presence of residual stresses results from two different mechanisms: Hertz pressure and hammering effect. The former is linked

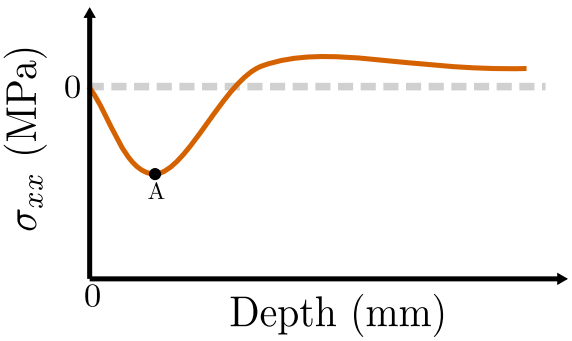

Figure 2.3 Usual averaged residual stress profile obtained using, for instance, the XRD $\sin^2\psi$ method. Subsurface compressive stresses are usually found down to a few millimetres below the surface. Tensile stresses are found deeper in the sample to satisfy the global mechanical equilibrium. Point A represents the highest compressive stress intensity.

to a repeated impacts-induced normal pressure field which creates maximum shear stresses at a certain depth. The shear stresses intensities and depths mainly depend on the contact radius. The latter corresponds to the subsurface plastic stretch induced by peening jet induced tangential forces.

The influence of residual stress on fatigue life depends on the impacted material as well as on the fatigue regime. Klotz et al. [7] performed both HCF and LCF tests on shot peened Inconel 718 samples to evidence the influence of residual stresses and process induced hardening on the fatigue life. The authors found that in the HCF regime, SP could enhance Inconel 718 fatigue life from 2 to 20 times, when compared to an unpeened specimen. According to the authors such enhancement is mainly attributed to compressive residual stresses developed under the surface. However, in the LCF regime, fatigue life was mainly driven by the surface roughness which tends to lower the treated sample fatigue life, when compared to an unpeened specimen.

Alternatively, Eleiche et al. performed HCF fatigue tests on shot peened high strength martensitic samples for which the residual stresses were relaxed through a thermal treatment. Shot peened specimens presented a 20% life improvement, when compared to an unpeened specimen. However, the authors found that relaxing the residual stresses only lowered the samples HCF life by 3%. In the case of high strength martensitic alloys, the treated part's fatigue life is therefore mainly improved by shot peening induced work hardening, rather than by the residual stresses.

An accurate prediction of **both** the material residual stress and hardening state after the process is necessary to feed fatigue life prediction models. Many works have therefore focused on SP numerical simulations. A short review of SP models is further provided.

2.1.2 Finite Element simulations

Accurate SP modeling requires representative prediction of a complex and random shot distribution. Many authors have therefore focused on shot modeling to accurately represent the shot-peened sample's loading history. Noughier-Lehon et al. [36] used Discrete Element Modeling (DEM) with constant target material absorbed energy to model shot behaviour. Murugaratnam et al. [33] and Tu et al. [13] performed a DEM-FEM coupling to study the influence of several process parameters on the induced residual stress field, accounting for shot kinematics. Alternatively, Badreddine et al. [26] used an analytical granular vibrated gas model to obtain the shot velocity distributions. The model provided satisfying shot trajectories and surface coverage predictions for ultrasonic SP, when compared to experimental

data. The approach was later used to model the shot flow on complex geometries [9, 10] by introducing the residual stresses induced by one impact of a flat sample into the complex geometry using the eigenstrains method. Few authors, such as Nguyen et al. [37] also used computational fluid dynamic softwares to model the shot peening jet flow.

Several works focused on Shot-Peening modeling for accurate residual stress predictions. The influence of the finite element simulation geometry [38], mesh size [11,39], friction and contact penalty coefficients [20, 40] on the global residual stresses prediction accuracy was already assessed.

Choice of the target material constitutive behaviour is crucial to accurately predict the process induced residual stresses and hardening as it has to account for the process conditions. Meguid et al. [20] modeled several impacts on an AISI 4340 high-strength steel using a 3D model with a strain rate dependent constitutive behaviour. Their study revealed that the process could involve strain rates up to 6.10^5 s^{-1}. Most SP finite element simulations modeled the substrate using macroscopic isotropic constitutive laws. Strain-rate dependency is usually accounted for using Johnson-Cook's constitutive relationship [39, 41, 42]. Also, impact repetition induces kinematic hardening in the target which has both an influence on the macroscopic residual stresses [43] as well as on the material's fatigue life [5]. Macroscopic kinematic hardening frameworks have therefore been used by several authors to account for such effect [32, 43–45].

Accurate modeling of shot kinematics and material constitutive behaviour for SP-induced loading history now provide accurate macroscopic residual stress predictions over many grains. Recent works have therefore used such model to study SP parameters influence on residual stresses. For instance, Gariepy et al. [46] studied the influence of shot velocity and size distribution on residual stresses and surface roughness, using a coupled FEM and Monte-Carlo approach.

Such works usually rely on comparison of predicted and XRD-measured residual stress profiles. The aforementioned models can therefore accurately predict the macroscopic residual stress average **only over many grains**. Such models remain relevant for isotropic materials, for which the grain size remains small, and with no particular crystal orientation textures.

2.1.3 Process influence at the crystal scale

In many cases, industrial materials' mechanical behaviour is driven by their microstructure. Prediction of the shot-peening induced residual stress and hardening distribution on such

materials at the microstructural scale **should therefore account for the material's local heterogenities.**

Castro-Moreno et al. [19] performed a complete CPFE SP simulation on a polycrystalline Representative Volume Element (RVE) with different initial grain sizes. Their work numerically evidenced the influence of initial material grain size on the SP-induced residual stress intragranular distribution. The authors however pointed out that the global average stress distribution was not much impacted by the RVE initial microstructure.

Such local heterogenities could drive the process' benefits for material's which mechanical behaviour has to account for different scales such as large grain microstructures, textured materials or multi-phased materials. Industrial applications of such materials are for instance:

- Single crystal structural parts such as high pressure turbine blades [47]
- Welded zones or additively manufactured parts which usually present a textured microstructure with elongated or colonar grains [48, 49]
- Precipitate hardened alloys such as most nickel based super-alloys.

Shot-peening induced residual stresses are therefore usually considered at different scales [4], as illustrated in Figure 2.4:

- **Type I** usually refers to the residual stresses averaged over many grains
- **Type II** represents the microscopic residual stress varying inside single grains

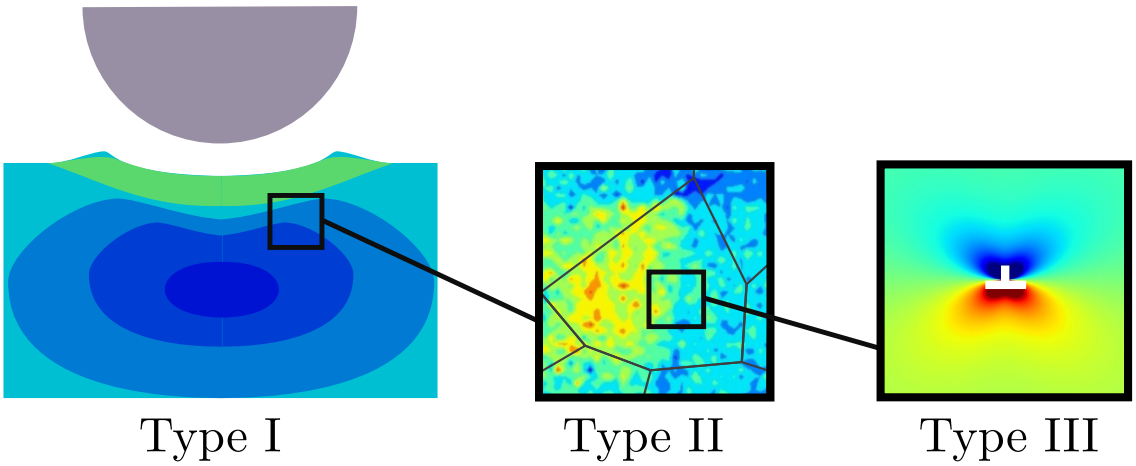

Figure 2.4 Residual stresses at different scales. Type I, II and III stresses refer to stress average over many grains, the micro stress variations inside a single grain and the stress at the crystal defect scale respectively.

- **Type III** is the sub-microscopic residual stress resulting from the local influence of crystal defects

Type II stresses are known to influence the material's HCF bevaviour as it favours early stage plasticity, crack initiation, and drives the crack propagation paths [15,16]. Musinski et al. [8] introduced residual stresses provided by isotropic FE calculations into a polycrystalline CPFE model, using the eigenstrains method. They then studied the predicted and measured intragranular stress redistribution and relaxation after one load cycle. Experimental and numerical relaxed stress profiles after one load cycle followed similar trends and amplitudes. Their study revealed that intragranular stress variations influence the residual stress relaxation over the first loading cycles. **Accurate prediction of Type II residual stresses is therefore crucial to assess the process performance in terms of fatigue life.**

Rousseau et al. [18] studied the influence of several SP parameters (impact velocity, angle and impact repetition) on the residual stress field and dislocation production predicted by a dislocation-based CPFE framework on a 2D polycrystal. Their work provided a numerical assessment of well-known experimental macroscopic observations and provided a methodology to predict the shot peening induced hardening at the grain scale, which is also crucial for fatigue life prediction [5, 47].

Predicting the process benefits at the microstructural scale however requires to use constitutive behaviour representative of this scale, such as crystal plasticity models. Such constitutive behaviours involve a large number of material coefficients which have to be identified:

- **Under the process conditions**, as shot-peening involves several impacts deforming the material cyclically at strain rates up to 10^5 s^{-1} [20].
- **At the surface scale**, as the process usually affects depths down to a few hundred microns, which implies that the solicited RVE has a large surface to volume ratio. This results in different plasticity mechanisms, as it will for instance be more favorable for a dislocation to exit the material through the surface.

The importance of those two factors on Type II residual stress and micro hardening prediction can be apprehended by looking at the strain rate field induced by a spherical impact. Figure 2.5 shows the von Mises equivalent strain rate distribution under an impact performed at 40 m·s on an isotropic elasto-plastic material using simple von Mises plasticity. Such simple analysis reveals that the highest strain rates are usually found very locally at the extreme surface underneath the contact periphery, where shears are the most predominant. **Strain-rate heterogeneities therefore drive Type II residual stress build up**.

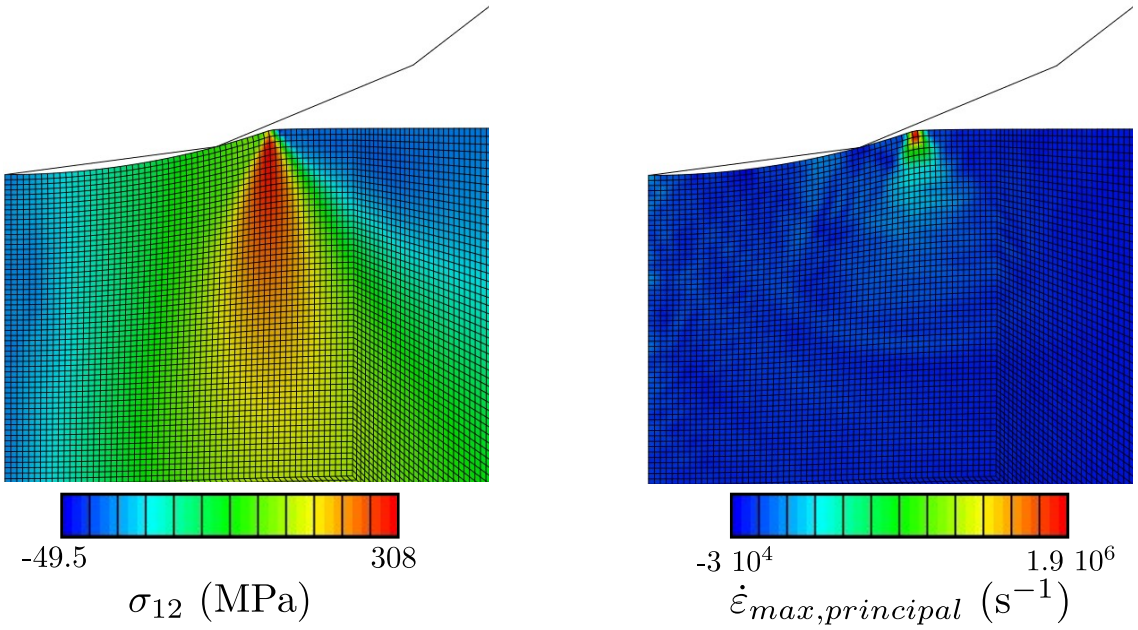

(a) (b)

Figure 2.5 Strain-rate distribution induced by an impact. 2D plane strain 40 m s^{-1} Impact simulation using an isotropic elasto-plastic constitutive behaviour for the target material: (a) Shear stress and (b) maximum principal strain rate under the impact. The highest strain rates are observed very locally at the contact periphery due to the high shear imposed to the material during the impact.

Models aiming at predicting stresses at such scale therefore have to describe the target material strain-rate dependent behaviour as accurately as possible, on a large strain rate range and at the surface scale.

The next section provides a short review of such crystal plasticity model in the perspective to use them for shot-peening simulations.

2.2 Crystal plasticity

2.2.1 Phenomenology

Crystalline materials are composed of an organized arrangement of atoms that can be described by a repeated pattern. Plasticity in such materials is related to the crystal lattice defects evolution.

As briefly recalled in Figure 2.6, the most usual case of crystal lattice defects usually considered to explain plastic deformation of metals are:

- Dislocations **nucleation**, **gliding** (mechanical) or **climbing** (diffusion)
- **Twinning**, which is an organized displacement of atoms resulting in two different crystals with a symmetrical lattice arrangement.
- **Phase transformations** which could be thermally or mechanically induced.

To simplify the problem, the present work will consider dislocations evolution as the only source of plastic deformation.

Dislocation glides follow the densest crystal lattice planes, usually called **gliding planes**. A

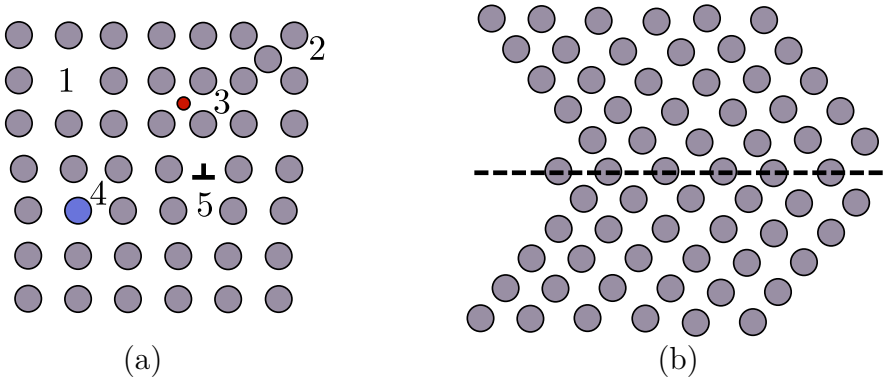

Figure 2.6 Illustration of several crystal defects. (a) point, linear and (b) planar (twinning) defaults. In figure(a): (1) vacancy, (2) self-interstitial, (3) foreign-interstitial, (4) foreign substitution atom and (5) dislocation

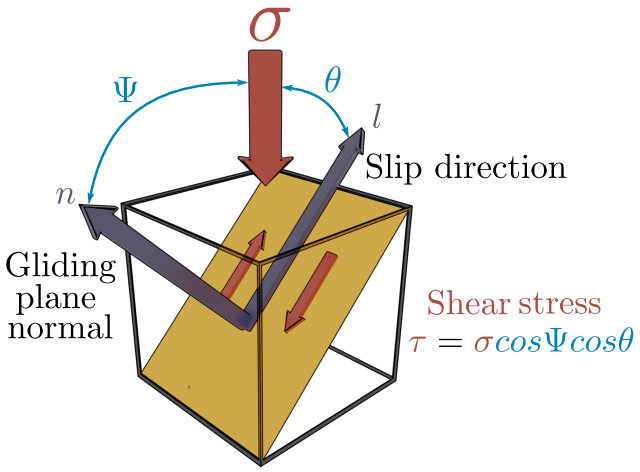

Figure 2.7 Illustration of the Schmid's law. Dislocations glide along a given direction l on a gliding plane of normal n. Gliding is controlled by the amount of shear applied to the gliding plane which can be found by projection of teh stress tensor onto the plane.

gliding system is defined by a gliding plane and a gliding direction. Dislocation glide is driven by shear and is therefore related to the stress projection on the gliding plane as shown in Figure 2.7. This is usually obtained thanks to the well-known Schmid's law as

$$\tau = \boldsymbol{\sigma} : \frac{1}{2}(\mathbf{l} \otimes \mathbf{n} + \mathbf{n} \otimes \mathbf{l}), \tag{2.1}$$

where τ is the projected shear stress, usually called the **resolved shear stress**, $\boldsymbol{\sigma}$ is the Cauchy stress tensor and $\mathbf{l}$ and $\mathbf{n}$ are vectors representing respectively the gliding direction and the normal to the slip plane. Crystal plasticity is therefore anisotropic.

For dislocation glide-driven plasticity, hardening is mainly related to the obstacles encountered by dislocations such as other dislocations, dislocation forests, precipitates, inclusions or grain boundaries. Generally, a distinction is made between [51]:

- **Self-hardening**, limited to interactions between dislocations in the same gliding system
- **Latent hardening**, which results from dislocation interactions from different gliding systems.

Hirth listed the most frequent interactions for Face-Centered Cubic (FCC) lattices [52]. To quantify the relative strength of each interaction, Franciosi et al. [53] performed tensile tests on single crystals under simple glide conditions. They then cut a new sample in the primary deformed one to conduct a second tensile test under simple glide conditions on the secant gliding system. The authors then introduced the hardening power induced by interactions between systems s and r as:

$$h_{sr} = \frac{\tau^r}{\tau^s}. \tag{2.2}$$

The different hardening configurations are listed in Table 2.1. The resulting interaction matrix for the 12 FCC gliding systems (listed in Table 2.2) is presented in Table 2.3. This matrix is used in most crystal plasticity constitutive laws for FCC lattices.

2.2.2 Classical models

Despite that dislocations represent discontinuities in the crystal lattice, the average behaviour of a large number of dislocations can be represented using a continuum mechanics approach. Crystal plasticity finite element frameworks relies on such hypothesis as it accounts for the averaged single crystal mechanical behaviour in a representative element volume.

Table 2.1 Interaction matrix coefficients. Relationship between the crystal hardening interaction coefficient h_i and the gliding system geometrical property for FCC crystal lattices. 6 coefficients are usually defined. n^s, n^r and l^s, l^r are respectively normal vectors to the slip planes and gliding directions of the gliding systems s and r.

Interactions	Geometric properties
Self hardening h_1	$\mathbf{n^s} = \mathbf{n^r}$ and $\mathbf{l^s} = \mathbf{l^r}$
Coplanar h_2	$\mathbf{n^s} = \mathbf{n^r}$ and $\mathbf{l^s} \neq \mathbf{l^r}$
Hirth lock h_3	$\mathbf{n^s} \neq \mathbf{n^r}$ and $\mathbf{l^s} \cdot \mathbf{l^r} = 0$
Collinear h_4	$\mathbf{n^s} \neq \mathbf{n^r}$ and $\mathbf{l^s} = \mathbf{l^r}$
Glissile h_5	$\mathbf{n^s} \neq \mathbf{n^r}$, $\mathbf{l^s} \cdot \mathbf{l^r} \neq 0$ and $\mathbf{l^s} \wedge \mathbf{l^r} = \pm\mathbf{n^s}$ or $\pm\mathbf{n^r}$
Lomer junction h_6	$\mathbf{n^s} \neq \mathbf{n^r}$, $\mathbf{l^s} \neq \mathbf{l^r}$ and $\mathbf{l^s} \wedge \mathbf{l^r} \neq \pm\mathbf{n^s}$ and $\pm\mathbf{n^r}$

Table 2.2 Numbering convention used in this manuscript for the 12 Face-Centered Cubic (FCC) gliding systems [50]

System number	1	2	3	4	5	6
Directions	$[\bar{1}01]$	$[0\bar{1}1]$	$[\bar{1}10]$	$[\bar{1}01]$	$[011]$	$[110]$
Planes	(111)	(111)	(111)	$(1\bar{1}1)$	$(1\bar{1}1)$	$(1\bar{1}1)$

System number	7	8	9	10	11	12
Directions	$[0\bar{1}1]$	$[110]$	$[101]$	$[\bar{1}10]$	$[101]$	$[011]$
Planes	$(\bar{1}11)$	$(\bar{1}11)$	$(\bar{1}11)$	$(11\bar{1})$	$(11\bar{1})$	$(11\bar{1})$

Table 2.3 System interaction matrix for an FCC crystal with 12 activable gliding systems. s and r refers to two gliding systems that can interact.

s\r	1	2	3	4	5	6	7	8	9	10	11	12
1	h_1	h_2	h_2	h_4	h_5	h_5	h_5	h_6	h_3	h_5	h_3	h_6
2		h_1	h_2	h_5	h_3	h_6	h_4	h_5	h_5	h_5	h_6	h_3
3			h_1	h_5	h_6	h_3	h_5	h_3	h_6	h_4	h_5	h_5
4				h_1	h_2	h_2	h_6	h_5	h_3	h_6	h_3	h_5
5					h_1	h_2	h_3	h_5	h_6	h_5	h_5	h_4
6						h_1	h_5	h_4	h_5	h_3	h_6	h_5
7							h_1	h_2	h_2	h_6	h_5	h_3
8								h_1	h_2	h_3	h_5	h_6
9									h_1	h_5	h_4	h_5
10										h_1	h_2	h_2
11											h_1	h_2
12												h_1

A myriad of crystal plasticity finite element frameworks have already been developed. The Kinematic frame usually relies on the decomposition of the deformation gradient tensor $\boldsymbol{F}$ into its elastic and plastic contributions $\boldsymbol{F^e}$ and $\boldsymbol{F^p}$ as:

$$\boldsymbol{F} = \boldsymbol{F^e} \cdot \boldsymbol{F^p}. \tag{2.3}$$

Applying only the plastic part of the deformation gradient results in the nucleation of crystal defects. In the absence of elastic strains, the resulting crystal is however relaxed which can only be possible if the crystal lattice is perfect. The multiplicative decomposition above can therefore be understood as the passage from a reference configuration to an intermediate relaxed configuration in which all dislocations are located at the crystal periphery as represented in Figure 2.8 [54].

It is interesting to note that lattice stretch and rotations are contained in the elastic part of the deformation gradient while the rigid body motions are contained in the plastic part, as the lattice structure is perfect in the intermediate configuration.

The velocity gradient tensor's plastic part $\boldsymbol{L^p}$ is usually decomposed as the sum of the contributions of plastic slips $\dot{\gamma^s}$ on every gliding system s:

$$\boldsymbol{L^p} = \sum_{s=0}^{N} \dot{\gamma^s} \mathbf{l} \otimes \mathbf{n}. \tag{2.4}$$

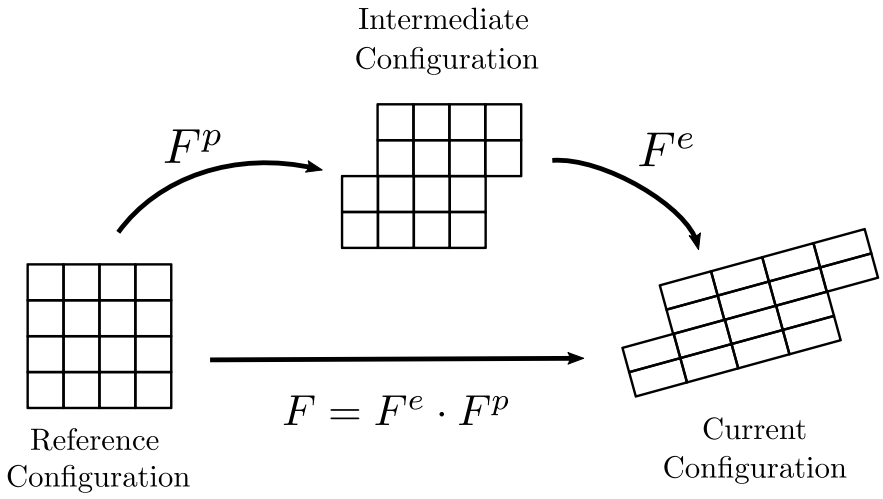

Figure 2.8 Decomposition of the total deformation gradient. In the intermediate configuration, all dislocations are supposed to be at the domain borders.

$\boldsymbol{F^p}$ can then be recovered by integrating the following equation:

$$\dot{\boldsymbol{F}}^{\boldsymbol{p}} = \boldsymbol{L^p} \cdot \boldsymbol{F^p}. \tag{2.5}$$

The material's resulting stress state can then be computed using Hooke's law:

$$\boldsymbol{\Pi} = \mathbf{C} : \boldsymbol{E}, \tag{2.6}$$

where $\boldsymbol{\Pi}$ is the large deformation first Piolat-Kirchhoff stress tensor, $\mathbf{C}$ is the material's stiffness matrix and $\boldsymbol{E}$ is the Green-Lagrange deformation tensor.

CPFE frameworks mainly vary in the law given for $\gamma^s(\tau^s)$. A large number of such laws have been reviewed by Roters et al. [54]. Both rate-independent and rate-dependent approaches were developed. However this work will only focus on rate-dependent approaches as it focuses on the importance of strain rate dependency.

Phenomenological approaches consider the average plastic straining on each gliding system as internal variables. For instance, the Meric-Cailletaud framework [1] considers that the resolved shear stress on each system τ^s is related to the system's shear strain rate according to a Norton's law using

$$\dot{\gamma^s} = \left\langle \frac{f^s(\tau^s)}{K} \right\rangle^n \operatorname{sgn}(\tau^s), \tag{2.7}$$

with

$$< x >= \begin{cases} 0 & \text{if} \quad x < 0 \\ x & \text{if} \quad x \geq 0 \end{cases},$$

K and n being material constants. An isotropic hardening term r^s is usually added to the flow rule f^s as

$$f^s(\tau^s) = |\tau^s| - r^s. \tag{2.8}$$

r^s results from the interactions between the different dislocation slip systems as:

$$r^s = R_0 + \sum_{q=1}^{N} h_{sq}(R_q - R_0), \tag{2.9}$$

where R_q is the hardening law at the system level, represented in this case by a Voce law:

$$R_q = R_0 + Q(1 - e^{-v^q b}), \tag{2.10}$$

where R_0 is the critical resolved shear stress, Q and b are two phenomenological constants, v^q

is the cumulative plastic slip for the q-th system and h_{sq} is the interaction coefficient between systems (s) and (q). It can be noted that h_{sq} has the same physical meaning as the hardening power previously defined in Section 2.2.1.

A common alternative approach [55] consists in relating τ^s to $\dot{\gamma^s}$ through a multiplicative definition:

$$\dot{\gamma^s} = \dot{\gamma_0^s} \left| \frac{\tau^s}{\tau_c^s} \right|^n \text{sgn}(\tau^s), \tag{2.11}$$

τ_c^s being the critical resolved shear stress for which gliding occurs on system s. Similarly as in the Meric-Cailletaud's approach, τ_c^s is related to hardening in system s using:

$$\dot{\tau_c^s} = \sum_{q=1}^{n} h_{sq} |\dot{\gamma^q}|, \tag{2.12}$$

According to Busso et al. [56], the additive and multiplicative approaches present similar behaviours even for multiaxial loadings. The major difference resides in the onset of plasticity which starts at the initial time using the latter approach, while the additive framework assumes that only elastic straining occurs for low stress values.

Physical approaches consider the average dislocation density in each gliding system as internal variables. Dislocation density based models provide a finer scale modeling, insights in substructure formation and better account for dislocation mechanics. In most classical CPFE models, hardening is most commonly related to the dislocation density using either the **extended Taylor equation**:

$$\tau_c^s = \mu b \sqrt{\sum_{q=0}^{N} a_{sq} \rho^q}, \tag{2.13}$$

or the **Orowan law**:

$$\dot{\gamma^s} = \rho_m^s b v^s, \tag{2.14}$$

where ρ^q is the dislocation density in system q, ρ_m^s is the mobile dislocation density, b is the dislocations' Burger's vector, μ is the material's shear modulus, a_{sq} is the interaction strenght between systems (s) and (q) and v^s is the mobile dislocations average velocity. Mechanisms influencing the dislocation density in every gliding systems, such as dislocation mobility, creation at sources, recovery, or annihilation, can then be accounted for by the sum of several terms in a dislocation evolution law $\frac{d\rho^s}{d\gamma^s} = g(\rho^s, T, \dot{\varepsilon}...)$. An extensive review of these possible terms is given in the review of Roters et al. [54]. One of the most common

expression for the dislocation density evolution is the Kocks-Mecking evolution law given as:

$$\frac{d\rho^s}{d\gamma^s} = \frac{1}{b}\left(\frac{\sqrt{\sum_{q=1}^{N} b_{sq}\rho_q}}{\kappa} - \gamma_c \rho\right), \tag{2.15}$$

where b is the Burgers vector amplitude, b_{sq} is an interaction matrix, κ represents the amount of obstacles seen by mobile dislocations and γ_c is the recovery rate coefficient. Equation 2.15 represents the balance between nucleation and glide of dislocations and their annihilation through recovery phenomena.

It is interesting to note that use of a Voce law in the Meric-Cailletaud framework provides a formulation that is compatible with Equation 2.15 [57]. Both approaches therefore usually yield similar results and mainly differ by the richness of information provided, as well as by the second interaction matrix b_{sq}.

Dislocation density based parameters identification can however hardly be experimentally performed, which constitutes the major drawbacks of such approaches. These parameters are usually obtained using Discrete Dislocation Dynamic (DDD) simulations as in the work of Devincre et al. [58].

2.2.3 Strain-rate dependency in crystal plasticity models

Strain-rate dependency of metals is closely related to their crystalline structure. Indeed, the underlying mechanisms related to strain rate dependency for FCC and Body-Centered Cubic (BCC) materials strongly differ.

At room temperature and for BCC structures, strain rate dependency is mainly attributed to athermal contributions such as Peierls stress (*e.g.* the stress required to move a dislocation) and lattice friction which increases the overall yield stress as the strain rate increases [60]

For FCC materials the underlying mechanism related to strain rate dependency depends both on the temperature and on the strain rate. Figure 2.9 shows the typical evolution of copper yield stress as a function of strain rate [59]. Two regimes can be observed:

- **A thermally activated regime** ($< 10^4$ s^{-1}) where strain rate dependency mainly influences strain hardening and does not have much influence on the yield stress
- **An athermally activated regime** ($> 10^4$ s^{-1}) characterized by a sudden raise of the yield stress with the strain rate.

In most metals, plastic straining is mainly accommodated by plastic slip. Such slip is possible

only if a sufficient shear stress is applied on the dislocations' respective gliding plane to overcome barriers such as other dislocations. Following the parallel recalled by Salvado et al. [61], each dislocation can be seen as a small oscillator with its own thermal energy. Schematically, the more a dislocation oscillates, the easier it is for it to overcome barriers. As the strain rate increases, less time is given for the thermal activation phenomena to occur, which results in a higher stress. At low strain rates, this is the main mechanism leading to strain-rate dependency for FCC metals.

This could be accounted for by considering the frequency v_1 of successful dislocation jumps over an obstacle, which can be related to the temperature using an Arrhenius law [61]:

$$v_1 = v_0 A exp\left(\frac{-\Delta G}{KT}\right), \tag{2.16}$$

where v_0 is the dislocation vibration frequency, A is a material constant representing the dependency to entropy, K is the Boltzmann constant and T is the temperature. In the above, ΔG represents the obstacles energy barriers. By neglecting the travel time of dislocations, this expression can then be related to the plastic strain rate using the Orowan equation which

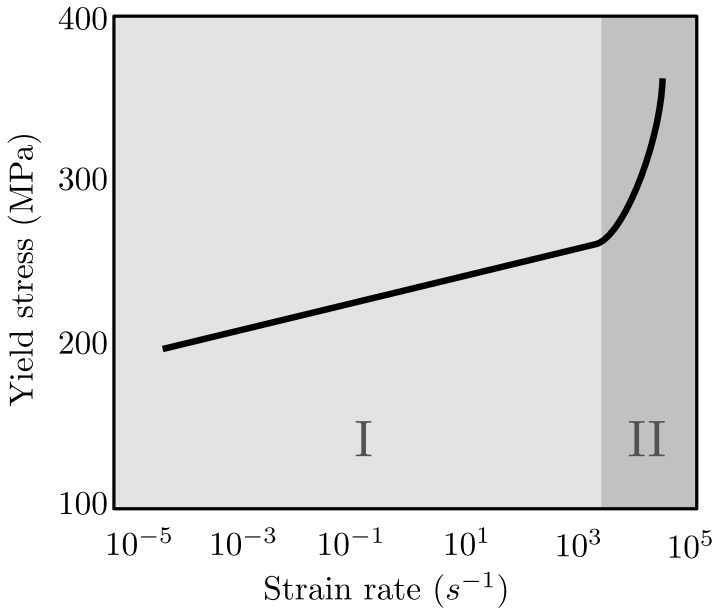

Figure 2.9 Typical evolution of copper yield stress with increasing strain-rate [59]. Two regimes can be observed: a thermally activated regime (I) where the strain rate has little influence on the yield stress and mainly influences strain hardening. An athermal regime (II) where the yield stress increases with the strain rate.

yields:

$$\dot{\gamma} = \frac{1}{Mv_1}\rho b \Delta l = \gamma_0 exp\left(\frac{-\Delta G}{KT}\right), \tag{2.17}$$

where M is the Schmid factor, ρ is the dislocation density, b is the Burgers vector and Δl is the distance between dislocation barriers.

The strain rate is then related to the stress by choosing a relevant form for the barrier energy ΔG. Kocks et al. [62] suggested a general form which has been used in many single crystal plasticity models for strain rate dependent applications [8, 63]:

$$\Delta G = \Delta G_0 \left[1 - \left(\frac{\tau}{\tau_0}\right)^p\right]^q, \tag{2.18}$$

where p and q are material constants.

For low strain rate ranges, the relationship between $\dot{\gamma}$ and $\exp\left(\frac{\tau}{\tau_0}\right)$ can sometimes be approximated as linear which leads to the Norton equation used in the Meric-Cailletaud framework and given by Equation 2.7 [64].

This reveals the limits of the Meric-Cailletaud framework in terms of strain-rate dependency, as it only remains valid for certain materials on a small strain-rate and temperature range.

As the strain rate increases (over 10^4 s^{-1}), dislocation inertial effects (such as phonon drag, scattering, radiative effects or lattice friction...) becomes the predominant mechanism [59,61, 65, 66]. Equation 2.7 can no longer be used in this regime due to the various non linearities occurring in the relationship between the applied stress and the dislocation velocity. It also does not account for a limiting velocity for the dislocation motion (usually taken as the speed of sound in the observed material). At even higher speed, the dislocation motion is supposedly subjected to relativistic effects as its velocity approaches that of the sound in the material. However, the literature still does not agree on this fact as no experimental evidence has yet been provided [66].

Under dynamic loading, and over 10^5 s^{-1} [43, 60, 67], several other contributions, have to be accounted for. According to Wang et al. [68] dislocation inertia plays a crucial role in the developing microstructures under high strain rate loading. Such effect was for instance successfully integrated in a macroscopic polycrystalline model by Rahaman et al. [69] using a dynamic flow rule with a micro-inertial term. The proposed framework successfully reproduced oscillations observed at the onset of plasticity for high dynamic loading of BCC molybdenum.

Under shock loading, plastic slip is accommodated by dislocation glide only if there is enough mobile dislocations. Otherwise, nucleation of new dislocations or alternate mechanisms are triggered [70] such as twinning, damage or phase evolutions. Propagation of an impact shock wave front toward a dislocation source could also result in dislocation avalanches [71].

Therefore, several authors focused on accounting for dislocation motion under dynamic loading to predict the capacity of mobile dislocations to accommodate plasticity. Luscher et al. [72] performed a numerical coupling of a dislocation density finite element model with a continuum dislocation transport and dislocation deformation incompatibility equation to study the influence of dislocation transport on material's response under shock loading. Several authors developed mesoscale continuous models for both isotropic [73] and orthotropic materials [65] using two (mobile/immobile) or three (mobile/immobile/pile-up) [74] dislocation densities internal variables to model the dynamic response of material's at high strain rates.

Accurate modeling of the high strain rate behaviour of materials under shock impact is therefore an active research field and remains a challenge. An extensive review of such work was performed by Salvado et al. [61] and several other models were also discussed by Djordjevic et al. [65]. Also, a very extensive review on the study of dislocation mobility at high velocity was provided by Gurrutxaga–Lerma et al. [66].

However, the models discussed above were developed for isotropic or orthotropic materials and would not be suitable for single crystal models as plasticity phenomena would certainly differ. Models accounting for anisotropy were developed but mostly at the scale of few dislocations using molecular dynamic simulations and would therefore not be relevant to model the process.

2.3 Mechanical surface properties characterization

Shot-peening affects depths generally around a few hundred microns under the treated part's surface. Local deformation close to the surface involves different straining mechanisms as compared to the bulk, as the constrained surface to volume ratio is high. For instance, plastic strain can be accommodated by dislocation annihilation at the surface around the impacts.

The impacted material's surface mechanical properties have therefore to be considered for accurate modeling of the process. This involves using experimental procedures with high surface to volume ratio representative of the process conditions in terms of strain rates.

Micromechanical testing such as micro-pillar compression [75], impact tests [76] offer such local observations and will thus be detailed in the following.

2.3.1 Micropillar compression

Micro-pillar compression consists in the compression of a micron-sized pillar using a diamond flat-punch in a Scanning Electron Microscope (SEM). This test provides a local load/displacement curve as well as insights into the material's local deformation mechanisms.

Such pillars can be manufactured by:

- **Surface lithography**, for which a mask is applied on the surface and is then submitted to ion-etching.
- **Focused Ion Beam (FIB)**, which consists in bombarding the surface with ions inside a SEM. This method usually leads to more reproducible geometries. It is nonetheless more time-consuming and expensive. FIB pillars are generally performed in several steps. First, high currents are used to build the raw pillar shape. Then, finishing steps are performed using low currents to avoid geometry changes due to material re-deposition.

FIB requires etching of a large area around the pillar - called a "bowl" - to allow SEM observations and to prevent the punch from touching the substrate. Based on numerical analyses, Zhang et al. [77] provided pillar geometry guidelines to accurately recover the material's local stress-strain curve.

Surface damage such as amorphisation or Ga^+ subsurface diffusion can occur down to a few nanometers when using FIB milling (see Figure 2.10 (3)). Xiao et al. [78] revealed an influence of Ga^+ subsurface diffusion on the observed yield strength for ultra-fine grain aluminum. No influence was observed for single crystal samples in their study. The pillar size therefore has to be large enough to make these effects negligible on polycrystalline samples.

Many works also suggest the presence of a size effect in pillars [79–81] (see Figure 2.10 (5)). The sollicited volume for which these effects occur depends on the tested material. For instance for copper, it is mainly predominant under 3 μm diameter and 6 μm height [82]. For sub-micronsize pillars, this effect is explained by many authors as a dislocation starvation effect in the pillar, which involves an inversely proportional relationship between the yield stress and the pillar dimensions [80]. Up to certain pillar dimensions, strain bursts are also usually reported in the litterature and could be inferred to dislocation avalanche for large-sized pillars and mechanical annealing for small-sized pillars [83]. **In general, several pillar**

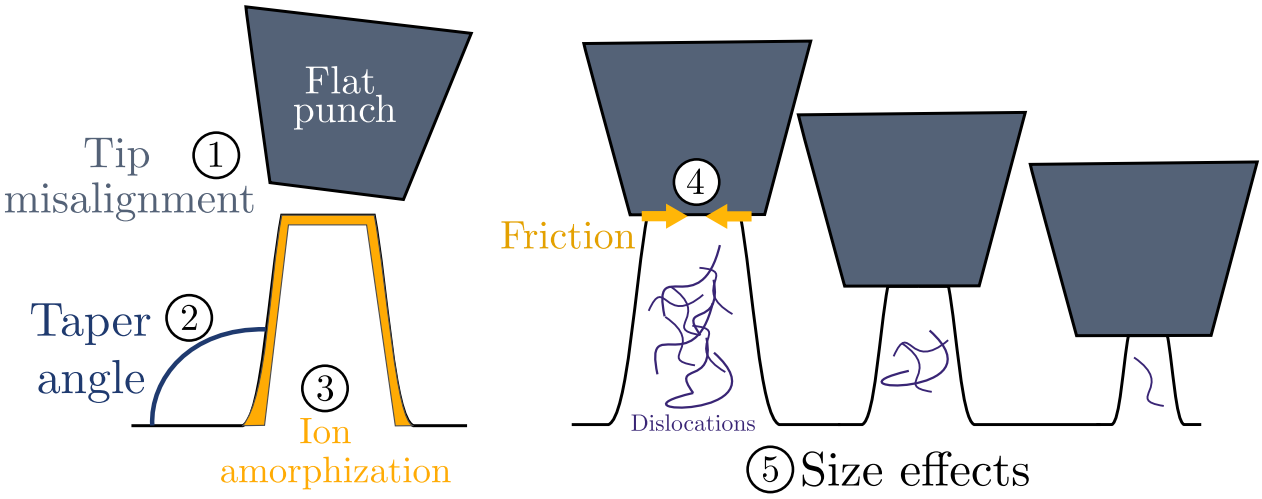

Figure 2.10 Micropillar compression test uncertainty sources. (1) Pillar/tip misalignment, (2) Taper angle, (3) Ga^+ ion amorphization, (4) Pillar/indenter friction, (5) Size effects.

sizes have therefore to be tested for material characterization to ensure that the measured properties are independent of the pillar size.

A slight pillar misalignment with respect to the indenter (see Figure 2.10 (1)) has a substantial influence on the Young's modulus estimation and could smear out the elastic-plastic transition [85]. For highly anisotropic single crystals, Soler et al. [85] showed that tip misalignment would lead to overestimations of the measured yield stress of about 12% for a 2° pillar to indenter misorientation. To correct possible misalignments inferred by sample non planarity, Singh et al. [86] measured the global surface geometrical angle, using a surface approach performed with an in-situ sharp nano-indenter, at several locations around the pillar. Experimental and predicted compressed pillars presented the same shapes and strain behaviour.

Pillar taper angle (see Figure 2.10 (2)) influences the pillar's stress distribution. Two effects can be considered: (i) yield stress overestimation due to a smaller pillar surface at the top and (ii) spurious strain hardening. According to Zhang et al. [77], this effect increases with the pillar-aspect ratio. It is therefore an important parameter to account for in simulations.

The load-displacement curve has to be corrected to account for the frame, the substrate and the indenter contribution to the measured displacements, as shown in Figure 2.11. The pillar displacement u_p is therefore expressed as:

$$u_p = u - u_{frame} - u_{indenter} - u_{substrate} = u - u_{frame} - \frac{F}{2rE^*_{ind}} - \frac{F}{2rE^*_{sub}}, \tag{2.19}$$

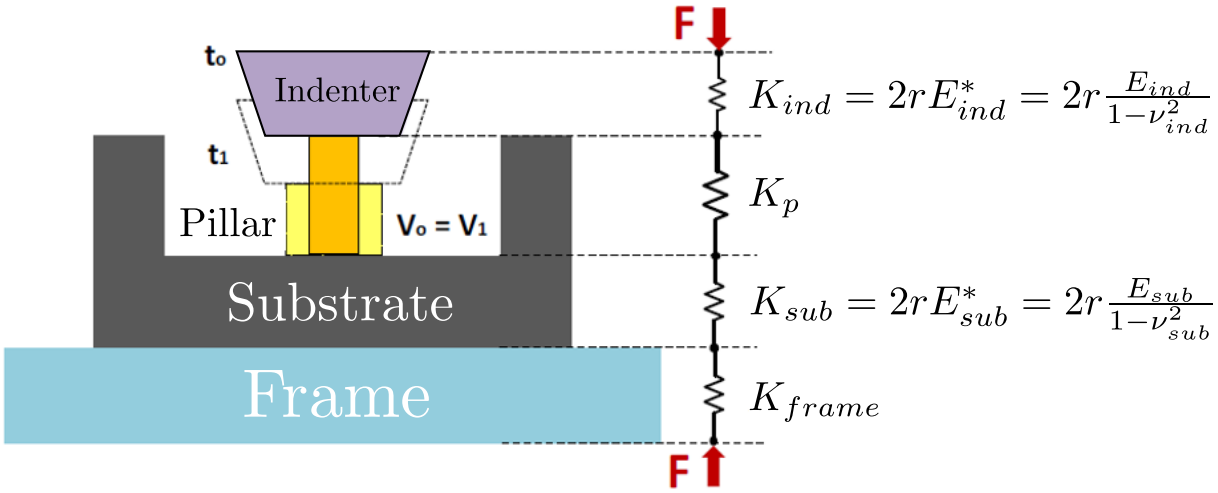

Figure 2.11 Displacement correction required to retrieve the pillar displacement, extracted from the work of D.Tumbajoy-Spinel [84]. The corrected curve accounts for the frame, the indenter and the substrate contributions.

where u is the measured displacement, E^*_{ind} and E^*_{sub} are respectively the indenter and the substrate reduced modulus, as defined in Figure 2.11, and r is the pillar's radius at a given time. For metals, the elasto-plastic transition is difficult to observe using micro-pillar compression as plasticity occurs for very small force values at the contact and at the pillar basis. The contact radius r can therefore be estimated by considering volume conservation of the deformed pillar in the plastic regime.

For anisotropic materials, the stress state in the pillar is rarely homogeneous. Zhang et al. [83] estimated the averaged stress-strain curve by evaluating the stress using the pillar's middle-height surface. Using the upper surface would provide an upper boundary of the stress experienced by the pillar. This alternative approach has for instance been used by Frick et al. [80]. These approaches provide pillar's geometry independent measurements of the local material's property. It therefore provides more relevant data for results comparisons.

Indenter to pillar friction (see Figure 2.10 (4)) should also be accounted for when perfoming micro-pillar FEA. Absence of friction leads to pillar buckling overestimations [77]. **However, the friction coefficient itself does not influence the load-displacement curve for single crystals** [81]. This hypothesis should however be validated when performing micro-pillar compression numerical studies. The indenter has therefore to be modeled to account for friction. It is usually taken as a flat rigid surface [75].

Figure 2.10 conveniently summarizes all the experimental uncertainties detailed above and

that should be accounted for when interpreting micropillar compression load displacement curves.

Cruzado et al. [87] performed crystal plasticity phenomenological constitutive law parameters inverse identification using micro-pillar compression testing on several Inconel 718 grains. Micro-pillar compressions were performed at different strain rates (10^{-4} s^{-1} up to 10^{-2} s^{-1}), pillar diameters and crystal orientations. Parameters were identified one by one using differentiating tests in single and multiple glide conditions. The identified parameters were then successfully used in a polycristaline model. **However, the well-posedness of the inverse problem was not demonstrated by the authors.**

Apart from the load-displacement curve, micro-pillar compression tests offers several other observation outputs. Gioacchino et al. [88] measured for instance the pillar rotation and strain fields after compression using Digital Image Correlation (DIC) on Oxygen Free High Conductivity Copper micro-pillars. Speckle pattern for DIC observations were made using FIB assisted deposition. This pattern deposition can be performed following a bitmap image. Their measured in-plane rotations were in good agreement with Electron BackScattered Diffraction (EBSD) measured crystal lattice misorientations.

In the works presented above, micro-pillar compression tests were performed in the quasi-static regime for strain-rates ranging from 10^{-5} to 10^{-2} s^{-1}. Recent developments now allows performing **high strain rate dynamic micro-pillar compression**. The set-up developed in the work of Guillonneau et al. [89] can achieve high strain-rates as high as 10^{3} s^{-1} for nickel nanocrystals. Such new experimental procedure provides new observation fields that could be used for high-strain rate constitutive law identification.

2.3.2 Impact tests

Several authors used high velocity single shot experiments to obtain material's surface properties. R. Guiheux [25] used a single impact shot set-up to study SP induced phase transformations of AISI 301LN austenitic steel. Nordin et al. [90] used single impact experiments to find a relationship between impact imprint geometrical characteristics and shot velocity to deduce low coverage SP shot velocity distribution.

The study of single impacts could be relevant for parameters inverse identification, at least in terms of strain rate dependency. K. Ekström [76] used single impact tests on SS2506 case hardened gear steel to assess the relevance of strain rate dependent framework parameters to simulate the impacted materials behaviour. To this end, the author compared predicted and

experimental impact imprint geometrical properties. However no parameter fitting the experimental impact geometries were found by the author. **Yet, no automated identification strategy was used in this study.** Also, the studied material presented impact-induced phase transformations which therefore required a more complex constitutive law to be used.

Impact tests should however provide experimental outputs, representative of the material's behaviour at SP strain rates and dynamic regime. It could be used for material's constitutive law parameters identification, provided choice and accurate measurement of the most relevant outputs.

Murugaratnam [91] developed an instrumented canon that can project shot peening medias at velocities ranging from 44 $m{\cdot}s^{-1}$ to 72 $m{\cdot}s^{-1}$ to study the dent shape, microstructural evolutions induced by single impacts as well as to obtain the coefficients of restitution (*e.g.* the ratio of the shot velocity after and before the impact event) of different impacts in different conditions. However, the author did not provide an analysis of the potential aiming accuracy of the system to perform repeated impacts at the same material spot.

Also, performing several impacts at the same material position would provide information on repeated impact induced cyclic effects at SP strain rates. Several authors used micropercussion experiments to obtain material's properties after repeated impact. The test consists in projecting a rigid indenter onto a surface by electromagnetic acceleration. The indenter is attached to a metallic rod which moves inside a cylindrical cavity. The apparatus can therefore perform several impacts at a given material spot [92].

Tumbajoy et al. [6] used micropercussion tests to study the influence of repeated impacts on mechanical properties gradient and microstructural evolutions of Fe-α samples. Al Baida [93] used micropercussion experiments to obtain the parameters of a power hardening law on a AISI M2 steel using the impact load and residual imprint radius after several impacts. The indenter diameter is usually around 2 mm which is large compared to industrial shot peening media. Also, the dynamic sollicitation differs from a projected shot as the whole system inertia and mass has to be accounted for.

In reality, shot peening involves a random distribution of repeated impacts at various velocities and angles. The induced residual stresses and hardening properties are closely related to such variety of impacts. For instance, Kobayashi et al. [29] used XRD-measured residual stress profiles after one and several impacts and indentation on steel polycrystals to show that multiple impacts were required to induce compressive stresses.

Material's mechanical behaviour identified using single impact experiments should therefore always be validated using multiple impacts tests at different material spots.

2.4 Microstructural state characterization

Assessing a model's capability to predict shot-peening induced residual stresses and hardening represents a challenge as their absolute value cannot be measured. However several methods provide estimations of residual stress and hardening variations. Those methods can be divided in two categories:

- **Non destructive methods** such as in-situ X-Ray Diffraction methods, ultrasonic or eddy current measurements
- **Destructive methods** such as hole drilling or ring core methods using for instance a Focused Ion Beam and a field measurement method (Digital Image Correlation, Moiré interferometry, or holography), crack-compliance methods, the contour method or High Angular Resolution Electron BackScattered Diffraction, XRD methods or nanoindentation.

Non destructive methods are useful for comparison with standard measurements on industrial parts that should not be destroyed but do not yet provide enough resolution and accuracy to estimate residual stress or hardening distributions on single crystals.

Diffraction based methods are the most promising methods to accurately measure residual stresses at the crystal scale as their resolution is of the order of the interaction volume (down to a few hundreds of nanometers). Such methods could be divided in two categories: X-ray diffraction and electron diffraction based methods.

2.4.1 Residual stress estimations

X-ray diffraction based methods

XRD is extensively used in the literature for material characterisation as it provides insights into the material's micro-structure, hardening, residual stresses, texture and chemical composition. XRD analyses consist in sending an X-ray beam ($0.1 \leq \lambda \leq 10\mathring{A}$, λ being the beam wavelength) on a sample and to measure the diffracted beam intensity, for various θ diffraction angles.

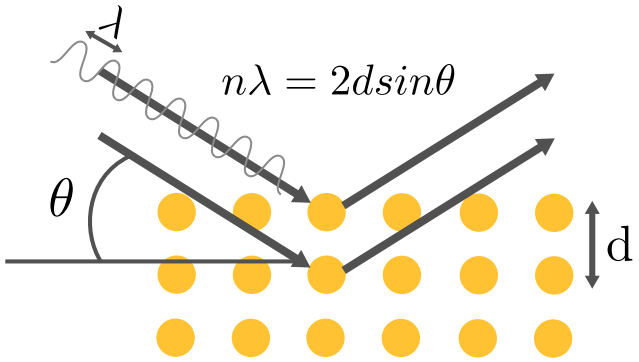

Figure 2.12 Schematic representation of the Bragg's law of Diffraction.

Analyses are usually based on a diffractogram showing the variations of the diffracted beam intensity with the diffraction angle. Residual stresses induce shifts in the local latice inter-reticular distance d. This results in slight shifts $\Delta\theta$ of the diffractogram peaks [94]. Most XRD residual stress estimations therefore relies on relating such peak shifts with the residual elastic strains.

The crystal lattice structure can be directly related to the diffraction angle according to the Bragg's law, as schematized in Figure 2.12. For instance, the $\sin^2\psi$ methods relies on the relationship between strain and peaks shifts given by Bragg's law. Stresses are then related to the lattice strain estimated with the peak shifts using Hooke's law for isotropic materials, usually with a plane stress conditions hypothesis. This usually results in a linear relationship between the peak shifts and a combinaison of the stress tensor's component, which parameters are found by varying the X-ray beam angle.

To obtain satisfactory results, the observed surface has to diffract for as many θ angles as possible. Therefore better results are obtained if the X-ray spot is positioned on a large number of grains.

This method therefore provides the residual stress average over a surface. Also, it is less efficient on coarse grain structures, textured or anisotropic materials, as it relies on Hooke's law expression for isotropic materials.

Alternatively, the Ortner method is an XRD based method that can provide residual stress average estimations over monocrystalline surfaces by varying the crystal orientation observed by the X-Ray beam. Morançais et al. [95] successfully applied this method to estimate the residual stress gradient induced in shot peened nickel superalloy specimens. Using the Monte-carlo algorithm, the authors assessed that the method provides stress tensor estimations

within an accuracy of 30 MPa, provided that at least 17 non colinear Bragg's angle are used for measurements.

However the resolution of the Ortner method is limited to a few dozen micrometers due to the large interaction volume of the X-ray beam in the probed material [47].

The aforementioned methods can be performed in a regular lab. The measured field resolution depends mainly on the spot sizes which ranges between a few millimeters to a few dozen micrometers (for micro-XRD). Also, the typical interaction volume depths are of the order of a few micrometers. Alternative methods such as micro-Laue diffraction provides residual stress and hardening diffraction with sub-micrometric resolutions when performed in a synchrotron [96]. Using polychromatic beams, the full stress tensor can be recovered [97] with an accuracy on the elastic strain measurement of 4.5 10^{-5} [98].

Such measurement are however quite tedious and expensive as they require a synchrotron.

High angular resolution electron backscattered diffraction

EBSD relies on the analysis of diffraction patterns produced by an electron beam on a crystalline material. A stationary electron beam is projected on a crystalline material in a SEM. The electron beam diffracts on the different crystal lattice planes in every directions, producing diffraction cones (see Figure 2.13 (a)). These cones produce several bands on a phosphor screen, captured by a Charge-Coupled Device (CCD) sensor. The resulting pattern is usually called a **Kikuchi diagram**. Figure 2.13 shows an example of Kikuchi diffraction diagram for [100] single crystal copper.

A Kikuchi diagram is specific of the observed crystal lattice and orientation. Classical EBSD consists in retrieving the local crystal orientation by diagram indexation based on the lattice parameters.

Local elastic strains and rotations produce small shifts in the Kikuchi diagram. These shifts are only sensitive to deviatoric strains and cannot account for hydrostatic changes [100]. It is therefore possible to retrieve the in-plane local rotation and deviatoric strain tensor by diffraction pattern cross-correlation with a reference pattern.

To relate those shifts with the residual elastic strain, a geometrical model has to be derived, such as the one derived by Maurice et al. [101]. If **dX** is a crystal lattice volume element,

corresponding to the beam position S, it will be mapped by a point P on the screen by:

$$\mathbf{SP} = \mathbf{r} = \alpha \mathbf{dX}, \tag{2.20}$$

as shown in Figure 2.14. If (x, y) are the coordinates of P on the screen and (X^*, Y^*, Z^*) the coordinates of the diffraction pattern center (PC) (the horizontal projection of the analyzed point), the gnomonic projection of a point on the screen can be expressed in the screen 3D reference frame as:

$$\mathbf{SP} = (x_p - X^*, y_p - Y^*, Z^*)^T. \tag{2.21}$$

Accordingly, a volume transformed by $\boldsymbol{F}$ will be mapped to a point P' on the screen by

$$\mathbf{SP'} = r' = \alpha' \mathbf{dx} = \alpha' \boldsymbol{F} dX = \mathbf{r} + \mathbf{q}, \tag{2.22}$$

where $\mathbf{dx}$ is the volume element in the transformed frame and q the shift vector.

Since every point on the screen has the same Z^* with respect to the sample's coordinate

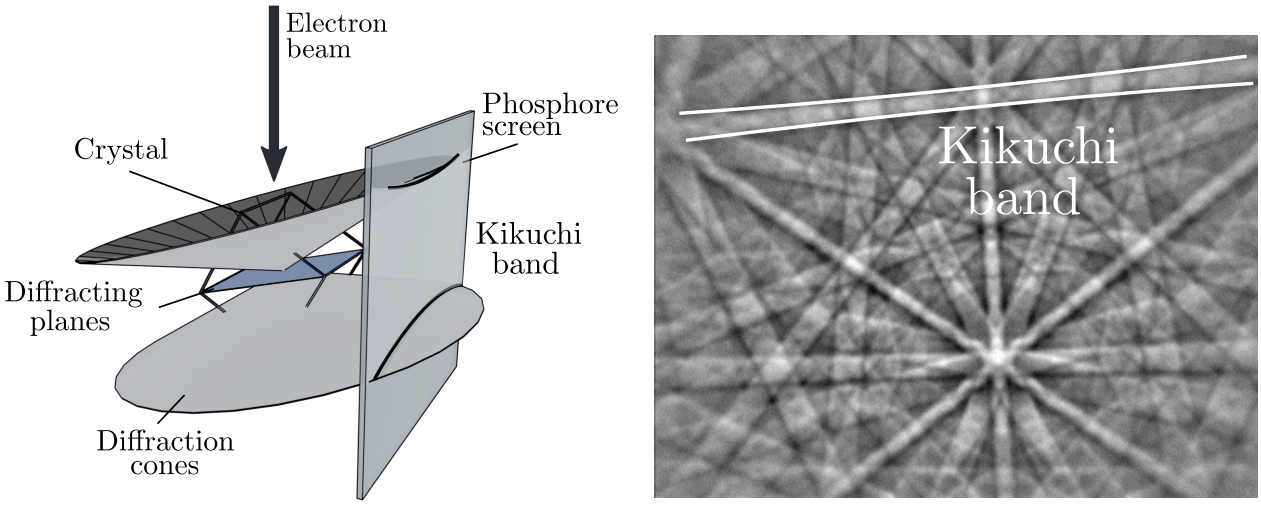

Figure 2.13 Formation of Kikuchi bands. (a) Incident electron beam on the sample diffracts in every direction, producing a diffraction cone. These cones produce straight bands on the phosphor screen, also called "Kikuchi bands" [99]. (b) Kikuchi diagram resulting from the combination of all the Kikuchi bands on the screen. A particular band has been highlighted in white.

.

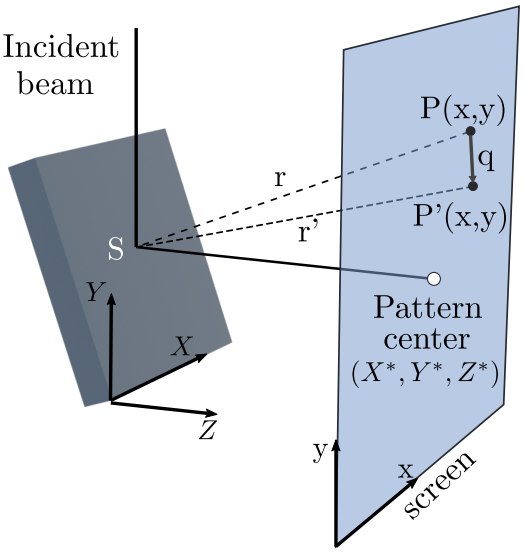

Figure 2.14 EBSD setup geometry. Schematic representation of the geometrical model used to relate band shifts and residual elastic strains.

.

system, one can write

$$\alpha' dx \cdot k = Z^*, \tag{2.23}$$

where k is the unit vector for the third coordinates in the screen 3D reference frame. Therefore, the transformation of r by $\boldsymbol{F}$ can be expressed as:

$$r + q = \frac{Z^*}{\boldsymbol{F}dX \cdot k} FdX. \tag{2.24}$$

A possible approach to find $\boldsymbol{F}$ is to find the shift q between a stress-free reference pattern and the observed pattern using cross-correlation and to find F that minimizes the following cost function [101]:

$$V(\boldsymbol{F}) = \sum_{i=0}^{N_{ZOI}} \frac{1}{2} \left\| \frac{Z^*}{\boldsymbol{F}.\mathbf{r_i}.\mathbf{k}} \boldsymbol{F}.\mathbf{r_i} - \mathbf{r_i} + \mathbf{q_i} \right\|, \tag{2.25}$$

where N_{ZOI} is the number of zone of interest (*e.g.* subsample of the pattern) chosen for the cross-correlation.

Pionnered by Troost [100] and further developed later by Wilkinson [102], this method provides the local rotations and in-plane components of the local elastic strain tensor with an accuracy of 10^{-4} [101]. The local stress tensor is recovered using Hooke's law given by Equation 2.6.

Historically, diffraction pattern cross-correlation was performed by the comparison of dif-

ferent Zone Of Interest (ZOI), dividing a global Region Of Interest (ROI) chosen on each Kikuchi diagram. Cross-correlation consists in minimizing the differences between the deformed reference and the observed ROI.

HR-EBSD still presents some limitations, especially for measurements in polycrystals. Assumptions have to be made on the residual stress state of the reference point. In a single-crystal, it is reasonable to assume a zero-stress state, far from the solicitation. **However, such hypothesis cannot be made in a polycrystal, for which HR-EBSD however gives an accurate estimation of the local orientations and strain variations.**

Also, as presented above, the pattern center position has a substantial influence on the estimated strain field and should therefore be determined with high accuracy. **Conventional calibration techniques provide an estimation of the PC position within an accuracy of 0.5% of the pattern width, which could result in phantom strains of the order of** 10^{-3} [103]. Several authors [104, 105] proposed new PC calibration methods based on comparison with dynamically simulated patterns. In particular, Tanaka et al. [105] used global optimization algorithm to obtain PC calibration within an accuracy of 10^{-5} of the pattern width.

Finally, recovery of the full stress tensor is generally done by assuming plane stress conditions at the probed surface [102]. Such an assumption can also be a source of errors, which could be negligible in most cases, as discussed by Hardin et al. [106].

Both diffraction methods therefore have their respective benefits and drawbacks. A comparison of the aforementioned methods can be found in Appendix A. Overall, HR-EBSD provides a better spatial resolution than micro-Laue diffraction and can be performed in a regular laboratory, even though it can only recover the stress variation relatively to a reference point.

The present work will therefore mainly focus on the use of HR-EBSD for residual stress measurements.

2.4.2 Geometrically Necessary Dislocation density estimations

Geometrically Necessary Dislocations (GND) (as opposed to Statistically Stored Dislocations (SSD)) designate the part of the total dislocation density that contributes to the lattice observed curvature **at a given scale** as schematized in Figure 2.15. Several methods based either on XRD or EBSD measurements can be found in the literature to estimate GND density variations. As GND estimations from EBSD measurement rely solely on the misorientation

field, such estimation can be performed using the data already gathered for residual stress estimations. Therefore, only the EBSD based method will be detailed in the following.

General principle

Considering an arbitrary surface S in a metallic material intersecting several dislocations, as represented in Figure 2.16 (a), the resulting Burgers vector of the intersecting dislocations B is related to the individual dislocation Burgers vector b and line vector t as [107]:

$$\mathbf{B} = \left(\int_S \mathbf{t} \cdot \mathbf{n} dS \right) \mathbf{b} = \int_S \boldsymbol{\alpha} \cdot \mathbf{n} dS, \tag{2.26}$$

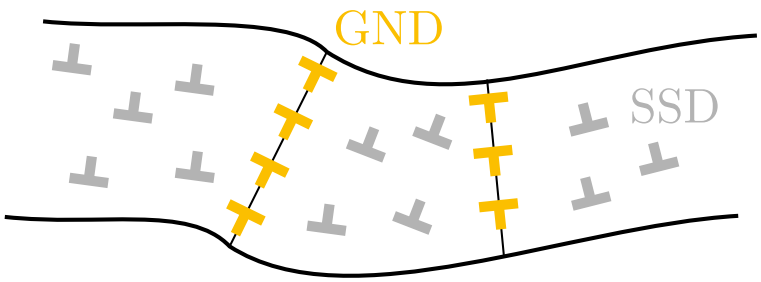

Figure 2.15 Schematic representation of Geometrically Necessary Dislocations (GND, in orange) contributing to the global lattice curvature at the observed scale, as opposed to Statistically Necessary Dislocations (SSD, in gray)

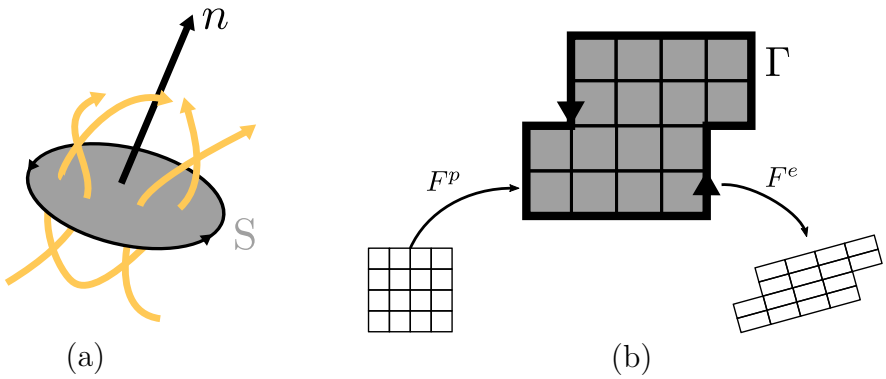

Figure 2.16 Estimation of GND densities using the Nye tensor. (a) Arbitrary surface S intersecting several dislocations (in orange). (b) S represented on the intermediate configuration of the multiplicative decomposition of F.

where $\boldsymbol{\alpha}$ is known as the Nye dislocation tensor. By restricting dislocation gliding to N slip systems, one can therefore write:

$$\boldsymbol{\alpha} = \sum_{s=1}^{N} \rho_s b^s \otimes t^s \tag{2.27}$$

Recalling the decomposition presented in Section 2.2.2 and recalled in figure 2.16 (b), the resulting Burgers vector of an arbitrary contour Γ can also be obtained by integrating a contour in the intermediate configuration as:

$$\mathbf{B} = \oint_{\Gamma} (F^e)^{-1} dx, \tag{2.28}$$

which results in the following relationship:

$$\alpha = curl((F^e)^{-1}). \tag{2.29}$$

For small strains, one can write [108]:

$$(F^e)^{-1} = (\boldsymbol{I} + \boldsymbol{\beta^e})^{-1} \approx I - \boldsymbol{\beta^e}, \tag{2.30}$$

where β^e is the displacement tensor, which results in:

$$curl(F^e) \approx curl((F^e)^{-1}) \tag{2.31}$$

Using the polar decomposition, we then have:

$$\alpha \approx curl(F^e) = curl(R^e U^e), \tag{2.32}$$

where R^e and U^e are respectively the rotation and stretch tensors. As previously mentioned, R^e is therefore the crystal lattice measured by EBSD indexation. By combining equations 2.27 and 2.32, one can derive a direct relationship between the lattice stretch and rotations and the GND density as:

$$\sum_{s=1}^{N} \rho_s b^s \otimes t^s = curl(R^e U^e) \tag{2.33}$$

It is really important to note that ρ_s in equation 2.33 is only the geometrically necessary part of the total dislocation density as it was obtained by integrating on an arbitrary surface at a given scale.

As classical EBSD only gives access to the lattice rotations, several authors [16, 109–111] neglect the elastic stretch contribution to the deformation gradient in equation 2.33 to es-

timate the GND density distribution. As pointed out by Acharya et al. [112] and further investigated by Mohamed et al. [113] **such estimation could lead to substantial errors in the estimation of the dislocation density tensor in the presence of residual elastic strains.**

For FCC crystal structure, 18 slip systems are usually chosen (12 pure edge and 6 pure screw). As EBSD only provides in plane measurements, only five out of the nine components and the difference between two components of the Nye dislocation density tensor can be recovered [109]. Equation 2.33 therefore only provides five equations for the 18 unknowns GND densities in each system. To better condition the problem, an additional quantity is usually minimized, such as the GND line energy [109,111], the total dislocation density [114], or the dislocation vector L^2 norm [115].

Such method therefore only provides a lower bound of the GND density, as demonstrated by Kysar et al. [110]. Also, as shown by Das et al. [108], the choice of the quantity to minimize has only an influence on the GND density distribution in each system but not on the total GND density estimation.

Usual smoothing techniques

GND estimations rely on the misorientation field computed using the EBSD obtained crystal orientations. It is therefore highly sensitive to noise in the orientation field as it rely on its derivative. Several authors uses filters on the orientation map to overcome this issue [116–118].

Hielscher et al. [117] and Seret et al. [118] compared the influence of several smoothing filters commonly used in the literature. Such methods usually result either in smoothing of the GND variations or apparition of blocky artefacts and spurious dislocation densities. Variational filters are the most promising as they rely on a formulation that is physically consistent with the filtered data. The general idea is to find a denoised field from the experimental field which minimizes a given energy functional relating the two. For instance, Seret et al. [118] suggested to minimize a functional which combines both the difference between the filtered and non filtered maps as well as the lattice curvature. The filter successfully preserved artificially noised low angle boundaries and was successfully applied on experimental data.

Another approach is to filter the Kikuchi diagrams directly to get smoother orientation maps by ensuring consistency between neighbooring analyzed points. For instance, the Non-Local Pattern Averaging Reindexing (NLPAR) [119] method consists in averaging each Kikuchi patterns with the neighboring pattern of the analyzed point. The method uses a weighted

average which accounts for the similarity of one pattern with its neighbors to ensure that high misorientations would not be smoothened by the algorithm. **Such method has the benefit to improve the indexation quality without altering the information and without producing spurious misorientation, as it acts directly on the diffraction pattern which can then be indexed using conventional methods.**

NLPAR was originally developed in IDL language and provided open source on the author's github. This language requiring a paid licence, the code was re-implemented in python in the frame of the present work to compare different diffraction pattern analysis methods for GND estimations. The code is provided as open source for further studies [1].

Dictionary indexing

Another way to improve EBSD indexation rate and obtain smoother orientation fields is to use alternative indexing methods. Indexation of Kikuchi pattern is typically performed by detecting the diffracted bands using the Hough transform [120]. Dislocations induce local lattice misorientations. When high dislocation densities are present, the observed Kikuchi diagram is an average of all the diagrams produced by all the crystal orientations present in the probed volume. This results in noisy diagrams in which the bands have less defined edges and are therefore harder to detect using the Hough transform.

Dictionary indexing [3] is an alternative indexing method which do not rely on band detection

[1] `https://github.com/simonBreumier/pyNLPAR`

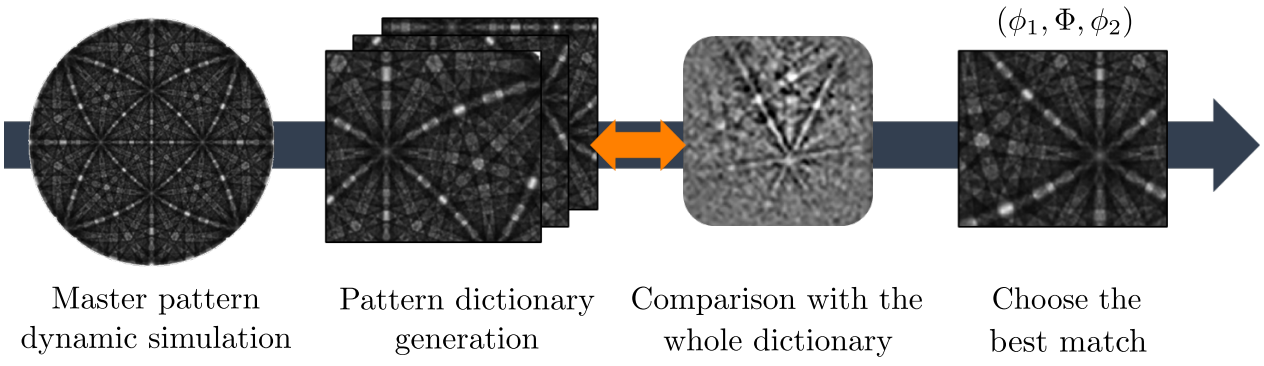

Figure 2.17 Dictionnary indexing algorithm [3]. First a master pattern is generated using dynamical simulations. The master pattern is then used to generate a dictionnary of Kikuchi diagram representative of a sample of the orientation space. The experimental diagram is then compared to every pattern of the dictionnary using a dot product metric and the best match is chosen a the probed volume orientation.

to find the probed crystal volume average orientation. The method consists in generating a dictionary of dynamically simulated pattern for a given sampling of the orientation space. Each experimental diagram is then compared to each simulated diagram of the dictionary using a relevant metric (typically, the dot product of the two diagrams). The experimental point orientation is then chosen as the orientation of the simulated diagram which is the most similar to the experimental one. Finally, the material point orientation is refined by orientation subsampling close to the found solution. Figure 2.17 conveniently summarizes the different steps of the method.

The method was successfully applied on shot-peened aluminium alloy by Singh et al. [121] and is also robust toward pattern similarities [122] and pseudo-symmetries [123].

Dictionary indexing usually requires high computation time, even when parallelized on a GPU as each pattern has to be compared to the whole dictionary. Recently, spherical indexing was proposed as a much faster alternative to standard dictionary indexing first by Hielsher et al. [124] and then implemented by Lenthe et al. [125]. The method relies on the comparison of the spherical harmonic transform of the experimental pattern projected on the Kikuchi sphere, and dynamically simulated Kikuchi sphere. The spherical transform being very fast to compute, the method provides near real-time indexing, depending on the discretization factor chosen.

These methods are therefore promising alternatives to the conventional Hough transform for EBSD map of highly deformed materials and could be used effectively for GND map estimations.

2.5 Constitutive theory parameters inverse identification

2.5.1 General principle

The identification of a constitutive theory's parameters p, in the admissible parameter space Θ of a constitutive law $\mathcal{L}$, considering input solicitations y^s, using observations y^r consists in fact in finding:

$$\mathbf{p} = \underset{\mathbf{p}\in\Theta}{\operatorname{argmin}} \|\mathcal{L}_p(\mathbf{y^s}) - \mathbf{y^r}\| \tag{2.34}$$

The identification is usually cast as a minimisation problem where the cost function measures the distance between experimental and numerical observations, by the use of optimization algorithms, such as:

- **First order algorithms**: Based on the calculation of the cost function first derivative. The best-known example is the steepest gradient descent algorithm for which the first derivative is used as the direction chosen for parameters choice at each step. Such algorithms are usually good for a first raw approach of the solution but does not converge very well when close to the solution.

- **Second order algorithms**: Based on the calculation of the cost function first and second derivatives. The best-known examples usually consist in the minimisation of the second order Taylor development of the cost function. The second derivative is usually approximated as it requires heavy calculations, unless it can be computed explicitly. For instance, the Levenberg-Marquardt algorithm uses the square product of the cost function's Jacobian to approximate the second derivative. Such algorithm converges in few steps with high precision, however they are not adapted for constrained optimization and are not adapted when starting far from the solution.

- **Sequential quadratic programming**: Based on successive minimization of the cost function using Lagrange multipliers. Constraints can be directly handled using such approach.

- **Statistical algorithms**: Based on a random choice of the parameters. The choice of the parameter statistical distribution is driven by the cost function values at each optimization step. The Monte-Carlo algorithm are one of the best-known examples. Those methods usually require many estimation of the cost function. However, it does not require to calculate the function derivatives and covers the whole solution space, hence reducing the possibility to fall in local equilibriums.

- **Mesh-based optimization algorithms**: Based on a mesh covering the whole solution space. The cost function is computed on well-chosen points of the mesh, which is then refined, depending on the actual mesh performances. The Mesh Adaptive Direct Search [126] algorithm is a good example of such approach. These algorithms usually converge in fewer steps than a probabilistic algorithm, without requiring derivative computations. However, they would generally require more steps to converge to the exact solution compared with a derivative-based approach.

2.5.2 Inverse problem conditioning

Observations generally vary by their nature (stress, strain...) and by their measurement accuracy: it is therefore necessary to perform identification on dimensionless variables and

to account for uncertainties. Usual cost functions are defined as [127] :

$$V(\mathbf{p}) = \frac{1}{N_v} \sum_{o=1}^{N_v} \sum_{i=1}^{N_o} \left(\frac{y_i^o(\mathbf{p}) - y_{e,i}^o}{sc_{y_i^o}} \right)^2, \tag{2.35}$$

where N_v is the number of variables, N_o is the number of observations for variable o, e is an index referring to experimentally observed variables, i the observation number and sc is a scale factor accounting for uncertainties computed as:

$$sc_{y_i^o} = \Delta y_{e,i}^o \sqrt{N_o}. \tag{2.36}$$

Converging on a solution only implies that a solution exists. To ensure that such parameters will represent the material's behaviour for different solicitations than those used for identification, parameters also have to be [51]:

- **Unique** : only one set of parameters $\mathbf{p}$ will satisfy $\mathcal{L}_{\mathbf{p}}(\mathbf{y^s}) = \mathbf{y^r}$.
- **Stable** : the parameters $\mathbf{p}$ vary continuously with the data $\mathbf{y^r}$. A small variation $\|\delta \mathbf{y^r}\|$ should only imply a small variation $\|\delta \mathbf{p}\|$.

These conditions will ensure that the chosen set of parameters will remain relevant for different initial conditions. The uniqueness and the stability of the optimization problem highly depend on the observation fields chosen. For instance, Chen et al. [128] showed that two parameters of a power hardening law could lead to the same Berkovich indentation-induced load-displacement curve. Therefore, for this identification problem, the sole use of the load-displacement curve does not provide unicity of the coefficients. For the power hardening law, this issue was solved by performing indentification on both the load-displacement curve and the residual indentation topology [129].

Guery et al. identified the Meric-Cailletaud framework parameters for 316L austenitic stainless steel, using polycrystalline tensile tests. Both load-displacement curves and local DIC strain measurements were used for the identification. To ensure the stability and uniqueness of their solution, the authors plotted the cost function values obtained using different parameters, to reveal the global *shape* of the cost function. The study showed that two isotropic hardening coefficients and three interaction matrix parameters could be identified using such experimental outputs.

However, inverse identification procedures usually require time-consuming simulations which does not allow to plot the cost function evolution. In such case, when using second-order optimization algorithms, the values of the cost function second derivative close to the solution

gives valuable information of the solution stability and uniqueness. Indeed, it provides information on the cost function convexity. Richard et al. [127] suggested to use an identification indicator I, defined as:

$$I = \log_{10}\left(\frac{\lambda_{max}}{\lambda_{min}}\right), \tag{2.37}$$

where λ_{max} and λ_{min} are the eigenvalues extrema of the approximated dimensionless hessian matrix close to the solution, defined as:

$$\overline{H}_{ij} = \sum_{t=0}^{T} \frac{\partial \overline{y}(t)}{\partial \overline{p_i}} \frac{\partial \overline{y}(t)}{\partial \overline{p_j}}, \tag{2.38}$$

where $\frac{\partial \overline{y}(t)}{\partial \overline{p_i}}$ is the sensitivity of the observable y to the parameter p_i and T is the number of acquisition points. The overline notation designates dimensionless quantities. This indicator can therefore be visualized as the ratio between the two axes of the ellipse of the cost function close to the solution. **This is therefore a local indicator of the solution stability and unicity.**

According to Richard et al. [130], a value of $I < 2$ is representative of a good conditioning of the inverse problem. However this value should not be taken as an absolute reference as it remains a local approximation of an ideal case.

Also, careful analysis of the sensitivities individual tendency should be carried out before

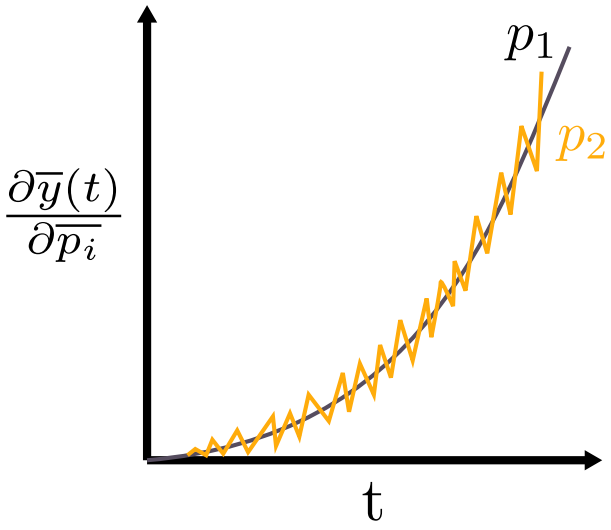

Figure 2.18 Influence of noise on the identifiability index. Variation of the sensitivity of an observed field y toward two parameters p_1 and p_2 with respect to time. Noise on the sensitivity variations to p_2 artificially decorelates the influence of the two parameters.

interpreting the value of I as it is highly sensible to noise. To understand this, consider the situation represented in Figure 2.18. The figure represents the evolution of the sensitivity of an observable y toward two parameters p_1 and p_2 with respect to time. Identification of such parameters using y as an observed field would obviously not be a well conditioned inverse problem as a given variation of the two parameters result in the same average variation of the observable. There is therefore a strong colinearity of the two sensitivity vectors. However, the strong noise observed on the variations of $\frac{\partial \overline{y}(t)}{\partial \overline{p_2}}$ artificially decorelates the influence of the two coefficients. Such effect could result in lower values of I as it represents the multicollinearity of the studied coefficients. In this case, the low value of I would therefore not be related to a well conditioning of the problem and should therefore be considered with great care. To better understand how I works and the influence of different parameters on its value, the reader is invited to read the Jupyter notebook implemented during this work[2].

This indicator was used in the research project of E. Renner [51]. This work focused on the identifiability of the Meric-Cailletaud crystal plasticity framework parameters using Berkovich indentation on nickel single crystals. The author identified the constitutive law parameters using the residual Berkovich indent topology measured by Atomic Force Microscopy (AFM) for several crystal orientations. Use of the I indicator revealed that the combination of two topologies obtained for different crystal orientations could lead to better uniqueness and stability of the nine Meric-Cailletaud parameters in a single identification procedure compared with the sole use of load-displacement curves.

The use of such indicators is therefore of crucial importance to assess the relevance of the observed output and the quality of the obtained solution.

2.6 Conclusion of the literature review

Only few works attempted to predict shot peening induced residual stress and hardening at the grain scale using CPFE calculation. Castro Moreno et al. [19] showed that the intragranular stress distribution depended on the initial material microstructure. Rousseau et al. [18] revealed that classical CPFE framework could predict hardening gradients induced by the process. Musinski et al [8] demonstrated that intragranular stress distribution could influence the stress relaxation over the cycles. However, the following limitations arise from the aforementioned works:

[2] `https://colab.research.google.com/github/simonBreumier/Play_with_I/blob/master/Playing%20with%20I.ipynb`

The influence of the initial crystal orientations on the induced microstructural changes and residual stresses at the grain scale was not yet assessed. Castro Moreno et al. [19] studied the influence of the initial microstructure on the intragranular stress distiribution, however their work was purely numerical. Also, the authors did not investigate initially textured microstructures. This could provide insights in the influence of crystal plasticity anisotropy on the induced residual stress field when peening textured or coarse grain structures such as welded or additive manufactured parts [48, 49].

The influence of the initial treated part geometry on microstructural evolution at the grain scale was not yet assessed. Recently new approaches have been developed to predict the shot peening induced residual stresses and hardening on complex geometries [9]. Several authors investigated the influence of the initial geometry on the global material's properties [131–134]. However the link between such properties and the microstructural evolution at the grain scale was not assessed. This would provide additional arguments to model the process at the grain scale.

Previous studies used CPFE frameworks identified on Split Hopkinson Pressure Bar (SHPB) tests which do not represent the material's surface behavior and do not entirely reach shot peening induced strain rates. Several authors developed crystal plasticity parameters identification procedure at local scales using either DIC [135,136] or nanoindentation [137]. However such tests can mainly be performed at low strain rates. The recent development of high strain rate microcompression experiments [89] allows to perform such local tests at strain rates up to 10^3 s^{-1}. The well-posedness of the identification problem will however need to be assessed before identification to ensure that such test is rich enough to provide insights in the role of each coefficient on the material's behavior. The identifiability index proposed by Richard et al. [130] as well as thorough analyses of the sensibility of the pillar stress strain curves to each coefficients could assess that such test is relevant for identification.

No experimental validation of the predicted residual stress distribution was provided in those studies: therefore the relevance of using classical crystal plasticity framework to model the process has not yet been assessed, nor was their capacity to predict impact induced residual stress distribution. Rousseau et al. [18] selected one of the impact dent produced by a shot peening treatment and compared the induced in-depth hardening to that predicted by simulations. However this methodology does not provide control on the impact conditions (velocity, angle, shot diameter). Also, measurement of these conditions is subjected to errors given the large number of impacts involved in the treatment. Single impact tests would provide such conditions, however, very few authors

developed accurately controlled impact experiments that fits the industrial process conditions [76, 91]. Also, such validation would require to estimate the residual stresses under the impact dent. Recent development in HR-EBSD could provide such measurements that could be compared to finite element simulations [138, 139].

The objectives of the present work are therefore the following:

1. Provide additional evidences of the relevance to predict the induced residual stresses and hardening at the grain scale.
2. Propose a methodology to identify CPFE behaviour at high strain rate and at the surface scale.
3. Develop tools to validate CPFE models using various experimental fields under the process conditions.

The project was therefore divided in the following parts summarized in Figure 2.19:

- Validation of the possibility to compare HR EBSD and CPFE stress output under spherical loading and study the influence of crystal orientation on the induced residual stress.
- Study of the subsurface microstructural evolutions induced by shot peening on non linear geometry to develop tools for microstructural characterization using different EBSD analysis techniques and assess the link between microstructural evolutions and the treated part geometry.
- Proposition of a CPFE model identification methodology at the surface scale using high strain rate micropillar experiments.
- Development of a shot peening canon to perform controlled shot experiments for the validation of the previously identified CPFE models using HR-EBSD residual stress and GND density estimations under single shot impacts.
- Exploring the possibility to use estimated HR-EBSD stress fields and impact displacement curve not just as a validation tool but to refine the identified coefficients.

In this thesis, it was assumed that accurate modeling of the material's response when subjected to shot peening could be achieved by considering only thermally activated phenomena *e.g.* using the Meric-Cailletaud framework with the classical Norton viscoplastic law. Indeed, the highest strain rate induced by the impacts are only restrained to a very small volume.

Also, it was assumed that the impact induced wave's pressure is small enough not to induce dislocation burst at sources, as such microstructural evolutions has not yet been reported for conventional SP.

Finally, copper was chosen to develop the identification and validation methodology as:

- It does not mechanically twin or exhibit phase changes during impact making dislocation glide the main plastic deformation mechanism. [67]
- It is a fairly well-known single-phased FCC material with well-identified coefficients for the Meric-Cailletaud CPFE framework [1, 2].
- It is a heavy material (atomic mass: 63,546 u) which therefore diffracts well and provides high quality EBSD diffraction patterns.

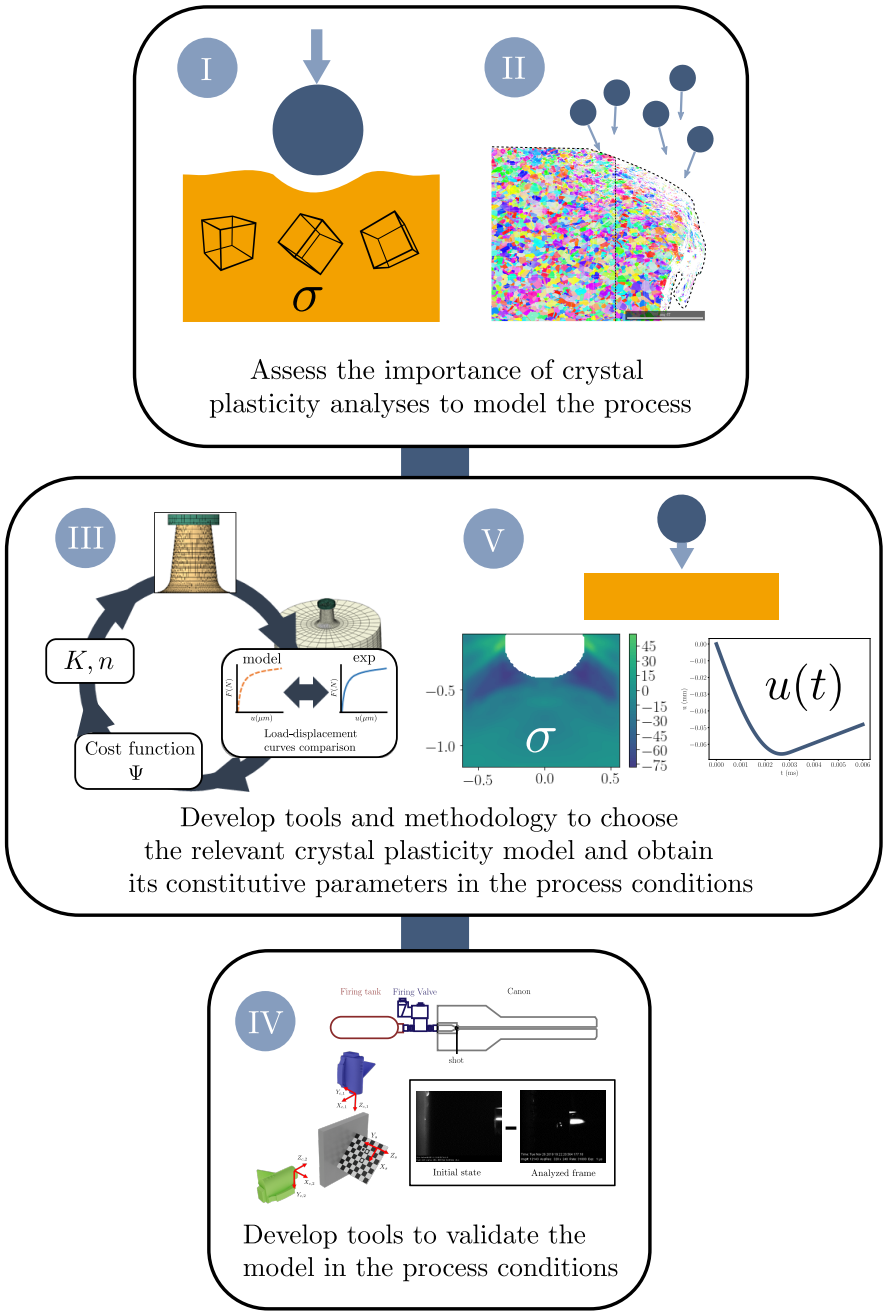

Figure 2.19 Summary of the different parts of the research project. The objective of the first two chapters was to assess the importance of modeling the process at the crystal scale for the prediction of both the residual stresses and the hardening. The next two chapters aim at developing tools for the choice of the most relevant crystal plasticity model as well as methods to obtain their constitutive parameters in the process conditions. Finally the last chapter will focus on the development of a shot peening canon to validate the previously identified model.

CHAPTER 3

Effect of crystal orientation on indentation-induced residual stress field: simulation and experimental validation

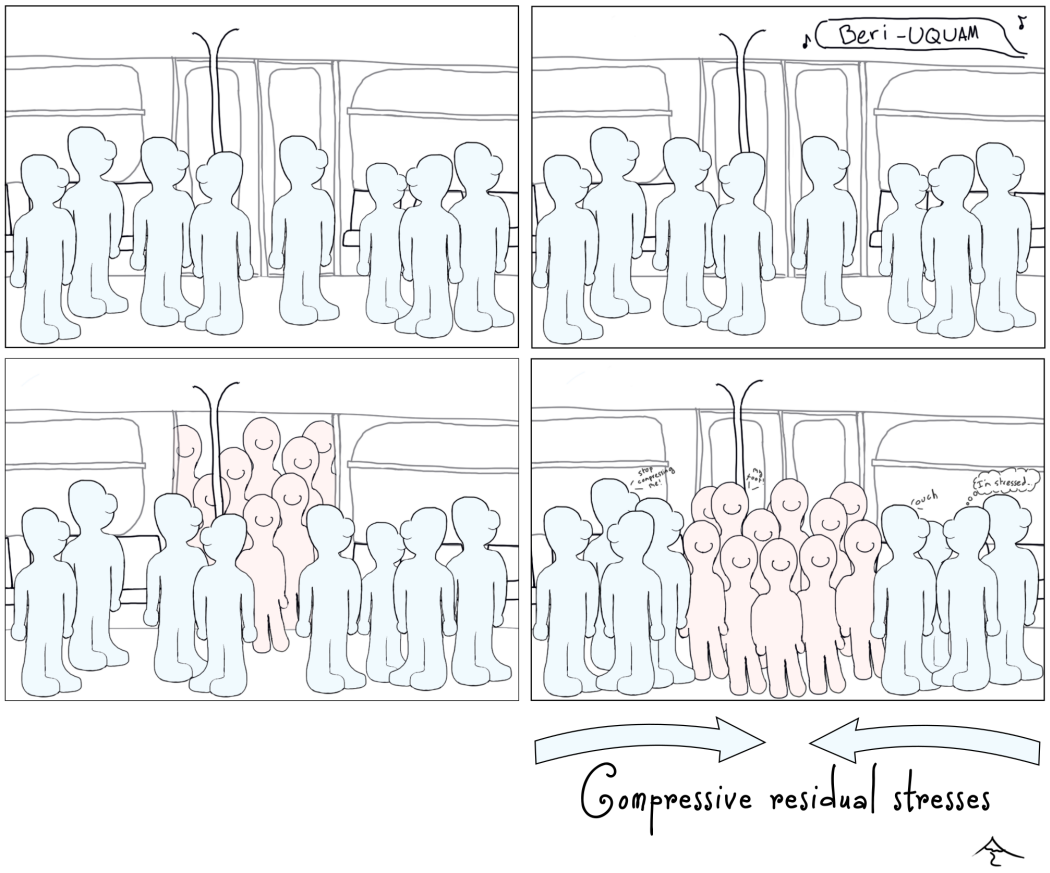

3.1 Introduction

Residual surface compressive stresses are known to significantly increase metallic alloys fatigue life, corrosion resistance and wear properties. Such stresses often result from plastic strains induced by impact mechanical surface treatments such as shot-peening. Predicting the residual stress field resulting from a given manufacturing process is challenging since numerous parameters must be accounted for: process parameters, material behavior, geometry, environment etc.

Very few authors have attempted to simulate shot impacts on models where grains are explicitely represented and where crystal plasticity constitutive laws are used [8, 19, 140]. The prohibitive computational time required to run such simulations and the challenges associated with measuring intragranular residual stresses might explain why such fundamental work has seldom been attempted.

Kobayashi et al. [29] used X-Ray diffraction measurements to show that the in-depth residual stress profiles produced on steel polycrystals by impact and quasi-static indentation were different. However, the spherical impacter and indenter they used had diameters of 50 mm and 75 mm, which is much larger than typical shot whose diameters can range from 0.1 mm to 2 mm [90]. Juran et al. [141] used Electron BackScattered Diffraction (EBSD) measurements to demonstrate that the orientation gradients produced on a single crystal by a 2.5 mm diameter ball impact at 100 m s^{-1} and spherical indentation are similar, for similar imposed loads. The strain rate involved in their study was about 100 s^{-1}, which is lower than usual shot peening strain rates, ranging from 10^4 s^{-1} to 10^6 s^{-1} [20]. However, these results suggest that the local residual stress field induced by spherical indentation could be used to estimate that induced by a shot impact.

Single crystals plastic flow resulting from indentation has been widely investigated in the past twenty years. Most researches investigated the so-called size-effect in metals [114, 142], or developed inverse methods to identify crystal plasticity parameters [143–145]. Other work also focused on the single crystal indentation-induced strain mechanisms by analysing either the pile-up/sinking-in patterns [2, 146, 147] or EBSD-measured crystal misorientation fields [148]. In particular, the orientation-dependent behaviour of such strain mechanisms has been widely studied [147, 149]. Similar studies on bicrystal have also been conducted to study the particular mechanisms induced near grain boundaries [150–152].

Fewer works focused on the residual stress field induced by indentation. Zheng et al [153] proposed an analytical model to predict the residual stress field produced by pyramidal indentation on silica. Boyce et al [154] evaluated the residual stress field produced by a

spherical impact on a Ti-6Al-4V polycrystal using X-ray diffraction and compared their experimental results to finite element simulations reproducing the same experiment. However, to the best of our knowledge, no work studied the in-depth residual stress field induced by indenting a single crystal.

High Resolution EBSD (HR-EBSD) [100, 102] has been extensively used in the literature to measure local elastic strains [101], with high accuracy. Britton et al [138] measured the residual elastic strain field around an imprint performed by pyramidal indentation on silicon using the HR-EBSD technique. They compared their measurements to Crystal Plasticity Finite Element (CPFE) simulations and obtained elastic strain fields with similar shapes and magnitudes. However, their study only provided surface measurements and no study of the in-depth residual stress field was provided.

This chapter investigates the residual stress field generated by spherical indentations on single crystals and was published in the Materials & Design journal [21]. The study builds on the experimental work of Juran et al. [141], more specifically on a <001> indented copper single crystal. Residual stress fields quantified by HR-EBSD are successfully compared to those predicted by CPFE simulations. CPFE simulations are further used to investigate the crystal orientation and repeated indentations effects on the subsurface residual stresses.

The chapter is organized as follows: the main theories and experimental methods we relied on are described in section 3.2. The Finite Element model used is presented in Section 3.3. The numerical model experimental validation, predicted indentation results for single indentations on different orientations and repeated indentations on the same crystal are detailed in Section 3.4. Finally the results are discussed in Section 3.5.

3.2 Background

3.2.1 Spherical indentation on a copper single crystal

The experimental data used in this work was extracted from the spherical indentation test presented in the work of Juran et al. [141] and is briefly recalled here for the sake of completeness. The copper single crystal was produced by directional solidification using a standard zone melting method based on a horizontal Bridgman-type apparatus. The samples were cut by electric discharge machining into parallelepiped-shaped specimens and mechanically polished. A final electro-polishing step removed remnants of mechanical hardening due to prior polishing. The indented surface was {100} oriented along the surface normal. The indents were performed using a load-controlled standard Brinell Hardness set-up with a 2.5 mm ball diameter indenter. The maximum indentation load was 100 N.

3.2.2 High Angular Resolution EBSD measurements

The analysis presented in this work was performed using an EBSD pattern iterative remapping algorithm and finite strain theory, as explained in Maurice et al. [101].

In-depth EBSD measurements were performed using a Zeiss supra 55-VP Field Emission Gun (FEG) Scanning Electron Microscope (SEM) operated at 20 kV with a probe current of 2 nA. The EBSD analysis was carried-out using an HKL system (Oxford instrument) composed of NordlysII camera and the Channel 5 software suite.

3.2.3 Crystal plasticity framework

The single crystal constitutive behavior was modeled using the Meric-Cailletaud large-strain formulation crystal plasticity framework [1] detailed in section 2.2.2.

The coefficients used in the finite element analysis for copper are those identified by Meric et al. [1] and recalled in **Tables 3.1**, **5.3** and **5.4**.

3.3 Finite element analyses

Finite Element Analyses were performed using ABAQUS Finite Element software to solve the global mechanical equilibrium. Z-set Finite Element software was coupled to ABAQUS to integrate the crystal plasticity constitutive law described in section 2.2.2.

The copper sample was modeled as a parallelepiped divided in two regions, as shown in

Table 3.1 Hardening interaction matrix parameters [1]

h_1	h_2	h_3	h_4	h_5	h_6
Self-hardening	Coplanar	Hirth lock	Collinear	Glissile	Lomer junction
1	4.4	4.75	4.75	4.75	5

Table 3.2 Elastic coefficients [1]

C_{11} (MPa)	C_{22} (MPa)	C_{44} (MPa)
159,300	122,000	81,000

Table 3.3 Norton law and isotropic hardening parameters [2]

K (MPa $s^{1/n}$)	n	R_0 (MPa)	Q (MPa)	b
5	10	10	6	15

Figure 5.3: a refined zone (Zone A) in the contact area and a border zone (Zone B) with progressively unrefined meshes to avoid border effects. Dimension R (Zone A) was chosen so as to contain all the elements where plastic strains occurred. The outside layer thickness b was chosen to avoid border effects on the residual stress field (see Appendix B). The dimension $b = R$ was chosen as the converged value.

The substrate was meshed with 3D hexahedric linear reduced integration elements (C3D8R) using an updated lagrangian formulation. Reduced integration was used to avoid locking effects resulting from plastic incompressibility [155]. Few mesh instabilities (e.g. hourglass effect) were observed and were corrected using a low hourglass stiffness (1 MPa). The mesh size was determined through a convergence study based on the residual stress field (see Appendix B). The converged element size was taken as 28 μm in the contact zone. The chosen mesh density also ensured that the maximum contact radius was composed of at least 10 elements.

The indenter was modeled as a rigid half-sphere meshed with tetrahedral elements. A penalty algorithm was used for the contact, which was considered frictionless. Simulations with

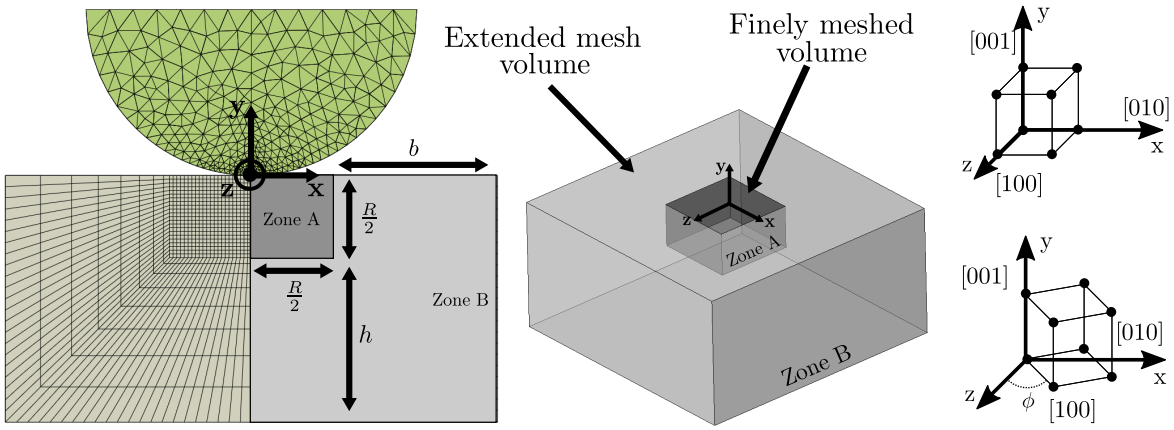

Figure 3.1 Spherical indentation finite element model. (a)Schematic view of the indentation model geometry and mesh. C3D8R hexahedral and C3D4 tetrahedral elements were used respectively for the copper sample and the indenter mesh. The indenter was modeled as rigid. The sample followed a CPFE law for copper. Contact was modeled as frictionless using a penalty method. (b)Representation of the substrate crystal orientation with respect to the global coordinate system. Simulations with an in-plane rotation $\phi = 20°$ and $45°$ were also performed to rule out any effect of the mesh on the residual stresses, using the same criterion as for the convergence study presented in Appendix B.

different friction coefficients were also performed and led to similar residual stress fields (see details in Appendix B).

The simulations were performed in three steps. (i) First, the indenter was moved (displacement-control) toward the substrate along the y-axis down to a depth of 40 μm. This corresponds to the experimental maximum indentation depth. (ii) The indenter was gradually removed from the contact surface to simulate unloading, following the y-axis. (iii) Finally, half the substrate's elements (with coordinates z>0 mm) were deactivated to model the sample's cutting. All displacements were blocked at the bottom of the parallelepiped through all the steps ($U_x = U_y = U_z = 0$). This reproduces the experimental boundary conditions, as the sample was stuck on a sample holder before indentation.

To recover the experimentally measured macroscopic behavior, the choice was made to vary only the critical resolved shear stress parameter R_0. This choice allows to retrieve the experimentally imposed load for a given indentation depth, without altering the simulated material's hardening behavior. The indent size as a function of the indentation force was plotted for several R_0 and compared to the experimental values obtained for the numerous indentations reported by Juran et al. The indent diameter is defined as the largest dent dimension along the x-axis. Figure 3.2 shows that $R_0 = 10$ MPa best fits the experimental data.

Simulation of a single indent aligned with the [001] crystal direction was performed for comparison with experimental data. The crystal [100] direction was aligned with the simulation x-axis. 20° and 45° rotated crystals around [001] (as sketched in Figure 5.3(b)) were also simulated to rule out any effect of the mesh on the residual stresses, using similar convergence indicators as those described in Appendix B. The influence of crystal orientation on the residual stress field was also studied using 43 simulations with different crystal orientations, as discussed in Section 4.2.

The stress redistribution during successive indents was investigated. Five successive indents were simulated following the indentation strategy presented in Figure 3.3, in the same simulation procedure. The fives indents were performed along the y-axis at $x = 0$ and for different z values. The first three indents' centers were spaced apart by a distance of d_{imp}. This distance corresponds to a single imprint diameter. The order chosen for these three indents is specified by the numbers in Figure 3.3. The two last indents were performed on the resulting dimples. Their centers were spaced by a distance of $\frac{d_{imp}}{2}$ from the first indent center. The geometry was expanded to contain the plastic strains in the refined mesh zone.

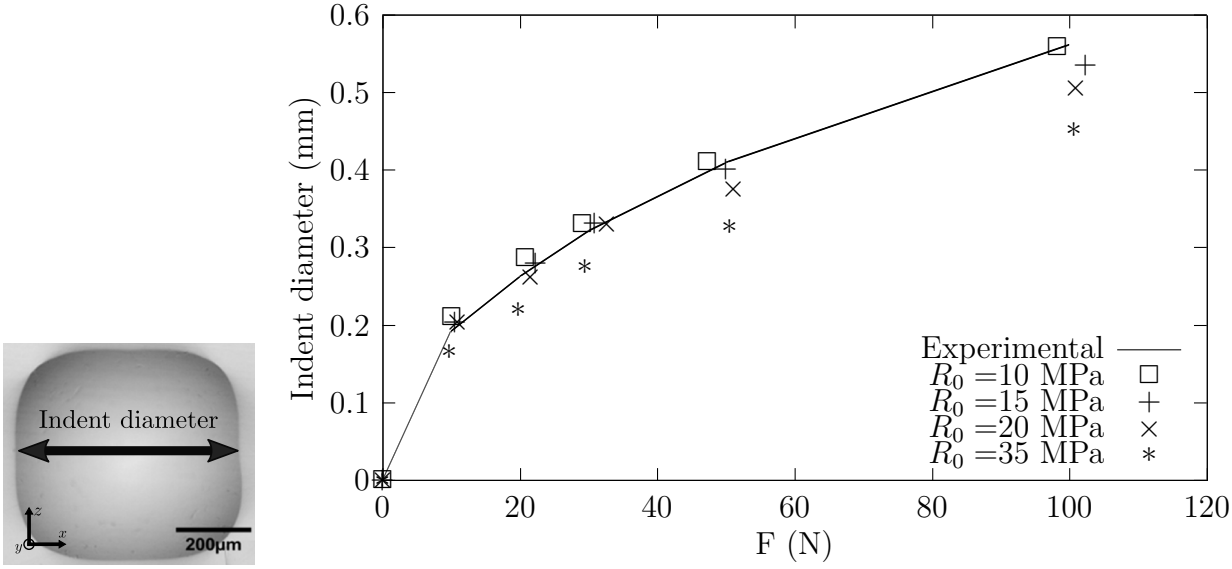

Figure 3.2 Variation of the indent diameter as a function of the applied force for different values of the yielding criterion R_0. The indent diameter is defined as the largest dent dimension along the x-axis. Results obtained for $R_0 = 10$ MPa seem to best fit experimental data, especially for the largest force values.

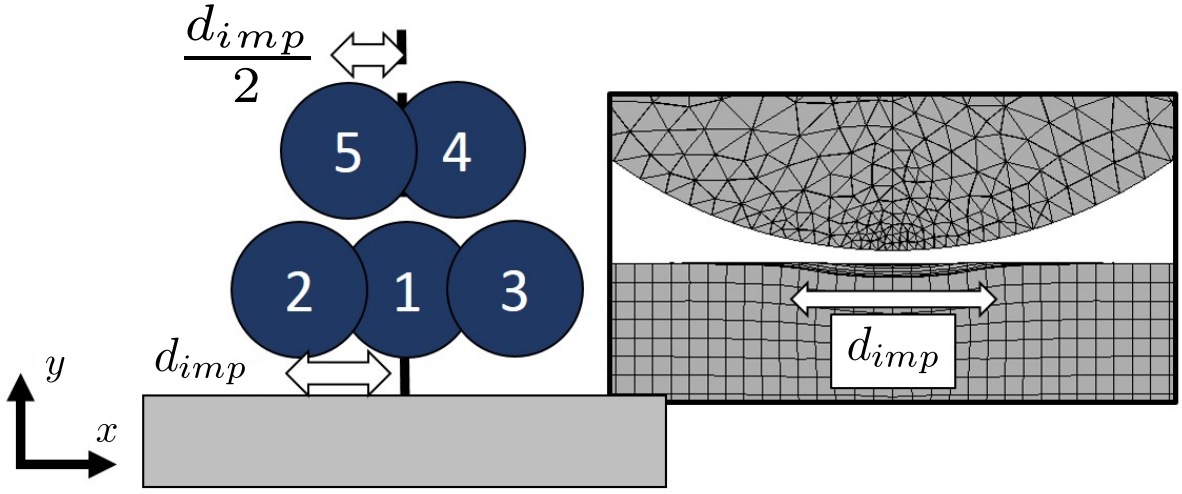

Figure 3.3 Indentation strategy chosen to study the influence of several indents. d_{imp} represents the first residual imprint diameter. Five successive indents were performed following the x-axis. First three indents were spaced apart from d_{imp}. Two last indents were performed on the resulting dimples.

3.4 Results

3.4.1 Numerical predictions comparison with experimental data

Figure 3.4 shows the simulated indentation imprint highlighted by the contact pressure field at maximum indentation depth. This imprint is compared to that experimentally measured. Both experimental and numerical imprints are square-shaped, as in the work of Juran et al, and have similar dimensions. It can however be noted that the experimental imprints present a rounder shape than the predicted one.

Figure 3.5 shows the experimentally measured and predicted σ_{xx} residual stress field over the specimen's cross-section after cutting. Please note that a zero-centered color scale was chosen for all the residual stress fields presented in this study to better emphasize the relative importance of tensile and compressive stresses. Figure 3.5 shows that the HR-EBSD method can capture local stress variations within the crystal. Figure 3.6 presents residual σ_{xx} profiles taken along two path located 70 μm and 493 μm below the surface for both simulation and experiment. This comparison suggests that there is a reasonable agreement between the experimentally measured and predicted residual stress fields. The measured residual stresses are more compressive under the surface at the indent center ($x = 0$ mm) than those predicted.

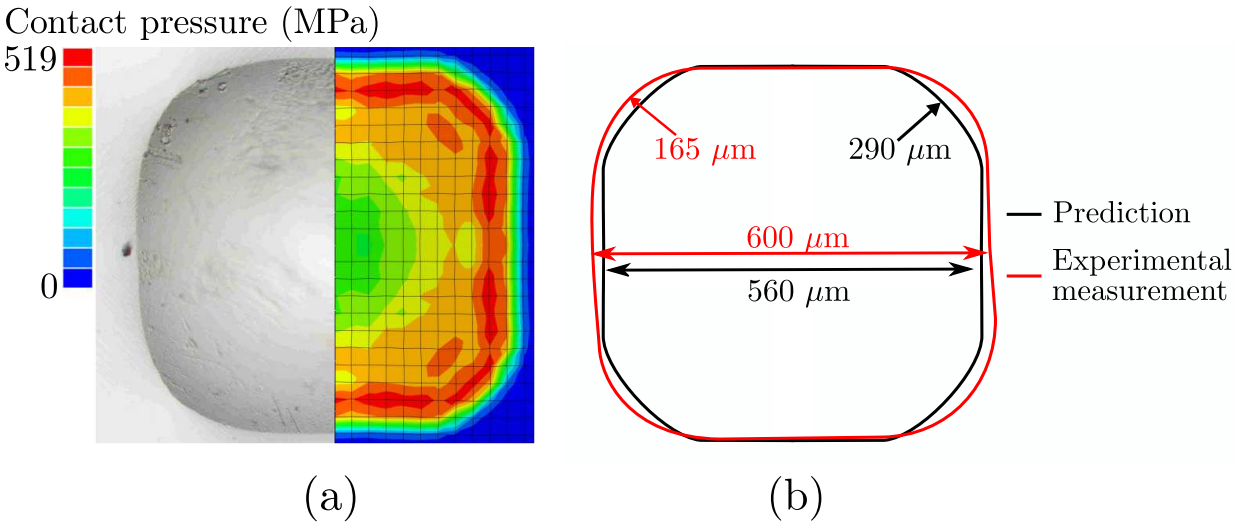

Figure 3.4 Indentation dent topography. (a) Topography of the resulting indent shape: comparison of the experimental (left) and numerical (right) residual indent enhanced by the contact pressure field. (b) Quantitative comparison of the predicted and experimentally measured imprint shape using the imprint diameters and the curvature radius at the imprint corners. Both imprint present similar dimensions. The experimental imprint is rounder than the predicted one.

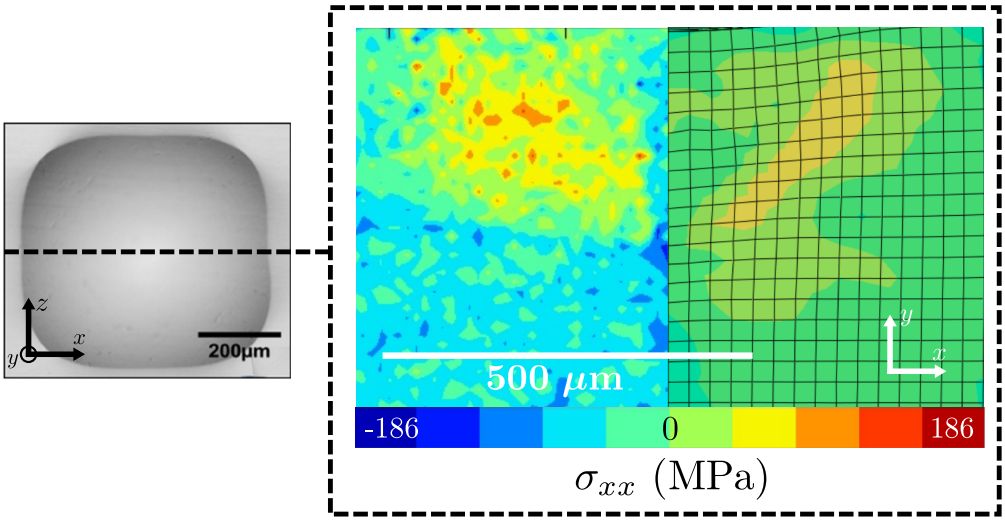

Figure 3.5 In-depth residual stress field after indentation and sample cutting at the indent center: HR-EBSD results (left) and Finite Element results (right). Both fields present similar shapes and amplitudes. Tensile residual stresses are observed in the first 200 μm under the surface.

Such a shift in the compressive stress values is also found deeper into the sample, at 493 μm below the surface (see Section 5).

A large tensile zone is present below the indent, for both the simulation and the experiment. These observations suggest that our simulation methodology is sufficiently robust to further investigate the crystal's orientation effect on the residual stress field during an indentation test, at least qualitatively.

3.4.2 Influence of crystal orientation on the residual stress field resulting from a single indent

Figure 3.7 shows the predicted residual stress field in an indented sample before cutting. This figure further confirms that spherical indentation in the crystal's [001] direction produces a large tensile residual stress zone beneath the indent.

The volume fraction f_t of elements for which the first stress invariant was positive in the refined mesh zone within the first 200 μm under the surface was computed as:

$$f_t = \sum_{i=0}^{N_e} A_i \frac{V_i}{V_{tot}}, \tag{3.1}$$

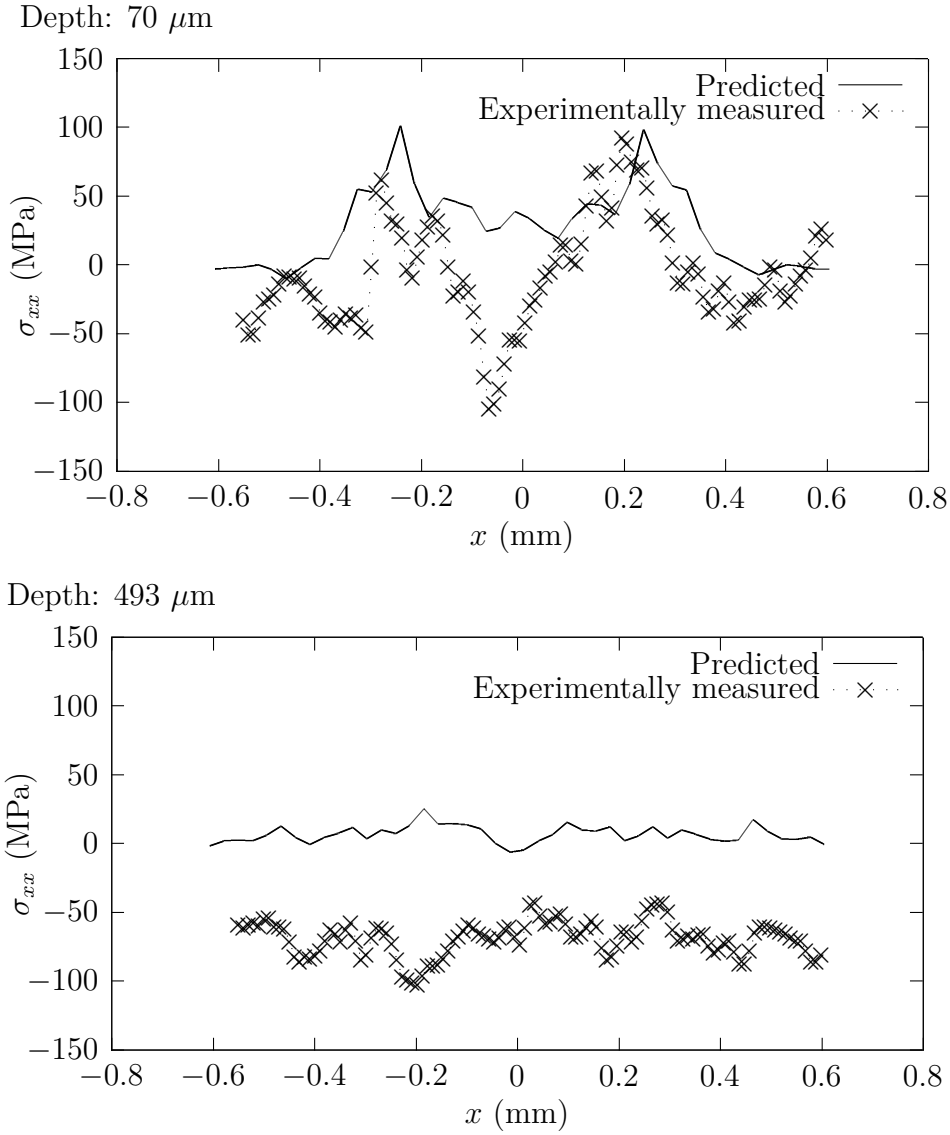

Figure 3.6 Experimentally measured and predicted σ_{xx} profiles after an indentation, along two paths 70 μm and 493 μm below the surface. The Finite Element model captures well the global shape and amplitudes of the field. The most compressive stresses are found experimentally under the surface at $x = 0$ mm. A deeper profile located 493 μm below the surface reveals a gap between predicted and experimentally measured stresses.

where

$$A_i = \begin{cases} 1 & \text{if} \quad \frac{\text{tr}(\boldsymbol{\sigma})}{3} \geq t \\ 0 & \text{if} \quad \frac{\text{tr}(\boldsymbol{\sigma})}{3} < t \end{cases} . \tag{3.2}$$

N_e is the number of elements in the first 200 μm below the surface, V_i the i-th element volume and V_{tot} the total volume of material from the sample's surface down to 200 μm

below the surface. t is a threshold filtering low stress values (taken as 20 MPa). The first stress invariant (i.e. the trace of the stress tensor) was used as an indicator since it does not depend on the crystal orientation axes. Figure 3.8(a) shows an Inverse Pole Figure (IPF) for f_t for 43 crystal orientations. Figure 3.8(b) shows the inverse pole figure obtained when considering the volume fraction of elements with a negative stress invariant, f_c, using a threshold t =-20 MPa. Appendix B details the methodology used to generate these figures. Please note that the figures do not complement each other as a stress threshold t was used to calculate both volume fractions.

These figures show that many crystal orientations can lead to tensile zones after one indent. The largest tensile zones were found for samples indented close to the [001] orientation while the smallest tensile zones were found for those indented close to the [101] orientation. However, Figure 3.8(b) shows that these orientations do not yield the largest compressive zones, which are found close to the [213] orientation.

Further simulations were performed on fourteen orientations ranging from [001] to [111] in the $(1\bar{1}0)$ plane to visualize the residual stress field evolution leading to the f_t and f_c values

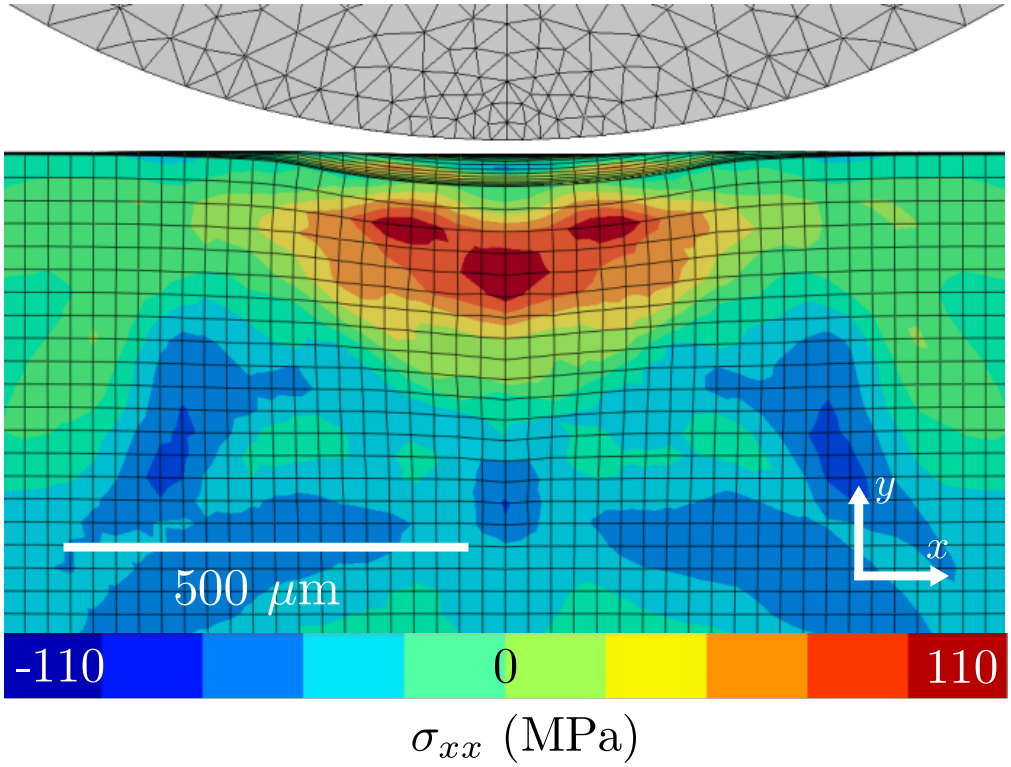

Figure 3.7 Finite Element in-depth σ_{xx} field after indentation in the [001] direction, before sample cutting. Tensile stresses are present down to 230 μm and therefore do not result from sample's cutting.

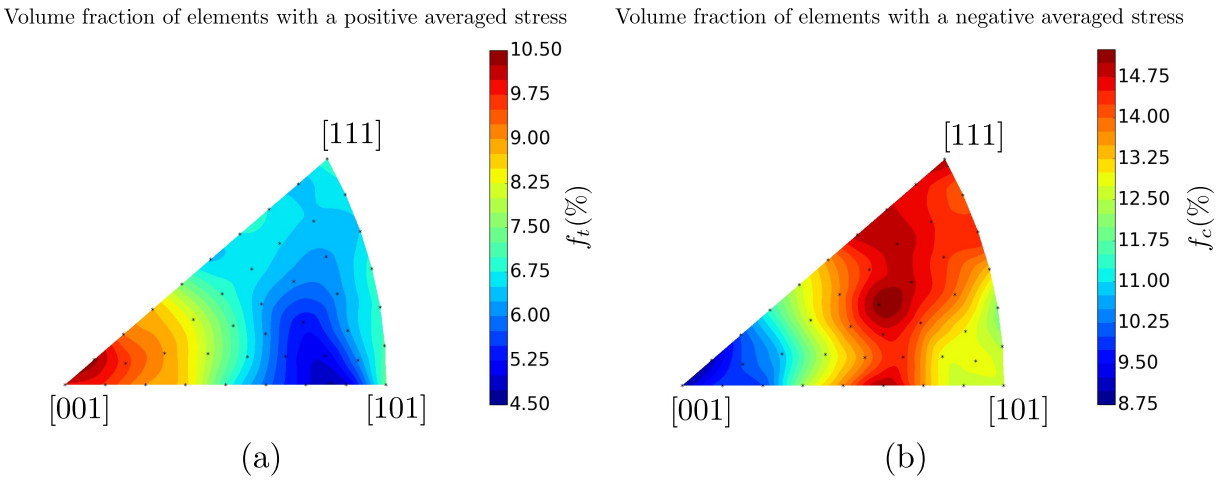

Figure 3.8 Inverse Pole Figure representing the volume fraction of elements with a positive (a) and negative (b) residual first stress invariant after one simulated indent. Each black mark represents a simulation result. Largest tensile zones and smallest compressive zones are found when indenting close to the [001] orientation. Please note that the figures do not complement each other as a stress threshold t was used to calculate both volume fractions.

presented in Figure 3.8.

Figure 3.9 shows the residual first stress invariant field evolution as a function of crystal orientation. The tensile residual stress zone observed for the sample indented along the [001] direction is confined, almost uniformly, close to the surface, when the indentation direction shifts toward the [111] direction. This is particularly emphasized in Figure 3.10 that reports the in-depth stress profile taken at the indentation center for three different orientations. For the sake of clarity, the curves presented in Figure 3.10 were smoothened to remove discretization-induced oscillations using a gaussian filter as:

$$\Gamma_{filtered}(x) = \int_{-\infty}^{\infty} \Gamma(x-t)\frac{1}{s\sqrt{2}}e^{-\frac{(t-\mu)^2}{2s^2}}\mathrm{d}t, \tag{3.3}$$

where $\Gamma_{filtered}$ and Γ are respectively the filtered and the raw curves, and s and μ are the gaussian parameters (taken as $\mu = 0$ and $s = 4$).

Figure 3.10 shows that, as the orientation approaches the [111] direction, both the compressive and the tensile residual stress zones reach lower extrema. The tensile stress zone tends to get narrower, as the compressive stress zone extends to a larger zone closer to the surface.

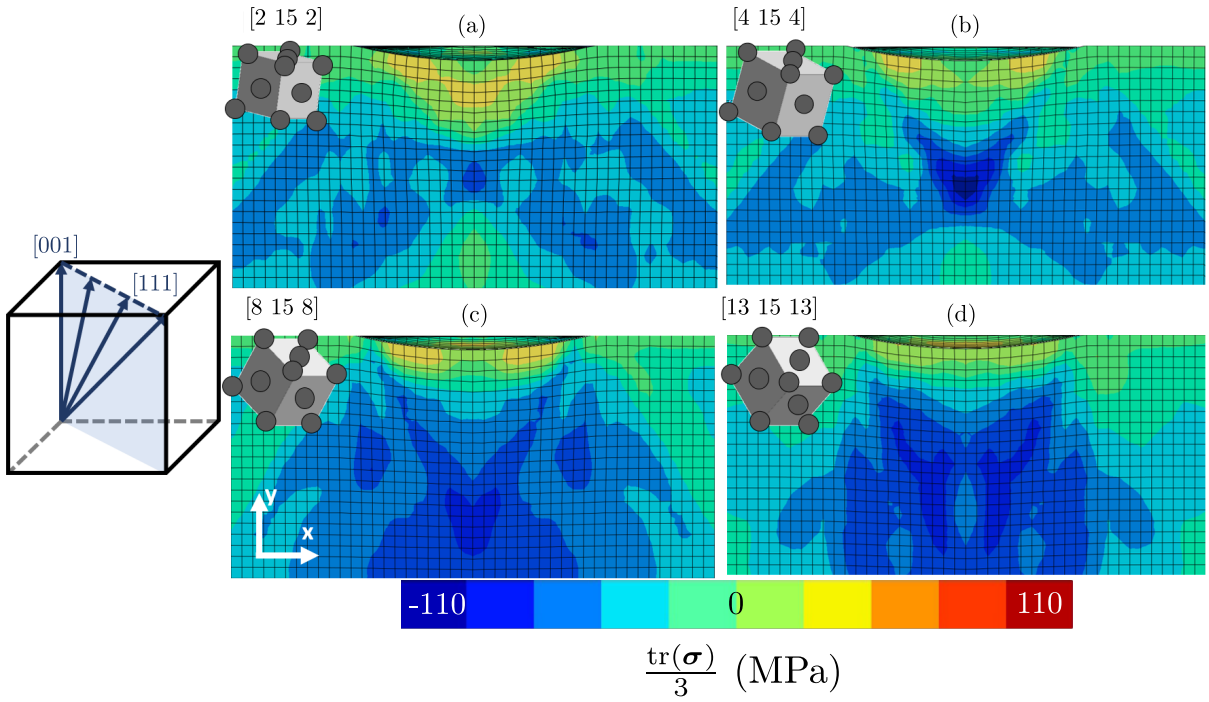

Figure 3.9 Evolution of the residual first stress invariant field with indentation orientation varying from [001] to [111]: (a) [2 15 2], (b) [4 15 4], (c) [8 15 8], (d) [13 15 13]. The tensile stress zone is present for several orientations and is confined, almost uniformly, close to the surface for orientations close to [111].

3.4.3 Stress redistribution after several indentations

The residual stress fields produced after each of the five indents are presented in Figures 3.11 and 3.12 for samples indented in the [001] and [111] direction, respectively.

A tensile residual stress zone is still present underneath the indented surface for the [001] oriented sample after five indents. By opposition, the residual stress field predicted after indenting in the [111] direction is purely compressive, and more compressive than that predicted for the [001] orientation. The depth where compressive residual stresses can be found is also deeper for the [111] oriented sample.

3.5 Discussion

Figure 3.6 shows that more compressive residual stresses are measured close to the indentation axis ($x = 0$ mm) and beneath the tensile zone deeper in the sample. Such bias in the compressive stress intensities could be induced by the HR-EBSD parameter choice. Errors

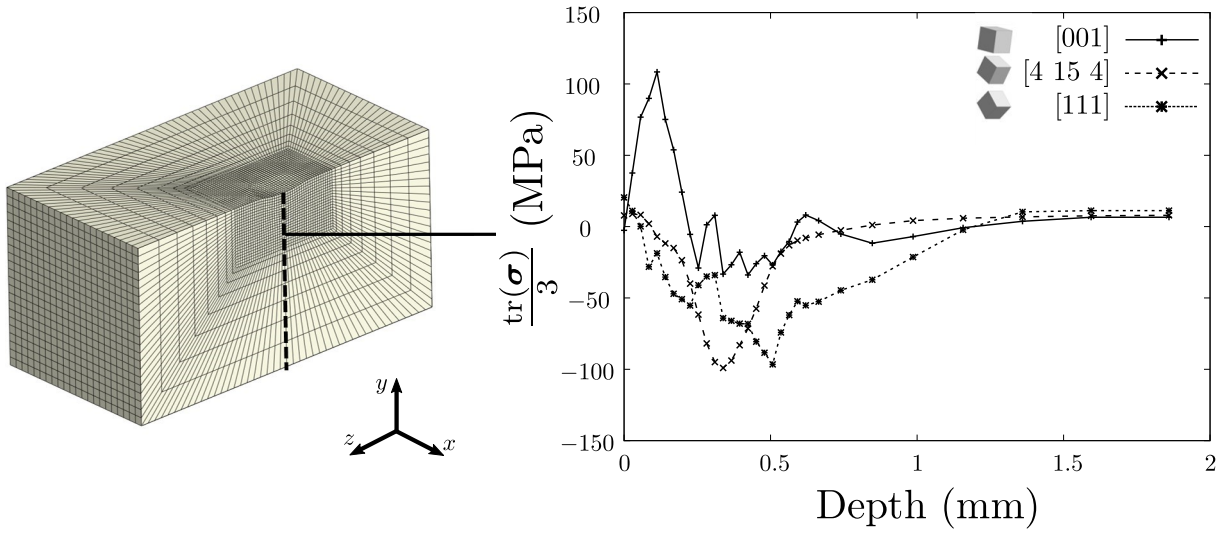

Figure 3.10 Residual stress profiles for orientations [001], [4 15 4] and [111]. The profiles are extracted on a path at the geometry center, as sketched at the left. A gaussian filter was applied to remove discretization-induced oscillations. These profiles emphasize the respective reduction and augmentation of the tensile and compressive zones close to the [111] orientation.

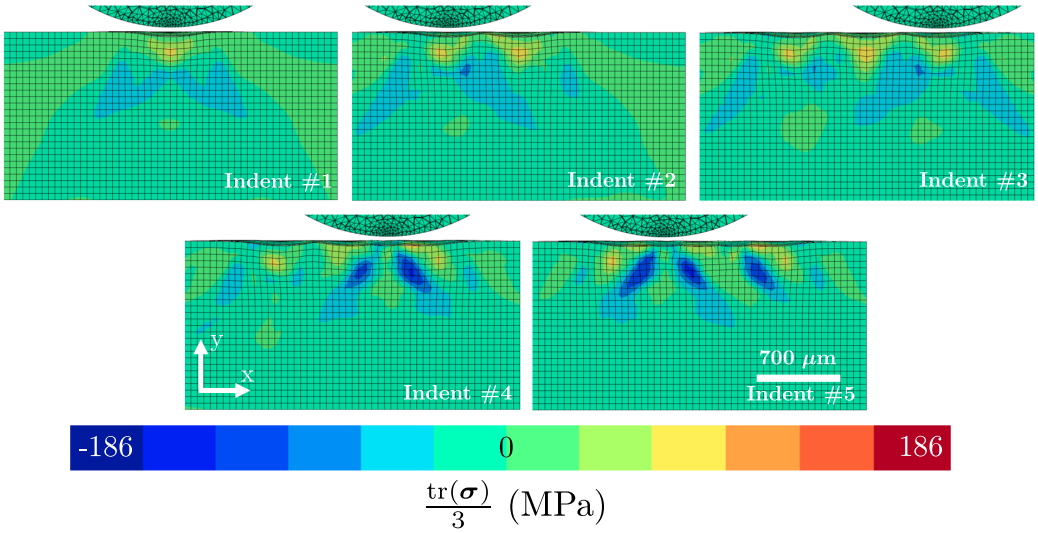

Figure 3.11 Redistribution of the residual first stress invariant field during the indents presented in Figure 3.3, when indenting in the [001] direction. Figure's numerotation corresponds to the indent number following Figure 3.3's convention. Tensile stresses are still present after 5 indents. The final residual stress field is highly heterogeneous

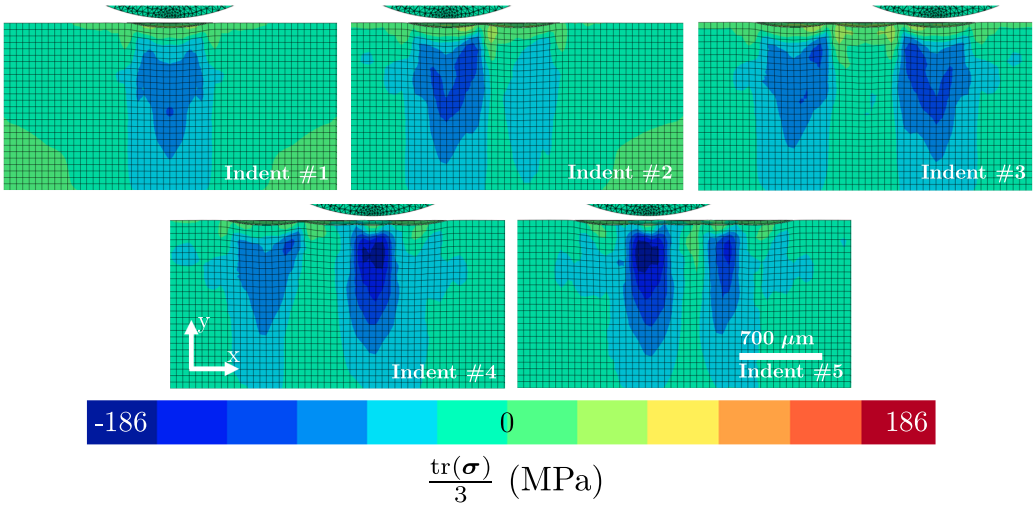

Figure 3.12 Redistribution of the residual first stress invariant field during the indents presented in Figure 3.3, when indenting in the [111] direction. The final field is more homogeneous and presents much deeper compressive stresses as in the [001] direction.

in the HR-EBSD pattern center coordinates, or in the reference pattern stress, could for instance lead to such bias [101, 156]. Also, small misalignments of the cutting plane with the indentation center could also contribute to such bias. This could also result from the simplicity of the procedure used to simulate sample's cutting: the numerical procedure assumes that no residual stresses have been generated through the cutting process.

Our model predicted a significantly spread tensile residual stress zone after spherical indentation, whose size depends on the crystal orientation. A tensile zone after dynamic impact has been reported before in the literature for large diameter balls by Kobayashi et al. [29]. The authors performed quasi-static spherical indents and impacts on a steel polycrystal. Only impact tests led to subsurface tensile residual stresses in their study. According to the authors, the tensile residual stress zone resulted from plasticity mechanisms brought by stress waves propagation and high strain rates. In our case, these residual stresses result from the anisotropic nature of crystal plasticity, as it has not yet been revealed using homogeneous macroscopic isotropic constitutive models.

Figures 3.11 and 3.12 showed that the volume of tensile residual stresses decreases with an increasing number of indents. However, these figures also suggest that there is a link between the relative volume of tensile and compressive residual stresses produced after one and several indents. The larger tensile stresses volumes after one indent result in shallower compressive stresses and a more heterogeneous stress field after several indents. For grains

whose dimensions are close to the contact radius, or for textured microstructures, the residual stress state of a treated material could therefore highly depend on its initial microstructure orientations.

Figure 3.8 showed that grains with orientations close to <001> have a higher probability to present subsurface tensile residual stresses. By opposition, indentation on grains with orientations close to the center of the IPF should exhibit larger compressive stresses volumes. Knowing the initial microstructure orientations, the IPF map of f_t and f_c can therefore provide insights in the shot-peening induced residual stress field heterogeneities and residual compressive stress depth. This orientation-dependent behavior could therefore have consequences for surface treatments involving spherical impacts on polycrystals with a coarse grain structure or with a particular texture. This could be particularly the case for the shot peening of welded zones [48, 49].

Works performed by Chen et al. [157] showed that this effect is also present after multiple impacts on a different material. The authors shot-peened a nickel-based superalloy single crystal along the [001] and [111] orientations at 80% and 400% coverage. Their work showed that compressive residual stress intensities decreased in the [001] single crystal, when compared to that in [111] oriented single crystal, even after a 400% coverage. Their results corroborate the results we presented in this paper. Future work will focus on the study of this orientation-dependent behaviour for materials which are known to present particular textures and for dynamic impacts.

3.6 Conclusion

The objective of this work was to investigate the residual stress field generated by spherical indentations on a single crystal and to assess the relevance of CPFE for mechanical surface treatment simulations. The main contributions are as follows:

- HR-EBSD observations revealed a large tensile residual stress zone after spherical indentation on a [001] oriented single crystal copper.
- A spherical indentation CPFE procedure using Meric-Cailletaud's crystal platicity framework was developed. A good agreement was found with HR-EBSD observations in terms of residual stresses.
- Single indentation simulations in 43 different crystal orientations revealed that the tensile and compressive stress fields highly depend on the initial crystal orientation. Indentation close to the [001] orientation lead to more tensile stresses and less compressive

stresses than for any other crystal orientations. Conversely, more compressive stresses and less tensile stresses were found when indenting close to the [213] orientation.

- Simulations of five successive indentations in the [001] and [111] directions showed that there is a link between the volume of tensile and compressive stresses induced by one and several indents. More tensile stresses and less compressive stresses produced by one indent leads to shallower compressive stresses and a more heterogeneous stress field after five indents.

Accounting for crystal plasticity anisotropy when simulating surface treatments could therefore reveal local tensile residual stresses and local stress heterogeneities in favorably oriented crystals. Provided that the grain sizes are sufficiently large, the initial material microstructure could therefore have an influence on shot peening efficiency. This conclusion should naturally depend on the shot-peening parameters. Stress heterogeneities revealed by this study could affect the fatigue life prediction of shot-peened parts. Local tensile stresses could favor crack propagation during fatigue. Shallower compressive stresses than those expected using macroscopic isotropic laws could result in overestimations of shot-peened part's fatigue life.

This analysis should be conducted with one and several high velocity impacts to validate its conclusions on real engineering mechanical surface treatments. CPFE simulations for strain rates close to those encountered in shot peening will require the development of new constitutive law identification methodologies at small scale, as presented in Chapter 5.

3.7 Data availability

The raw data required to reproduce these findings cannot be shared at this time as all experimental results were extracted from the work of Juran et al. [141]. However, finite element result files, simulation input files as well as meshing tools used for this study can be found at `https://zenodo.org/record/2550820` and can be reused.

CHAPTER 4

Microstructural and mechanical characterization of a shot-peening induced rolled edge on direct aged Inconel 718 alloy

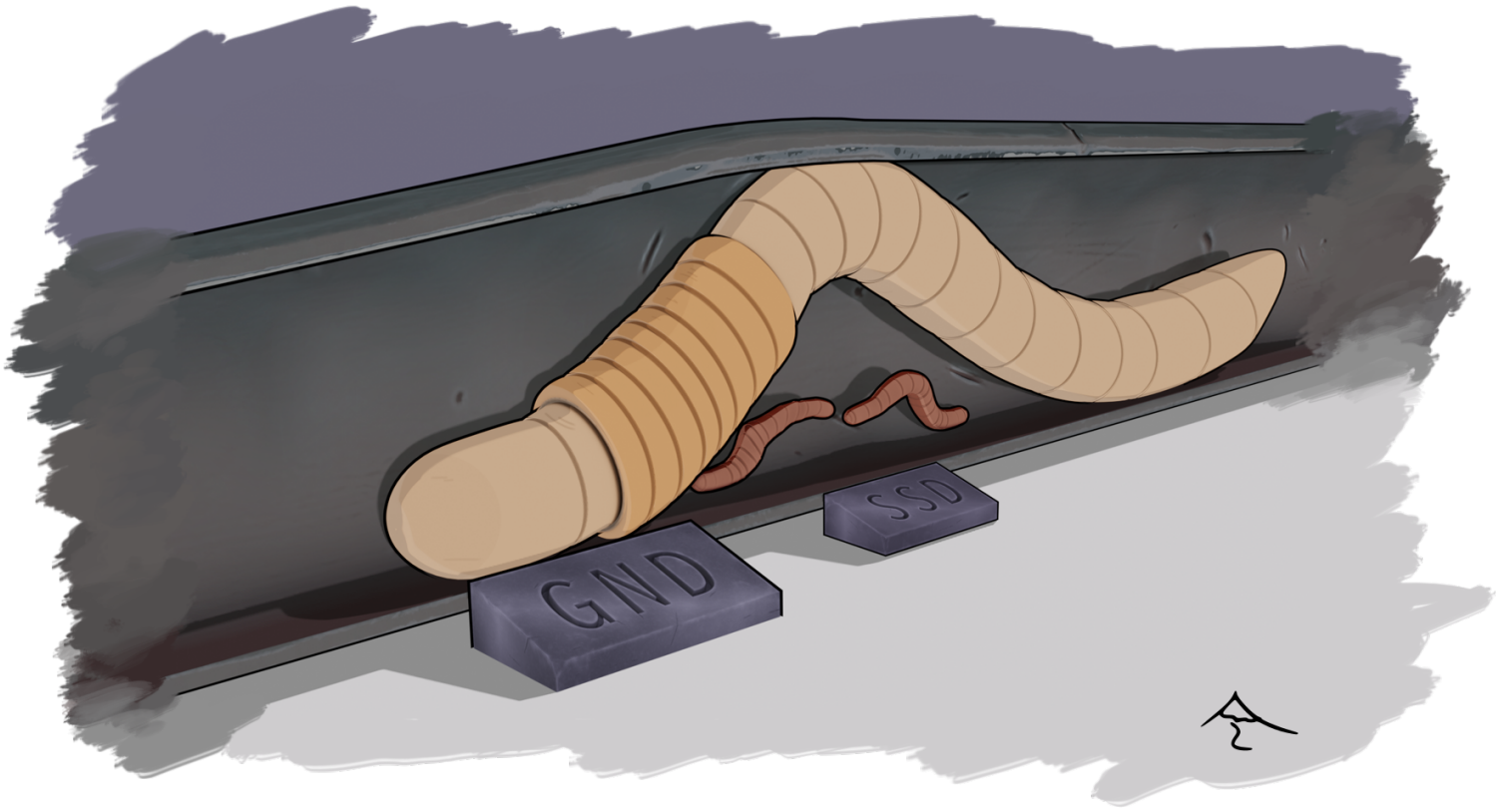

Introduction

Several works focused on the application of shot-pening models on complex geometries for industrial applications. Most of these approaches assumed that shot peening involved similar strain mechanisms in a flat sample than in a complex geometry. For instance, Gallitelli et al. [10] modeled the shot peening of a spur gear by computing the residual stress field induced by single impacts of different velocities. These fields were then introduced in the geometry using the eigenstrains method, following an impact velocity field predicted by a discrete element model.

Shot peening of geometric singularities, such as sharp corners or holes, can induce a bulge at the border of the treated part. This situation results from the peened material's stretching and rolling over the sharp corner onto the orthogonal face. As the material rolls onto itself, these bulges are often referred to as rolled edges or "elephant-tails". The influence of such rolled edge on fatigue life has been investigated by a few authors both in low cycle fatigue (LCF) and high cycle fatigue (HCF) regimes. Klotz et al. [131] and Sun et al. [132] investigated the influence of the initial edge geometry on the fatigue life of shot peened parts respectively for the Inconel 718 alloy and the Ti-17 alloy. Differences in crack initiations were related by both studies to rolled-edges acting as local stress concentrators resulting in a shorter fatigue life. In particular, Sun et al. [132] revealed that significant rolled edges could result in a shorter fatigue life than that of an unpeened specimen. He et al. [134] and You et al. [158] also showed that removing the rolled-edge by grinding would improve the sample's LCF life. Understanding rolled-edges formation and material properties is therefore crucial as it could cancel all the beneficial effects of the process.

Apart from such geometrical effect, the material's mechanical properties induced in the rolled edge were scarcely investigated. Sun et al. [132] performed finite element simulations of laser shock peening (LSP) on a specimen edge. The authors found that rolled edges presented larger plastic strains and higher compressive stress values as the laser shock waves interacted with the sample edges. Such result was however not confirmed experimentally, nor reported for conventional shot peening, for which shock wave intensities are negligible when compared to those occurring during LSP. A modified microstructure and hardening state could play a crucial role in the material's local hardness, mechanical properties or corrosion resistance, thus possibly impacting the material's fatigue life.

Advances in the past thirty years in electron backscattered diffraction (EBSD) characterization methods could provide insights on such heterogeneous hardening. Wright et al. [116] introduced alternative indexing methods such as dictionary indexing (DI) to perform EBSD

observations on surfaces producing noisy diffraction patterns. Also, as demonstrated by Pantleon et al. [109], misorientation maps generated by EBSD can provide an estimate of the GND density distribution. Such estimations could provide insights in the work hardening gradients resulting from surface process treatments.

Other hardening sources could contribute to the material's mechanical properties, such as the Hall-Petch effect or precipitate hardening. Tumbajoy-Spinel et al. [6] combined nanoindentation testing, micropillar compression and kernel average misorientation (KAM) maps to decorrelate the effect of each hardening contributions on micro-percuted surfaces. As pointed out by the authors, instrumented nanoindentation testing provides a local estimate of the material's hardening gradients considering all the contributions. Such test could therefore be combined with EBSD GND estimations to decorrelate work hardening from other sources.

The objective of this work is to characterize the differences in microstructure and hardening induced in a rolled edge compared to a reference flat shot peened surface. This work was performed in collaboration with Safran Tech and was submitted for publication in the Journal of Materials Processing Technology [22].

First, microstructural evolutions in the rolled edge were characterized using EBSD with DI. GND densities were estimated using the method described by [109]. The ability of DI, when compared with the usual Hough indexing, to extract misorientation in the shot peened zone was investigated. DI was then used to compare the rolled edge hardening state with a shot peened reference taken at the sample center. Finally, GND density variations were related to instrumented nanoindentation measurements to assess the differences in mechanical properties in the rolled edge zone due to work hardening.

4.1 Materials and methods

4.1.1 Sample preparation

Inconel 718 direct aged parallelepipedic samples with sharp edges and a section measuring 0.5 mm×15 mm were shot peened with a 22.5 mmA intensity and a 400% coverage using the set-up schematized in Figure 4.1. The shot peening treatment induced rolled edges at the sample's border, as shown in the micrograph represented in Figure 4.1. A 10 mm long sample was then cut using a niobium carbide circular saw and coated in a conductive resin (PolyFast, Struers) for automatic polishing. The sample was then mechanically polished with P200 to P1000 SiC grit paper then successively with a 3 μm and 1 μm diamond suspension (Metadi, Buehler) and vibro-polished during one night using a Mastermet solution (Buehler). A 1.25 nm platinium layer was finally deposited on the sample to make the observation

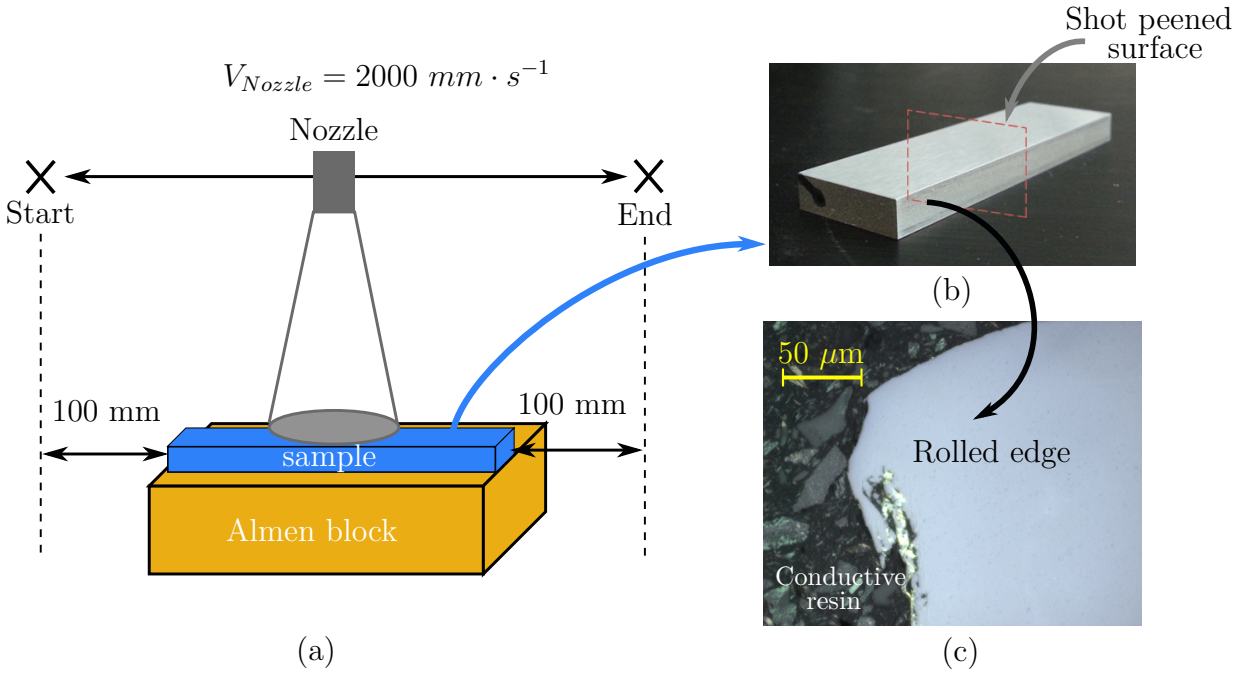

Figure 4.1 Experimental methodology for rolled edge observation. (a) Schematic of the shot peening set-up used in this study. (b) Shot peened sample. (c) Micrograph showing the shot peening induced rolled edge. The nozzle velocity V_{Nozzle} was 2000 mm·s^{-1}. Shot peening at the sample's borders induced rolled edge as visible on the micrograph at the bottom right.

surface fully conductive, using a Leica ACE600 high vacuum sputter coater. The coating limited electron beam drifting when observing the sample's extreme surface during EBSD acquisition.

4.1.2 EBSD analysis

Pattern acquisition

The EBSD acquisition was performed using a Zeiss Merlin equipped with a field emitting gun (FEG) Gemini 2 column. EBSD patterns were captured using a Brucker e-FlashFS camera with a 70° tilt angle at 20 kV acceleration voltage, 20 nA probe current and a 150 nm step. The pattern resolution was 160×120 (4×4 binning) and six patterns were averaged for each measured point to reduce noise. Only the austenitic face-centered cubic matrix γ was indexed.

Two EBSD maps were successively captured at the rolled edge and from the rolled edge to the sample's flat part to observe the full property gradient induced close to the sample's border. A third map was also performed in the sample's bulk to compare the surface properties with

the non-peened material reference.

Dictionary indexing

Indexation of the Kikuchi pattern is classically performed by detecting the pattern's bands using the Hough transform. However, this technique usually fails to characterize severe plastic deformations as it usually results in noisy patterns, making band detection difficult. Dictionary indexing is based on the comparison of a diffracted pattern with dynamically simulated patterns generated from an orientation subspace. Since it does not rely on band detection, it is therefore more robust toward noise induced by large plastic deformations.

Diffraction patterns were indexed using the dictionary indexing (DI) methods implemented in the *EMsoft* software using the methodology developed by Jackson et al. [3]. A master pattern was generated using *EMsoft* forward model with the input parameters given in Table 4.1. This master pattern was then used to discretize the orientation space using 100 cubochoric samples for a first raw indexation. The indexing success threshold angle was set at 1.5°. The indexed points' orientations were then refined by orientation space sub-sampling close to the first solution using the *EMFit* program, with a 0.03 refinement step size.

GND estimations

GND density distributions were estimated using the *Matlab mtex* toolbox introduced by Bachmann et al. [159] following the methodology described by Pantleon et al. [109] and detailed in section 2.4.2. The material's Poisson's ratio and the norm of the Burgers vector were respectively taken as 0.3 and 0.26 nm.

It should again be noted that the methodology only provides a lower bound of the GND density. It can however be used for comparison purposes. Also, the chosen minimized quantity should only have little effect on the total dislocation density, which was the only quantity considered in this work.

4.1.3 Nanoindentation

Nanoindentation tests were performed to map the process induced hardness gradient close and far from the rolled edge. A MTS DCM nanoindenter with a diamond Berkovitch tip was used. The test consists in indenting a material's surface using a diamond tip down to a few hundred micrometers while measuring the indentation load and displacement. The material hardness is then obtained by estimating the contact surface between the tip and the indented material.

Table 4.1 Parameters used to generate the Dictionary Indexing master file [3]

Crystal system	Lattice Parameter	Space Group	Atomic Number	Debye-Waller factor
1 (cubic)	0.35236 nm	225	28	0.0035 nm^2

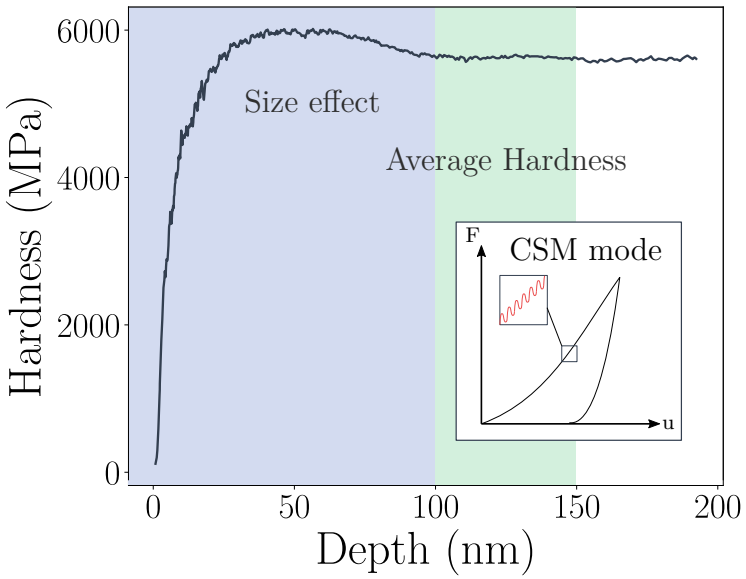

Figure 4.2 Typical hardness variation with indentation depth obtained using the CSM mode. An oscillating displacement is imposed to the indenter during the test, hence providing a continuous measure of the material's hardness and reduced modulus with indentation depth. Size effects down to 100 nm results in higher hardness values. The final hardness value is taken as the average in the stable zone, between 100 nm and 150 nm.

The nanoindenter continuous stiffness measurement (CSM) mode developed by Oliver et al. [160] was used. An oscillating displacement was imposed to the tip at a 75 kHz frequency allowing the continuous measurement of the contact stiffness. In the present work, it was considered that the elastic modulus remained the same wherever the indentation was performed. This provided hardness estimations without any assumption on the contact geometry, nor the material's residual stress state.

At small indentation depth, size effects resulting from the small dimensions of the loaded volume could occur. Such size effects usually result in higher hardness values at small depths, as the loaded volume to dislocation density ratio is not representative of the bulk. As illustrated in Figure 4.2, the method provides insights in the depth where size effects occurs, as the measured hardness is higher at lower depths. The final hardness measurement is then given as the hardness average in the zone where the hardness becomes constant. In this study, the hardness value was obtained by averaging hardness values for depths varying from

100 nm to 150 nm depth. Indentations were performed with a load control set-up. The indentation depth was limited to 200 nm.

4.2 Results

4.2.1 Microstructure analysis

Figure 4.3 shows an assembly of the two inverse pole figures (IPF) relative to the sample's normal obtained using the dictionary indexing method from the rolled edge to the sample's flat part. A drift in the orientation data between the two maps can be observed and results from EBSD beam drift due to the long time required for the acquisition.

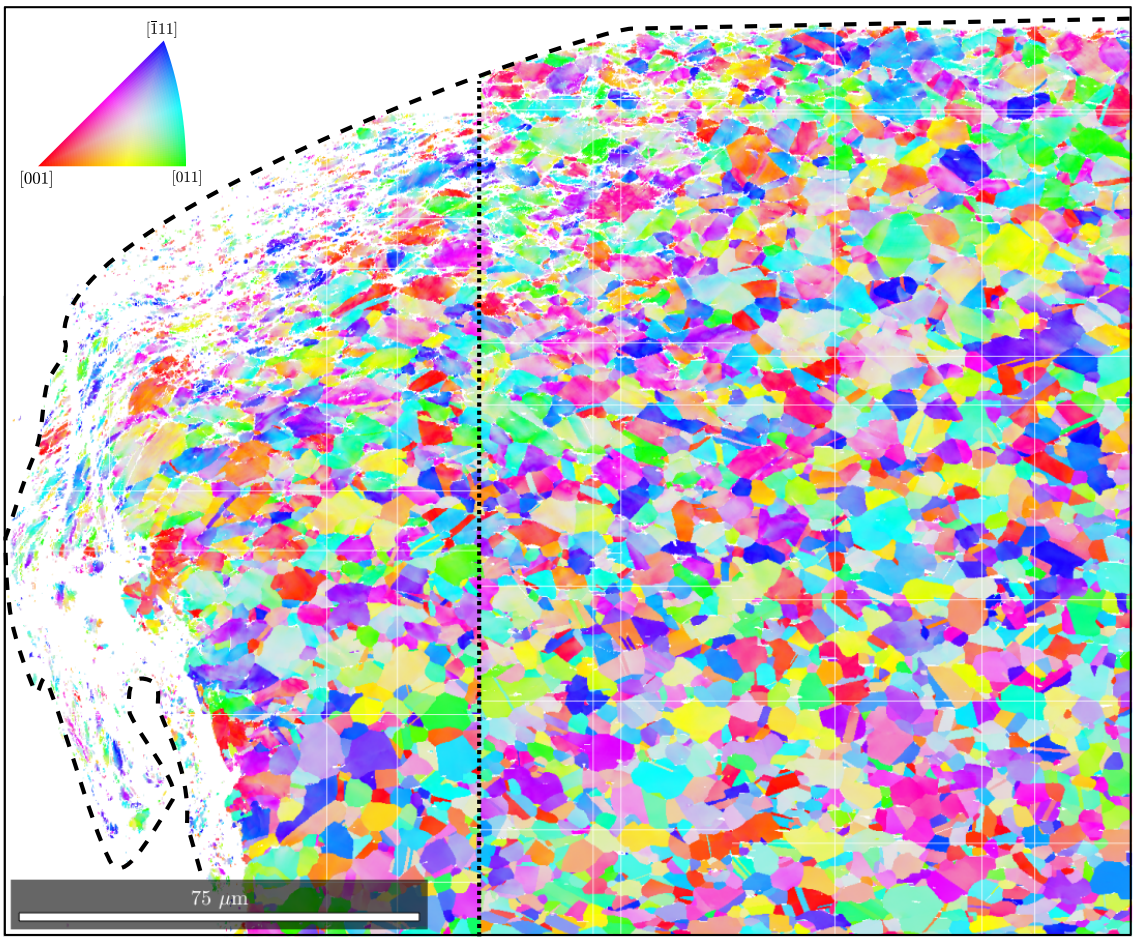

Figure 4.3 Inverse Pole Figure (IPF) map relative to the sample's normal obtained next to the rolled edge zone. Dashed lines represents the samples border to emphasize the zones that were not indexed. Elongated grains are observed next to the surface at the edges. The dotted line represents the limit between the two EBSD acquisitions. A drift in the orientation data due to the long acquisition time can be observed close to this limit at the bottom of the map.

Large plastic deformation close to the rolled edge led to lower indexing rates, even using the dictionary indexing method. The bulk and the flat part of the sample were composed of equiaxed grains. Elongated grains were found in the rolled edge close to the surface. No grain refinement was observed.

4.2.2 Hardening distribution

Reference shot peened zone

Figures 4.4 (a) and (b) show the GND distributions estimated in the reference zone at a minimum distance of 150 μm from the rolled edge with conventional Hough and dictionary indexing respectively. Figure 4.5 shows the relative position of the different maps shown in Figure 4.4 for better clarity. Both methods exhibited a GND density gradient from the surface to the bulk due to shot peening induced work hardening. The density gradient is however more pronounced when using the dictionary indexing method. Figures 4.4 (c) and (d) show the GND density distribution estimated in the bulk using Hough and dictionary indexing, respectively. The average density observed in the bulk qualitatively matches those represented at the lower depths in Figure 4.4 (a) and (b). This reveals that the maps acquired for the shot peened reference captured the whole surface gradient induced by shot peening. This is confirmed by Figure 4.6 which shows the average GND density depth profiles computed on 15 μm high bands at different depths. The average bulk GND density was 4.2×10^{14} m^{-2} using DI and 7.7×10^{14} m^{-2} using Hough indexing. The affected depth is therefore 125 μm deep.

Figure 4.6 quantitatively reveals the GND gradient induced by shot peening work hardening from the surface to the bulk. As already visible in Figure 4.4, the main difference between the two indexing methods was found in the bulk. The average density estimated using Hough indexing was 1.8 times higher, when compared to that obtained with DI. Such difference could be explained by spurious dislocation density due to noisy orientation data in the bulk when using conventional Hough transform. DI should therefore provide a better estimation of the GND density.

A Taylor hardening model was used to compare the estimated GND density gradient with experimentally measured hardening gradients. GND density ρ_{GND} was related to the critical resolved shear stress τ_c in a given system with:

$$\tau_c = \alpha G b \sqrt{\rho_{GND}}, \tag{4.1}$$

where α is an empirical constant representative of the plasticity mechanism, taken as 0.3, as

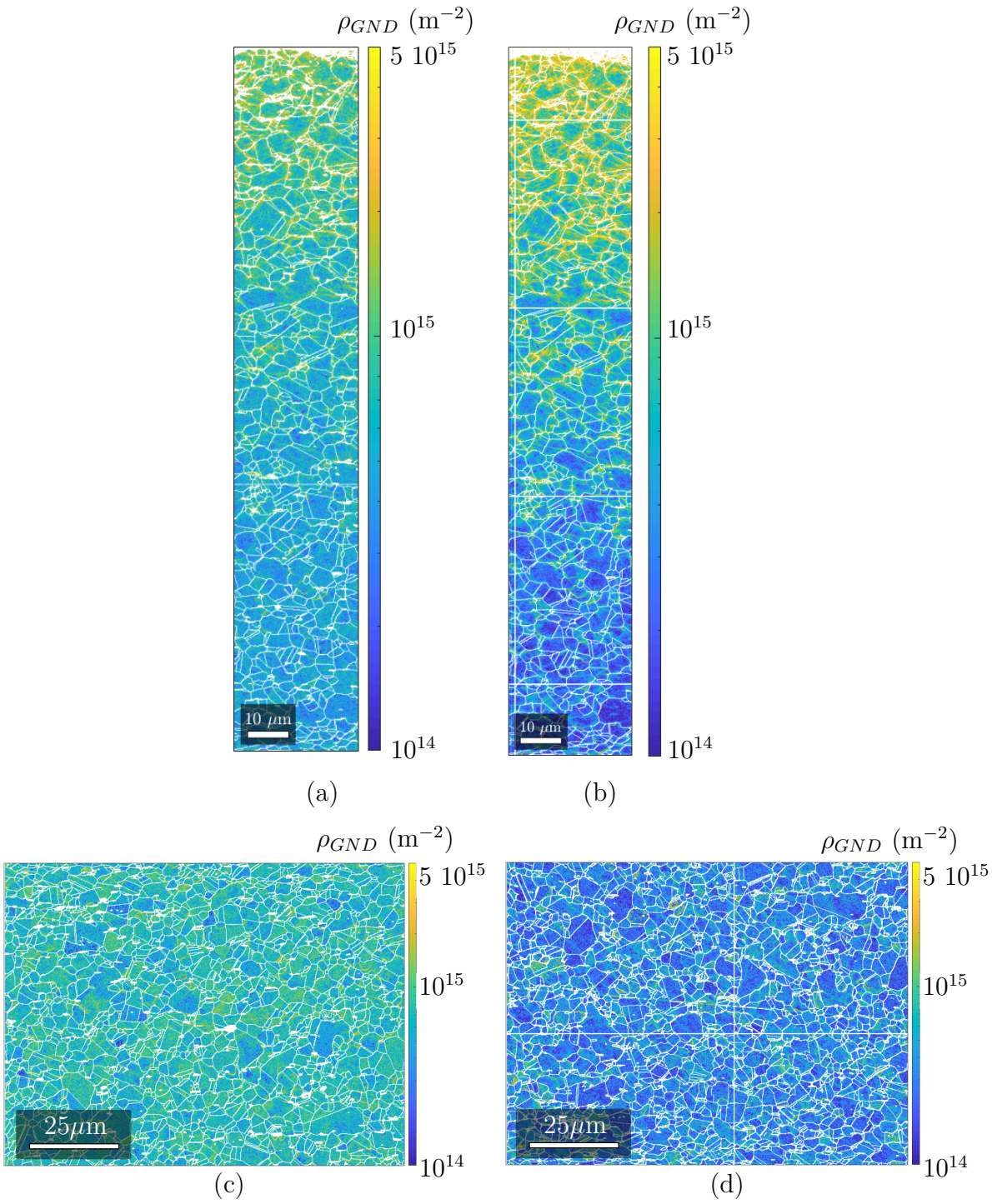

Figure 4.4 GND density map estimated far from the sample edges close to the surface and in the bulk using (a)(c) conventional Hough transform and (b)(d) Dictionary indexing. Both figures reveals a hardening gradient induced by shot peening from the surface to the bulk. The dictionary indexing approach provides a better contrast inside each grain and reveals a higher dislocation density gradient. The average dislocation density observed at the bottom of (b) seems to match the average hardening level of the sample bulk.

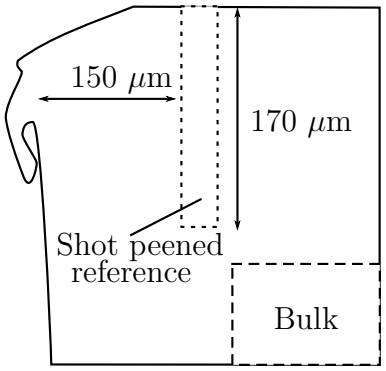

Figure 4.5 Position of the two different EBSD maps represented in Figure 4.4. The dotted lines represents the shot peened reference zone close to the surface. The dashed lines represents the bulk zone.

.

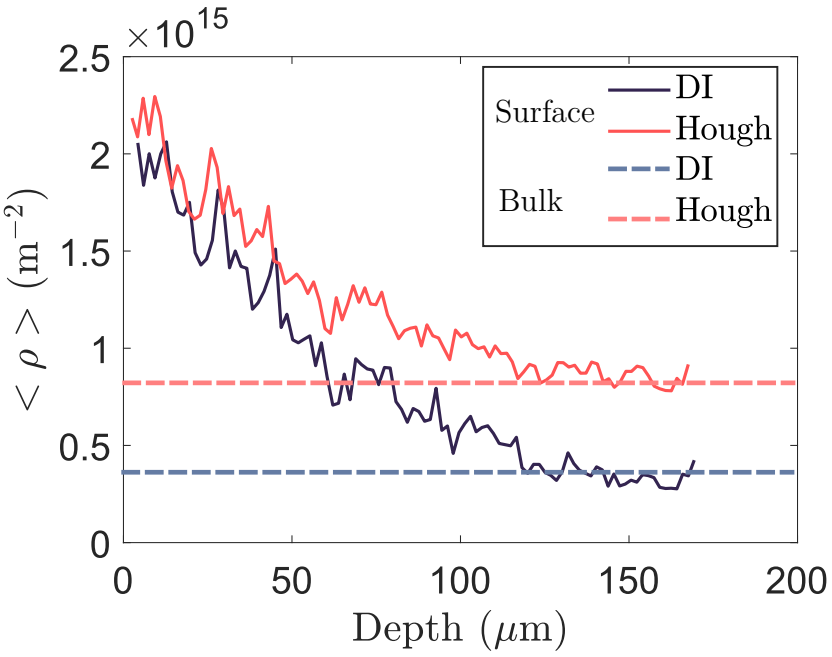

Figure 4.6 GND density average variations with depths using conventional Hough transform and Dictionary indexing. A higher GND density gradient is quantitatively found using DI. Higher density values in the bulk using conventional Hough transform result from higher noise on the orientation values.

suggested by Mughrabi et al. [161], and G is the material shear modulus taken as 76 GPa. The critical resolved shear stress was then related to the material's hardness H using Tabor's relation as:

$$H = 3\sigma_y, \tag{4.2}$$

where σ_y is the material's yield stress estimated as:

$$\sigma_y = \frac{1}{m}\tau_c, \tag{4.3}$$

where m is the Schmid factor, which was here assumed as constant and taken as $\frac{1}{\sqrt{6}}$. Such relations do not provide quantitative assessment of the hardness absolute value using the GND density as they are purely empirical and rely on strong hypotheses. They however provide an order of magnitude of the hardness differences resulting from shot peening induced work

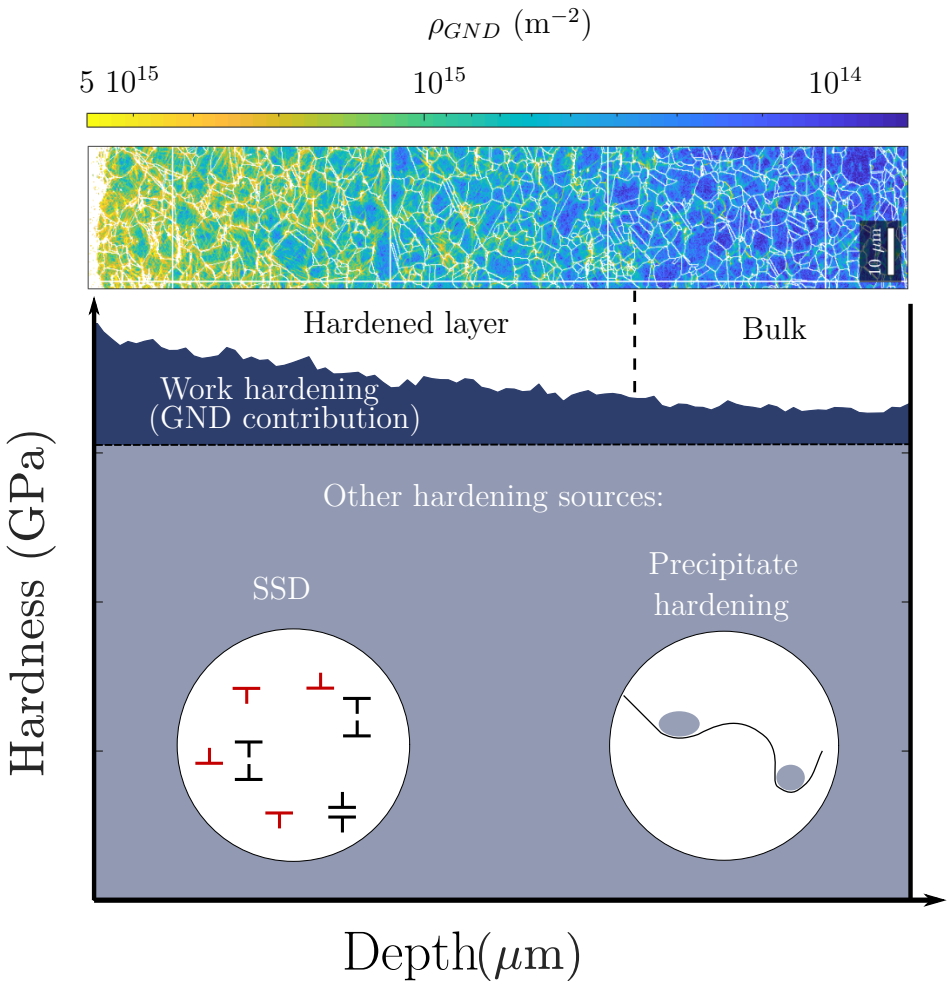

Figure 4.7 Shot peened IN718 specimen sources of hardening. EBSD estimations only provides insights in the work hardening GND contribution to the global hardness, represented as the dark blue area. This contribution is small compared to other contributions such as precipitate hardening or the presence of SSD, represented by the gray area. Indentation measurements are representative of both areas. The contribution of GND induced work hardening on the hardening gradient can be extracted using EBSD based GND estimations.

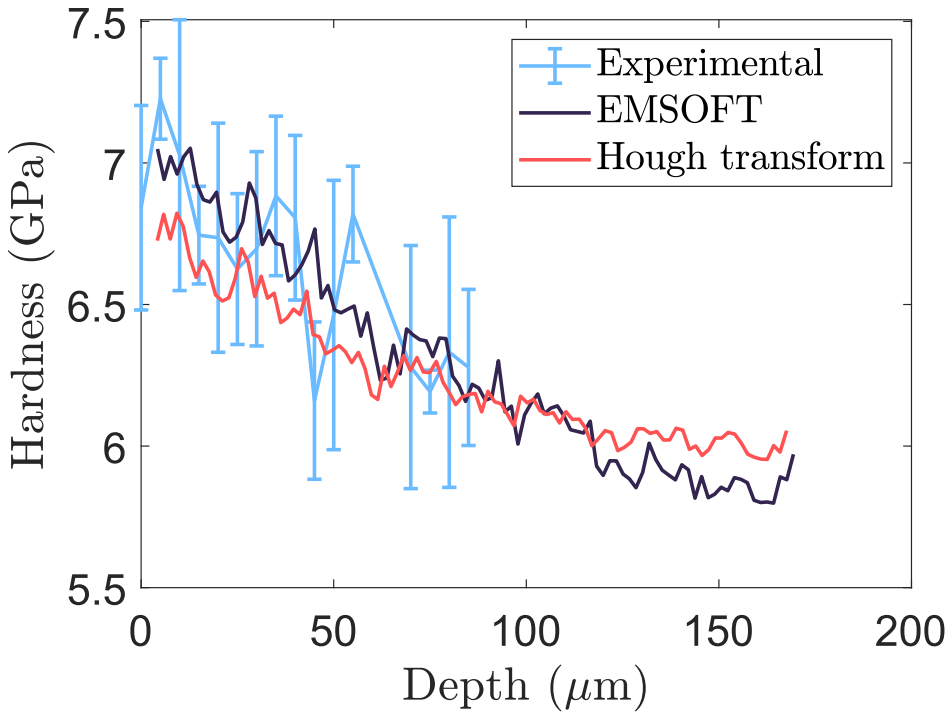

Figure 4.8 Comparison between experimentally measured indentation hardness and hardness estimations from the EBSD GND densities. The difference between the indentation measured hardness and the GND estimations at 90 μm depth was added to the estimated hardness to compare only the hardness gradient resulting from the dislocation density gradient, without accounting for other sources of hardening. Experimental hardness have a large dispersion. The estimated hardness gradient follows well the experimental one for both indexing methods.

hardening.

Also, this estimation only accounts for GND induced Taylor work hardening and not for other contributions such as precipitate hardening which is predominant for the studied material. As schematized in Figure 4.7, these other contributions have to be added to the estimated hardness value to be compared to experimental hardness. To compare only the hardening gradient, the indentation measured hardness value at 90 μm depth was added to the GND estimated hardness.

Figure 4.8 shows the comparison of experimentally measured hardness values with the GND estimations using both indexing methods. Despite the large variability of the indentation hardness measurements, a good correspondence can be found with the GND estimations for both methods. The difference in GND densities observed between Hough indexation and Dictionary indexing only resulted in a 300 MPa hardness difference, which is negligible when compared to the material's hardness.

Rolled edge zone

Figure 4.9 shows the GND density distribution close to the rolled edge. Higher densities were observed close to the rolled edge as compared to the flat part of the sample. Also, severe plastic deformation close to the rolled edge surface prevented the EBSD indexing.

To compare the material hardening state between the reference and the rolled edge at the same depth, a depth map between a given point and the sample surface was computed as shown in Figure 4.10 (a). The sample's surface was drawn manually using Bezier Curves with the Inkscape software . The minimal distance between a given point and the curve was then computed using a Matlab script. This provided GND density data bands at a given depth such as those shown in Figure 4.10 (b).

Figure 4.11 shows the average GND density variation from the rolled edge to the sample center at 20 μm and 80 μm depths. The figure confirms that higher dislocation density

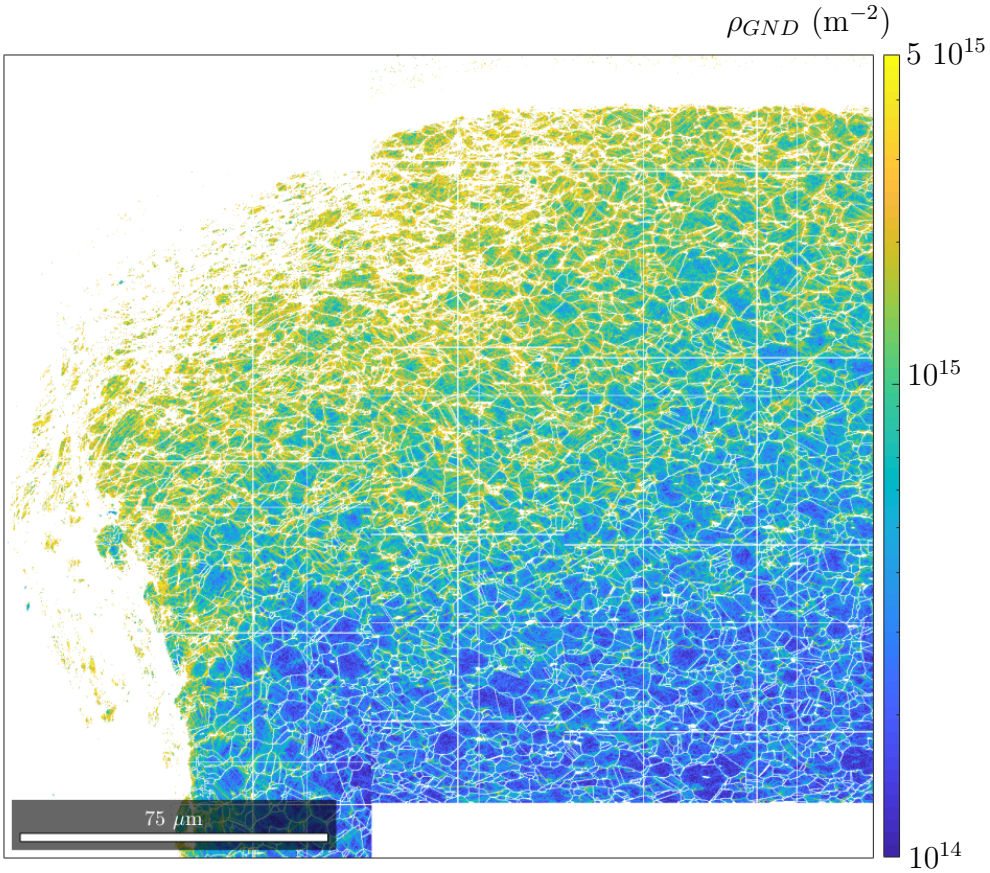

Figure 4.9 GND distribution in the rolled edge estimated using dictionary indexing. Higher density values can be observed next to the rolled edge than in the shot peened reference.

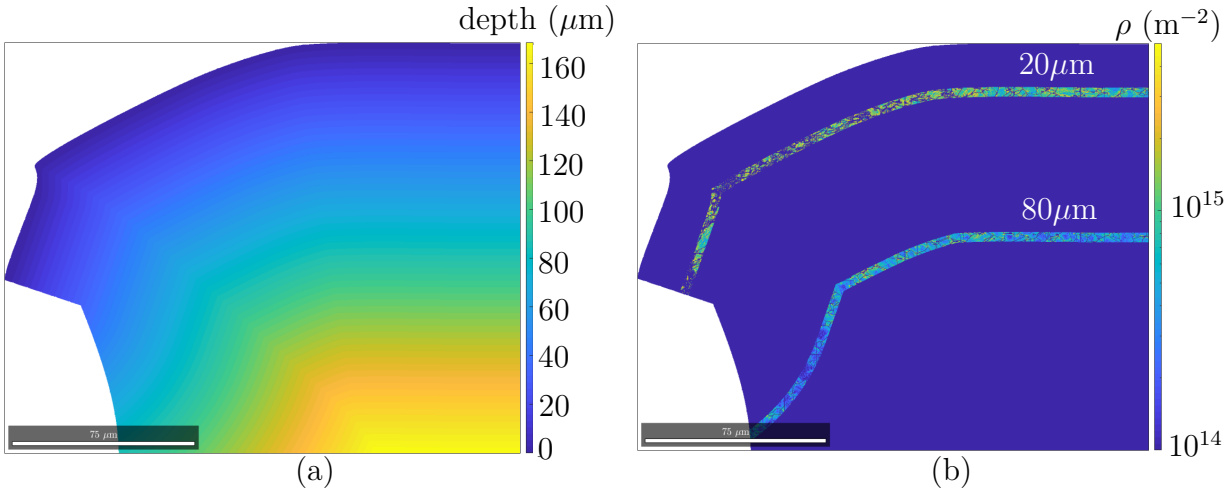

Figure 4.10 Methodology for average GND density estimation at constant depth. (a)Depth map computed for the rolled edge zone to compare average dislocation values between the rolled edge and the reference at the same depths, despite the geometry of the rolled edge. (b)GND density maps on two bands taken at 20 μm and 80 μm. Average dislocation density variation from the edge to the sample center was computed on the two bands by computing the dislocation average on 100 slices of those bands.

values are found close to the rolled edge. Figure 4.12 (a) shows a comparison between the GND density variation with depth, close to the rolled edge and in the reference zone. The resulting Taylor hardening estimation is shown in Figure 4.12 (b). This further confirms the results shown in Figure 4.11. It also reveals that the density gradient is higher in this zone, as the same bulk density was found at similar depths as in the reference zone. Figure 4.12 reveals that such GND gradients could result in hardness differences of 500 MPa close to the surface.

Figure 4.13 (a) shows a comparison between experimentally measured hardness in the rolled edge at three different locations and in the reference at two different locations, as detailed in Figure 4.13 (b). The figure reveals an average subsurface hardness increase of 1 GPa between the rolled edge and the reference. This confirms the results obtained using GND estimations from EBSD analyses. Let us note that the order of magnitude is correct even though there is a 500 MPa difference between both methods. Such a difference could be explained by the low indexation rate obtained next to the rolled edge surface. The choice of a constant Schmid factor, the use of the Taylor hardening law as well as the high indentation measurements standard deviation (326 MPa in average) could also explain such a bias.

Also, it should be noted that EBSD observations do not provide access to the statistically stored dislocation densities, which could also contribute to the observed hardness.

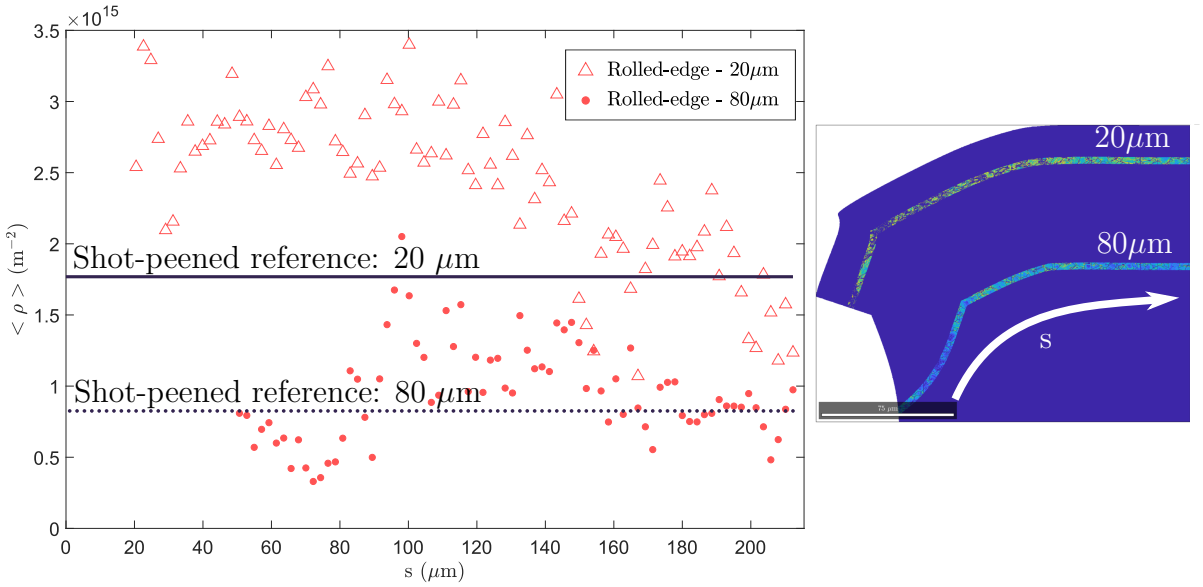

Figure 4.11 Average GND density variation from the rolled edge (s=0μm) to the reference zone (s=220 μm) with the curvi-linear abscissa s following the bands presented in figure 4.10. Decrease in the dislocation density from the edge to the center can be observed at 20 μm depths.

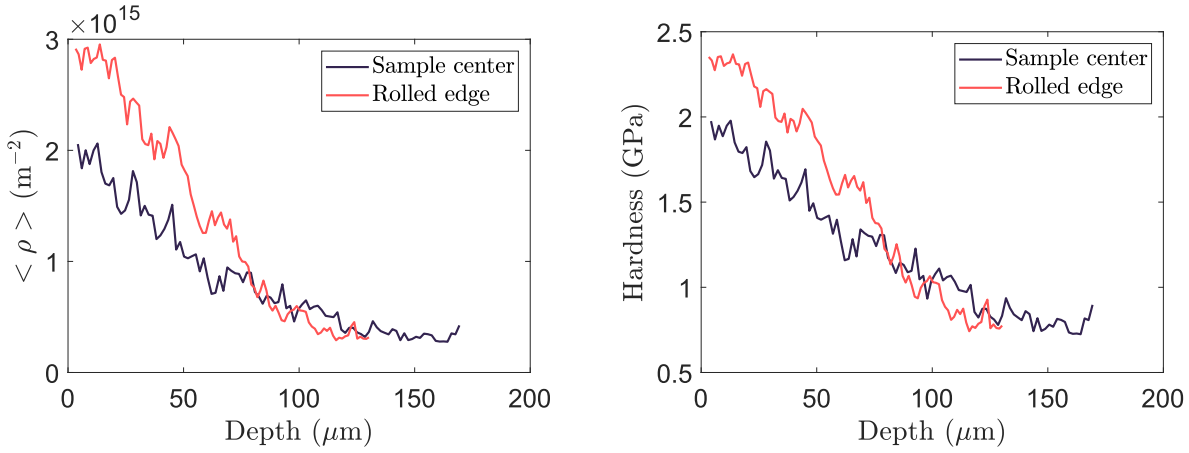

Figure 4.12 Average in-depth GND density and hardness variations. (a) Average GND density variation with the depth represented in Figure 4.10(a) next to the rolled edge ($0 \leq s \leq 90\ \mu m$) and in the reference zone ($190\ \mu m \leq s \leq 220\ \mu m$). (b) Taylor hardening estimations in the rolled edge and reference zones. Higher GND densities are found close to the rolled edge beneath the surface. This results in hardening differences of roughly 400 MPa at the surface between the rolled edge and the reference zone.

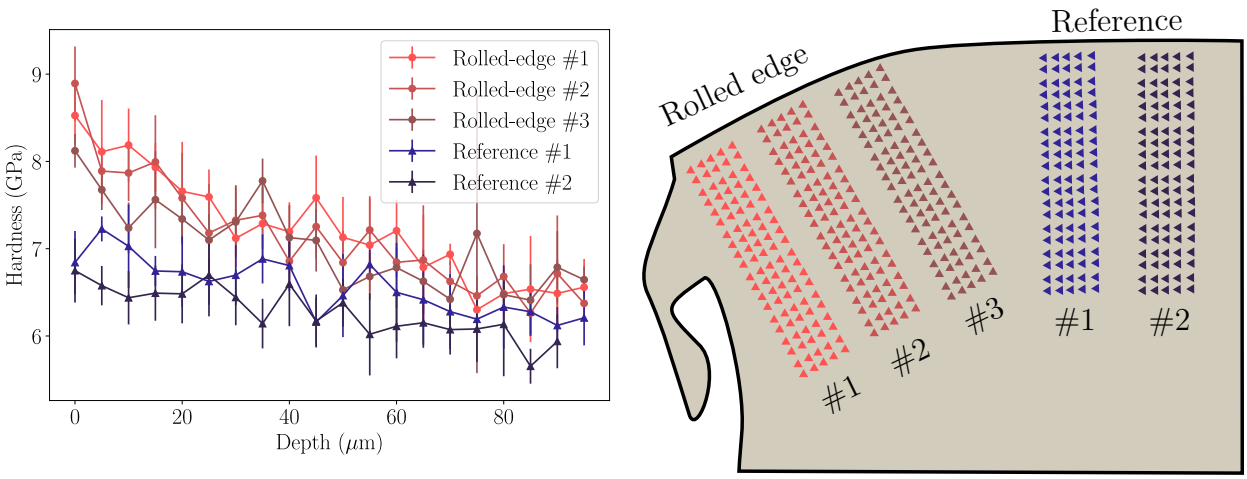

(a) (b)

Figure 4.13 Indentation hardness measurements. (a) Hardness gradient in the rolled edge and in the reference zone for respectively two and three different indentation tests at different locations sketched in Figure (b). Subsurface hardness increase of 1 GPa in the rolled edge compared with the reference was experimentally observed.

4.3 Discussion

DI resulted in lower estimated GND densities than those predicted by Hough indexing in the bulk. Such a difference could be attributed to a better performance of the DI method toward noisy patterns. Figure 4.6 however reveals that similar densities were found by the two methods in the shot peened surface, where the largest plastic deformations should occur. Thus, DI did not improve indexation toward severe plastic deformation. Also, the difference between the two methods resulted in hardness differences close to the nanoindentation measurement uncertainties. Such differences are therefore negligible when considering hardness estimations. This partly results from the Inconel 718 high hardness resulting from precipitate hardening. Such difference should however be more significant on softer materials and would better assess the relevance of the method.

Microstructural evolutions induced by severe plastic deformations are related to the shearing mechanisms imposed to the material. According to Segal et al. [162], simple shear leads to grain rigid body rotations and favors grain refinement. Inversely, pure shear results in higher grain size ratio and higher intragranular dislocation densities. In the present work, higher dislocation densities and the absence of grain refinement close to the rolled edge therefore resulted from a pure shear state induced by shot peening close to the sample's border.

Figure 4.14 summarizes the proposed deformation mechanism leading to the rolled edge

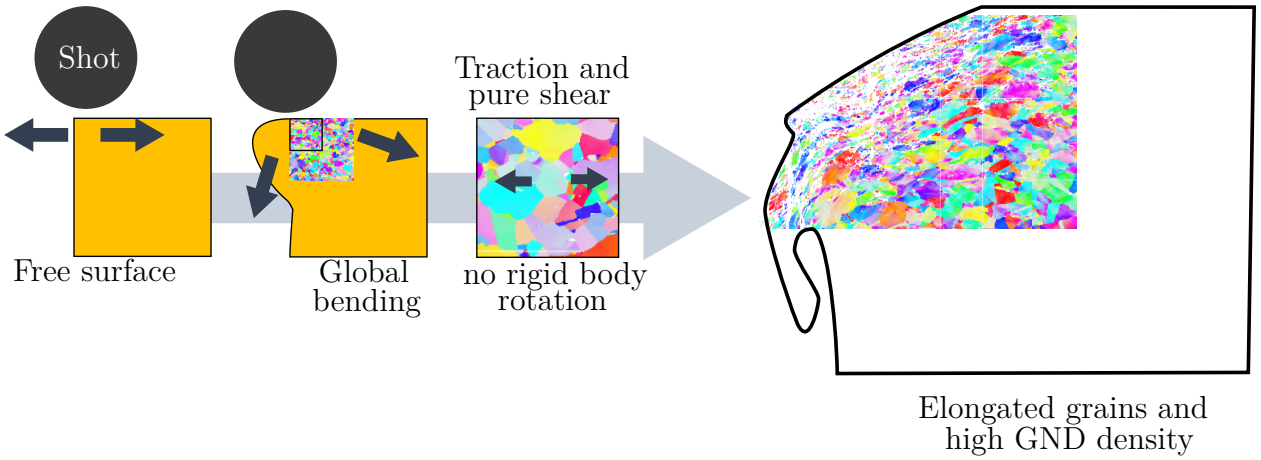

Figure 4.14 Summary of the proposed deformation mechanism in the rolled edge. Early shots induces surface stretching bulging the surface where the material is free to deform. When further impacted, stretching results in a global bending of the forming rolled edge. This induces pure shear stress state in the grains.

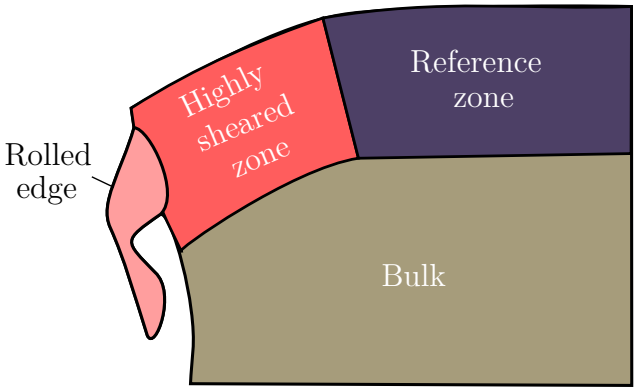

Figure 4.15 Summary of the different hardening areas induced by shot peening of an edge. Higher GND densities and hardening gradient than that found in the reference zone was induced by the pure shear state close to the edge. The induced rolled edge being more free the deform suffer was subjected to less shear when further impacted as compared to the highly sheared zone.

microstructural state. As opposed to the reference zone, represented in dark blue in Figure 4.15, the impacts occurred on a partially free surface. Therefore, early shot induce material stretching, which produces a bulge where the material is free to deform. When the initiated bulge is further impacted, a global bending develops in the bulge zone, which leads to a rolled edge and to a highly sheared zone as depicted in Figure 4.15. Since the highly sheared zone is free to rotate, individual grains experience no rigid body rotation. Such bending induces

high tensile stresses in the rolled edge grains, resulting in a pure shear stress state, as the deforming grains are blocked by the bulk. This results in highly elongated grains and a high dislocation density in the highly sheared zone. Such mechanism is similar to that observed by Mattei et al. [163] after microstructural analysis of a highly bent AA6016 sheet. Once formed, the rolled edge is more free to deform as opposed to the highly sheared zone and is therefore less subjected to shear when further impacted.

These differences in hardening could have an influence on the treated parts' fatigue life. Klotz et al. [164] investigated the influence of shot peening induced hardening and residual stresses on the Inconel 718 alloy fatigue life. The authors found that shot peening induced cold work reduces the negative effect resulting from surface roughness in the LCF regime. The hardening state of the Inconel 718 sample has therefore a critical impact on its LCF life properties, independently of the residual stresses induced in the material. In the present study, work hardening has a negligible influence on the Inconel 718 properties compared to precipitate hardening. The increased hardness observed in the present work should therefore only have little effect on the material's fatigue life in the LCF regime.

Also, for the Inconel 718, the influence of the rolled edge higher hardening values on the fatigue life should be negligible in the HCF regime, as it is mainly driven by the materials' residual stress state, as evidenced by Klotz et al. [164]. Eleiche et al. [5] performed HCF tests on flat shot peened high strength martensitic steel specimens for which the residual stresses had been relaxed by a thermal treatment. Shot peened specimens presented a 20% fatigue life improvement, when compared to non-treated specimens. However, the residual stress relaxation only degraded the material's fatigue life by 3%. The increased hardness observed in the rolled edge could therefore have an impact on the HCF fatigue life of such materials.

Higher dislocation densities could also have an effect on the corrosion properties of the treated material. Naeini et al. [165] studied the pitting resistance of an accumulative roll bonded 5052 aluminum alloy sample. An increase in dislocation density resulted in a less protective oxide layer hence degrading the material's resistance to corrosion. Similar results were also found by Singh et al. [166] after cold rolling of an AISI304 steel and also by Laleh et al. [167] on a AZ91D magnesium alloy after surface mechanical attrition treatment (SMAT). The higher hardening state of the rolled edge as well as its non-linear shape could therefore have a negative impact on the treated part's corrosion resistance.

Finally, as evidenced by Figure 4.11, the rolled-edge formation influences the sample's hardening gradient in a zone surrounding the edge, and not solely inside the rolled-edge. This reveals that removing the rolled edge, as suggested by You et al. [158], would not entirely remove the hardening heterogenities resulting from its formation.

4.4 Conclusion

The objective of this work was to study the mechanical behaviour of a shot peened induced rolled edge as compared to a flat shot peened zone for the Inconel 718 alloy. The main contribution are:

- DI indexed EBSD maps presented lower GND densities than those obtained from Hough indexing. This was attributed to spurious GND densities due to noisier orientation data when using Hough indexing.
- Nanoindentation hardness measurements revealed that shot peening induced rolled edges present a hardness increase of 1 GPa and a higher hardness gradient as compared to the reference zone.
- This hardening was directly related to the GND densities estimated in the rolled edge using a Taylor hardening model. This revealed that the measured hardness increase is mainly due to work hardening.
- The rolled edge surface presented elongated grains which might be explained by a pure shear state imposed to the material during severe plastic deformation.
- Such hardening and microstructural heterogeneities were not only found in the rolled-edge but also in its surrounding.
- Comparison between GND gradient maps and nanoindentation data provided a methodology to assess the process influence on complex geometries which is crucial to understand potential effects on the treated parts fatigue's life or corrosion resistance.

The zone surrounding a shot peened induced rolled edge could therefore present different fatigue and corrosion resistance properties than a flat shot peened zone, even after the removal of the excess of matter. This influence should however be investigated through HCF and LCF fatigue tests on material for which work hardening is predominant, such as martensitic stainless steel or alpha-iron alloys, as well as corrosion tests, to confirm this influence.

This study therefore further confirms the necessity to model the process at the grain scale as the induced properties are intimately related to the microstructural evolution occuring during the process. Also, it confirmed that GND estimations using the method developed in Pantleon et al. [109] could be an interesting tool for crystal plasticity framework validation as it provides a good estimate fo the induced hardening gradients.

CHAPTER 5

Identification of single crystal copper strain-rate dependency at high strain rate at the surface scale

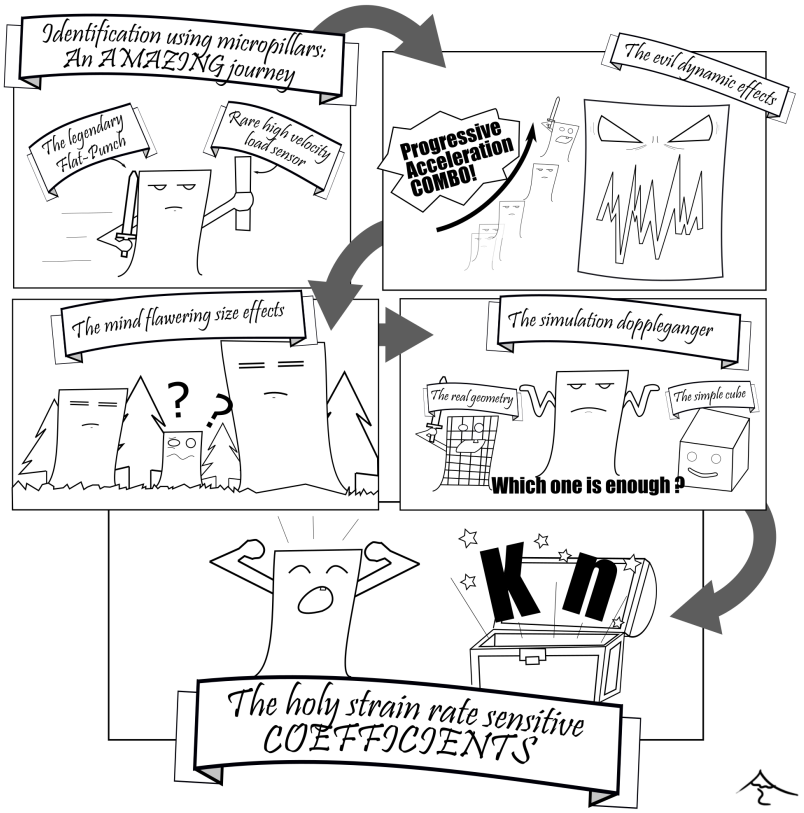

Introduction

Shot-peening modeling requires the knowledge of the treated material's behaviour for strain rates up to 10^6 s^{-1} [20]. Thus, parameters identification for such models is classically performed based on split Hopkinson pressure bar tests (SHPB) [41–43, 168]. However, SHPB remains a macroscopic mechanical test since the solicited volumes range from a few cubic millimeters to a few cubic centimeters [169]. Thus, it cannot be used to characterize material's surface behavior as it is only applicable on low surface to volume ratio specimens. Dynamic indentation was also used by several authors [170,171] to obtain metals high-strain rates load displacement curves for plastic zone radius down to a few hundreds of micrometers [169].

Most studies attempting to model shot-peening at the grain scale relied on crystal plasticity finite element frameworks (CPFE) whose input properties were extracted from macroscopic SHPB or cyclic tests [8,18,19]. High strain rate tests performed at the crystal scale are however required to identify CPFE coefficients representative of the material behaviour during peening. Macroscopic tests such as SHPB are therefore highly impractical in such context as it is usually difficult to produce large single crystals for most alloys shot peened in the industry [172]. Also, tests used for identification must be representative of the surface behaviour as the depth affected by shot-peening is usually of a few hundreds of microns.

Nanomechanical tests such as micropillar compression could provide such local measurements as they provide local stress-strain curves at the grain scale. Cruzado et al. [87] used such test for material parameters identification at low strain rates. The authors performed microcompression tests on a nickel-based super alloy in single slip and double slip conditions. The constitutive framework coefficients were deduced directly from the load displacement curves in single slip orientations. However, the study did not investigate the well-posedness of the inverse problem. Also, the proposed methodology could not be used on materials for which single crystals cannot be produced as it requires microcompression in perfect single glide conditions. When multiple gliding planes are activated, the load displacement curves can hardly be interpreted analytically as the pillar strains are highly heterogeneous.

Several works used finite element model updating (FEMU) to obtain crystal plasticity coefficients using experimentally obtained heterogeneous fields [136, 144, 173]. The method consists in varying the input material parameters of a finite element model to minimize the difference between experimental and predicted observation fields. It is therefore a promising methodology for crystal plasticity coefficients identification on multiple glide pillar compression tests as it would consider the heterogeneous straining of the pillar during identification. To the author's knowledge, FEMU parameter identification using micropillar compression

load-displacement curves has never been performed.

Using a piezo-based sensor with high eigen-frequencies, Guillonneau et al. [89] recently performed microcompression tests at strain rates up to 10^3 s^{-1} on nanocrystalline nickel specimens. Such test procedure provides useful data for parameters identification at high strain rates, at the local scale. Also, microcompression at high strain rates has never been performed on single crystals.

This work investigates the possibility to obtain a unique solution of a CPFE framework strain rate dependent coefficients by FEMU using high strain rates micropillar compression tests on single crystal copper. This work aims to develop a methodology for identification of a single crystal high strain rate surface behavior. The well-posedness of the inverse problem was thoroughly investigated using an identifiability indicator. This ensures that the chosen experimental conditions contains sufficient information for identification, which has not yet been investigated using micropillar compression tests. Copper single crystal has been extensively studied since the early days of crystal plasticity and was thus chosen to validate the proposed methodology. The content of this chapter was published in the Materials & Design journal [23].

The chapter is organized as follows: the experimental as well as the numerical models and identification methodology used in the study are presented in Section 5.1. The performance obtained using the inverse identification methodology, first, on a virtual material, then, on the experimental results are detailed in Section 5.2. Finally, the results are discussed in Section 5.3.

5.1 Materials and Methods

5.1.1 Materials and specimen preparation

Micropillar compression tests were conducted on pure single crystal copper specimens obtained by directional solidification using a conventional Bridgman apparatus. Three crystals were grown in the [111], [110] and [100] orientations, respectively. A 1×1 cm square with a thickness of 0.5 cm was cut from each specimen using a diamond wire saw.

The samples were mechanically polished using SiC grit paper from P400 to P1000 and then electro-polished to provide a sufficiently good surface finish for EBSD observations. This was necessary to obtain the single crystal's exact orientation (given in Table 5.1) by conventional Hough indexation, using an HKL system (Oxford instrument) composed of a NordlysII camera and the Channel 5 software suite.

Micropillars were machined by focus ion beam (FIB) machining using a Thermo Scientific Helios NanoLab DualBeam microscope. First, high currents (30 kV, 2.5 A) were used to dig the raw pillar shape. Smaller currents (30 kV, 80 pA) were then used to refine the geometry. Size effects were investigated using 3 μm, 6 μm and 8 μm diameters pillars for every orientation. Compression tests at different velocities were performed on 6 μm and 8 μm diameters pillars. The targeted pillar diameter to height ratio was 1:2, as suggested by Zhang et al. [77] to prevent pillar buckling.

The exact pillar dimensions were required to reproduce the pillar geometry in the numerical simulations. Figure 5.1 shows the measured pillars dimensions (top (D_t) and bottom (D_d) diameters and height (h)). The pillars dimensions means and standard deviation are summarized in Table 5.2. The measurements were performed directly on scanning electron microscope (SEM) pictures, using one observation angle.

5.1.2 High dynamic micropillar compression tests

Micropillar compression tests were conducted using an ALEMNIS in-situ nanoindenter apparatus in a Zeiss Gemini supra 55VP Scanning Electron Microscope (SEM). The test consists in compressing a small pillar with an instrumented diamond flat-punch to extract the local load-displacement curve. The load applied on the specimen was measured with a 50 kHz acquisition rate using a high dynamic SmarTip load cell placed under the specimen holder. Such an apparatus can reach high strain rate microcompression testing up to 10^3 s^{-1}, as detailed in the work of Guillonneau et al. [89].

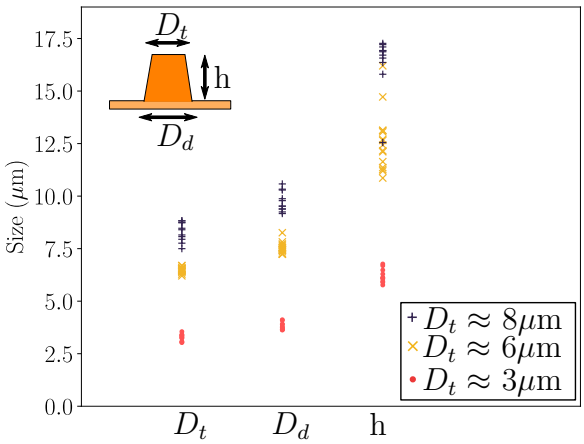

Figure 5.1 Pillars top and bottom diameters (D_t and D_d) and height (h) for the three crystal orientations. Targeted pillar top diameters were 3 μm, 6 μm and 8 μm. The target diameter to height ratio was 1:2.

Table 5.1 Single crystal's experimentally measured orientation Euler angles

Target	$\phi_1(°)$	$\Phi(°)$	$\phi_2(°)$
[100]	128,2	3,42	59
[110]	84,15	44,22	0.1
[111]	290,96	51,37	47,22

Table 5.2 Micropillar dimensions means and confidence interval (95%) for the three aimed sizes.

Target D_t	D_t	D_d	h
3 μm	3.27 $\pm$ 0.1	3.81 $\pm$ 0.11	6.21 $\pm$ 0.20
6 μm	6.48 $\pm$ 0.07	7.54 $\pm$ 0.13	12.57 $\pm$ 0.69
8 μm	8.31 $\pm$ 0.26	9.74 $\pm$ 0.27	16.39 $\pm$ 0.76

Pillars were compressed with nominal strain rates of 10^{-2} s^{-1} and 10^{2} s^{-1}. Note that the nominal strain rate is defined as the maximum displacement divided by the pillar initial height and by the compression time.

Figure 5.2 shows a typical displacement profile imposed to the indenter during a microcompression test. For high strain rate tests, the pillar is not in contact with the indenter at its initial position. The indenter accelerates progressively to reach the targeted constant displacement rate without triggering the piezoStack actuator natural frequencies. For each test,

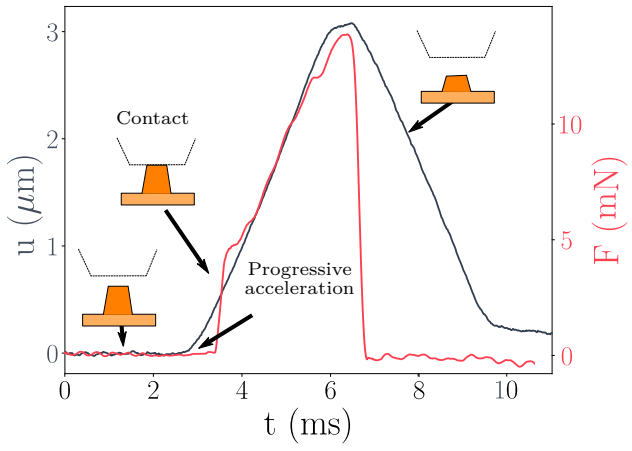

Figure 5.2 Example of a typical high dynamic imposed displacement profile $u(t)$ and resulting measured load $F(t)$. The indenter accelerates progressively to reach the pillar surface at a constant displacement rate. The sudden load increase provides the time of contact. This prevents from triggering the actuator natural frequencies.

the contact onset was taken as the time for which the measured load exceeds the average noise value. The critical acceleration to reach before the actuator vibrates was estimated through several tests in the void.

The inertial force induced by the indenter acceleration was also investigated and corrected using sinus displacement profiles in the SEM void, following the methodology detailed by Guillonneau et al. [89].

The measured displacement u_{mes} was corrected to remove the influence of the frame elastic deformation using:

$$u_{pil} = u_{mes} - \frac{F}{K_{frame}}, \tag{5.1}$$

where u_{pil}, F, K_{frame} correspond to the pillar displacements, the measured load and the frame stiffness respectively. Copper being a very ductile material, the influence of the substrate displacement was considered negligible. The load displacement curve was filtered to remove part of the experimental noise using a built-in moving average smoothing filter (10 points length).

All the microcompression data generated in this work are available for download as detailed in the Data availability section. Each pillar is associated to a file containing the raw and the treated load displacement curve, as well as SEM pictures of the pillar both before and after compression.

5.1.3 Material parameters identification

Finite Element Model Updating (FEMU) procedure

The single crystal constitutive behaviour was modeled using the Meric-Cailletaud large-strain formulation crystal plasticity framework [1, 21] detailed in section 2.2.2. The interaction matrix coefficient was chosen as the one identified by Meric et al. [1].

The Norton law K and n coefficients were identified using FEMU to assess the material's strain rate sensitivity. The finite element model developed for identification used the experimentally measured pillars geometries and is detailed in Section 5.1.4. The procedure was first tested using load-displacement curves generated by a virtual material. Those curves were obtained using the full pillar geometry simulations with coefficients $K = 7$ MPa $\mathrm{s}^{1/n}$ and $n = 4$.

The identification procedure consisted in varying the Norton law coefficients K and n to

minimize the following cost function:

$$\Psi_\sigma(K,n) = \frac{1}{2T}\sum_{m=0}^{N_{exp}}\sum_{t=0}^{T}\left(\frac{\sigma_m(\varepsilon(t),K,n) - \sigma_{m,exp}(\varepsilon(t))}{\max_t(\sigma_{m,exp}(\varepsilon(t)))}\right)^2. \tag{5.2}$$

In Equation 5.2, T is the number of acquisition points which was chosen as 100 for every simulation, N_{exp} is the number of stress-strain curves used for identification, $\sigma_{m,exp}(\varepsilon(t))$ and $\sigma_m(\varepsilon(t),K,n)$ are respectively the experimental and predicted stress. Despite the finite strain formulation of the crystal plasticity framework presented in Section 2.2.2, the identification procedure was restricted to the small strain range of the curves. The experimentally measured stress was therefore computed using

$$\sigma_{m,exp}(t) = \frac{P_{m,exp}(t)}{\pi r_{avg}^2}, \tag{5.3}$$

where $P_{m,exp}(t)$ is the experimental load at time t and r_{avg} is the average of the pillar initial top and bottom radii.

Note that using the stress defined as in Equation 5.3 for identification is equivalent to using the load as the identification variable. In the present work, the stress was used to compare the identification performance of the present model with a single-element model, as presented in Appendix C.

The Levenberg-Marquardt algorithm was used to minimize Ψ_σ. The coefficients used as a first guess in the procedure were those identified by Meric et al. [1] and recalled in Tables 3.1, 5.3 and 5.4.

To compare the experimentally measured and predicted data at the same strain values, the experimental stress was interpolated linearly at the strain values chosen for comparison. Only the loading part of the curve was used.

Identifiability indicator

Given the computational cost of the full pillar geometry model, the identifiability indicator I defined in the work of Richard et al. [130, 137, 144, 174] was used as an indicator of the solution uniqueness and stability. This indicator is based on the cost function hessian close to the cost function minimum. It is defined as:

$$I = \log_{10}\left(\frac{\lambda_{max}}{\lambda_{min}}\right), \tag{5.4}$$

Table 5.3 Elastic coefficients [1]

C_{11} (MPa)	C_{22} (MPa)	C_{44} (MPa)
159,300	122,000	81,000

Table 5.4 Norton law and isotropic hardening parameters [2]

K (MPa s$^{1/n}$)	n	R_0 (MPa)	Q (MPa)	b
5	10	10	6	15

where λ_{max} and λ_{min} are the eigenvalues extrema of the approximated dimensionless hessian matrix close to the solution, defined as:

$$\overline{H}_{ij} = \sum_{t=0}^{T} \sum_{m=1}^{N_{exp}} \frac{\partial \overline{P_m}(t)}{\partial \overline{\theta}_i} \frac{\partial \overline{P_m}(t)}{\partial \overline{\theta}_j}. \tag{5.5}$$

In the above, $\frac{\partial \overline{P_m}(t)}{\partial \overline{\theta}_i}$ is the load-displacement curve sensitivity to the θ_i parameters. This sensitivity was here defined as:

$$\frac{\partial \overline{P_m}(t)}{\partial \overline{\theta}_i} = \frac{P_m(t, \theta_i + \delta\theta_i) - P_m(t, \theta_i)}{\max\limits_t(P_m(t, \theta_i))\delta\sqrt{T}}, \tag{5.6}$$

where δ is a perturbation factor chosen as 5%. Equation 5.6 defines the dimensionless load variation to a perturbation δ on parameter θ_i. Normalisation by $\sqrt{T}$ provides a sensitivity definition consistent with Equation 5.2 and ensures that I does not depend on the number of acquisition points. A good identifiability of the solution can be achieved for $I \leq 2$, as explained by Richard et al. [130].

As pointed out by Renner et al. [137], normalization by $\max\limits_t(P_m(t, \theta_i))$ is equivalent to consider an absolute uncertainty on the load measurement. Such assumption relies on the highly repeatable experimentally measured stress for a given strain at a given strain-rate, as well as by the high signal to noise ratio provided by the piezo load sensor.

5.1.4 Finite element model

The experimentally measured pillar geometry was used to model the microcompression experiment. The model used the Abaqus 2018 software coupled with Zset using the Zmat module. The pillar geometry and mesh is represented in Figure 5.3. Substrate dimensions were chosen to prevent any effects of the boundary conditions on the load displacement curve

(see Appnedix C). The mesh was composed of linear reduced hexahedric elements (C3D8R) to prevent locking effects arising from high plastic incompressibilty [155].

Hourglass was corrected by adding an artificial stiffness to the elements. Only a small correction was necessary (15 MPa) as little hourglass was observed. The mesh size varied from 0.14 μm in the pillar to 1.4 μm in the substrate and was determined after a convergence study (see Appendix C).

Using the converged model, the computational time for each simulation was between six to ten hours using 4 threads on an Intel Xeon Gold 6132, 2.6 GHz CPU with Abaqus 6.14 version.

The indenter was explicitly modelled as a rigid surface to account for the friction occurring between the tip and the top pillar surface. The friction coefficient f was set to 0.2 to prevent pillar buckling (as it was not observed experimentally). The influence of a friction coefficient variation on the load displacement curve was negligible for $f \geq 0.2$, as presented in Appendix C. The indenter experimental displacement profile was imposed to the rigid indenter reference point.

Internal heat generation induced by the pillar high strain rate plastic straining was not considered in the model as it was considered negligible on the pillars material properties, as detailed in Appendix C.

5.2 Results

5.2.1 Virtual material identifications

Inverse identification was first performed on virtual data generated using the full pillar geometry model with $K = 7$ and $n = 4$. The solution obtained is given in Table 5.5. The Levenberg-Marquardt minimization found the virtual material coefficients in 25 iterations with a relative error of 0.57% and 4.75% for K and n, respectively. The resulting identifiability indicator value was $I = 1.5$. This confirms that the overall identification procedure

Table 5.5 Solution of the identification procedure using the real pillar geometry compared with the chosen virtual material parameters. The discrepency between the input and identified K and n are respectively of 0.57% and 4.75%.

	K (MPa s$^{1/n}$)	n
Virtual material	7	4
Identification solution	6.96	3.81

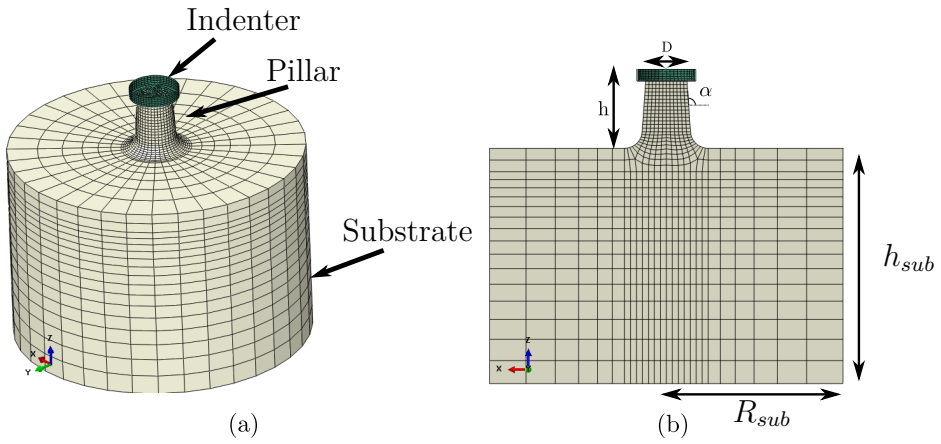

Figure 5.3 Micropillar compression FE model. (a) Finite element mesh used for the micropillar compression simulation. The indenter was modelled as rigid. The mesh was refined in the pillar and is progressively coarsened toward the substrate borders. (b) Geometry of the finite element model. h_{sub} and R_{sub} are the substrate height and radius. h, D and α are the pillar height, diameter and tapper angle.

could provide a satisfying solution in terms of uniqueness and stability.

Figure 5.4 (a) shows the L_2 norm of the sum of all load sensitivities to a 5% variation of the K and n coefficients around the cost function minimum, computed as:

$$\left\| \frac{\partial \overline{P_m}(t)}{\partial \overline{\theta_i}} \right\|_2 = \sqrt{\sum_{k=0}^{T} \frac{\partial \overline{P_m}(t)}{\partial \overline{\theta_i}}^2}. \tag{5.7}$$

Figure 5.4 (a) reveals that the variation of both coefficients have a similar effect on the global predicted load-displacement curves absolute amplitudes.

Figure 5.4 (b),(c),(d) shows the variation of the load sensitivity with the applied displacement for each computed nominal strain rates. The influence of the two coefficients on the curve is non collinear for each strain rate. Also, the sensitivity values for a given displacement reveals that the higher the nominal strain rate, the higher the sensitivity. Experimental load-displacement curves at the highest strain rates hence provides more valuable data for identification as it is more sensitive to the coefficients variation.

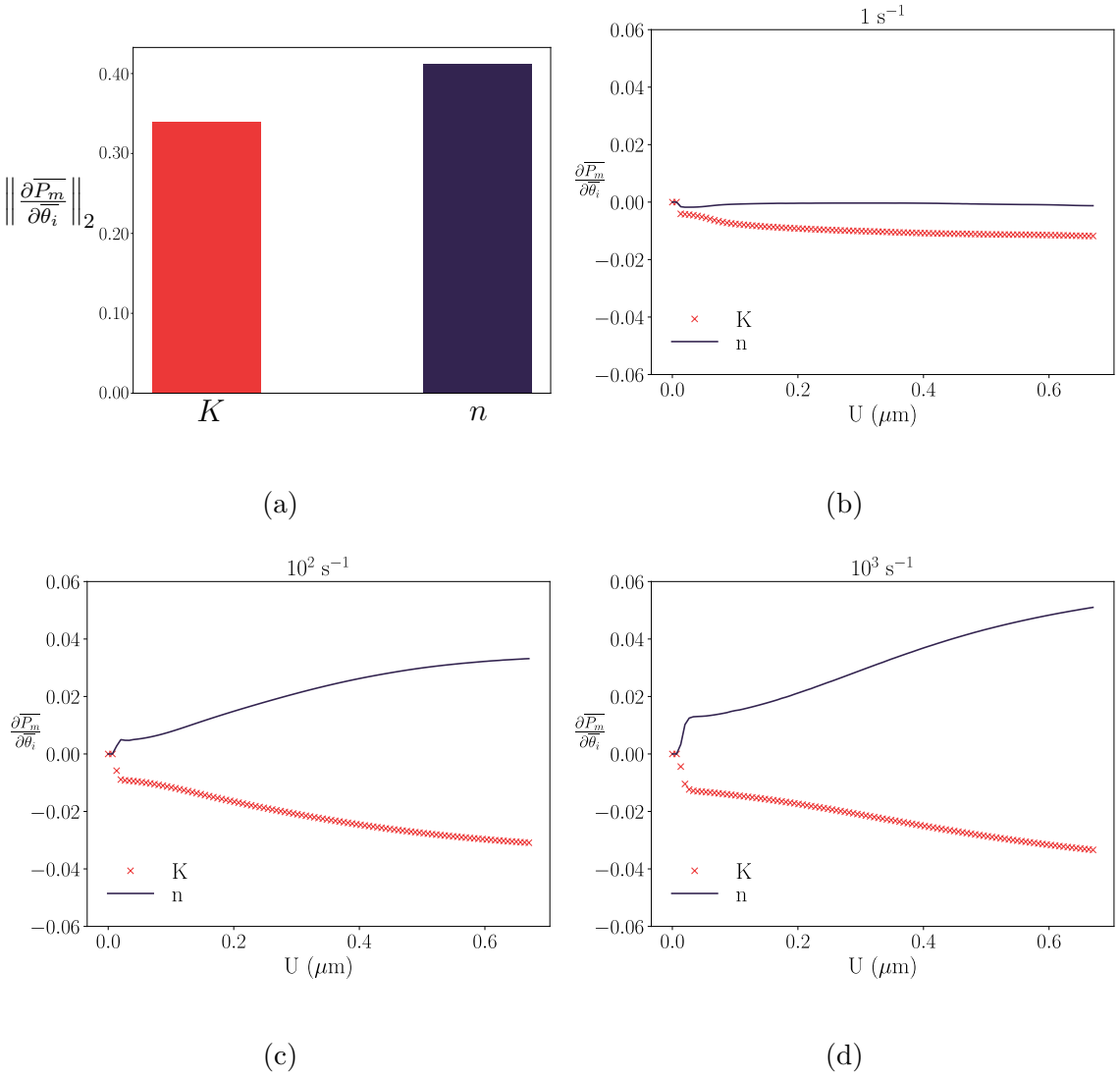

Figure 5.4 Load displacement curve sensitivity to a 5% varation of K and n close to the cost function minimum using the experimentally measured pillar geometry. (a)L_2 norm of the total sensitivity. Evolution of the predicted load sensitivity with the imposed displacement at (b)1 s^{-1}, (c)10^2 s^{-1} and (d)10^3 s^{-1} nominal strain rates. The load displacement curve is sensitive to a variation of both coefficients with a similar amplitude. Sensitivities for each strain rates reveals that the higher the nominal strain rate, the higher the load sensitivity amplitude.

5.2.2 Identification on microcompression tests

Experimental results

Size effects were investigated using the three pillar sizes as presented in Appendix C. The 3 μm-sized pillars systematically presented a pronounced size effect and higher result vari-

ability and were therefore not accounted for. The 6 μm-sized pillars were used for high strain rate compression (since the smaller pillars allows to reach the highest strain rates). The 8 μm pillars were used for low strain rate compression (as they presented less variability at low strain rates than the 6 μm pillars).

Figure 5.5 shows the stress-strain curves obtained by microcompression testing at different strain-rates for the three different orientations. In the [100] orientations, pillars #3 and #4 presented a slightly different behaviour from the others. Figure 5.7 shows the three 6 μm diameter pillars deformed shapes after microcompression at $\langle\dot{\varepsilon}\rangle \approx 10^2$ s^{-1}. Pillars #1 and #2 both presented a clearly marked double-slip pattern. Pillar #3 presented a barrel shape

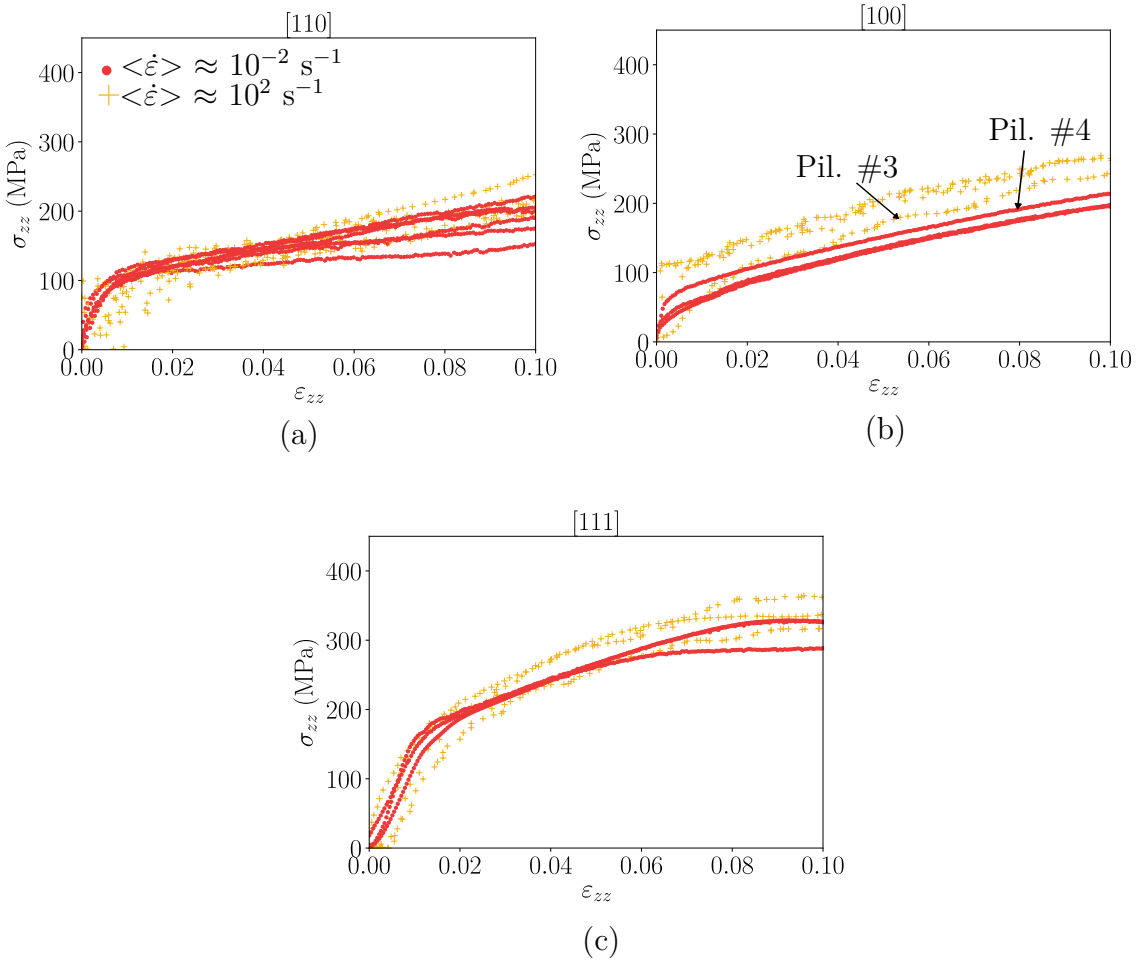

Figure 5.5 Microcompression stress-strain curves for (a) [110], (b) [100] and (c) [111]-oriented pillars 6 and 8 μm top diameters compressed at average strain-rates of 10^{-2} s^{-1} and 10^{2} s^{-1}. Stress-strain curves measured in the [110] orientation presented a larger discrepancy than the others. Pillar #3 and #4 were discarded for the [100] orientation.

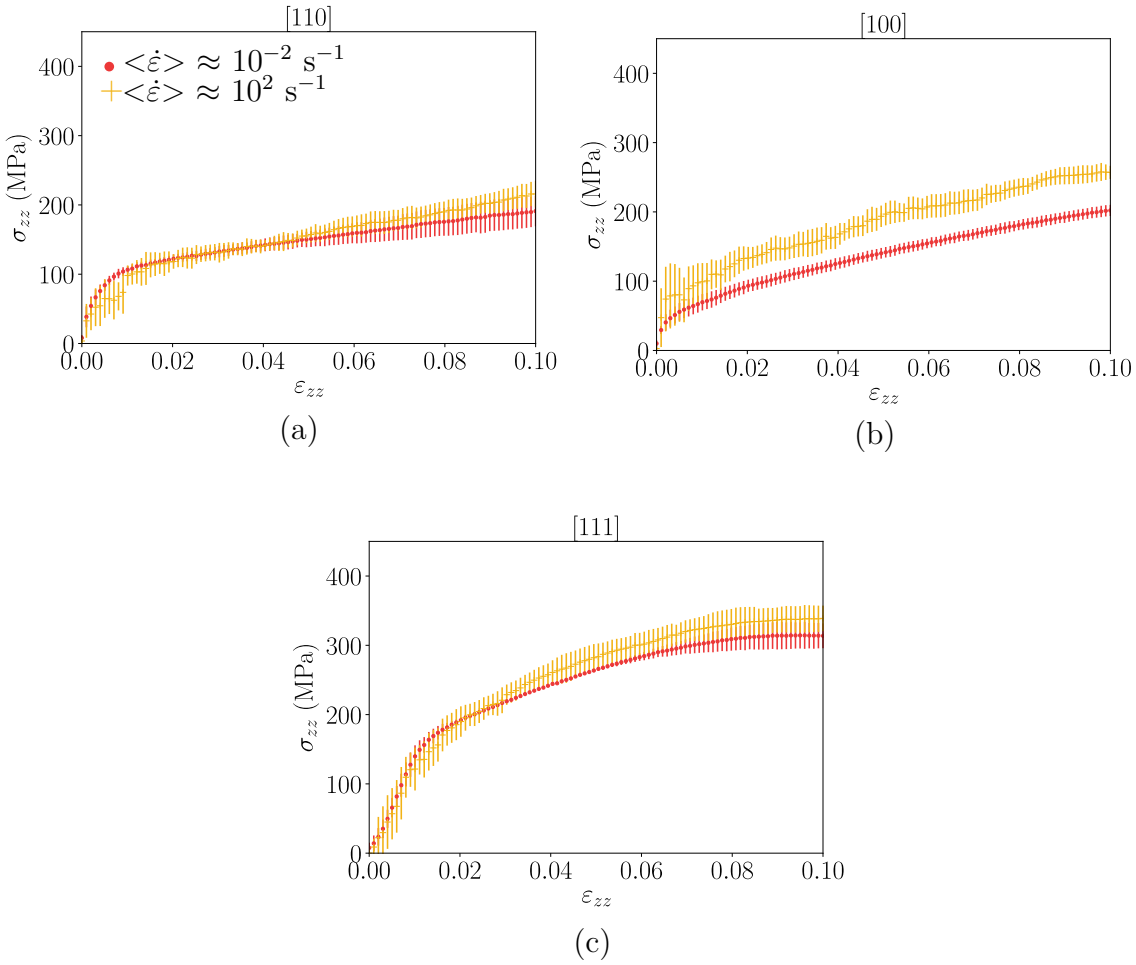

Figure 5.6 Microcompression stress-strain curves mean and standard deviation for (a) [110], (b) [100] and (c) [111]-oriented pillars compressed at average strain-rates of 10^{-2} s^{-1} and 10^{2} s^{-1}. Hardening strain-rate sensitivity was observed for the [100] orientation. The stress-strain curves discrepancy in the [110] and [111] orientations prevents quantitative assessment of the orientation sensitivity.

with no sign of slip bands. Pillar #3 will therefore not be considered for material parameters identification as it encountered different plasticity mechanisms than the other pillars, which could not be represented using the presently used crystal plasticity framework.

Pillar #4 stress-strain curve presented a constant stress shift when compared with other stress-strain curves at $\langle\dot{\varepsilon}\rangle \approx 10^{-2}$ s^{-1}. As this compression test was performed first, load drifts due to SEM void stabilization sill occurred. Such drift might explain the stress shift observed for pillar #4. This curve was therefore also not considered for material parameters identification.

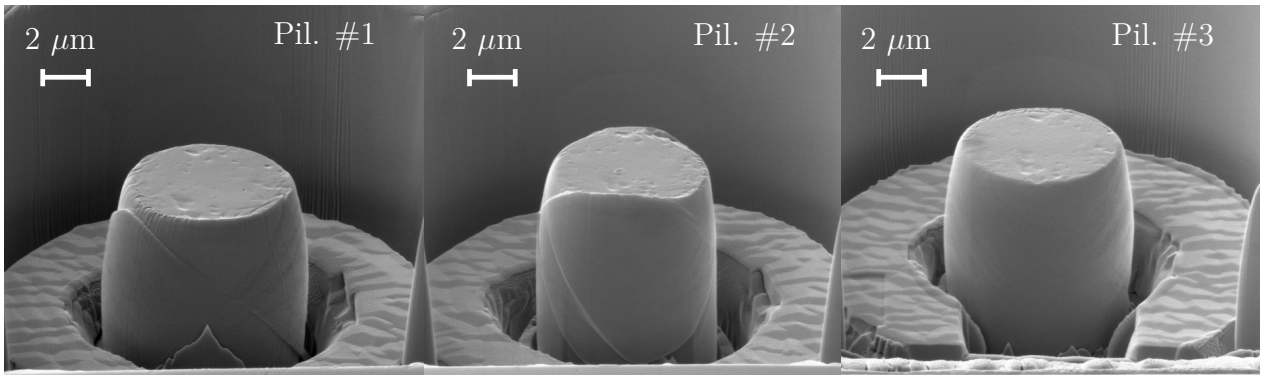

Figure 5.7 6 μm top diameter pillars deformed shapes after microcompression at $\langle\dot{\varepsilon}\rangle \approx 10^2\ \mathrm{s}^{-1}$. Pillars #1 and #2 both presented a clearly marked double-slip pattern. Pillar #3 presented a barrel shape with no sign of slip bands. The deformed pillar shapes explains the differences in the stress-strain curves observed in Figure 5.5.

Figure 5.6 shows the averaged microcompression curves obtained after putting aside pillars #3 and #4. A significant strain rate effect was observed for microcompression in the [100] orientation. Also, the stress-strain behaviour presented a good repeatability for a given approximated strain rate. A weaker effect was observed in the [110] and [111] orientations. The large results variability for a given strain rate prevented quantitative assessment of the stress-strain curve sensitivity in these orientations.

The overall good repeatability of the stress-strain curves suggest that the strain-rate dependency observed does not depend on the pillar size, owing to the statistical nature of size-effects. Several tests would be required to confirm such results, which is not in the scope of this paper. The pillar diameters used were however consistent with the literature [175,176]. Kiener et al. [82] estimated that no size effect would occur in copper micropillars with diameters larger than 5 μm.

In the following, the stress-strain curves obtained in the [100] orientations were used for strain-rate sensitivity material parameters identification as it presented the most repeatable results. The assessment of the solution uniqueness was performed to ensure that a single orientation was sufficient for identification.

Material parameters identification

The identification procedure using the real pillar geometry was applied to the experimental load-displacement curves obtained with the [100] crystal orientation at two different strain rates. The resulting stress-strain curves obtained with the identified parameters are presented

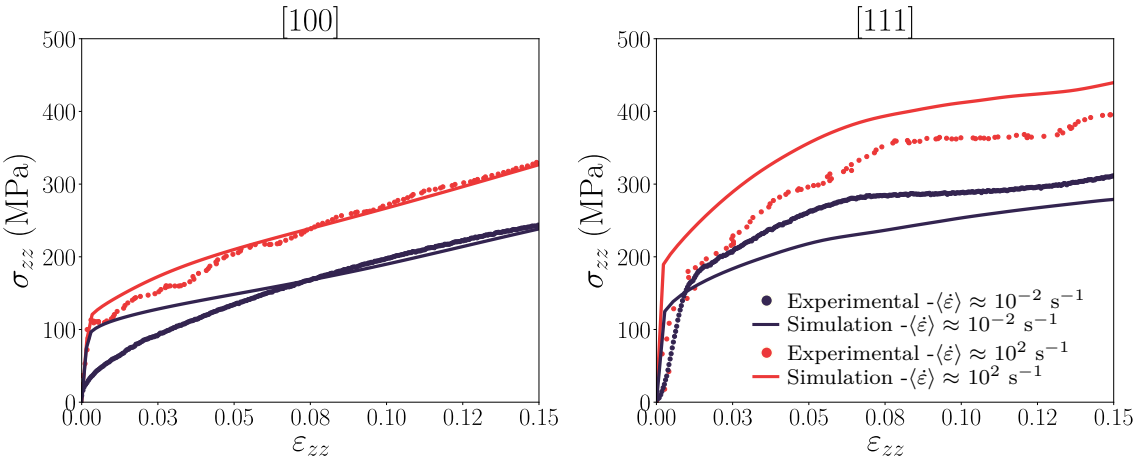

(a) (b)

Figure 5.8 Experimental and numerical stress-strain curves obtained after material parameters identification using the real pillar geometry, with the experimental data obtained in the [100] crystal orientation. (a) Comparison with the experimental curves used for identification. (b) Performance of the identified model in the [111] orientation. The model captured well the material's hardening strain-rate sensitivity in the [100] orientation. The yield stress dependency with the strain-rate was not well represented. Also, the strain-rate sensitivity orientation dependency was not well captured by the model either.

in Figure 5.8 (a).

The solution represented well the copper specimen hardening strain-rate sensitivity in the [100] orientations. The experimentally observed and numerical yield stress evolution with the strain rate were however different.

The stress-strain curve obtained using this solution in the [111] crystal orientation were compared with the experimental results in Figure 5.8 (b). The strain-rate sensitivity orientation-dependency was not well reproduced by the model.

The identifiability indicator computed after identification was $I = 1.31$. Figure 5.9 shows the cost function computed for a hundred different parameters and confirms the well-posedness of the inverse problem. This confirmed the quality of the solution found in terms of uniqueness and stability. Also, it reveals that using a single orientation for identification is sufficient to obtain a unique solution. Using both orientation for identification would therefore not have resulted in an orientation dependent sensitivity closer to the experimental one.

The material's behaviour at low strain rate was also very similar to the experiment. This gives confidence in the physical relevance of the hardening and interaction coefficients taken

from the literature.

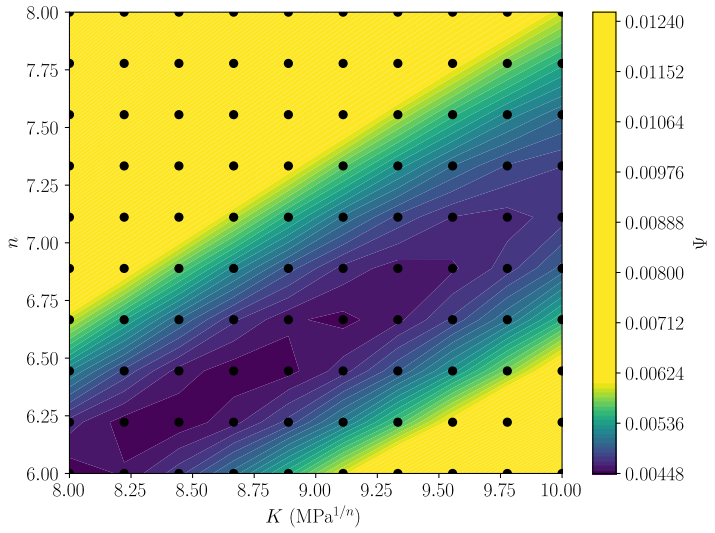

Figure 5.9 Minimization problem cost function in the viscinity of the solution. The black dots represents the parameters used to plot the function. The convex shape of the function close to the equilibrium confirms the well-conditioned nature of the problem.

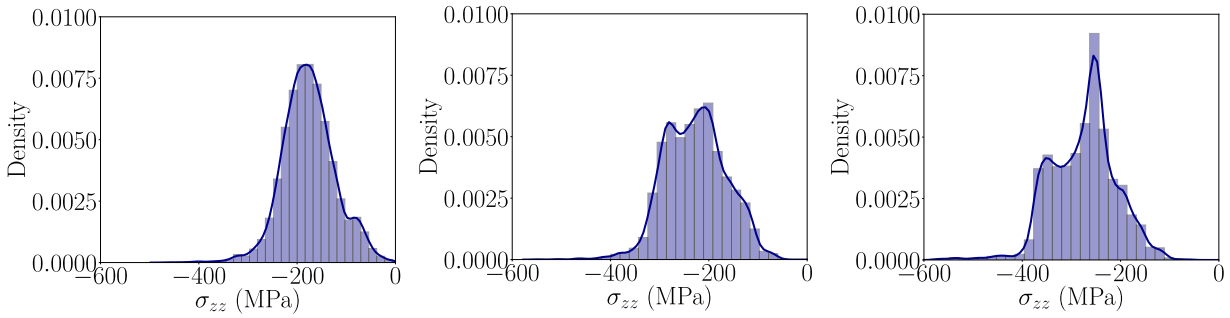

Figure 5.10 Stress distribution in the pillar volumes obtained from the virtual material simulations using the real pillar geometry submitted to an average imposed strain rate of (a) 1 s^{-1}, (b) 10^2 s^{-1} and (c) 10^3 s^{-1}. A uniform stress distribution was found at 1 s^{-1}. Higher strain rates induced higher stress heterogeneities inside the pillar.

5.3 Discussion

5.3.1 Strain rate induced stress heterogeneities

Figure 5.10 represents the σ_{zz} distribution in the pillars, for the virtual material simulations and for three different strain rates. The figure reveals that the higher the strain rate, the more heterogeneous the stress state is in the pillar. As the strain rate increases, the stress distribution changes from a uni-modal to a bi-modal shape. For high strain rates, the pillar can therefore no longer be considered as homogeneously loaded.

Figure 5.11 shows the $\sigma_{zz} - \langle\sigma_{zz}\rangle$ variations at the pillar center in the x-z plane. The mean stress values has been subtracted from the stress to compare the changes in stress distribution with the strain rate, independently of the stress amplitude variations. At 1 s^{-1}, the highest stresses are concentrated in the shear bands. The stress state in the zone below and above those bands is similar. This zone therefore represents the unique peak observed in the stress distribution. At 10^2 s^{-1} and 10^3 s^{-1}, the stress amplitude raises above the shear bands but not bellow. This results in a bimodal stress-distribution.

To better understand these heterogeneities, the strain-rate variations at the pillar center in the x-z plane, normalized by the pillar average strain rate, were represented in Figure 5.12,

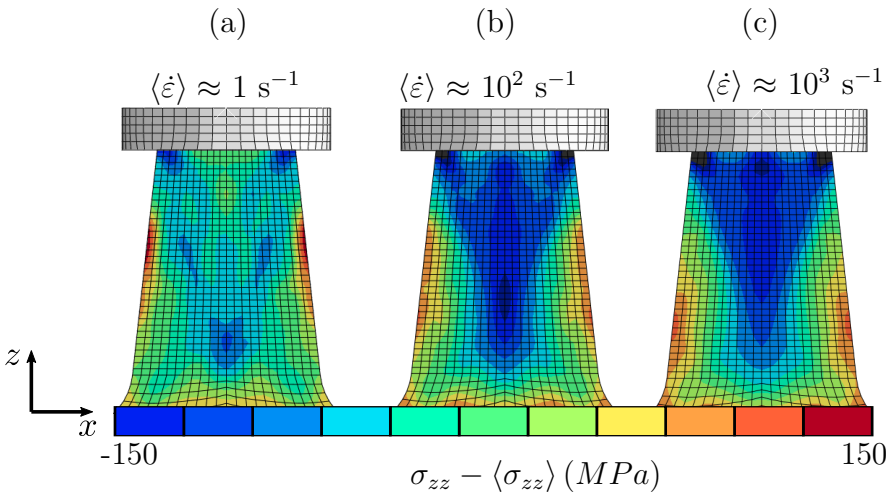

Figure 5.11 σ_{zz} average, on the x-z plane, obtained from the virtual material simulations for an average imposed strain rate of (a) 1 s^{-1}, (b) 10^2 s^{-1} and (c) 10^3 s^{-1}. At 1 s^{-1}, the stress below and above the shear bands present similar values. At 10^2 s^{-1} and 10^3 s^{-1}, the stress above the pillar rises significantly, resulting in a bimodal stress distribution in the pillar volume.

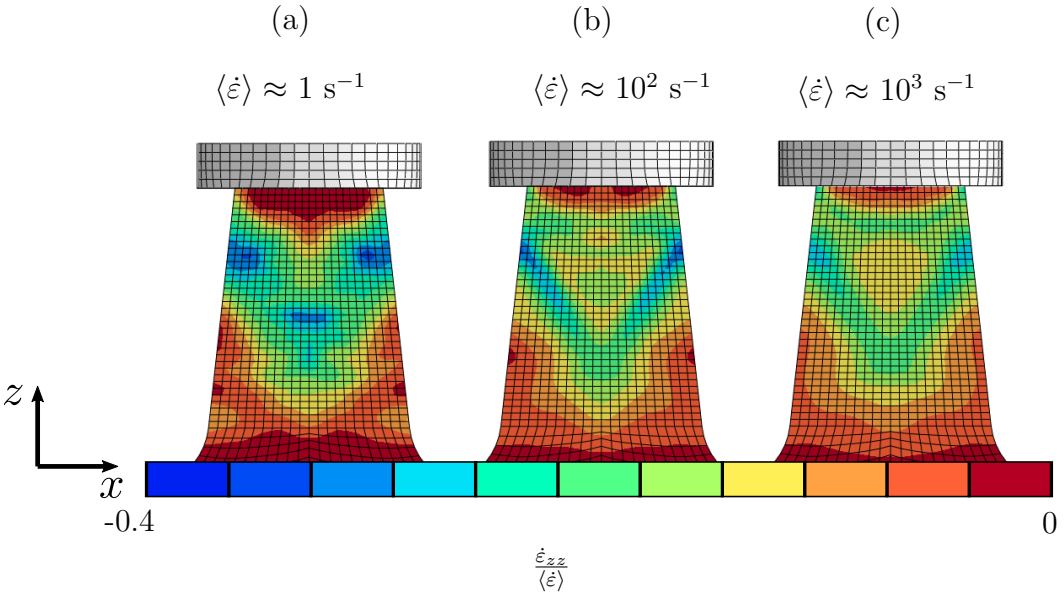

Figure 5.12 Normalized strain-rate distributions in the pillar in the x-z plane obtained from the virtual material simulations for an average imposed strain rate of (a) 1 s^{-1}, (b) 10^2 s^{-1} and (c) 10^3 s^{-1}. For the highest velocity, the highest strain rates are concentrated in the shear bands.

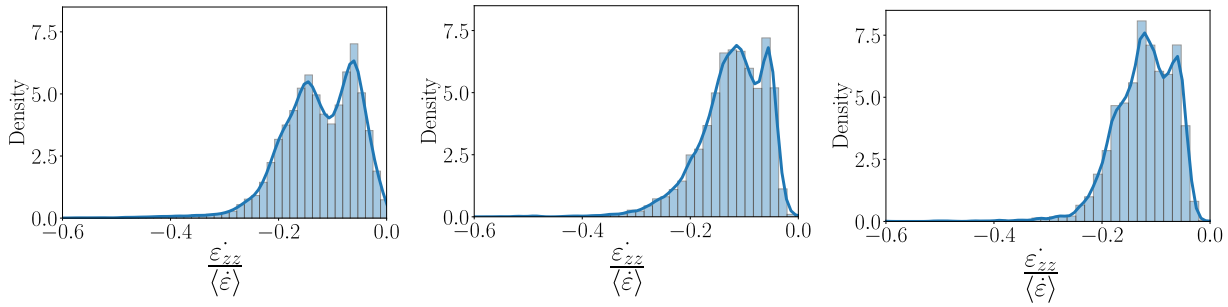

Figure 5.13 Strain rate $\dot{\varepsilon}_{zz}$ distribution inside the pillar obtained from the virtual material simulations using the real pillar geometry at an average imposed strain rate of (a) 1 s^{-1}, (b) 10^2 s^{-1} and (c) 10^3 s^{-1}. A bimodal strain rate distribution is observed both at low and high strain rates in the pillar.

for the three velocities. The figure shows a highly heterogeneous strain rate distribution in the pillar. The highest strain rates were found in the slip bands. Figure 5.13 shows the strain

rate distribution in the whole pillar volume. The figure confirms that a bimodal strain rate distribution is also found in the whole pillar volume for all the modeled strain-rate.

This strain rate localization induces different strain mechanisms in the pillar since the global strain rate increases. Figure 5.14 shows the equivalent von Mises plastic strain field at the pillar center. For low strain rates, plastic strains are localized in the slip bands, with higher values at the pillar lateral surfaces. As the strain rate increases, the material in the shear bands requires higher stresses to strain further since it deforms more rapidly. This results in less plastic strains in the bands, when compared to those predicted for the low strain rate simulation. As yielding occurs in the bands, the material requires higher stresses to deform and the strain is therefore redistributed in the zone above the shear bands. This results in the plastic yielding of this zone, the bottom zone remaining elastic. This explains the bimodal stress state observed in Figure 5.10.

There is therefore a structural effect, which enhances the apparent strain rate sensitivity influence on the load-displacement curve. As detailed in Appendix C, modeling the pillar as single element or using the experimental stress-strain curve for strain-rate sensitivity direct estimation cannot account for such structural effects. Such approximations therefore results in a non unique solution for the strain-rate coefficients.

This structural effect could explain that using only the [100] orientation was sufficient to

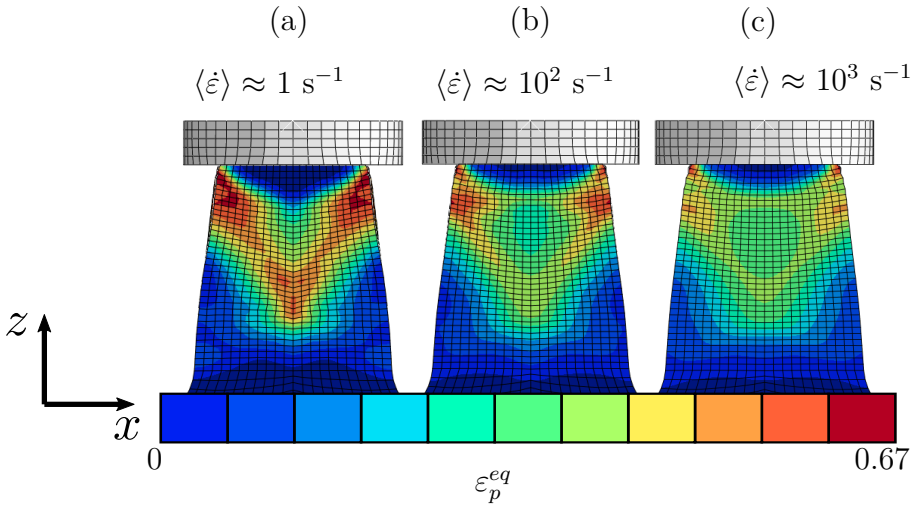

Figure 5.14 Equivalent von Mises plastic strain ε_p^{eq} distribution in the pillar on the x-z plane obtained from the virtual material simulations at an average imposed strain rate of (a) 1 s^{-1}, (b) 10^2 s^{-1} and (c) 10^3 s^{-1}. At low strain rates, plastic strain is concentrated in the shear bands. As the strain rate increases, the top of the pillar plastifies more homogeneously, as higher stresses are required for further plastic straining in the shear bands.

obtain a good identifiability indicator value. The stress contrast induced in the pillar as the strain rate increases could explain the highest load sensitivity revealed in Figure 5.4. However, the amplitude of this structural effect should be related to the material's sensitivity. For low sensitivities, strain rate concentration in the slip bands would induce lower hardening contrasts as with the virtual parameter values used in this study.

5.3.2 Orientation-dependent strain-rate sensitivity

Copper strain rate sensitivity orientation dependency has already been observed in the literature [177, 178]. Rawat et al. [178] performed SHPB (4.5 10^3 s^{-1}) and quasi-static (3.3 10^{-3} s^{-1}) tests on copper single crystals in the [100] and [110] orientations. Despite the different strain rate ranges, similar orientation dependent sensitivities were observed for the stress-strain curves. The [110] orientation presented almost no strain rate sensitivity, when compared to that observed for the [100] orientation. According to Horstemeyer et al. [177], this observation cannot simply be explained by the geometry of slip but more by the nature of dislocation interactions in a given slip system.

Wang et al. [179] performed dislocation dynamic simulation on fcc single crystals at different strain rates on three different orientations. The three different orientations presented differences in the cross-slip activity leading to higher dislocation dipole annihilation for the [111] and [211] oriented crystals as the strain rate increases. Such differences in plasticity mechanisms could explain the anisotropic strain rate dependency observed in Figure 5.6.

The mismatch in sensitivity orientation dependency between the model and experimental observations is therefore a consequence of the crystal plasticity model chosen. This was also observed by Khan et al. [63]. The authors used three different crystal plasticity frameworks to model single crystal compression at various strain rates (ranging from 10^{-4} s^{-1} to 10^3 s^{-1}). The first framework used a similar formulation as presented in Section 2.2.2 and could not account for orientation dependent strain rate sensitivity. The second model consisted in adding a strain rate dependent hardening behaviour, accounting for yield stress strain rate sensitivity. The predicted and experimentally measured stress strain curves were in good agreement but only for the orientation used for identification. The third approach used a dislocation based crystal plasticity model with a Kocks-Mecking evolution law. This approach captured well the single crystal strain rate sensitivity on the various orientation tested.

In such models, dislocations interactions and strain rate sensitivity are implicitly related by the dislocation density evolution law. This could explain its good performances on several different orientations. This confirms that the Meric-Cailletaud framework is not relevant to model the crystal behaviour for a large strain rate range. However, dislocation based frame-

work usually involves several parameters which could hardly be identified using experimental observations. An intermediate scale model would therefore be required for potential high strain rate industrial applications.

Also, such models could not account for the strain-rate dependent recovery mechanisms evidenced by Wang et al. [179] and could therefore fail to represent the highly anisotropic strain rate dependency observed in Figure 5.6. Kocks et al. [64] and Galindo-Nava et al. [180] developed dislocation density based models accounting for a strain-rate dependent recovery. Finite element integration of such framework however requires further extensive work as it involve several numerical challenges.

This orientation dependent effect could however be used wisely for parameters identification. Indeed, micropillar compression enables to select the tested orientation and therefore the activated gliding systems - In contrast with nanoindentation testing for which all gliding systems are usually activated. It is therefore possible to select the most strain rate sensitive orientations to fully capture the material's viscoplastic behaviour.

Yield stress strain rate dependency is usually very subtle at intermediate strain rates for most face-centered cubic (fcc) materials [71]. The use of the Meric-Cailletaud framework for low strain-rates for those materials relies on the fact that strain-rate sensitivity only influences hardening. In this work, yield stress sensitivity was already visible at $\langle \dot{\varepsilon} \rangle \approx 10^2$ s^{-1}. Future works will focus on the validation of the proposed identification procedure using a more representative crystal plasticity framework.

In this work, copper was solely used to validate the proposed identification methodology. The results reveal that this methodology could provide a unique solution to crystal plasticity viscoplastic coefficients using a single crystal orientation, which, to the authors knowledge, has never been demonstrated before. It also provided guidelines for the choice of the most relevant crystal plasticity model to use to accurately model a single crystal strain rate dependency, over a large strain-rate range, using a limited amount of material. The proposed methodology will therefore be applied on materials for which single crystals are more difficult to produce in future studies.

5.3.3 Crystal plasticity framework accounting for strain rate dependency anisotropy

According to Wang et al. [68], strain-rate sensitivity anisotropy could arise at high strain rates for single crystal copper due to differential recovery depending on the activated slip systems. In dislocation-based crystal plasticity models, recovery by dislocation annihilation is classically accounted for using the Kocks-Mecking relationship (2.15).

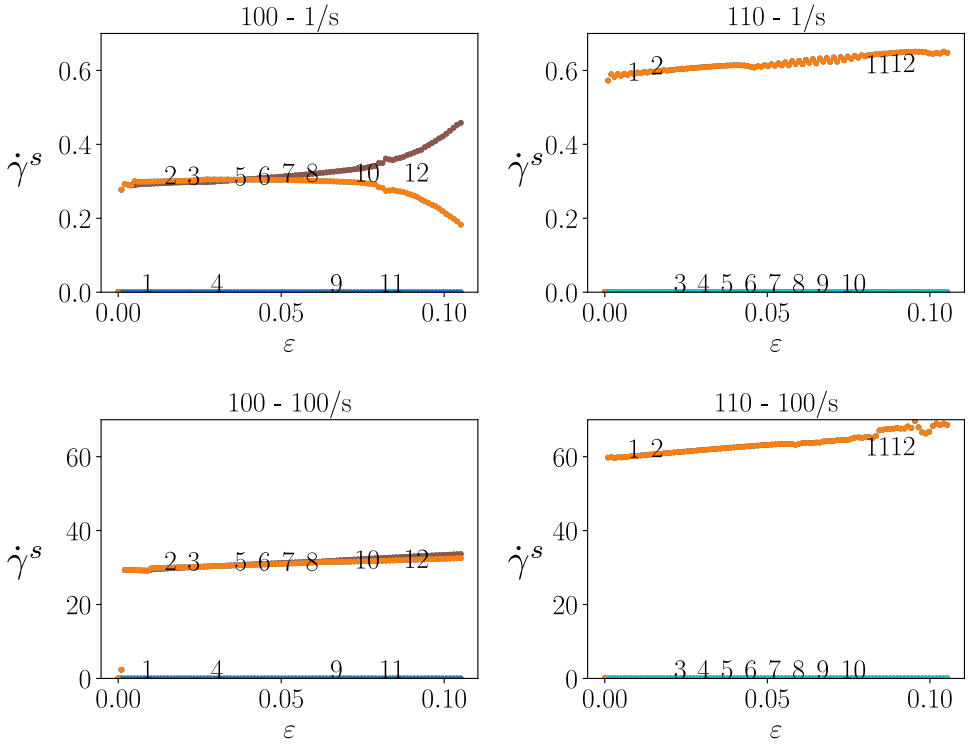

Figure 5.15 Evolution of $\dot{\gamma^s}$ for each slip system during simple traction of a single C3D8R element in the [100] and [110] orientations at 1 s^{-1} and 100 s^{-1}. The slip system number is indicated next to each curve following the convention given in table 2.3. The slip rate on each slip system is higher for the [110] orientation as compared to the [100] orientation, as predicted by Schmid's law.

By integrating Equation 2.15 with respect to γ_s under simple glide conditions, one can show that this equation is equivalent to the Voce hardening law given by Equation 2.10 by defining:

$$b = \gamma_c \qquad Q = \mu b \left(\frac{1}{2K\gamma_c} - \sqrt{\rho_0} \right) \qquad R_0 = \mu b \sqrt{\rho_0}. \tag{5.8}$$

Accounting for a strain rate dependent recovery in a Meric-Cailletaud framework can therefore simply be performed by seting the recovery rate as a function f of the strain rate, as

$$\gamma_c = f(\dot{\gamma^s}). \tag{5.9}$$

Figure 5.15 shows the evolution of $\dot{\gamma^s}$ for the twelve slip systems obtained for simple traction of a single C3D8R element in the [100] and [110] orientations at 1 s^{-1} and 100 s^{-1}, respectively. The figure reveals that higher slip rates per system are reached for the [110] orientation,

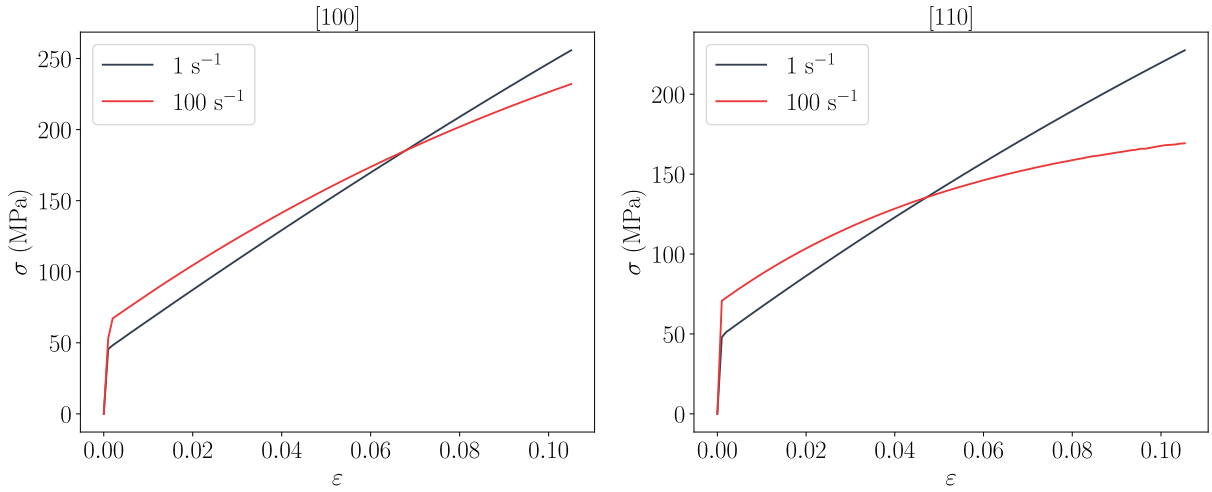

Figure 5.16 Stress strain curves resulting from the compression of single C3D8R elements in the [100] and [110] orientations at 1 s^{-1} and 100 s^{-1} using a sigmoidal recovery rate function. A strain-rate dependency anisotropy is observed but does not reproduced the one observed in Figure 5.8.

when compared to those predicted in the [100] orientation. This observation results from a higher Schmidt factor per system for a stress aligned with the [110] crystal orientation. If the strain rate dependency anisotropy observed in Figure 5.6 results from a strain-rate dependent recovery, f should therefore be an increasing function of $\dot{\gamma^s}$ as more pronounced recovery effects were observed in the [110] orientation. Also, according to Kocks et al. [64], the larger the strain rate, the less the recovery when performing tests at low strain rate. The function f should therefore be chosen to have less influence at low strain rates.

The recovery rate function was therefore chosen as a sigmoid as:

$$y_c(\dot{\gamma^s}) = A + \frac{B}{1 + e^{-C\dot{\gamma}}}, \tag{5.10}$$

where A, B and C are three material's parameters representing respectively the asymptotic values and the increasing rate of the sigmoid function. For this preliminary study, values of A and B were chosen so that b and Q would take values close to that found in the literature ($A = 5$, $B = 20$ and $K = 0.006$) [2]. Also, the value of C was chosen so that the maximum increasing rate of the sigmoid function would be for values of $\dot{\gamma^s}$ close to 100 s^{-1}.

To investigate the possibility to obtain an anisotropic strain rate dependency using this approach, a plug-in was implemented in the Zset software. Note that such approach is

purely phenomenological and is here only used for investigations purposes. Indeed, the thermodynamical admissibility of the above form has not been investigated. Also, such approach does not accurately account for the material strain history as unloading would lead to a decrease of the hardening R_q. It should therefore only be used for monotonic loading.

Figure 5.16 shows the resulting stress strain curve when compressing a single C3D8R element in the [100] and [110] orientations at 1 s^{-1} and 100 s^{-1}. The figure reveals that the proposed framework can model a strain-rate dependency anisotropic behaviour. However, it does not well reproduce the experimentally observed anisotropy as it mainly acted on the strain hardening rate at large strain while Figure 5.6 presents anisotropic effects at the onset of plasticity.

5.4 Conclusion

The objective of this work was to investigate the possibility to identify crystal plasticity strain-rate dependent parameters by FEMU using high strain rate micropillar compression experiments. The main contributions are as follows:

- Crystal plasticity strain rate sensitivity coefficients were identified for copper single crystals by FEMU using microcompression tests at strain rates up to 10^2 s^{-1}.
- The quality of the identification in terms of uniqueness and stability was assessed using an identifiability indicator.
- Identification using only compression in the [100] crystal orientation was sufficient to obtain a unique and stable solution for the strain-rate sensitivity coefficients.
- The satisfying quality of the solution was attributed to a strain rate sensitivity enhancing structural effects resulting from shear band strain localization.
- Experimental compressions revealed a strong influence of crystal orientation on the material's apparent strain-rate sensitivity.

Our experimental procedure only allowed to reach strain rates up to 10^2 s^{-1}. This is partly related to copper highly ductile behaviour, implying low load values in comparison to stiffer materials (such as silica glass [181]). To reach higher strain rates, identification using alternative experimental set-ups such as single shot impacts will be investigated in the next chapters.

Also, the model could not account for the material's yield stress strain rate dependency, nor for the high orientation influence on strain rate sensitivity observed experimentally. An

alternative model acounting for strain-rate dependent recovery was developed. The model succeeded in reproducing an anisotropic strain rate dependency. However, it was not sufficient to match with the experimental observations. The observed anisotropy should therefore not result from differencial recovery and should therefore be further investigated, using for instance TEM observations of the deformed micropillars.

Finally, the relevance of the identified coefficient will be assessed on a different loading case than that used for identification. This will be performed using single impact shot and micropercussion experiments in Chapter 6.

Data availability

All the simulation input files, the optimisation script and raw and treated experimental microcompression stress-strain curves, pillar dimensions and deformed images can be found at `https://zenodo.org/record/3801034` and can be reused.

CHAPTER 6

Constitutive behavior validation under process conditions

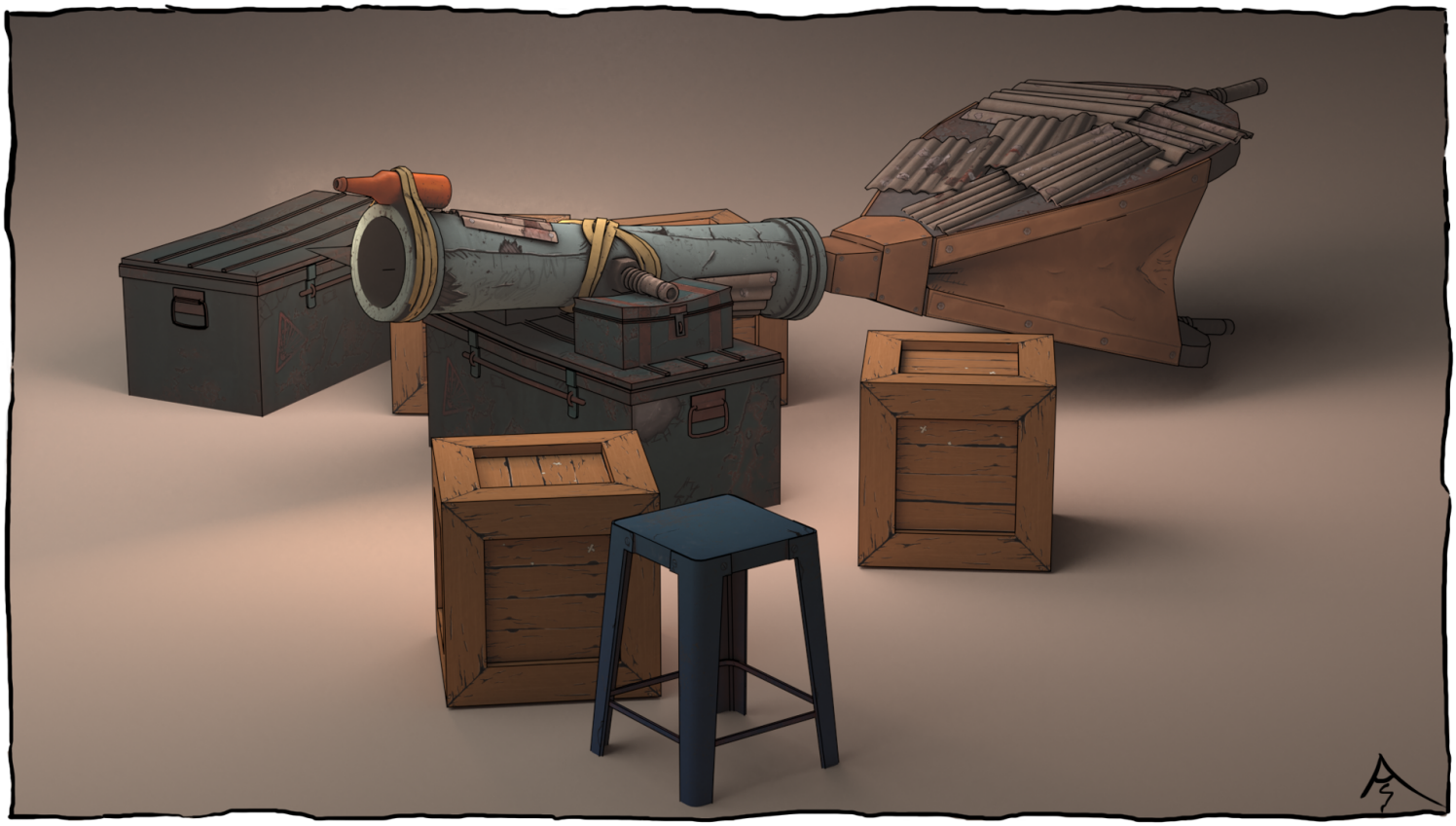

6.1 Introduction

The objective of this chapter is to develop a methodology to validate the ability of the identified Meric-Cailletaud constitutive framework to predict impact induced residual stresses and hardening. The philosophy of this approach is to ensure that the constitutive behaviour chosen, as well as the conditions under which it was identified were relevant to model the shot peening process. Validation therefore has to be performed using mechanical tests as close as possible to the process conditions. **This requires an experimental procedure in which input parameters can be measured as accurately as possible to be used as input in a finite element model.**

This work aimed at developing a shot-peening test rig that could propel controlled shot over a wide velocity range, with different angles and using industrial shot of different diameters.

Part of the challenge in developing such a setup was to provide an accurate methodology to measure the 3D shot displacement. An in-house code based on a pinhole camera model was therefore developed [182] to account for perspective, lens distortion and uncertainties in the setup positioning. The accuracy of the setup and methodology was thoroughly assessed and validated through two different applications presented in this manuscript:

- Determination of coefficients of restitution (CoR) for different shooting angles and wide velocity ranges.
- Impact on a copper single crystal and comparison with numerical simulations.

This work was performed in collaboration with Mëkanic and was submitted for publication in Strains [24].

Validation of the constitutive model also requires to develop a methodology for accurate estimation of residual stresses and hardening using HR-EBSD and GND estimations. This aspect was however not achieved in this project as the surface preparation was not sufficient for residual stress estimations due the high ductility of the copper samples. All the tested approaches for sample preparation are nonetheless provided in Appendix E to provide a starting point for future studies.

This chapter is organized as follows: The test setup and the methodology used for the shot trajectory estimation are presented in section 6.2. The estimated accuracy and performances of the setup are detailed in Section 6.3. Two potential applications of the test rig for (i) CoR determination with different shot diameters, velocities and shooting angles and (ii) crystal plasticity constitutive behavior validation using single impact tests on single crystal copper are then presented in Section 6.4. Finally, section 6.5 concludes the works.

6.2 Experiments and methods

6.2.1 Experimental setup

Figure 6.1 summarizes the functioning mechanism of the test rig. The shot is propelled by releasing pressurized nitrogen gas with a controlled pressure onto the media. The media is then guided by the cannon walls to achieve a better aiming precision. Figure 6.2 (a) shows the global setup. The cannon can project single shot on a fixed target sample.

The shot trajectory is captured by two high frequency Phantom v310 cameras, positioned with a 90° relative angle to capture the shot spatial coordinates. The shot is lit using a 150 W continuous Olympus LG-PS2-5 LED light. With the current lighting setup, the cameras can record the shot trajectory at shooting frequencies up to 31 000 frames per second. The camera recording is triggered automatically when the gas release valve opens. This trigger signal activates the first camera which then triggers the second one. A small delay should then be expected between the two cameras recording, as further explained in section 6.2.2. A red laser pointer can be positioned onto the cannon barrel to aim at a given position. The sample can be accurately positioned using the micrometric table handles shown in Figure 6.2 (c). A stereomicroscope was also positioned next to the cannon to observe the impacted surface before and after the impact.

Figure 6.2 (b) shows a close up of the cannon. The barrel is unscrewed to introduce the shot media and the shot is positioned in a hole which has the same diameter as that of the barrel. Three different barrels have been machined to send shot of 0.5 mm, 1.19 mm and 2.5 mm in diameter. The gas pressure can be varied between 0 to 2 MPa (300 psi) and is the main

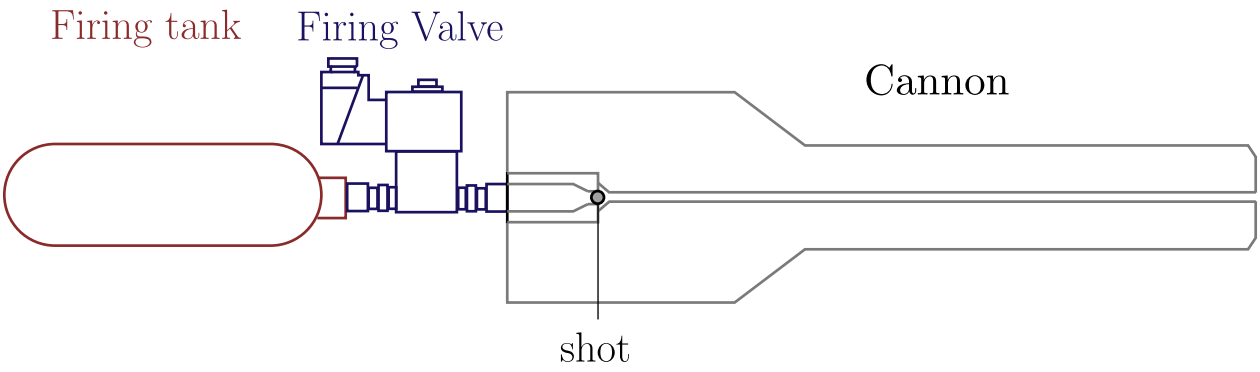

Figure 6.1 Functional schematic of the shot peening cannon setup. The shot is propelled by releasing the gas tank content with a controlled pressure onto the media. The media is then guided by the cannon walls to achieve a better precision.

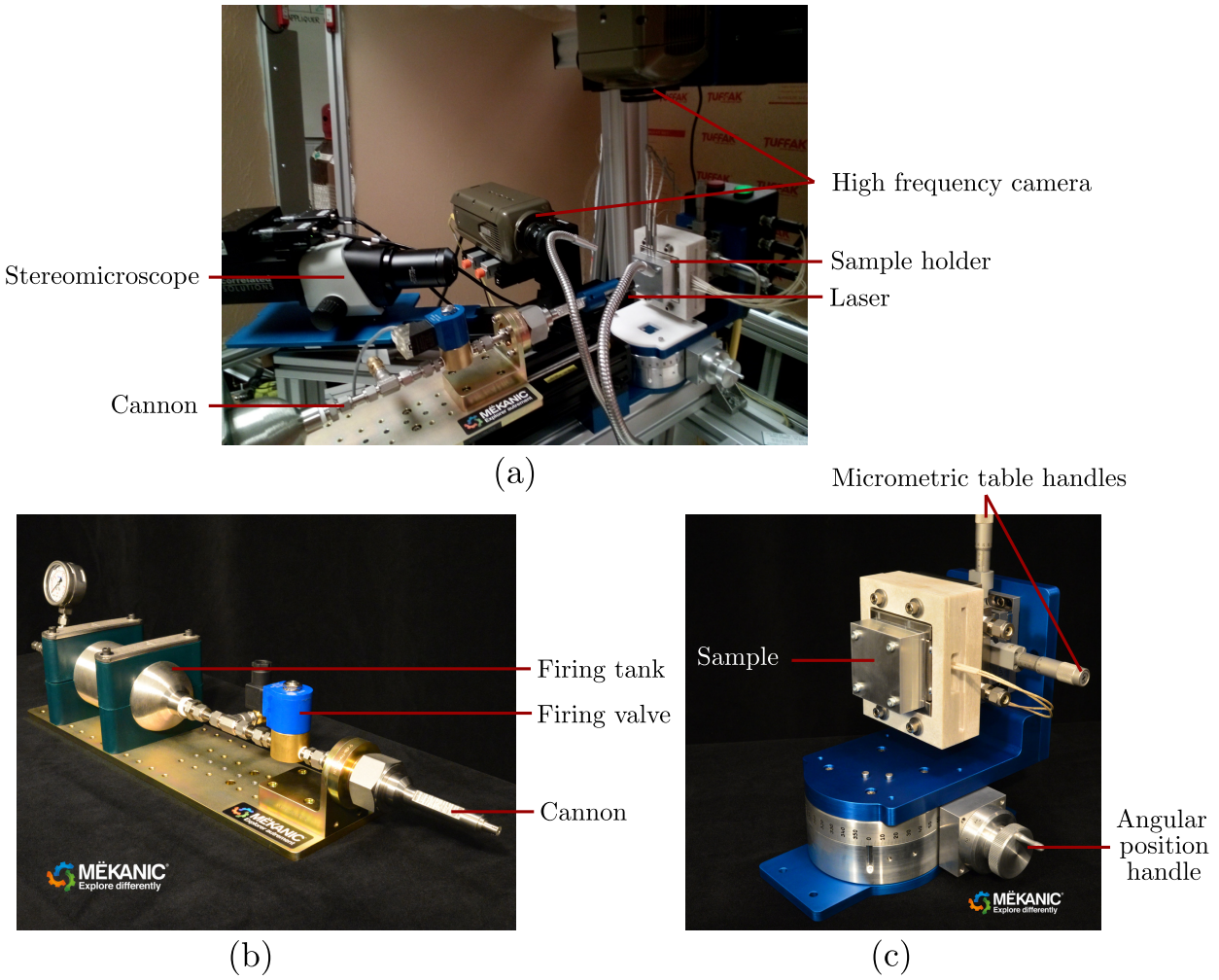

Figure 6.2 Shot-peening test rig pictures. (a) Shot-peening cannon setup (b) cannon close-up (c) Sample holder close-up. The shot is projected by pressured nitrogen onto a sample positioned on a micrometric table. The trajectory is recorded by two high frequency cameras to be reconstructed in 3D.

parameter that drives the projected shot velocity.

Figure 6.2 (c) shows a close-up of the sample holder. The samples have to be 6.35 cm x 6.35 cm x 2 cm squared plates with four riveted holes to be fixed on the holder. The sample can be heated at temperatures up to 400°C. Finally, the holder is positioned on a rotative table that allows impacting angles ranging from -60° to 60°.

6.2.2 3D trajectory reconstruction

Camera parameter calibration

The shot's three dimensional trajectory can be recovered using the pictures provided by the two cameras to:

- Obtain the relation between the input gas pressure and the resulting shot velocity for different shot diameters.
- Accurately estimate the shot trajectory to use it as input in FEA.
- Estimate the setup ability to perform several impacts at the same position.

A pinhole camera model was used to obtain a relationship between the three dimensional coordinates of an object in the sample's frame and its coordinates on the picture [183]. As represented in Figure 6.3, the projection on the screen of a point P with coordinates (X, Y, Z) in the world referential is the intersection of the screen with the line connecting the point to the camera's optical center.

Knowing the coordinates of the optical center projection on the screen (c_x, c_y) and the camera focal length f, the relationship between the point's world coordinates and its pixel coordinates

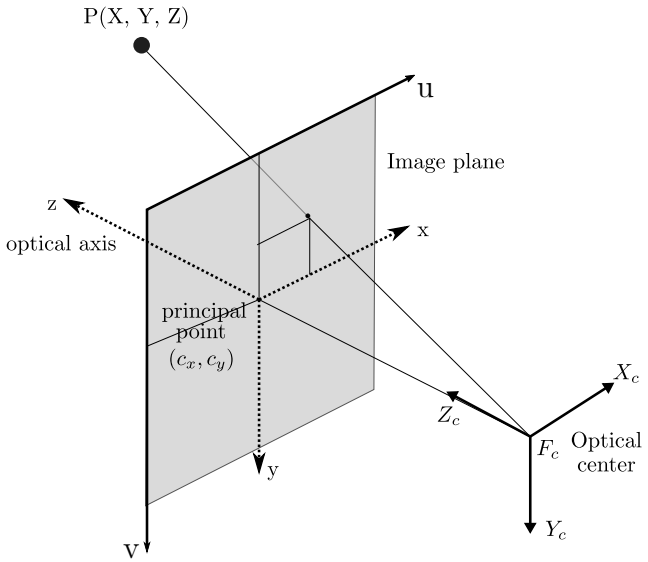

Figure 6.3 Schematization of the pinhole camera model [183]. The projection of a point P in 3D space on the image plane is obtained by tracing a line between P and the camera optical center. Note that the optical center is not aligned with the image center.

on the screen (u, v) is given as:

$$\begin{bmatrix} su \\ sv \\ s \end{bmatrix} = \begin{bmatrix} f_x & 0 & c_x \\ 0 & f_y & c_y \\ 0 & 0 & 1 \end{bmatrix} \begin{bmatrix} r_{11} & r_{12} & r_{13} & t_1 \\ r_{21} & r_{22} & r_{33} & t_1 \\ r_{31} & r_{32} & r_{33} & t_1 \end{bmatrix} \begin{bmatrix} X \\ Y \\ Z \\ 1, \end{bmatrix} \tag{6.1}$$

where r_{ij} and t_{ij} are the components of the rotation matrix and translation vector between the world referential in which (X, Y, Z) are expressed and the camera reference frame (X_c, Y_c, Z_c). In general, two different focal length f_x and f_y are introduced as pixels are generally not perfectly squared. In the above, s is a scaling factor used to account for the third coordinate of point P when mapping on the screen. Coordinates (su, sv, s) are usually referred to as homogeneous coordinates and should be divided by s to retrieve the effective pixel coordinate of the projection of P on the screen. Parameters (f_x, f_y, c_x, c_y) are generally called the camera intrinsic parameters.

Intrinsic parameters are relative to the camera and have to be calibrated for each camera. Such calibration is usually performed using an object with an accurately defined pattern such as a chessboard. First, several pictures of the chessboard are successively taken in different chessboard positions. Then, a first estimate of the intrinsic parameters, as well as the rotation and translation matrices between the chessboard and the camera frame is chosen. This first estimate is used to project the coordinates of each corner of the chessboard on the screen, knowing the coordinates of each intersection in the chessboard frame. The corners coordinates on the screen are then detected using a classical feature extraction algorithm and are compared with the coordinates obtained by projection. If the projected and effective corner positions are the identical, the parameter estimation is considered correct, otherwise, the estimation is changed so as to minimize the distance between the two sets of coordinates. This calibration was entirely performed using the OpenCV library [184].

Camera position calibration

Once the camera parameters are known, the relationship between the camera and the observed sample coordinate system has to be found. This relation can be obtained using the same principle, by positioning a chessboard perpendicularly to the sample, as shown in Figure 6.4. The optimization procedure detailed in Section 6.2.2 is then used to find the rotation matrix and translation vector between the chessboard and the camera coordinate system, assuming that the intrinsic and distortion parameters were already found. Note that the

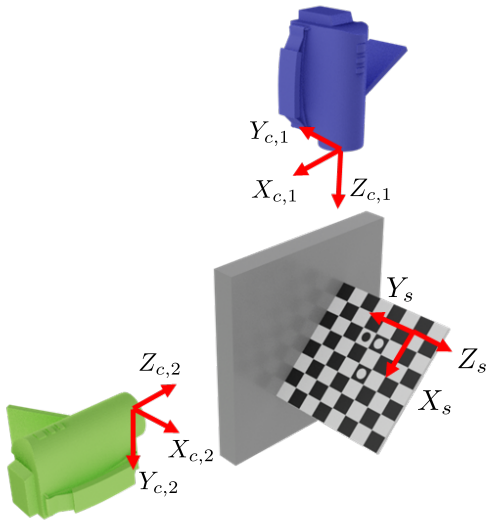

Figure 6.4 Representation of the camera position calibration procedure. A picture of a chessboard positioned perpendicularly to the sample is taken simultaneously by the two cameras to obtain the transformation matrices between each camera coordinate system $(c, 1)$ and $(c, 2)$ and the sample coordinate system s.

chessboard has to be visible by the two cameras for the same picture so that the chosen sample's coordinate system is the same for the two cameras.

The chessboard used was also marked with three circles so that the calibration procedure automatically recognizes the chessboard orientation. This was necessary to ensure that the same coordinate system was taken for the two cameras. If the chessboard is positioned at a perfect 90° angle from the sample, then X_s and Z_s provides the shot coordinates on the sample plane. Deviation from this angle could therefore result in errors in the shot position. Using the Blender 3D software, it was however estimated that a 0.2° deviation still provides an accuracy below 200 μm on the shot position, as detailed in Appendix F.

Shot detection

The next step is to find the position of the shot on each picture taken by the cameras, in pixel units. In this study, it was simply considered that the shot was the only moving object in the image. The shot is therefore detected by applying a threshold on the difference between the analyzed picture and a picture taken before the shot enters the frame. The shot position is then taken as the barycenter of the pixels for which the difference reaches a certain threshold. Figure 6.5 summarizes the main steps of this approach.

This approach presents several drawbacks. First, when the sample surface is too reflective,

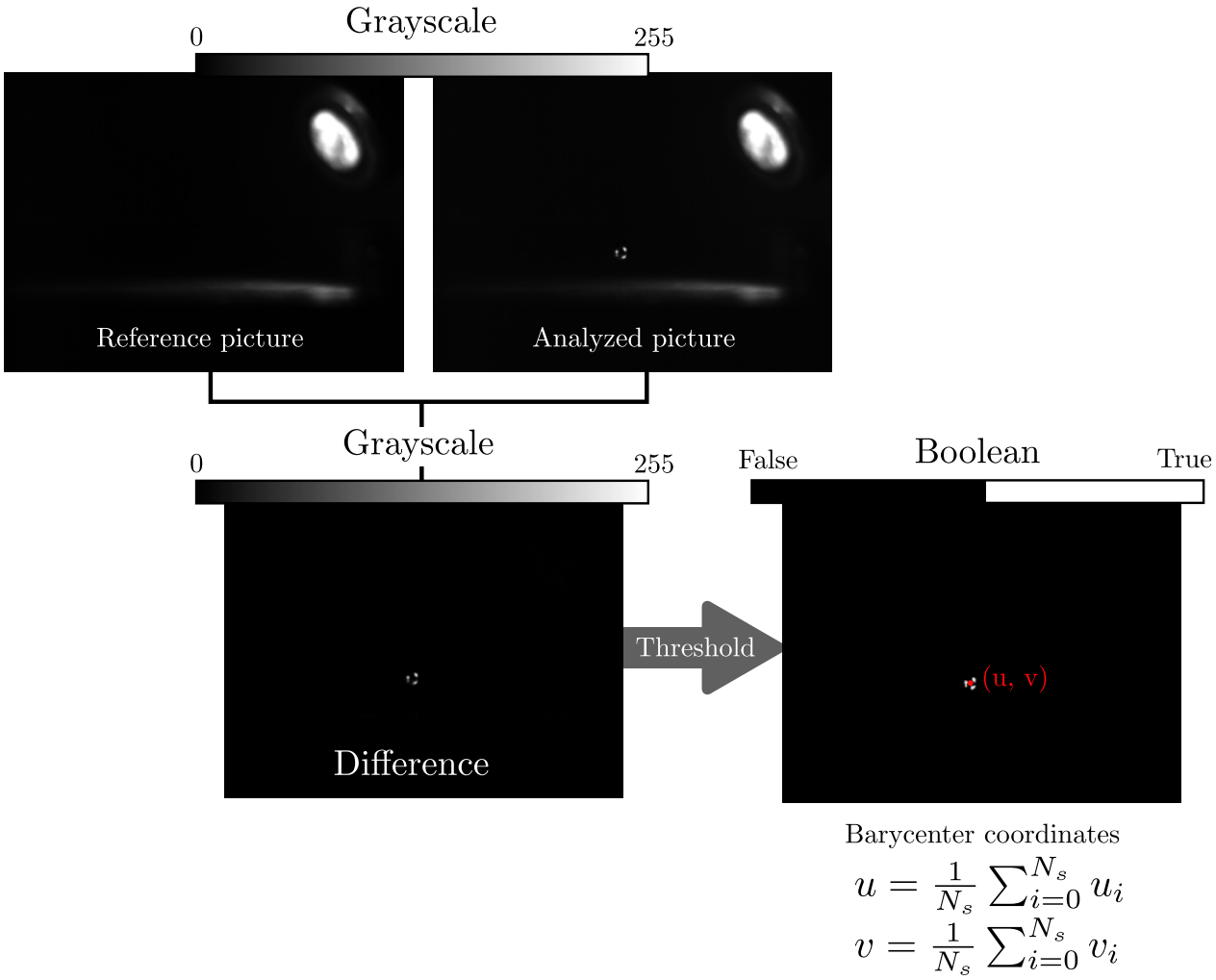

Figure 6.5 Shot detection procedure used in this study. The shot is detected by applying a threshold on the difference between the analyzed pictures and a reference picture without shot. The shot coordinates (u, v) are then taken as the barycenter of the N_s points (u_i, v_i) overcoming the threshold.

the reflection and the shadow of the shot on the sample becomes a moving object as the shot approaches the surface which induces non negligible errors on its estimated position. A mask is therefore applied on each treated picture to remove the sample surface from the analysis. Also, when the shot only partially appears in the screen, its true position cannot be recovered as its barycenter cannot be correctly computed. This often happens in the first picture but can be avoided simply by starting the analysis at the second picture. Finally, other moving elements such as light reflections on the shot, dust particles or moving lights during the impact can alter the detected position. Most of the times, adjusting the detection threshold was however sufficient to obtain satisfactory results.

Shot position estimation

Knowing the two cameras intrinsic matrices $\boldsymbol{M_1}$ and $\boldsymbol{M_2}$, as well as the transformation matrices $\boldsymbol{T_1}$ and $\boldsymbol{T_2}$ between each camera and the sample coordinate system, equation 6.1 then provides four equations for the three unknown shot coordinates. To find the shot coordinates, a first estimate is obtained by solving three of these four equations, considering that the two equations given for the coordinates of the axis oriented in the shot direction are redundant, as the Y_s, $Y_{c,1}$ and $X_{c,2}$ axes shown in Figure 6.4 are almost colinear. However, the information provided by the two cameras is not always consistent as the shot position determination is not always exact and the two cameras are triggered with a small time delay τ.

When simply solving the system, the shot trajectory found can therefore be subjected to residual reprojection errors. This error can be estimated by computing the pixel distance between the detected and the reprojected coordinates on each camera as schematized in Figure 6.6 (a). Figure 6.6 (b) shows the evolution of the reprojection error with time for a shot experiment performed on an aluminum 6061 sample with a 45° angle for a pressure of 0.07 MPa. High reprojection errors up to 8 pixels can be observed before the impact event when applying no correction on the data, partially resulting from the time delay between the two cameras.

Knowing the time delay τ between the two cameras, the 2D pixel trajectory of the left camera can be linearly interpolated with respect to time using the values at time t to estimate the position values at time $t+\tau$. This provides shot positions on the two cameras which are taken at the same time and could help reducing the reprojection error, by using the interpolated values of the 2D trajectory to make a new estimation of the 3D coordinates. However, in practice, τ is difficult to estimate experimentally as this effect is more pronounced at high speed, for which only few pictures of the shot are available.

To estimate the value of τ, the estimated coordinates (X, Y, Z) in the sample reference frame are reprojected on each camera using equation 6.1 and compared to the interpolated shot pixel position on each picture. The difference between the projected coordinates and the shot coordinates is then minimized using scipy stochastic differential evolution optimization function [185] by varying the value of τ.

Figure 6.6 (b) shows a comparison of the reprojection error obtained with and without using the time-delay optimization. The figure reveals that the optimization procedure significantly reduces the reprojection error before the impact. Higher reprojection errors can be observed after the impact due to light variations on the shot that induces a bias on the shot detection.

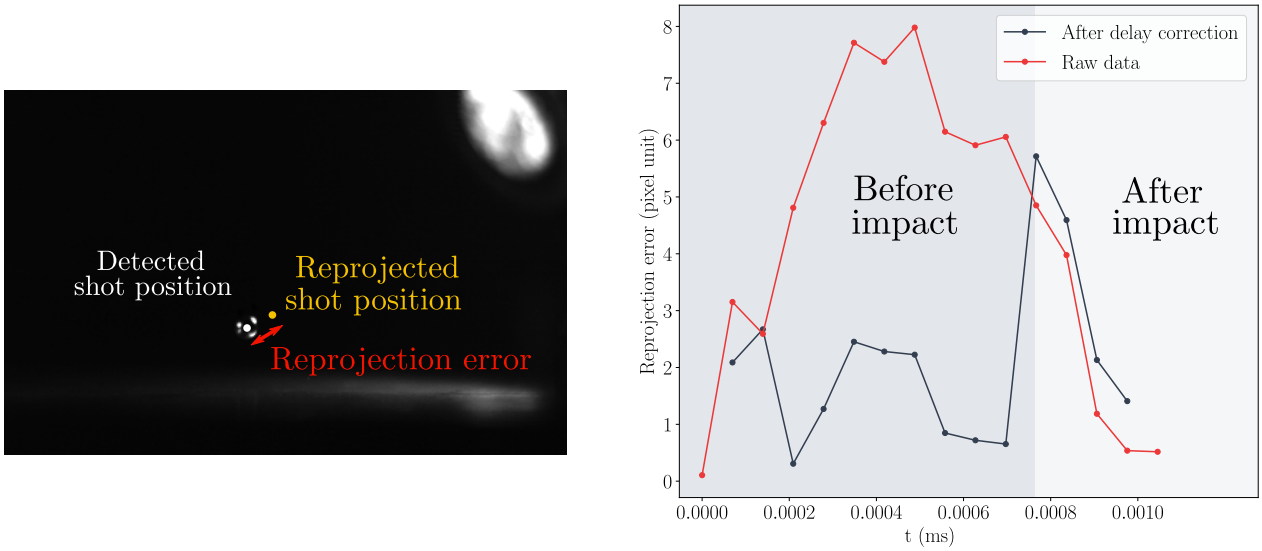

(a) (b)

Figure 6.6 Comparison of the detected shot trajectory and the reprojected shot trajectory obtained for a shot experiment performed on an aluminum 6061 sample with a 45° angle at 0.07 MPa. (a) Schematization of the reprojection error calculation. (b) Reprojection error with respected to time using the raw detected shot coordinate and using the corrected coordinates accounting for the delay between the two cameras. The correction overall reduces the reprojection error. Residual errors result from an incorrect detection of the shot position.

The resulting reprojection errors could be reduced by enhancing the shot detection algorithm in future works, for instance, using one of the more advanced feature detection algorithms provided by the OpenCV library [184] or using particle tracking velocimetry [186].

Figure 6.7 summarizes the complete methodology developed to retrieve the shot trajectory. The full procedure was implemented in Python using the openCV library [184]. The code can be found on github [182] and is fully reusable under 3-Clause BSD license.

The implementation was fully tested on virtual shot pictures generated using Blender 3D software [187] as presented in Appendix D. The procedure was shown to be at least 22 times more accurate than a simpler method not accounting for perspective, for an ideal case modeled using Blender. Also, one of the main benefits of this approach is that it provides indicators of the error made on the position, as the estimated trajectory can be reprojected on each camera using the intrinsic matrix and compared to the detected shot pixel position. The Python code provides the reprojection error obtained after each test for each camera to guide the choice of the detection parameters and to provide uncertainties on the estimated trajectory, as further detailed in the next section.

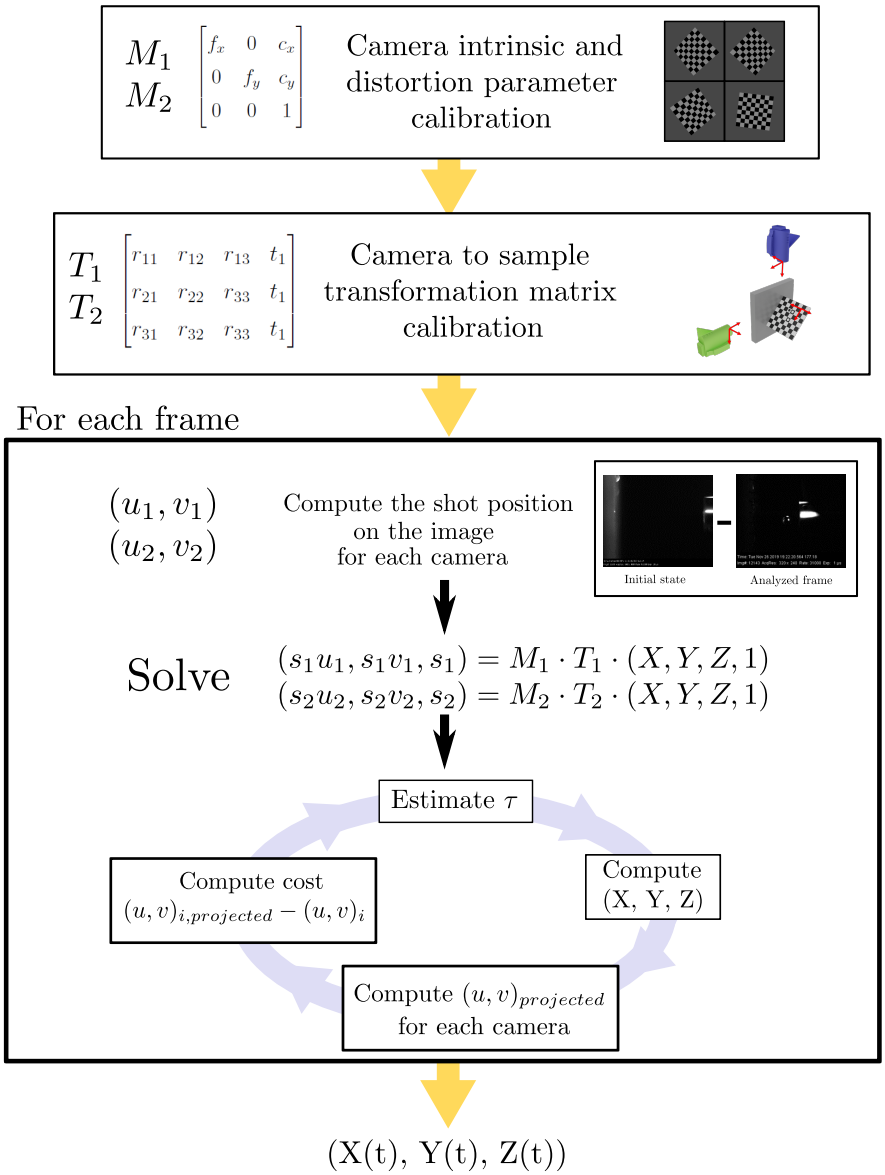

Figure 6.7 Summary of the shot 3D trajectory reconstruction procedure.

6.3 Setup accuracy and performances

6.3.1 Position uncertainty estimation

The difference between the reprojected shot pixel and the detected shot coordinates on each camera screen provides an estimate of the error made on the shot position, in pixel units. By estimating the ratio between a pixel length and the equivalent length measured at the camera focus distance δ_{pcm}, this error can also provide an estimate of the shot position uncertainty in centimeters.

To estimate such ratio, an image of a ruler was taken at the camera focus distance for each camera, as presented in Figure 6.8. The maximum reprojection error between the two cameras was then multiplied by δ_{pcm} to estimate the shot position uncertainty.

Note that this estimate is neither a higher nor a lower bound of the real position error as it depends on the relative position of the ruler with respect to the camera. It however provides an order of magnitude of the error resulting from the shot detection, the camera calibration quality and the time delay between the two cameras.

To assess the trajectory reconstruction accuracy and illustrate the interest of such error estimation, four shot were propelled and aimed at the same sample spot with 440C stainless steel 0.5 mm diameter bearing balls on an aluminum 6061 specimen. Figure 6.9 (a) shows a micrograph of the impacted surface obtained using a binocular microscope. The red dots corresponds to the impact position measured using the ImageJ software [188], considering the top left corner of the picture as the position origin. Figure 6.9 (b) shows a comparison of the shot position obtained with the trajectory reconstruction procedure and those measured with the binocular microscope. For each point, the red circles corresponds to the uncertainty estimated using the reprojection error.

A translation and a rotation were applied to all the measured coordinates to ease the comparison, as the micrograph coordinates were obtained in the micrograph picture reference frame. The effective translation and rotation to apply were determined by minimizing the distance between all measured positions with the estimated one using scipy differential evolution genetic function [185]. Figure 6.9 (b) reveals that the procedure performs an overall good estimation of the effective shot position on the sample. The largest error on these four tests was 215 μm and the estimated detection uncertainty on this test was 195 μm.

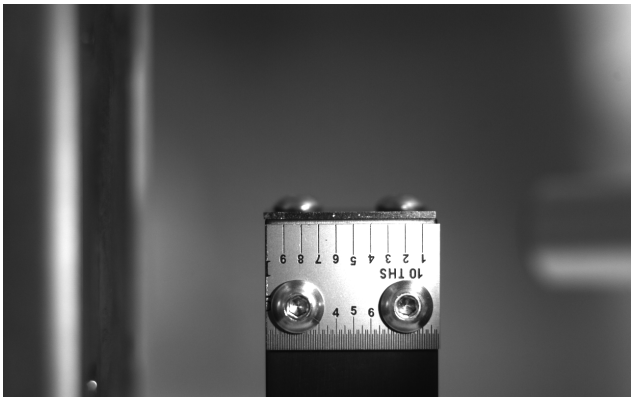

Figure 6.8 Ruler picture used to estimate the camera pixel to centimeter ratio at the camera focus distance.

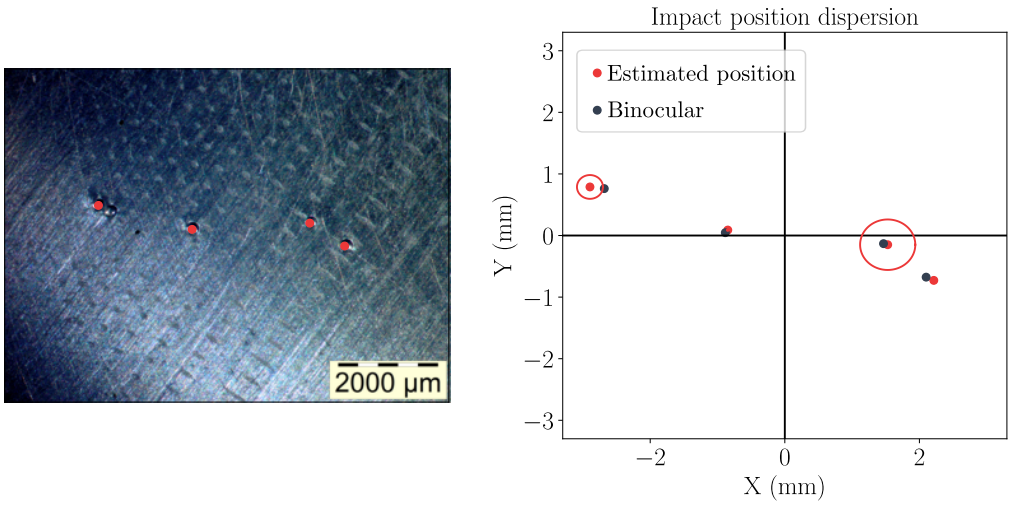

(a) (b)

Figure 6.9 Shot position estimation precision. (a) Micrograph showing the impact dent induced by four 0.5 mm shot impact aiming at the same sample spot. The red dots corresponds to the dent center coordinates estimated using imageJ [188]. (b) Comparison between the shot position measured with a binocular and the position estimated by the procedure detailed in section 6.2.2. The red circles corresponds to the position uncertainty. The procedure estimates well the effective shot position.

6.3.2 Aiming accuracy and velocity range

Several tests were conducted to characterize the shot velocity reached by a shot for a given pressure for the three different shot diameters. For each test, the shot velocity was estimated using the procedure detailed in Section 6.2.2. At least three shot were propelled for each tests to study the output velocity repeatability.

Figure 6.10 shows the evolution of the estimated velocity for the three different cannon diameters available. The relationship between the velocity and imposed pressure follows an inverse exponential tendency. The velocity that can be achieved by the cannon ranges from 0.8 m·s^{-1} to 143 m·s^{-1}, which covers the full shot-peening velocity range [26]. The achieved velocity ranges for each barrel diameter are summarized in Table 6.1.

The ability of the apparatus to shoot twice at the same spot was also characterized. When a spot is aimed at, using the precision laser, shot positioning variability could result from

Table 6.1 Shot velocity ranges obtained for the three shot diameter

Barrel diameter (mm)	0.5	1.19	2.5
Velocity range (m·s^{-1})	[1.5, 83]	[0.8, 90]	[1.2, 143]

either (i) misalignment between the laser and the cannon barrel center or (ii) shooting angle variability due to collisions of the shot with the internal walls of the barrel.

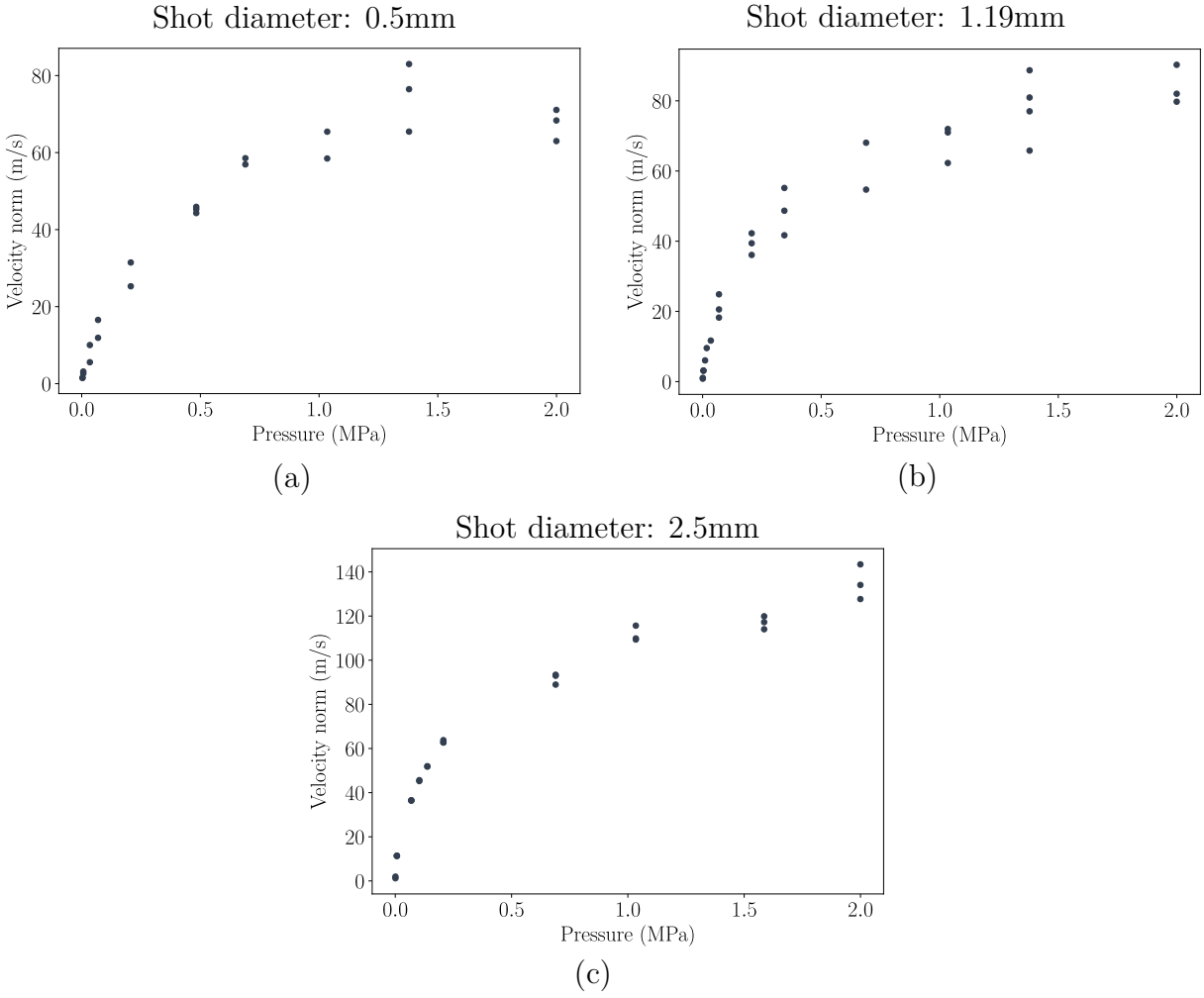

Figure 6.10 Evolution of the shot velocity with the input pressure for the three different shot diameters. A large velocity range between 0.8 $m{\cdot}s^{-1}$ and 143 $m{\cdot}s^{-1}$ can be achieved, covering the whole shot-peening velocity range.

Table 6.2 Average shot position and standard deviation with respect to the cannon barrel center.

Pressure range (MPa)	0.5 mm	1.19 mm	2.5 mm
[0, 0.2]	1.48 ± 0.79	1.65 ± 1.20	0.31 ± 0.16
[0.2, 0.69]	1.06 ± 0.14	0.83 ± 0.53	0.25 ± 0.13
[0.69, 1.38]	0.93 ± 0.24	0.45 ± 0.24	0.18 ± 0.04
[1.38, 2.07]	0.92 ± 0.49	0.43 ± 0.18	0.22 ± 0.13

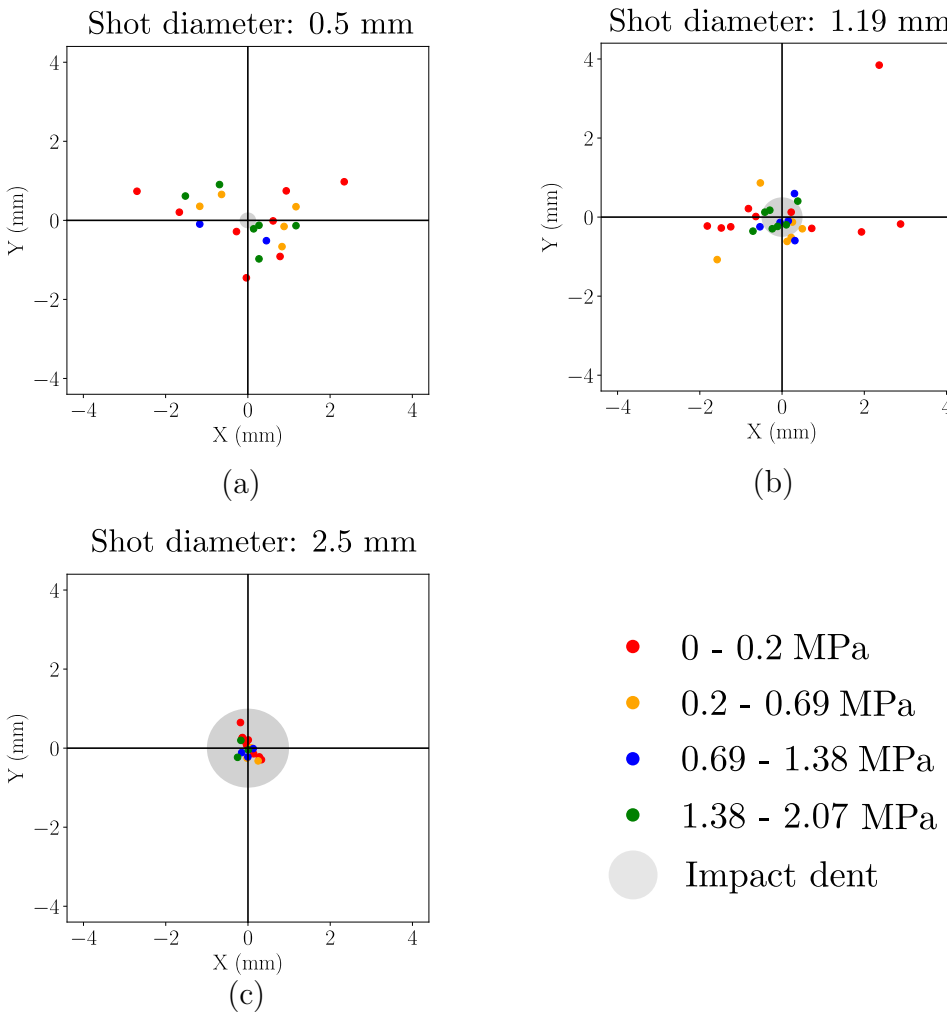

Figure 6.11 Dispersion of the shot position on the sample relatively to the barrel center for the three different shot diameters. The gray circle represents the average impact dent usually obtained for each shot diameter. The shooting accuracy increases with the shot diameter and with the input pressure. Overlapping impacts can be performed using the 2.5 mm and 1.19 mm shot diameter but not using the 0.5 mm shot diameter cannon.

To reduce the first source of variability, a position mark was engraved both on the laser and on the cannon barrel to ensure the same positioning over all the tests. The second source of variability can be fully characterized using the shot trajectories provided by the methodology developed in section 6.2.2, as it estimates the shot position at the moment of impact in the sample's coordinate system.

Figure 6.11 (a), (b) and (c) show the position of each shot relatively to the center of the barrel exit at the moment of impact for the three cannon diameters respectively. The cannon accuracy increases with the applied velocity and the shot diameter. This phenomenon results

from relative machining precision being easier to achieve for larger shot diameters. Table 6.2 summarizes the average shot position vector norm on the sample for different pressure ranges and for the three different diameters with their standard deviations.

The gray circle in Figure 6.11 represents the average impact dent obtained for each shot diameter on aluminum samples, to better visualize the possibility to perform several shot at the same position. It reveals that there is a low probability to perform two shot at the same position when using the 0.5 mm diameter cannon with the current setup. However the apparatus can be used to perform controlled overlapping shot using 1.19 mm and 2.5 mm diameters media. Also, the shot trajectory reconstruction procedure provides sufficient input to reproduce the experimental shot sequence.

6.4 Applications

6.4.1 Application 1: Coefficients of restitution

Modeling of the shot kinematics during the shot-peening process usually requires knowledge of the shot/target coefficient of restitution (CoR) which represents the ratio of the energy absorbed by the material during the impact event, mainly by plastic deformation, elastic wave propagation or thermal dissipation [189]. Most often, the kinematic CoR [190], which is the ratio of the shot velocity after and before the impact, is used.

Several authors used FEA to estimate the CoR values for different velocities and impacting angles to be used as input in DEM [13,191–193]. Alternatively, few authors determined CoRs experimentally using single shot experiments [91, 194, 195]. Fathallah et al. [194] recorded the velocities of several shot during shot peening of a manganese steel using a non contact optical device. Seifried et al. [195] performed repeated low velocity impacts using a shot attached on a pendulum dropped by a magnet to obtain the evolution of CoR values over several impacts on a 6060 aluminum sample. Murugaratnam [91] developed a cannon that can propel industrial shot at velocities between 44 $\mathrm{m}\cdot s^{-1}$ to 72 $\mathrm{m}\cdot s^{-1}$ with a high precision to estimate the CoRs values for different shot velocities on a titanium alloy.

Yet very few studies provided the CoR values for a large velocity range, as the aforementioned setups could only reach either low or high velocities. The CoR values over a wide velocity spectrum, particularly in the range where the elastic/elasto-plastic transition occurs, could however be relevant for shot peening simulations as shot rebounding multiple times could reach low velocities during the process.

Also, only the normal component of the velocity is usually considered as the tangential part is difficult to measure since it requires the three dimensional trajectory of the shot. Also, the

tangential restitution depends on several factors such as the shooting angle, the shot spin velocity or the shot/target friction coefficient [196, 197].

As the procedure detailed in Section 6.2.2 provides the three dimensional coordinates of the shot velocity, it can be used to extract the tangential components of CoR using the detailed methodology on shot impacting with different angles. Also, the shot peening test rig can send shot with velocities ranging from 0.8 $m{\cdot}s^{-1}$ to 143 $m{\cdot}s^{-1}$. The ability of the setup to find consistent CoR values over a wide velocity range and for different shot diameters was therefore also investigated.

Methodology

Several shot were propelled on an as received aluminum 6061 sample. The sample was not polished, which could result in a dispersion of the rebounding direction. However, the shot diameters were deemed to be sufficiently large to be unaffected by the initial surface roughness. 440C stainless steel bearing balls with 0.5, 1.19 and 2.5 mm diameter were shot at different pressures ranging from 689 Pa to 0.69 MPa. Each test condition was at least repeated twice to ensure the measured CoR's repeatability. The space between each shot was at least three times the surrounding shot dent diameter to avoid interactions with the plastic strain induced by previous shot.

1.19 mm diameter shot were also propelled with a 15° and 30° angles from the surface normal at pressures ranging from 689 Pa to 0.69 MPa to investigate the evolution of the tangential CoR with the shooting angle. The calibration of the transformation matrix between the camera and the sample was performed at each angle to obtain the 3D coordinates of the velocity in the rotated sample system.

Results

Influence of shot velocity and shot diameter

Figure 6.12 (a) shows the evolution of the CoR values obtained for different shot velocities for the three shot diameters investigated. For the lowest velocities, a CoR of 0.7 is obtained, which is consistent with results found in the literature [195,198]. Note that a CoR of 1 cannot be reached as around 10% to 20% of the energy loss is related to elastic wave propagation and thermal effects [198]. Also, according to Johnson [198], normal shot velocities required for a perfectly elastic impact are theoretically bellow 0.14 $m{\cdot}s^{-1}$, which could not be reached using the current setup.

Figure 6.12 (a) also reveals that the estimated CoRs were independent of the shot diame-

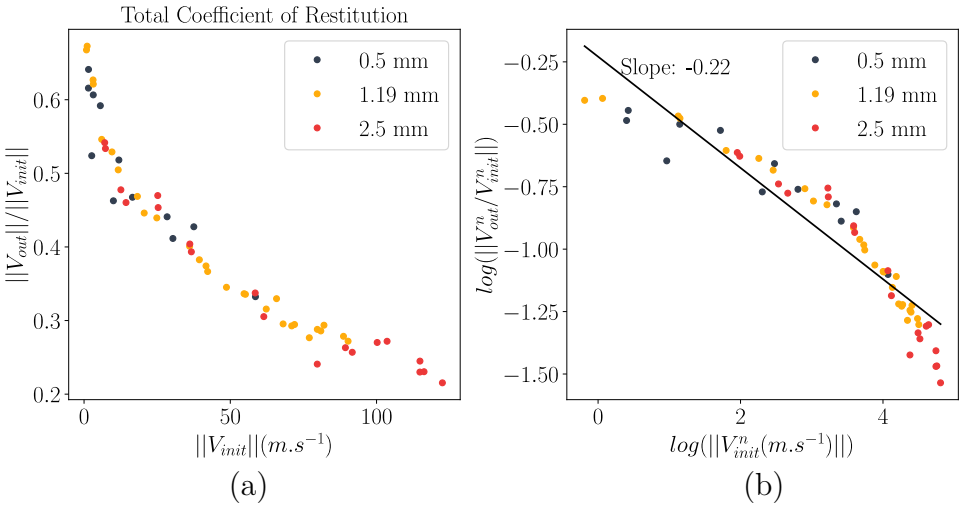

Figure 6.12 Estimated CoR values for the three shot diameters. (a) Evolution of the kinematic CoR with the velocity before impact for different shot diameter. The CoR variation is independent of the diameter. (b) Log variation of the kinematic CoR with respect to the log of the velocity before impact. The average slope of the CoR data is 0.22 which is consistent with the $\frac{1}{4}$ exponent suggested by Johnson [189]

ter. This is consistent with the literature as it was previously demonstrated that the CoRs mainly depend on the shot/material mechanical properties ratio [199]. This result therefore demonstrates that the procedure developed in Section 6.2.2 provides consistent results for the three different shot diameters, despite a potential lower shot detection accuracy for smaller diameters as the shot represents less pixels on the screen.

Using Hertzian contact theory and perfect plasticity assumptions, Johnson [189] provided the following expression of the CoR :

$$\frac{V_{out}}{V_{init}} \approx 3.8 \left(\frac{\sigma_Y}{E^*}\right)^{1/2} \left(\frac{\rho}{2\sigma_Y}\right)^{-1/8} V_{init}^{-1/4}, \tag{6.2}$$

where σ_Y is the yield stress, ρ is the target material's density and E^* is defined as:

$$\frac{1}{E^*} = \frac{1-\nu_{shot}^2}{E_{shot}} + \frac{1-\nu_{target}^2}{E_{target}}, \tag{6.3}$$

where E_{shot}, E_{target} and ν_{shot}, ν_{target} are respectively the Young's modulus and Poisson's ratio of the shot and the target.

Figure 6.12 (b) shows the evolution of the log of the kinematic CoR with $log(||V_{init}||)$. The black line corresponds to a linear fit of the data. The average slope is close to the $-\frac{1}{4}$

exponent found by Johnson [189]. The CoR's variation tendency is therefore consistent with what was previously found in the literature.

Influence of shooting angle

Figure 6.13 (a) shows the evolution of the total CoR with velocity for three different angles. The figure reveals that the total CoR value (*e.g.* accounting for both the tangential and normal velocity component) increases with the shooting angle. This results from the fact that less energy is absorbed by plastic deformation as the normal impact pressure decreases as the angle increases, as already demonstrated experimentally on aluminum samples by Sheldon et al. [200].

Figure 6.13 (b) shows the evolution of the CoR obtained using only the normal component of the velocity. The normal CoR is almost identical for the three angles, as the energy ratio for a normal impact for a given velocity depends mainly on the shot and sample's material properties. Brauer et al. [201] and Wu et al. [196] respectively experimentally and numerically evidenced a dependence of the normal CoR with the impact angle. Their works both demonstrated a decrease of the CoR at angles above 30° for low velocity impacts ($<10 \mathrm{m \cdot s^{-1}}$). This was explained by the authors as a change of the contact area geometry as the angle increases. However, the angle tested in this study were not sufficiently high to observe this effect.

Figure 6.13 (c) shows the variation of the CoRs obtained using the tangential component of velocity. The tangential CoR presented a larger dispersion than the normal one at the lowest angle as the tangential velocity is small and more sensitive to measurement errors at such angles.

Despite the CoR discrepancy for impacting angles of 15°, it seems that the average tangential velocity ratio slightly increases as the angle increases. This could result from the shot sliding on the surface rather than gripping, as explained by Cross [202]. Note that it was here assumed that the shot impacts the sample without any angular velocity.

6.4.2 Application 2: Single impact tests on single crystal copper samples

The methodology detailed in section 6.2.2 provides the three-dimensional trajectory of the shot which could then be used as input for FEA for constitutive behaviour validation. In this section, the shot peening test rig was used to validate a crystal plasticity finite element impact model using the constitutive parameters identified in chapter 5.

The ability of the model to reproduce the experimentally measured shot displacement during

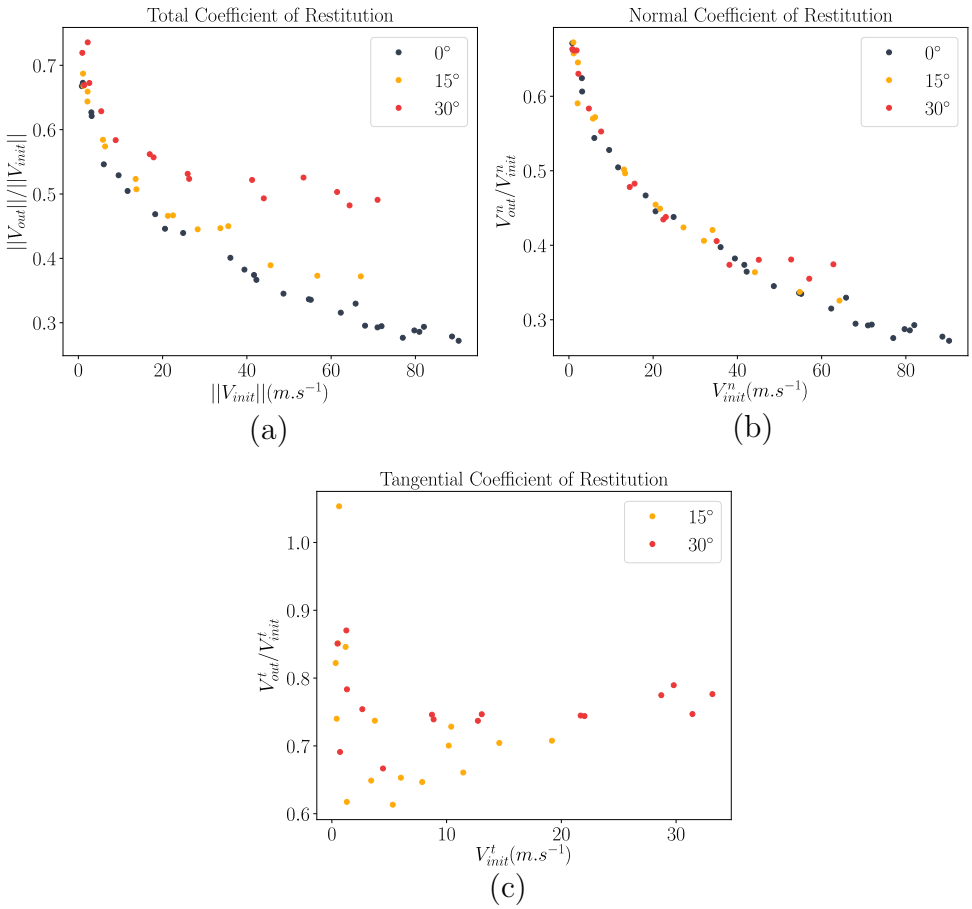

Figure 6.13 Evolution of the kinematic CoR with the velocity before impact for different shot diameters (a) Total velocity norm ratio. (b) Normal velocity ratio. (c) Tangential velocity ratio.

and after the impact and the dent topography was investigated. Electron backscattered diffraction (EBSD) analyses were also performed to confirm that the model could predict the crystal misorientation induced by the impact in the cross-section beneath the impact dent.

Methodology

Impact tests were performed on copper single crystals with the top surface oriented along the [100] and [110] orientations, respectively. Two 0.5 cm thick samples for each orientations were cut using a diamond wire saw. The sample surface to be impacted was polished with SiC grit paper P600 and P1000 and then using diamond suspension of 3 μm and 1 μm to reduce the impacted surface roughness.

As the cannon sample holder was developed only for plate samples of given dimensions, an

adapted sample holder was developed to hold small single crystal samples. The sample holder is presented in Figure 6.14 and consists of a plate with a rectangular hole which is screwed on a parallelepiped to compress the sample. The sample holder dimensions were chosen to match those of the standard cannon sample dimensions. The holder was 3D printed using a Formlabs Grey Resin using a Formlabs Form2 printer.

For each sample, impact tests were performed at 26 $m{\cdot}s^{-1}$ and 64 $m{\cdot}s^{-1}$ target velocities using 0.5 mm hardened bearing-quality 440C stainless steel balls. The impact positions were chosen so that the distance between each impact was at least three times the shot diameter to prevent any interaction with plastic strains induced by previous impacts.

The impact dent topography was then measured using a polychromatic confocal microscope with a 1 μm lateral resolution to compare the dent shapes with simulations.

The cross-section preparation procedure is schematized in Figure 6.15. The samples were cut using a diamond wire saw at a distance of a 100 μm from the dent center to reveal the cross-section below the impact dent. The resulting cross-sections were then polished for EBSD observations using a Jeol Ion beam cross-section polisher with a 5 kV beam current for 5 h followed by a 30 min refining step at 4 kV. The dent was filled with silver painting to prevent surface topography induced by the beam encountering heterogeneities at the surface.

Finite element model

The impact was modeled using Abaqus dynamic explicit 6.14 solver with an automatic time

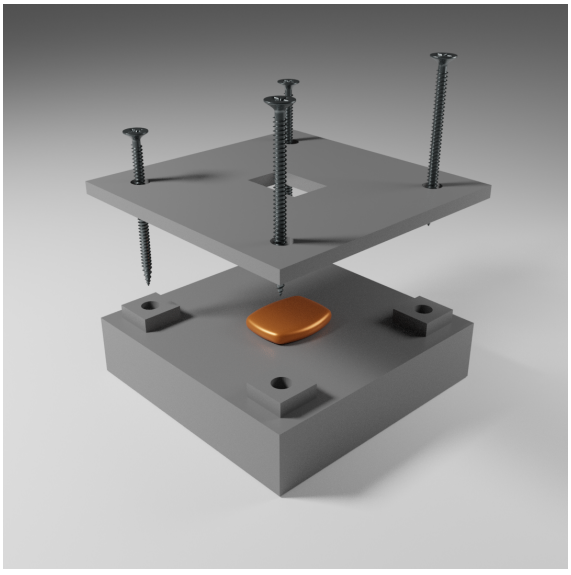

Figure 6.14 Sample holder used to maintain the copper samples during the tests.

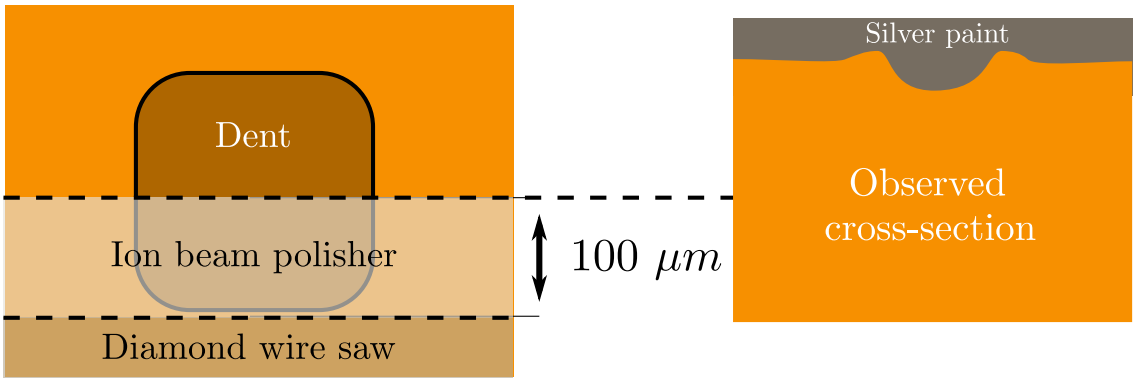

Figure 6.15 Cross-section preparation procedure. The dent is represented as a square with rounded edge as the impact was performed along the [100] orientation of the single crystal [21]. The sample is first cut a 100 μm away from the dent center. The remaining distance from the center is removed by Ion beam polishing. The impact dent is filled with silver paint to prevent surface topography induced by the beam encountering the dent. The observed surface is the cross section under the center of the dent.

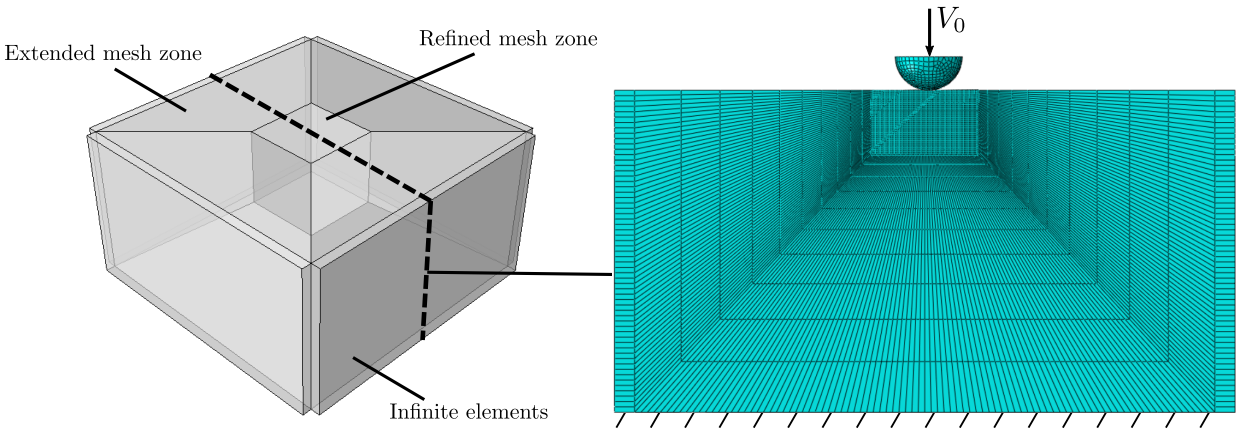

Figure 6.16 Finite element model used for impact simulations. The sample geometry is divided in three zones: a refined mesh zone at the impact location, surrounded by an extended mesh zone to limit the effect of boundary conditions and infinite elements around the sample to damp residual stress field oscillations.

step procedure. The model geometry and mesh is presented in Figure 6.16. The size of the refined mesh zone was chosen so as to contain all the plastic deformations. The substrate was modeled using linear reduced integration hexahedric elements (C3D8R). To reduce potential spurious oscillations of the residual stress field, infinite CIN3D8 elements were positioned around the sample as shown in Figure 6.16. All degrees of freedom were blocked at the bottom

of the mesh. The mesh density was chosen after a convergence study on the displacement curve as detailed in Appendix G.

The shot was modeled as rigid with a friction coefficient of 0.2. Only half of the shot was modeled and its moment of inertia I was computed as:

$$I = \frac{2}{5} m_{shot} r^2, \tag{6.4}$$

where m is the shot mass estimated as:

$$m_{shot} = \rho_{shot} \frac{4}{3} \pi r^3, \tag{6.5}$$

where r is the shot radius and ρ_{shot} is the shot density taken as 7.110^{-3} g·mm^{-3}. The initial shot velocity is imposed at the rigid body reference point. The initial velocity was taken as the velocity vector obtained experimentally before the moment of impact.

Since the experimental sample faces are not perfectly parallel, the shot was performed with an additional angle which is not accounted for by the calibration procedure detailed in section 6.2.2. The average plane of the sample was therefore determined using the experimental topography measurement by minimizing the difference between a perfect plane and the measured topography. The additional rotation is then accounted for using the following relation:

$$v_{FEM} = R \cdot v_{shot}, \tag{6.6}$$

where v_{FEM} is the initial velocity vector applied in the finite element model, v_{shot} is the velocity vector measured by the procedure detailed in section 6.2.2 in the setup coordinate system and R is the rotation matrix between the setup coordinate system and the average impacted plane determined using the topography.

The sample material was modeled using the Meric-Cailletaud crystal plasticity finite element framework [1] using Zmat 8.7.1 with Runge-Kutta 4 explicit integration using the material parameters identified in chapter 5. Copper density was taken as 8.98 10^{-3} g·mm^{-3}.

Table 6.3 summarizes the different impact conditions used. The initial impact velocity corresponds to that measured experimentally. Those conditions were chosen to model tests with at least two different crystal orientations and two different velocities. The tests with the smallest impact angles and the lowest reprojection errors were selected.

Table 6.3 Conditions selected for the finite element simulations.

cannon pressure (MPa)	crystal orientations	Initial velocity vector ($m \cdot s^{-1}$)
0.21	[100]	(0.47, -26.59, 1.37)
0.69	[100]	(0.70, -63.62, -0.87)
0.21	[110]	(-1.32, -24.01, 1.23)

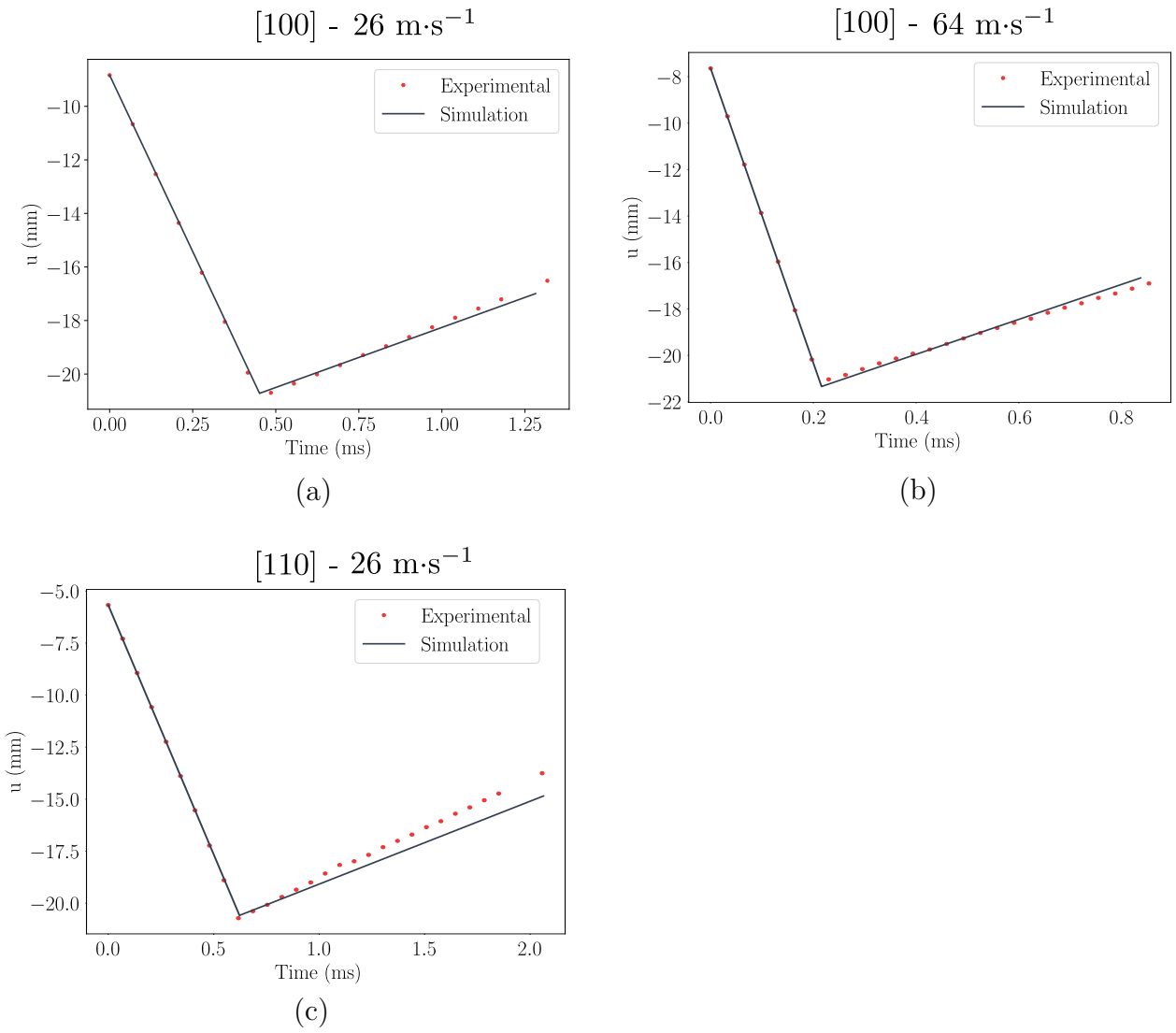

Figure 6.17 Comparison of experimental and linearly extrapolated numerical displacement curves for test conditions (a) [100] - 26 $m \cdot s^{-1}$, (b) [100] - 64 $m \cdot s^{-1}$, (c) [110] - 26 $m \cdot s^{-1}$. A good correspondence can be observed, especially for the impacts performed along the [100] orientation.

Results

Displacement curves

The finite element model provides the evolution of the shot displacement during the impact. Experimental curves mainly provide the shot velocity before and after the impact as well as the impact duration, but the time resolution is not yet sufficient to observe what happens during the impact. In future works, the test lighting condition will be improved to increase the reachable cameras framerates. To compare the experimental and numerical displacement curve, the displacement of the latter was therefore extrapolated linearly before and after the impact, assuming the shot velocity vector is always constant except during the impact event.

Figure 6.17 (a), (b) and (c) show a comparison of the resulting numerical displacement along the direction normal to the sample with that measured experimentally. A very good

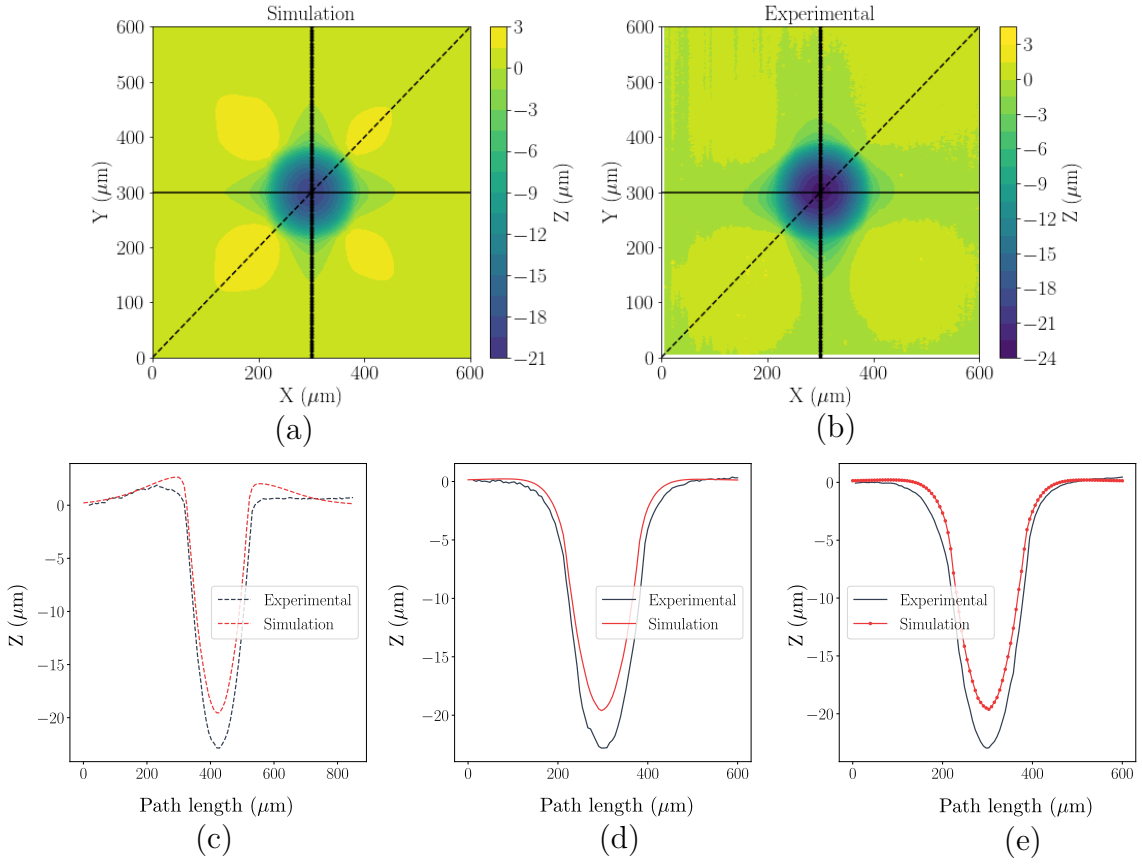

Figure 6.18 Comparison between experimentally measured and numerically predicted imprints after an impact performed at 26 $m{\cdot}s^{-1}$ along the [100] orientation. (a) FEM imprint topography (b) Experimentally measured topography. Comparison along a (c) diagonal, (d) horizontal and (e) vertical path.

correspondence is observed between the experimentally measured and numerically predicted output velocity when performing impacts along the [100] orientation for the two shot velocity conditions.

For the [110] orientation, the normal experimental velocity after impact was 5.17 $m \cdot s^{-1}$ whereas the predicted velocity was 3.98 $m \cdot s^{-1}$. The absolute error on the velocity for this orientation was therefore around 23%. Such error could result from the anisotropic strain rate dependency observed in chapter 5. It could also result from errors on the plastic parameters that were not identified such as the interaction matrix. Indeed, gliding interactions tend to have less impact on the total plastic deformation when impacting along the [100] orientation when compared to impact along the [110] orientation as gliding systems are more heterogeneously activated in the latter case.

Imprint topography

Figures 6.18, 6.19, and 6.20 shows a comparison of the predicted and experimentally measured imprint topography for impacts performed at 0.21 MPa and 0.69 MPa along the [100] orientation and at 0.21 MPa along the [110] orientation, respectively. Figures 6.18, 6.19, and 6.20 (a) and (b) reveals an overall good correspondence of the predicted and experimentally measured imprint shapes for the two different orientations and velocity conditions.

This is confirmed by Figures 6.18, 6.19, and 6.20 (c), (d) and (e) which compares the topography along a diagonal, horizontal and vertical path, respectively, which are represented in Figures 6.18, 6.19, and 6.20 (a) and (b). The largest error is found for the prediction of the dent depth and is respectively of 16.5%, 14.9% and 11.9%.

Renner et al. [137] investigated the possibility to obtain the Meric-Cailletaud constitutive parameters by inverse identification with FEA using the topography of an imprint induced by Berkovich indentation. Their analysis revealed that the imprint shape was sensitive enough to a variation of the plastic parameters to obtain all those parameters by inverse identification using several indents in different crystal orientations.

The error observed in Figures 6.20 (c) and (d) could therefore result from the material's constitutive behavior parameters used. Also the overall good correspondence gives confidence in the velocity vector provided by the procedure detailed in Section 6.2.2. The shot peening test rig could therefore be used for parameters identification using the dent topography.

Crystal misorientation

The EBSD analysis provided the crystal misorientation variations induced by the impact

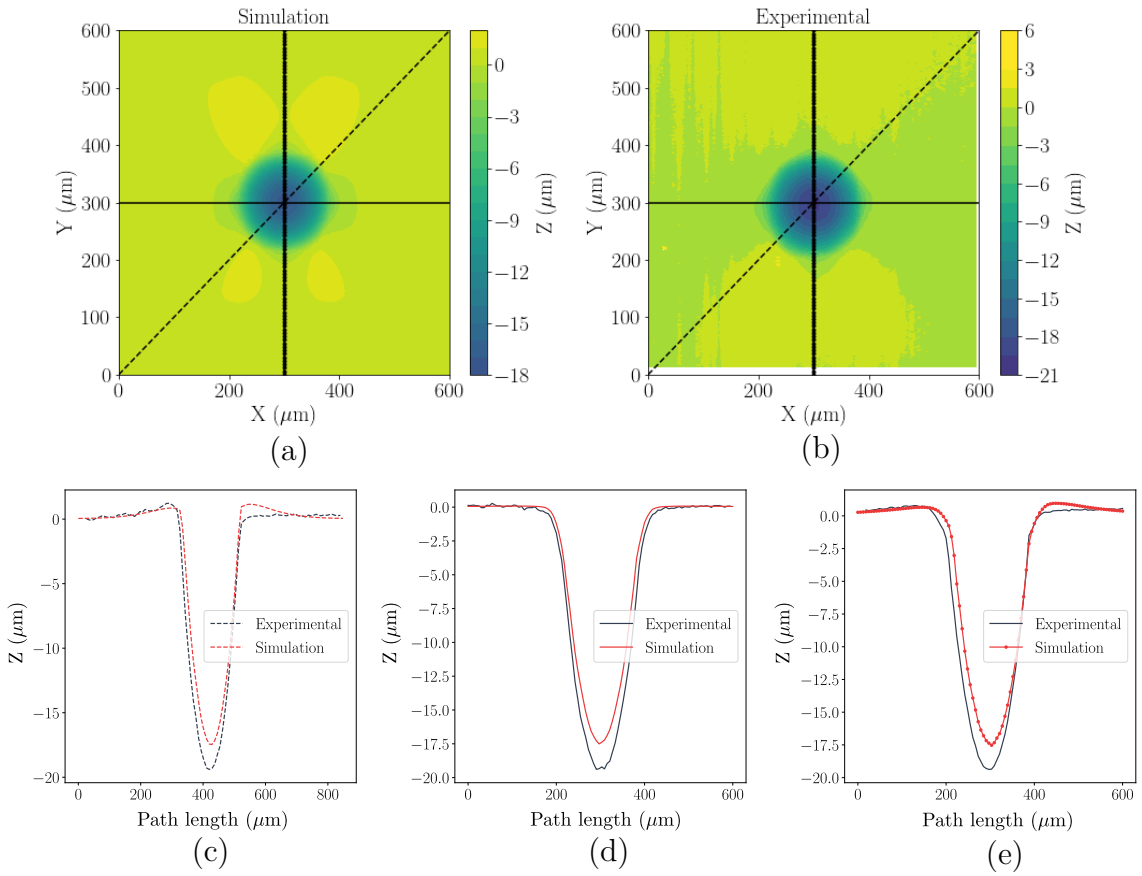

Figure 6.19 Comparison between experimentally measured and numerically predicted imprints after an impact performed at 64 m·s^{-1} along the [100] orientation. (a) FEM imprint topography (b) Experimentally measured topography. Comparison along a (c) diagonal, (d) horizontal and (e) vertical path.

in the cross-section under the impact dent center. This misorientation field ϕ can also be recovered numerically using the rotation tensor R^e extracted from the elastic part of the deformation gradient tensor. To compare the same quantity, the rotation field in the cross-section under the impact dent was converted to an MTEX [159] EBSD object in matlab, using the rotation tensor R^e computed at each integration point.

Figure 6.21 (a) and (b) respectively show the numerically predicted and the experimentally measured crystal misorientations relatively to a material point taken at the highest measured depth. The impact dent diameter and affected depth (*e.g.* the depth down to which misorientation higher than 40% of the highest misorientation value can be found) were both estimated respectively using imageJ [188] measurements and MTEX analyses. The figure reveals a very good correspondence of the affected depths and impact diameters.

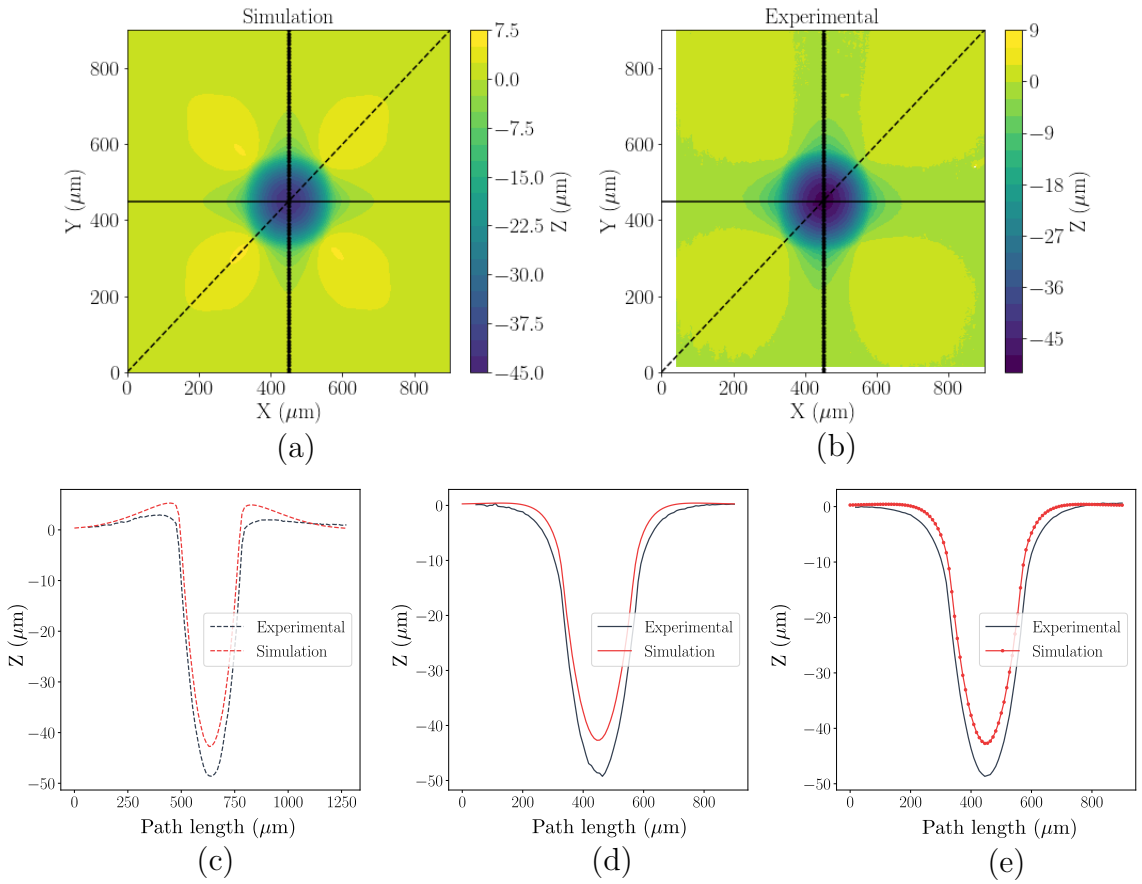

Figure 6.20 Comparison between experimentally measured and numerically predicted imprints after an impact performed at 26 $m \cdot s^{-1}$ along the [110] orientation. (a) FEM imprint topography (b) Experimentally measured topography. Comparison along a (c) diagonal, (d) horizontal and (e) vertical path.

Some characteristics of the rotation field can be found both numerically and experimentally. However the shapes of the two fields is slightly different. This could result from the experimental observations being made not exactly at the center of the indent.

The good correspondence between the experimentally measured and numerically predicted displacement curves, impact geometry, affected depths and misorientation values confirms the possibility to model the impact event produced by the cannon using the data estimated by the procedure detailed in section 6.2.2 and use such model for constitutive parameters identification.

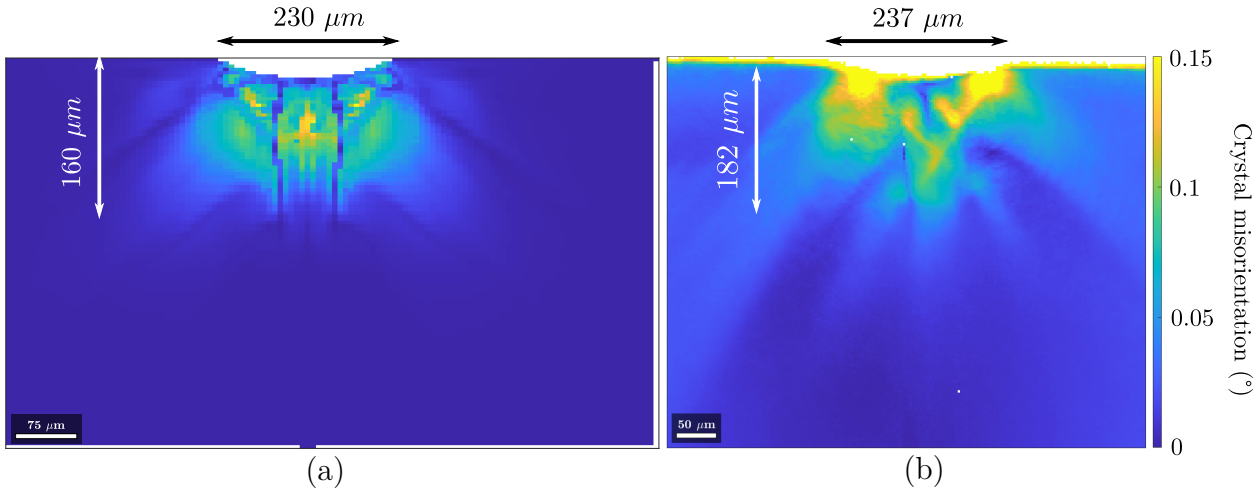

Figure 6.21 Comparison of the (a) numerically predicted and (b) experimentally measured crystal misorientation in the cross-section under the impact center for a test performed along the [100] orientation. A good correspondence is found for the impact diameter, affected depth and misorientation values.

6.5 Conclusion

A shot peening test rig was developed to propel industrial shot at different velocities and angles with high accuracy. A methodology to estimate the propelled shot 3D trajectory was developed using a pinhole camera model and implemented in an open source code available on github [182]. The developed methodology provides the shot coordinates with at best a 70 μm accuracy, in the absence of reprojection errors, accounting for perspective, camera lens distortion and potential time delay between the two cameras. The methodology also provides an estimate of the error on the reconstructed shot position using the trajectory reprojection on each camera.

The setup was characterized using the developed methodology. The cannon can propel shot with three different diameters (0.5 mm, 1.19 mm and 2.5 mm) at velocities ranging from 0.8 m·s^{-1} to 143 m·s^{-1} and with an aiming accuracy of respectively 1.48 mm, 1.65 mm and 0.31 mm for the three shot diameter under 0.69 MPa input pressure and 0.93 mm, 0.45 mm and 0.22 mm over 0.69 MPa input pressure. Note that the aiming accuracy was estimated by shooting at a 2 cm distance between the cannon and the sample to prevent the shot from bouncing back on the cannon barrel. This accuracy can however be improved by lowering this distance and setting a small sample angle. The cannon can therefore be used to perform several impact at the same material spot but only using the largest diameters.

The setup was successfully used to measure the coefficient of restitution of an aluminum 6061

sample. Our study revealed that the 3D trajectory estimation procedure provides consistent results for the three shot diameters as the measured CoR values were independent from the shot diameter. Shot propelled with different angles also revealed that the procedure could extract both the normal and tangential CoR values. The developed cannon and methodology could therefore be very useful for shot peening simulations using discrete element modeling.

Finally the shot displacement, dent topography, affected depth and misorientation values obtained by impacting a copper single crystal along two different crystal orientations were measured using the developed methodology and EBSD analyses. This analysis confirmed that the setup could be used to validate crystal plasticity constitutive behavior as the test was successfully reproduced by FEA.

Data Availability Statement

The data that support the findings of this study are openly available in Zenodo at `http://doi.org/10.5281/zenodo.4001762`.

CHAPTER 7

Impact tests for high strain rate parameter identification

7.1 Introduction

In the previous chapter, a shot peening canon was developed to validate the ability of the model to reproduce the shot displacement curve, dent topography and, as a perspective, the residual stress field induced by single impacts under controlled conditions, when using coefficients identified by high strain rate micropillar compression. As explained in section 2.1.3, the residual stress field is a direct consequence of impact induced plastic deformation. It could therefore contain sufficient information, not just for model validation, but also for plastic constitutive parameter identification, if the impact induced residual stress field is sensitive enough to the constitutive law parameters variations.

The benefit of such an approach is that the residual stress field is induced by an impact under industrial process conditions at the usual process strain rates. **The identified coefficients would therefore be fully representative of the process conditions**. This would also provide a methodology for parameter identification at higher strain rates, as compared to SHPB or micropillar compression tests, as the strain rate reported for single impact events could reach 10^5 s^{-1} [20].

The shot displacement curve with respect to time also contains relevant information about the material strain rate sensitivity. Indeed, it is directly representative of the energy dissipated by the material during impact. It could therefore also be used for viscoplastic parameter identification.

In this chapter, the possibility to identify the viscoplastic parameters K and n of the Meric-Cailletaud constitutive behaviour was investigated using different crystal orientations and impact velocities. Note that no identification was performed in this work as the objective was only to investigate the potential well-posedness of the problem. The identifiability analysis was performed using the impact finite element model detailed in Section 6.4.2. This work was submitted for publication in the Journal of Theoretical, Computational and Applied Mechanics [203].

The chapter is organized as follows: the identifiability analysis methodology used in this study is detailed in Section 7.2. The identifiability of the viscoplastic parameters using the shot displacement curve and the residual stress field under the impact dent is analyzed in Section 7.3. The results of the identifiability analyses are discussed in Section 7.4 and finally, section 7.5 concludes the work.

7.2 Identifiability analysis

Assessing the possibility to identify a model constitutive parameters using a given set of observations consists in demonstrating that the problem to solve is well-posed *e.g.* (i) that there is a reasonably low number of admissible solutions, (ii) that each identified parameters have a distinct influence on the model's outputs and (iii) that those outputs are sufficiently sensitive to each of the parameters with similar amplitudes. These conditions were investigated for the identification of the Meric-Cailletaud K and n viscoplastic parameters using either the shot displacement $u(t)$ or the residual stress field in the cross section under the impact dent.

A typical numerical unidirectional shot displacement curve is shown in Figure 7.1. The curve can be divided in three parts:

- Before impact where the shot velocity is almost constant.
- During the impact where the velocity decreases and changes sign when the shot starts to rebound.
- After impact where the shot velocity reaches a lower constant value.

The velocity measured before and after the impact, combined with the impact event duration, are representative of the energy absorbed by the material during the impact which is mainly

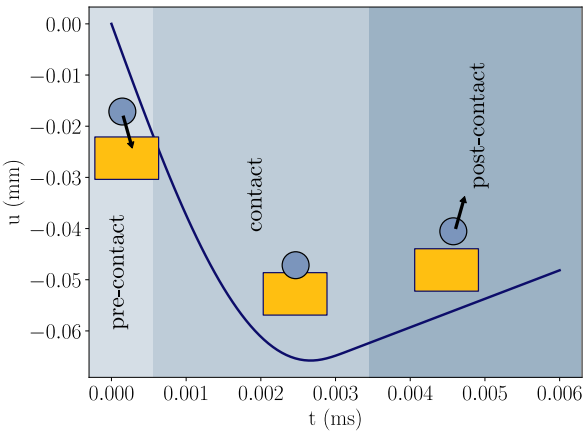

Figure 7.1 Typical single impact displacement curve with respect to time obtained by finite element simulations. The velocity first progressively decreases and changes sign when the shot starts to rebound to finally reach a constant velocity after the impact.

dissipated by plastic deformation and elastic wave propagation, if temperature effects are negligible [198].

In reality, the shot trajectory is three dimensional and three different curves have to be analyzed for the three different space directions. However, this study only focuses on unidirectional impacts as it only aims at laying the basis of an identifiability analysis and identification methodology.

The displacement curve sensitivity to a constitutive parameter variation is defined as follows:

$$\frac{\partial \overline{u}}{\partial \overline{\theta}}(t) = \frac{1}{\max(|u|)\epsilon\sqrt{T}} \left(u(\theta + \epsilon\theta, t) - u(\theta, t)\right), \tag{7.1}$$

where T is the number of acquisition points taken as 100, ϵ is the perturbation factor, $u(t)$ is the shot displacement at time t and θ_i is the constitutive parameter to be identified. The overline notation designates dimensionless quantities.

Figures 7.2 (a), (b) and (c) show respectively the variation of the σ_{xx}, σ_{yy} and σ_{xy} residual stresses under the impact dent obtained numerically using the reference material's coefficient, for an impact along the [100] crystal orientation at 40 m$\cdot s^{-1}$. The identifiability analysis was conducted on the stress values at the integration point of elements positioned in the cross-section of the middle of the impacted sample. As future identification will be performed by comparing numerical results with experimental EBSD fields, the stress field at the integration point was then linearly interpolated on a regular square grid. A 80 × 80 grid was used for the identifiability analysis to match with the grid size used for the finite element simulation. Note that linear interpolation was chosen to remain consistent with the use of C3D8R elements.

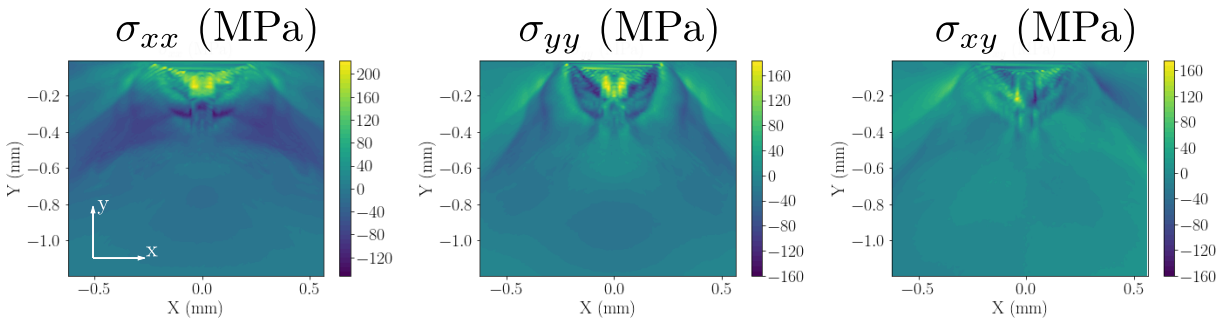

Figure 7.2 Typical stress variations under the impact dent obtained for the reference material after an impact of a shot propelled at 40 m$\cdot s^{-1}$ along the [100] crystal orientation and interpolated on a 80 × 80 regular grid. (a) σ_{xx}, (b) σ_{yy} and (c) σ_{xy} components.

The sensitivity of a given stress component σ_{ij} under the impact dent center, to a variation of parameter θ, was defined as:

$$\frac{\partial \overline{\sigma_{ij}}}{\partial \overline{\theta}}(x,y) = \frac{1}{\max(|\sigma_{ij}|)\epsilon\sqrt{N}} \left(\sigma_{ij}(\theta + \epsilon\theta, x, y) - \sigma_{ij}(\theta, x, y)\right), \tag{7.2}$$

where N is the number of sampled points on the grid taken as 6400, x and y are the 2D spatial coordinates in the cross-section plane. Note that a constant uncertainty was assumed both for the stress and shot displacement value in equations 7.1 and 7.2 as the sensitivity value was normalized by the maximum value of the field. This hypothesis is taken as only the absolute variation of the fields are of interest.

The sole analysis of the sensitivity values is not sufficient to assess that a problem solution is unique and stable. The identifiability of the identified coefficients was therefore assessed in this work by computing the identifiability index I presented in the work of Richard et al. [130], defined as:

$$I = \log_{10}\left(\frac{\lambda_{max}}{\lambda_{min}}\right), \tag{7.3}$$

where λ_{max} and λ_{min} are the eigenvalues extrema of the approximated dimensionless hessian matrix close to the cost function minimum, defined as:

$$\overline{H}_{ij} = \sum_{t=0}^{N} \frac{\partial \overline{y}(t)}{\partial \overline{\theta_i}} \frac{\partial \overline{y}(t)}{\partial \overline{\theta_j}}, \tag{7.4}$$

where N is the number of acquisition points, $\frac{\partial \overline{y}(t)}{\partial \overline{\theta_i}}$ is the sensitivity of the observation y to the parameter θ_i. According to Richard et al. [130], a value of $I < 2$ is representative of a good conditioning of the inverse problem.

Three different impact conditions were modeled to investigate the influence of impact velocity and crystal orientation on identifiability. The chosen conditions are summarized in Table 7.1

Table 7.1 Modeled impact test conditions

Test name	Crystal orientation	Shot velocity ($\mathrm{m}\cdot s^{-1}$)
Condition 1	[100]	40
Condition 2	[100]	80
Condition 3	[110]	40

7.3 Results

7.3.1 Displacement curves

Figure 7.3 (a) shows the evolution of the displacement sensitivity with respect to time when varying the coefficients K and n respectively by 5% of their initial values. The figure reveals that K and n have an opposite influence on the displacement. However, the absolute value of the sensitivity is very similar for the two variables, suggesting a strong correlation of their influence on the shot displacement. Figure 7.3 (b) shows the L_2 norm of the sensitivity for the two variables. The figure reveals that K has a much stronger influence on the displacement than n for the tested impact conditions.

The value of I was computed for different values of T, to ensure its independence on the number of acquisition points. Figure 7.4 shows the variation of I for the three test conditions as a function of the number of acquisition points. The values of I is stable and converges for a very low number of acquisition points. This results from the fact that only the slope of the displacement curve after the impact is influenced by a variation of K and n, which can be described with a low number of acquisition points.

The value of I obtained for a perturbation of 5% with an initial shot velocity of 40 $\mathrm{m}\cdot s^{-1}$ along the [100] orientation (condition 1) was $I = 3.1$. This confirms that identification using only the shot displacement curve is an ill-posed problem as the two variables have opposite but very similar effects on the displacement. The number of possible solution for K and n is therefore large when using only a single shot displacement curve.

However, the problem well-posedness could be improved by changing the test conditions such as the impact velocity or the crystal orientation. To illustrate this point, similar simulations have been performed along the [100] orientation with a velocity of 80 $\mathrm{m}\cdot s^{-1}$ (condition 2) and along the [110] orientation with a velocity of 40 $\mathrm{m}\cdot s^{-1}$ (condition 3).

Figures 7.3 (c,d) and (d,e) show the sensitivity evolution with time and the sensitivity norms for conditions 2 and 3 respectively. The figure reveals that changing the impact velocity has a higher influence on the displacement sensitivity to a variation of n than to a variation of K. Inversely, changing the crystal orientation has a higher influence on the sensitivity to a variation of K than to a variation of n.

Table 7.2 shows the values of I obtained for the three different conditions. For a constant crystal orientation (*e.g.* [100]), a higher velocity value leads to a higher value of I. This result shows that as the velocity increases, the correlation between the sensitivities of the shot displacement to K and n also increases, which has a negative impact on the identifia-

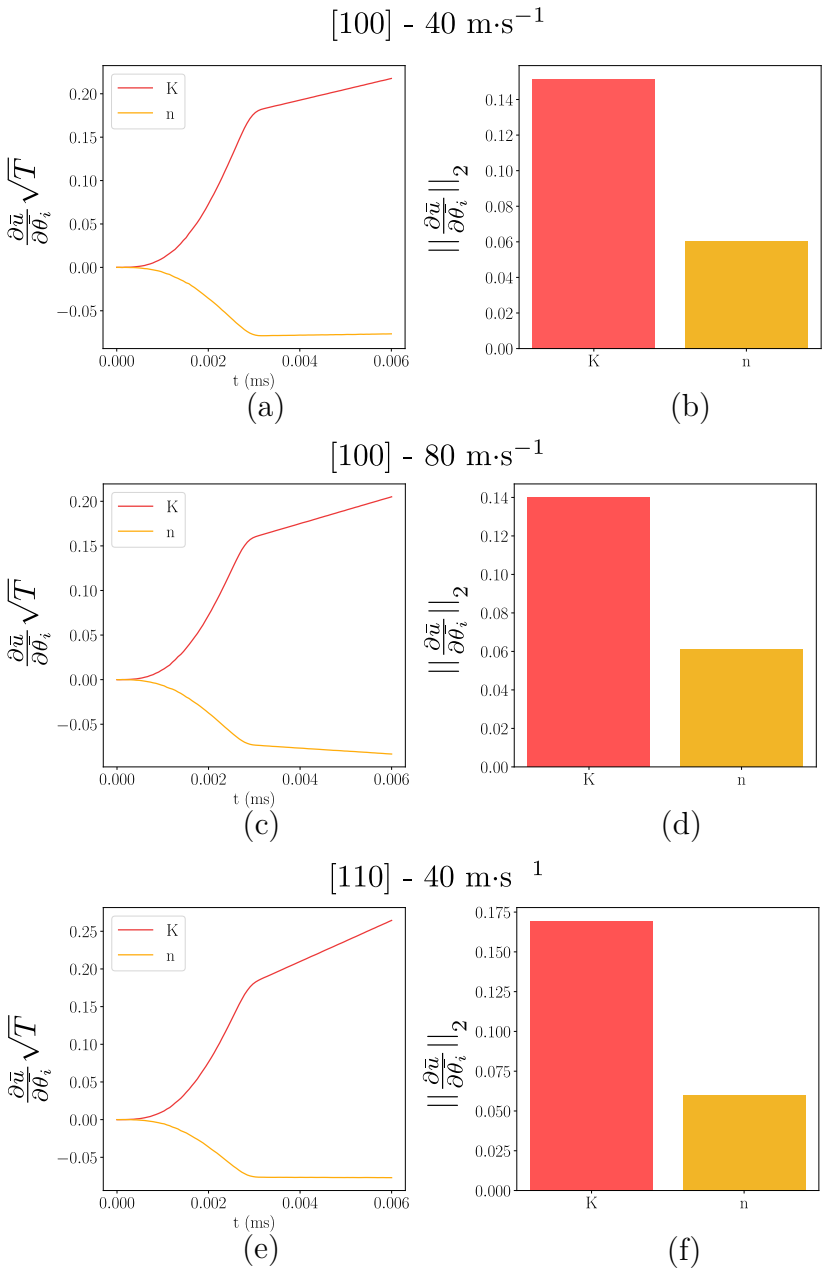

Figure 7.3 Sensitivity of the displacement to a 5% variation of K and n for a shot propelled (a,b) at 40 m·s^{-1} along the [100] orientation, (c,d) at 80 m·s^{-1} along the [100] orientation and (e,f) at 40 m·s^{-1} along the [110] orientation. (a,c,e) Evolution with respect to time of the sensitivity of the displacement to a 5% variation of K and n. (b,d,f) L_2 norm of the sensitivity variation over the whole time domain. The displacement curve is at least twice as sensitive to a variation of K than a variation of n. The two variables present a similar absolute sensitivity variation. Changing the shot velocity has a higher influence on the sensitivity to n than to that of K and inversely for the orientation.

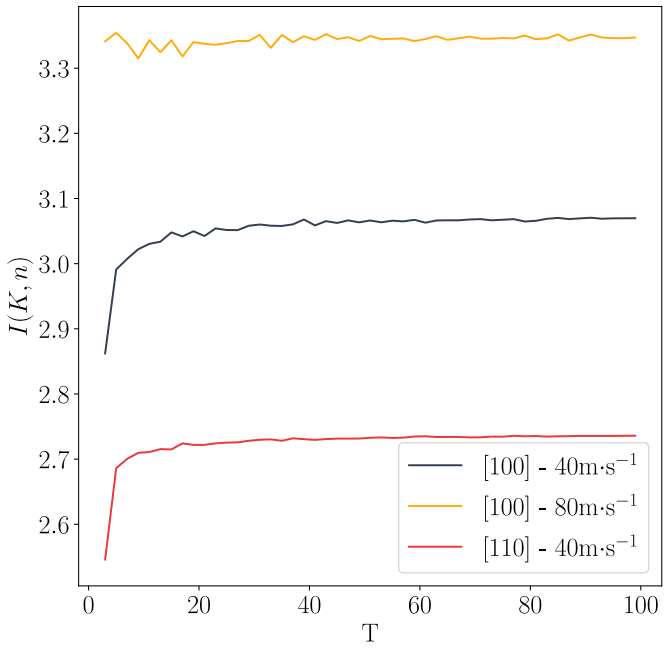

Figure 7.4 Evolution of I with the number of acquisition points. The value of I converges to a constant value for a very low number of acquisition points for the three test conditions.

Table 7.2 Values of I obtained for the three different conditions.

Velocity (m·s^{-1})	Orientation	I
40	[100]	3.1
80	[100]	3.3
40	[110]	2.7

Table 7.3 Values of I obtained for the combination of two different conditions.

	80 m·s^{-1}/[100]	40 m·s^{-1}/[110]
40 m·s^{-1}/[100]	3.0	2.7
80 m·s^{-1}/[100]		2.6

bility. Inversely, changing the orientation reduces the value of I which shows that it tends to decorelate the effect of the two variables.

To investigate the influence of the combination of two different tests on the identifiability

value, the hessian matrix was computed as:

$$\overline{H}_{ij}^{kl} = \sum_{t=0}^{T} \frac{\partial \overline{u_k}}{\partial \overline{\theta}_i}(t) \frac{\partial \overline{u_k}}{\partial \overline{\theta}_j}(t) + \sum_{t=0}^{T} \frac{\partial \overline{u_l}}{\partial \overline{\theta}_i}(t) \frac{\partial \overline{u_l}}{\partial \overline{\theta}_j}(t), \tag{7.5}$$

where u_k and u_l corresponds to the displacement obtained for two of the conditions detailed in Table 7.1. The values of I obtained when combining the three different tests two by two are presented in Table 7.3. Note that adding additional information did not result in an improvement of the identifiability in every case. The best value of I is 2.6 and is obtained when combining two different crystal orientations with two different shot velocities. However, the highest value of I obtained is not sufficiently low to lead to a well posed problem.

7.3.2 Residual stress field

Extracting relevant sensitivity information

The sensitivity of the σ_{xx} component of the stress for an impact along the [100] orientation at 40 m·s^{-1} was first considered to investigate the different treatments that should be performed on the residual stress field before using it for identifiability analyses. Indeed, as opposed to the previous section, the identifiability analysis was performed on a two dimensional field which makes the influence of numerical noise on the sensitivities correlation more difficult to evidence. Indeed, the two dimensional sensitivity variations for the two variables cannot

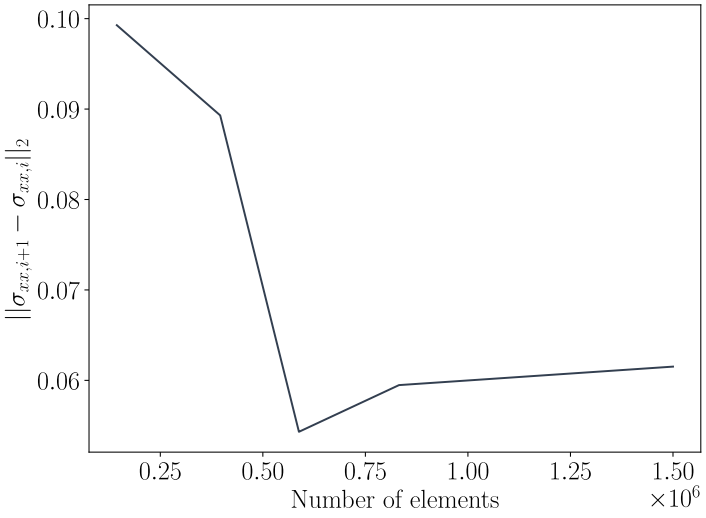

Figure 7.5 Evolution of the L_2 norm of the difference between the σ_{xx} fields obtained with two successive meshes. Convergence is observed for 832 000 elements.

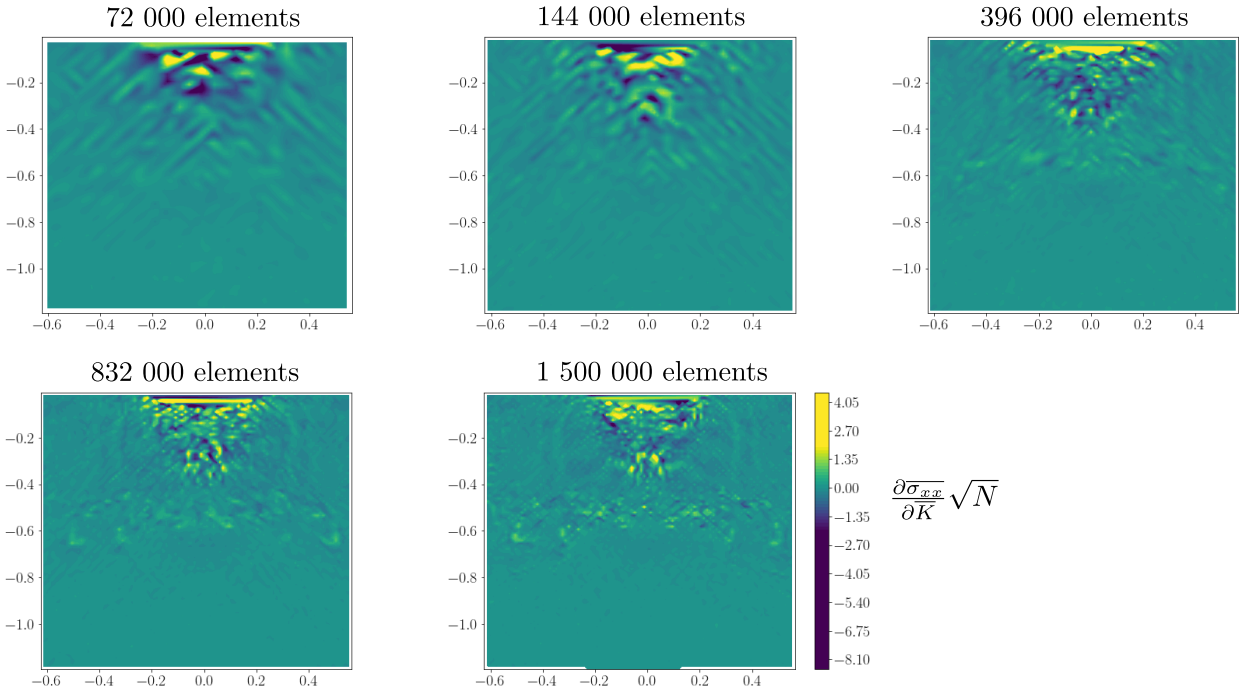

Figure 7.6 Evolution of the sensitivity of σ_{xx} to a variation K with the number of elements. The sensitivity underneath the impact dent does not converge to a consistent shape.

be superposed as in Figure 7.3 on a one dimensional plot to visually observe a potential correlation of the sensitivities.

Also, dynamic explicit analyses induce numerical uncertainties as no residual is minimized over the analysis. Such uncertainties accumulate with the time steps resulting in small erratic variations of the final field which should not be physically interpreted. This effect should be even stronger when non-linear behaviors are involved such as contact or plasticity. The influence of numerical uncertainties on the sensitivity should therefore be investigated to account only for the parts of the sensitivity field that have a physical relevance. This is not only important to assess the well-posedness of the problem but also for the identification itself to prevent the identification to be driven by numerical uncertainties that have no physical relevance.

Figure 7.5 shows the evolution of the L_2 norm of the difference in horizontal components of stress σ_{xx} between two consecutive meshes for an impact along the [100] orientation at 40 m$\cdot s^{-1}$. The figure reveals that the stress field converges for 832 000 elements, which is consistent with the convergence study performed on the shot displacement detailed in Appendix G. However the sole convergence of the stress field is not sufficient to obtain

converged sensitivity values. Figure 7.6 shows the convergence of the sensitivity of σ_{xx} to a variation of 5% of the K coefficient. The figure reveals that the sensitivity field does not seem to converge qualitatively under the dent.

Sensitivity values in this zone are highly sensitive to numerical uncertainties and convergence errors which result in noisy sensitivity variations. Using the field without masking the noisy sensitivity values under the dent would thus artificially decorrelate the influence

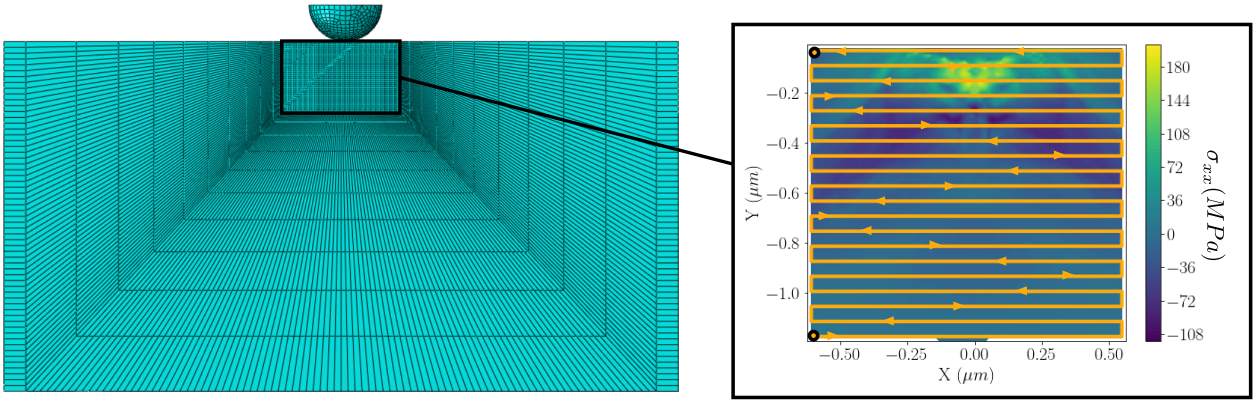

Figure 7.7 Path chosen to compute the values of I on different parts of the field. Only the refined zone of the mesh was studied as no stresses were presents on the extended mesh zone. The path is going back and forth between the left and the right side of the residual stress field and moves progressively toward the impact dent.

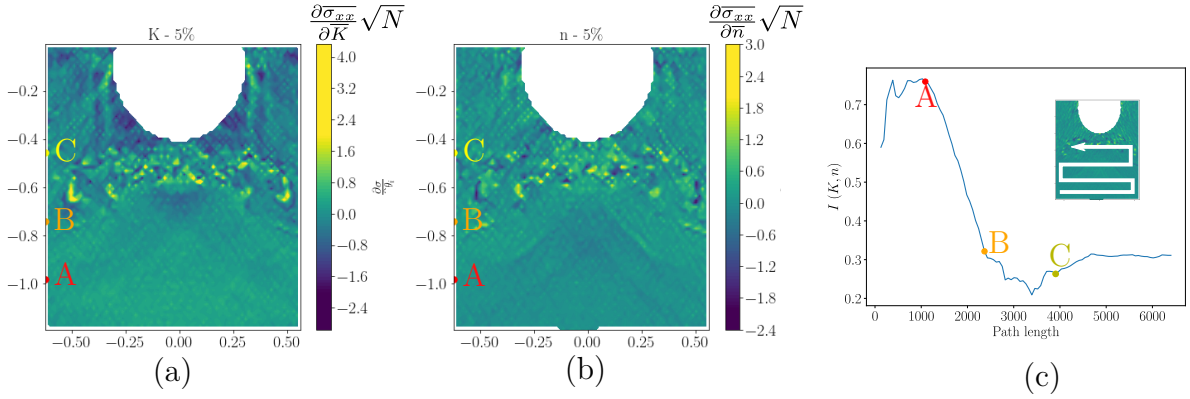

(a) (b) (c)

Figure 7.8 Sensitivity of σ_{xx} to a 5% variation of (a) K and (b) n. The two variables have a distinct influence on σ_{xx} as its sensitivity variations to K and n are not similar. (c) Evolution of the value of I computed on a path starting from the bulk and going progressively to the surface with the path length. The very low value of I results from the noisy variation of the sensitivities which artificially decorelates the influence of the two variables.

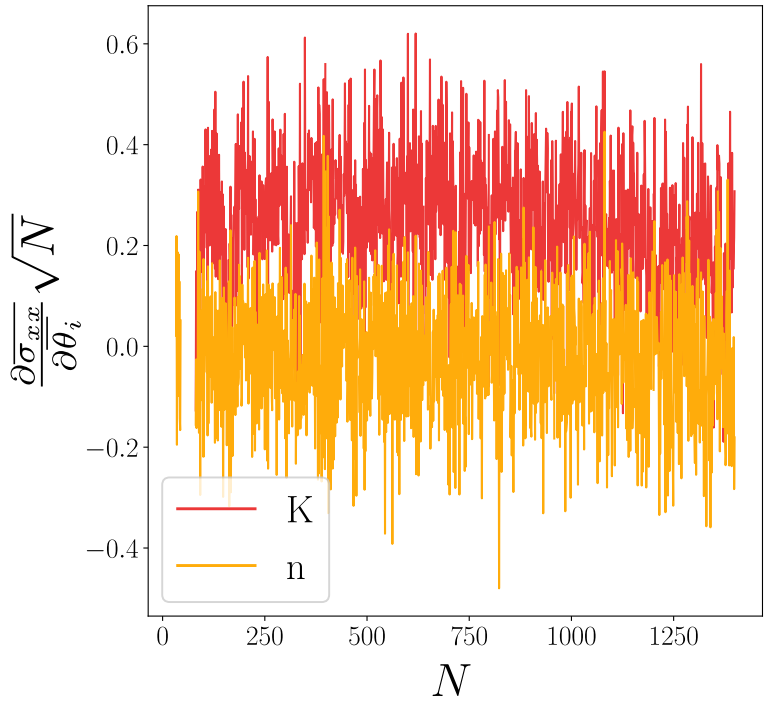

Figure 7.9 Sensitivity variation of σ_{xx} to a 5% variation of K and n on the path shown in Figure 7.7 at the bottom of the sample, up to the point A indicated in Figure 7.8. The noise on the sensitivity variation is of the same order of magnitude than the average value of the sensitivities.

of the identified coefficients on the residual stress field. Such errors could result from the explicit integration scheme, contact integration errors but also from the strong plastic strain gradients present in such zone that could not be captured with the current mesh. This zone should therefore not be used for identification of K and n as the stress variations would not entirely result from a variation of each coefficients. In the following, a spherical mask was therefore applied to the sensitivity field to exclude the zone where the sensitivity field did not converge.

To understand the influence of the different parts of the residual stress field on the identifiability, the value of I should be computed on a well chosen path that conveniently separates the different zone of interests of the field. The path chosen is represented in Figure 7.7. Only the refined zone of the mesh was studied as no stress was present in the extended mesh zone. The path is going back and forth between the left and the right side of the residual stress field and moves progressively toward the impact dent where most of the plastic deformations occurred.

The sensitivity of σ_{xx} to a variation of 5% of K and n are presented in Figure 7.8 (a) and (b). The evolution of I as the length of the path represented in Figure 7.7 increases (from

top to bottom) is presented in Figure 7.8 (c). The value of I is very low when compared to that obtained with micropillar compression curves in Chapter 5 (*e.g.* $I = 1.31$), even at the bottom of the sample where almost no plastic straining occurred.

The variations of the sensitivity at the bottom of the sample, along the path shown in Figure 7.7, up to the point A indicated in Figure 7.8, are shown in Figure 7.9. The average sensitivity to K and n are slightly different at the bottom of the sample, which could partially explain the low value of I found in this zone. However, the amplitude of the noise on the sensitivity variations are of the same order of magnitude as that of the average difference between the sensitivity of K and n. This reveals that the residual stress field is still too noisy to compute relevant values of the identifiability indicator, as this noise is sufficiently substantial to artificially decorelate the influence of the two variables.

Figures 7.10 and 7.11 show the variation of the σ_{xx} sensitivity field for different values of perturbation of K and n respectively. The figures show that the sensitivity field is relatively noisy for low values of the perturbation. This could result from the use of a dynamic explicit finite element scheme introducing numerical uncertainties of the same order as that of the sensitivity for low perturbation values.

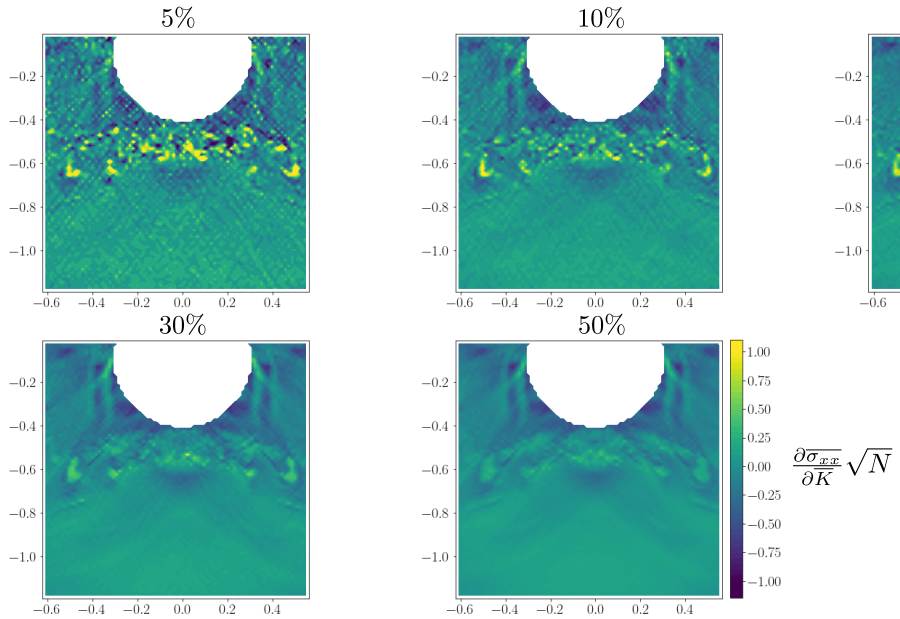

Figure 7.10 Sensitivity of σ_{xx} to a variation K for different perturbation factor (5%, 10%, 15%, 30%, 50%). The noisy variation of the sensitivity for low perturbation value result from low stress variations of the same order of magnitude than the numerical uncertainties.

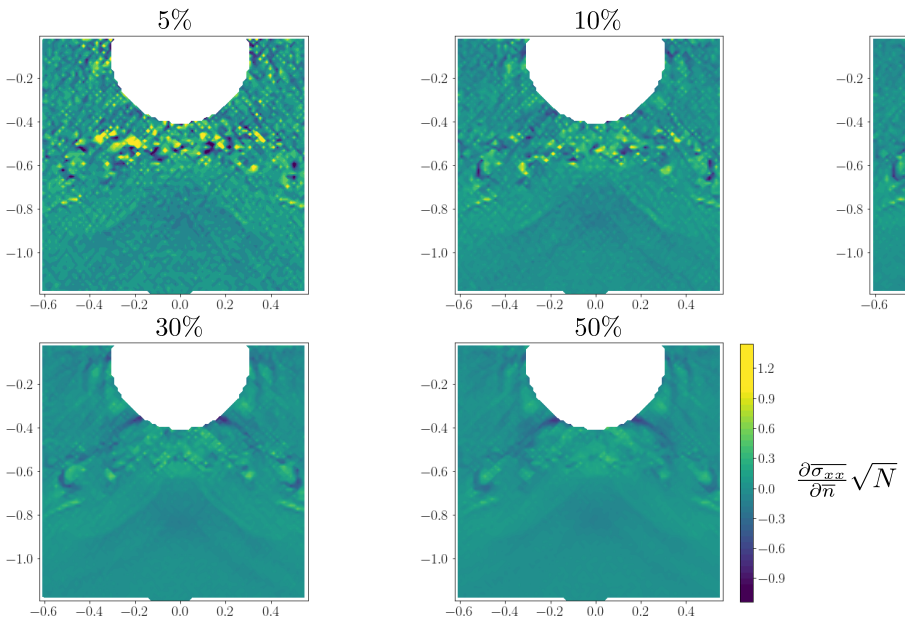

Figure 7.11 Sensitivity of σ_{xx} to a variation n for different perturbation factor (5%, 10%, 15%, 30%, 50%). The sensitivity field for the higher perturbation are different than those obtained for a perturbation of K. This confirms the low correlation of the two variable effects.

The sensitivity fields for perturbations larger than 15% also reveal that K and n have a non colinear effect on σ_{xx} as the two variables induce different sensitivity variations. However such observation does not provide enough information to state on the problem well-posedness. It only implies that the influence of the two coefficients on σ_{xx} can be differentiated but not that the information is rich enough to obtain the two coefficients values simultaneously.

To illustrate the influence of noise, a Hamming window was applied on the residual stress field Fourier transform to filter the high frequency noise [204]:

$$\omega(x_i, y_i) = \left[\left(0.54 - 0.46 * \cos\left(\frac{2\pi x_i}{\sqrt{N}-1}\right)\right)\left(0.54 - 0.46 * \cos\left(\frac{2\pi y_i}{\sqrt{N}-1}\right)\right)\right]^r, \qquad (7.6)$$

Where x_i and y_i are the discrete spatial coordinate on the field and r is a factor controlling the window radius (*e.g.* the filter bandwidth).

Figure 7.12 shows a comparison of the sensitivity of σ_{xx} to K for different perturbation values using a low pass filter with a Hamming window radius of 10. Filtering removes the differences between the high and low perturbations at least down to perturbation values of 10%. Figures 7.13 (a) and (b) show the sensitivity of σ_{xx} to K and n to a perturbation of 15%. Figure 7.13 (c) shows the variation of I on a path going from the bulk to the surface. Using the

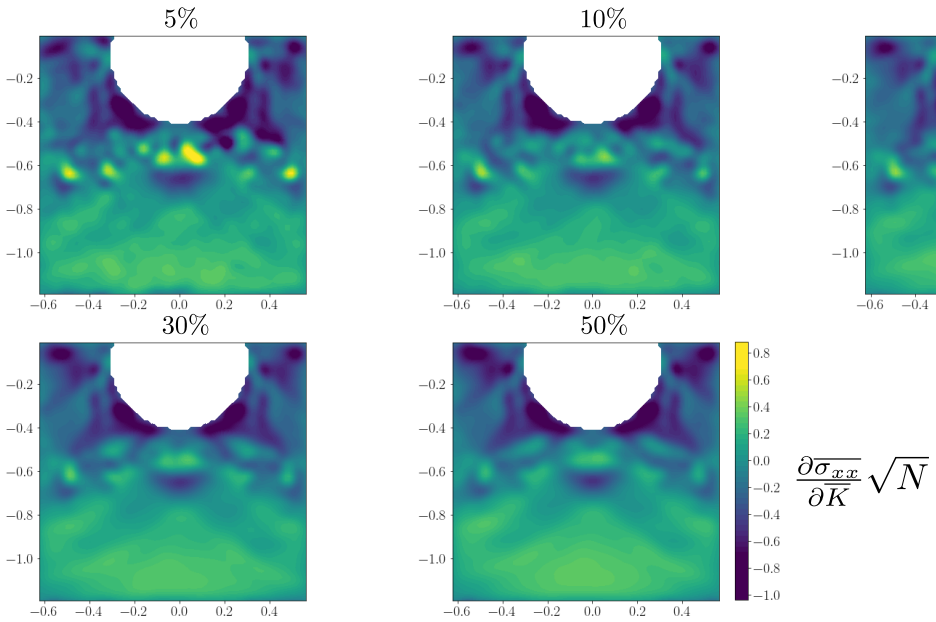

Figure 7.12 Sensitivity of σ_{xx} to a variation K for different perturbation factor (5%, 10%, 15%, 30%, 50%) after applying a low-pass filter with a radius of 10. The filter smoothened the variation of the sensitivities and removes the noise down to pertubation of 10%.

filter resulted in more believable values of I at the bottom of the field.

Up to point A, the value of I progressively rises as the sensitivity fields are almost constant in this zone but with distinct values for the two coefficients. From point A to point B, a large decrease of I is observed down to a value of 0.7. This is consistent with the variations of the sensitivity field observed in Figures 7.13 (a) and (b) as both variables seem to have a different influence on this part of the field, with similar amplitudes. Between point B and C, a small decrease of I is also observed due to higher variations of both sensitivity fields in different directions.

To assess the value of I independently of the Hamming window radius, the value of I obtained using the whole σ_{xx} field was computed for different window radius. Figure 7.14 (a) shows the evolution of I with the filter radius. The figure reveals that the value of I follows an inverse exponential tendency and saturates for a radius of 1500.

To ensure that the value of I at saturation did not result from the Fourier space resolution being too low, the value of I was computed with a filter radius of 3000 for different grid sizes. Figure 7.14 (b) shows the evolution of the value of I with the number of points on one side of the square grid. The value of I at saturation oscillates with the mesh size until 4000 points, which is a lower resolution than the finite element grid size on which the stress was

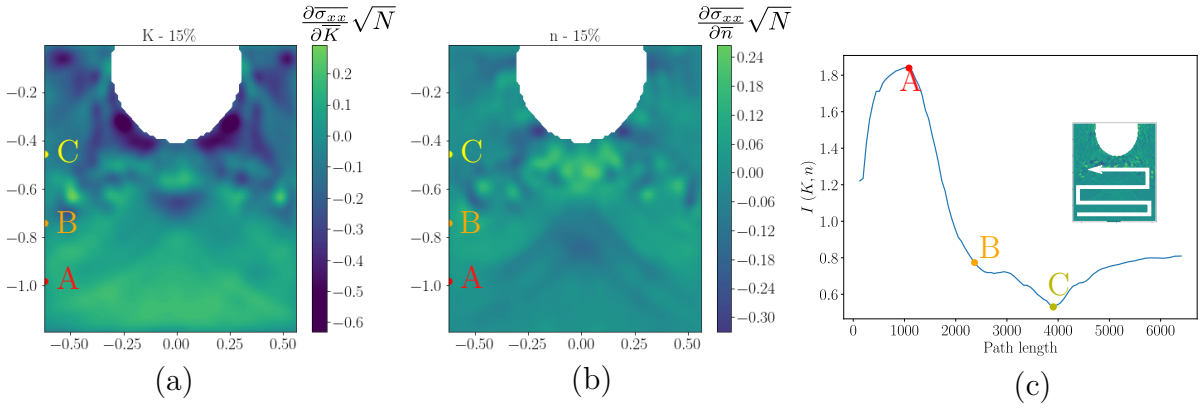

Figure 7.13 Sensitivity of σ_{xx} to a 15% variation of (a)K and (b)n after applying a low-pass filter with a radius of 10. (c) Evolution of the value of I computed on a path starting from the bulk and going progressively to the surface with the path length. The low pass filter allows to find more realistic values of I.

interpolated. Therefore the saturation of I does not result from the resolution of the Fourier

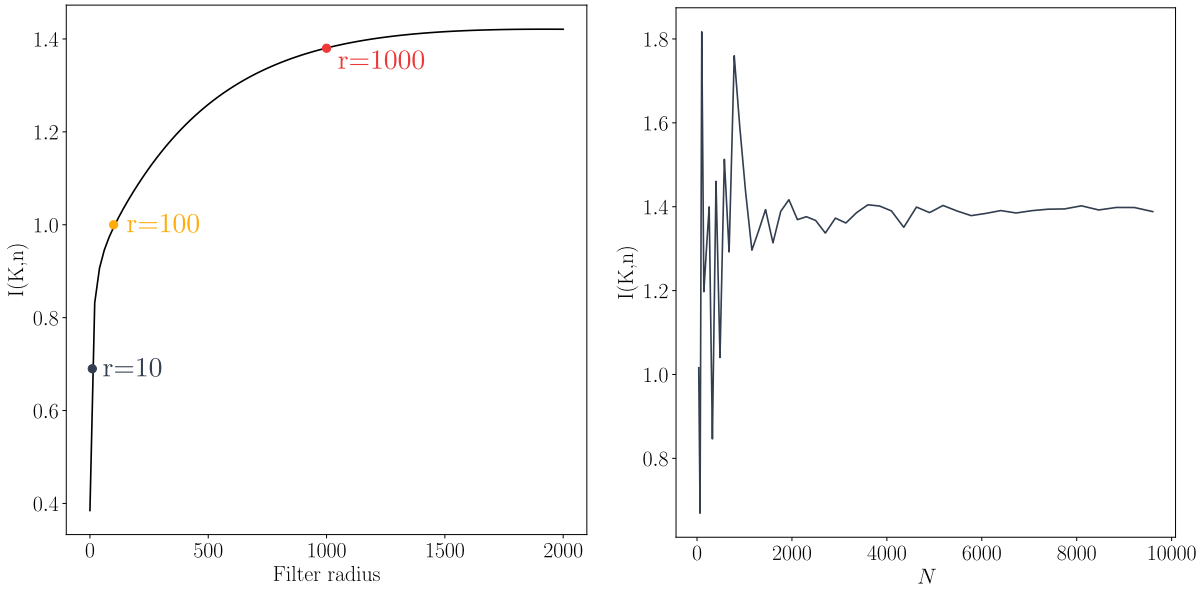

Figure 7.14 Influence of the filter on I. (a) Variation of I with the Hamming window radius. (b) Variation of I for large Hamming window radius with the grid size. For large window radius, the value of I saturates to a constant value. This constant values converges with the grid size for 50 points on one side of the grid.

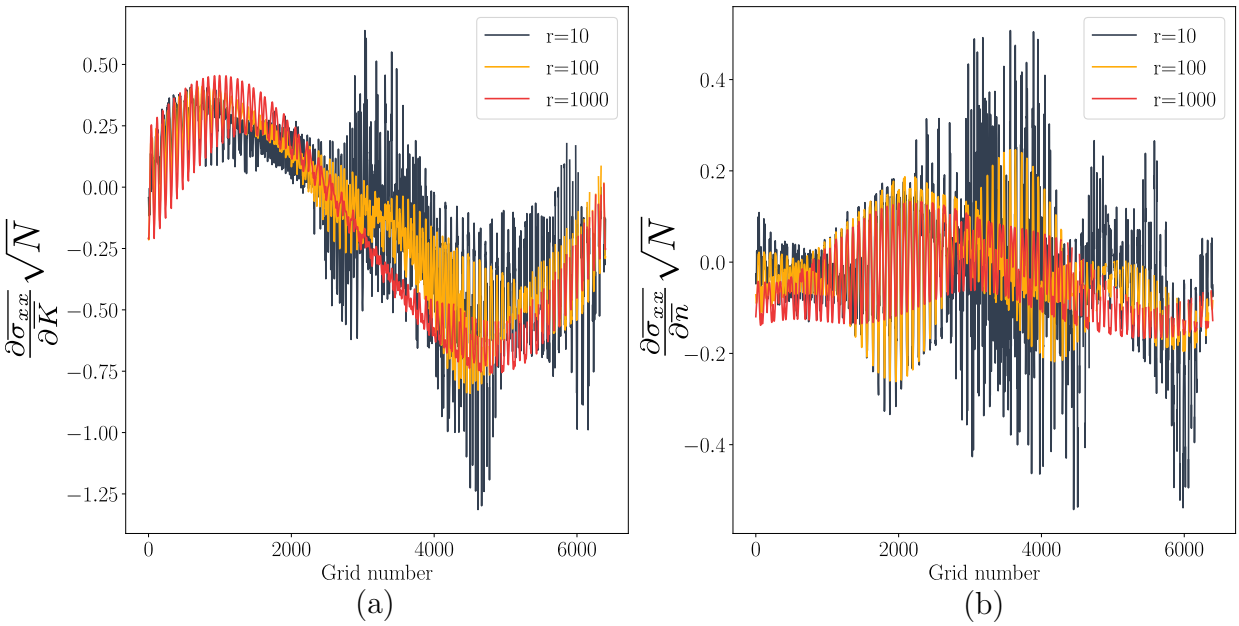

Figure 7.15 Sensitivity of σ_{xx} to a variation of (a) K and (b) n with respect to the path length for different filter radius r. The sensitivity for high filter radius represents the average sensitivity variation of the non filtered field.

space being too coarse.

Figure 7.15 shows the variation of the sensitivity to (a) K and (b) n for different window radius r on the path shown in Figure 7.8. The figure shows that the sensitivity variations obtained for a large value of r represents the average variation of the non filtered sensitivity. Therefore, the value of I is representative of the average sensitivity of σ_{xx} to K and n. The filter only removes the high frequency variations of the field and does not add spurious information. The corresponding value of I for the three filter radius are represented by color dots in Figure 7.14.

The value of I obtained for large filter radius can therefore be considered a higher boundary of the identifiability index value that can be obtained. In the following, the value of I given for the residual stress field will therefore be the value of I that saturates with the Hamming window radius.

To investigate the potential complementarity of the information provided by the shot displacement and the residual stress field, the value of I obtained when combining the two

observation fields was computed using the following expression for the hessian matrix:

$$\overline{H}_{ij} = \sum_{t=0}^{T} \frac{\partial \overline{u}}{\partial \overline{\theta}_i}(t) \frac{\partial \overline{u}}{\partial \overline{\theta}_j}(t) + \sum_{p=0}^{N} \frac{\partial \overline{\sigma_{xx}}}{\partial \overline{\theta}_i}(x_p, y_p) \frac{\partial \overline{\sigma_{xx}}}{\partial \overline{\theta}_j}(x_p, y_p). \tag{7.7}$$

Note that, in the above expression, the same weight was given to both fields as all the variables are dimensionless. The combination of the two observation fields for the same impact along the [100] orientation at 40 m·s^{-1} led to $I = 1.1$ which is slightly better than the value obtained using only the residual stress field ($I = 1.4$).

Influence of the stress component

A similar methodology was applied to study the identifiability of K and n using the other components of the residual stress field induced by an impact. As experimental residual stress estimations is to be provided by EBSD analyses, only the in-plane components of the stress tensor were investigated. Figures 7.16 and Figures 7.17 (a), (b) and (c) show respectively the sensitivity of σ_{yy} and σ_{xy} to a 15% variation of K and n and the resulting variation of I along a path. Similar conclusions as with σ_{xx} can be drawn. Also, low values of I are found at the bottom of the field resulting from large differences in the influence of the two variables on this stress component.

Table 7.4 summarizes the value of I obtained using every grid points for large values of the filter radius for the three different components. The low values of I demonstrate that each component contains sufficient information for identification of the K and n coefficients.

Table 7.5 shows the identifiability index values obtained when combining the stress components two by two using the following expression for the hessian matrix:

$$\overline{H}_{ij}^{kl,mn} = \sum_{p=0}^{N} \frac{\partial \overline{\sigma_{kl}}}{\partial \overline{\theta}_i}(x_p, y_p) \frac{\partial \overline{\sigma_{kl}}}{\partial \overline{\theta}_j}(x_p, y_p) + \sum_{p=0}^{N} \frac{\partial \overline{\sigma_{mn}}}{\partial \overline{\theta}_i}(x_p, y_p) \frac{\partial \overline{\sigma_{mn}}}{\partial \overline{\theta}_j}(x_p, y_p), \tag{7.8}$$

Combining two different components of the residual stress field only slightly enhances the identifiability index value. Finally, combining the three components resulted in $I = 1.3$ which is slightly higher than the best value of I obtained when combining two components of the stress. Thus, adding additional information for identification did not result in a better conditioning of the problem but rather diluted the relevant information.

Figure 7.18 (a,c,e) shows the variations of the sensitivity to a 15% variation of K and n on the three components of stress, respectively, on the path presented in Figure 7.7. For σ_{xx} and σ_{xy}, only small variations of the sensitivity to n are observed along the path, when

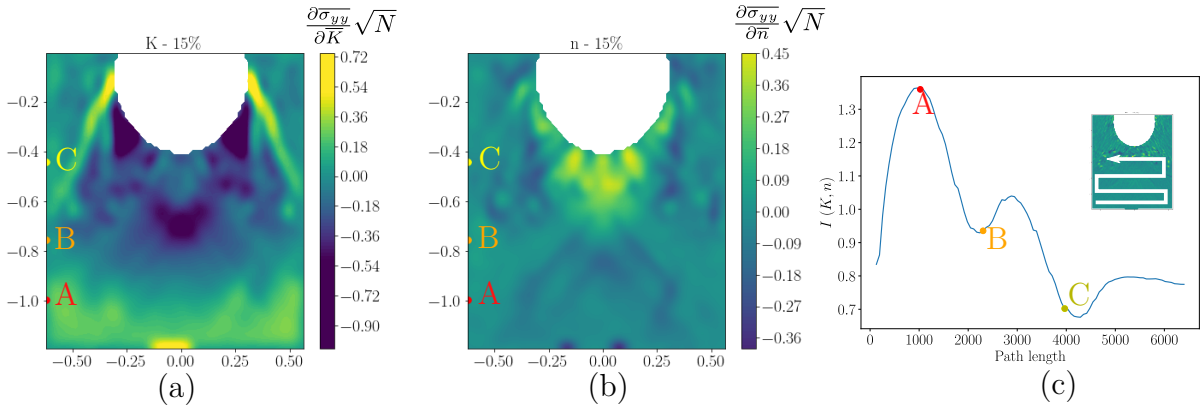

Figure 7.16 Sensitivity of σ_{yy} to a 15% variation of (a) K and (b) n after applying a low-pass filter with a radius of 10. (c) Evolution of the value of I. Similar conclusions as with σ_{xx} can be drawn.

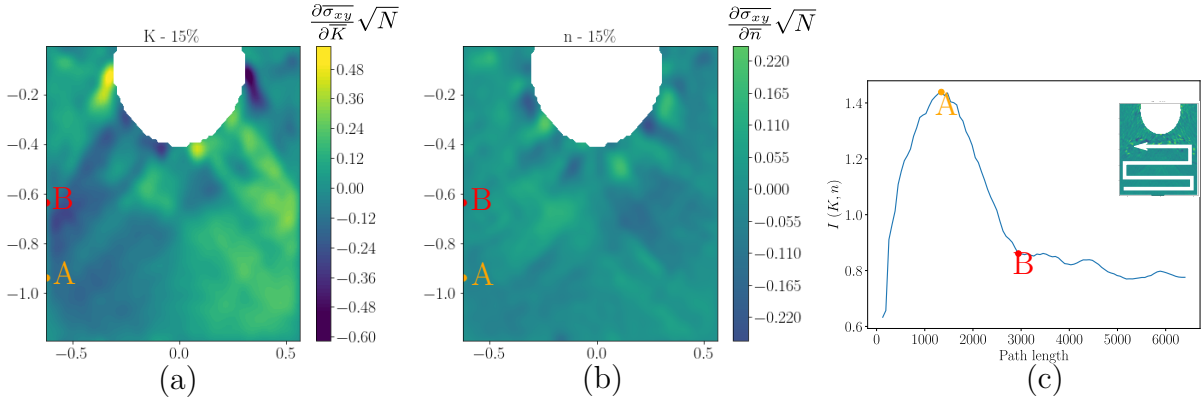

Figure 7.17 Sensitivity of σ_{xy} to a 15% variation of (a) K and (b) n after applying a low-pass filter with a radius of 10. (c) Evolution of the value of I. The variation of the sensitivity to n up to point A are very subtle. The value of I should therefore be interpreted with great care.

compared to the sensitivity to K. The sensitivity of the two variables are therefore not as firmly uncorrelated as those observed for σ_{yy} which explains the slightly better value of I found for this stress component. This also explains why combining σ_{xx} and σ_{xy} does not

Stress component	σ_{xx}	σ_{yy}	σ_{xy}
I	1.4	1.3	1.4

Table 7.4 Identifiability index values obtained for the different stress components for large Hamming window radius.

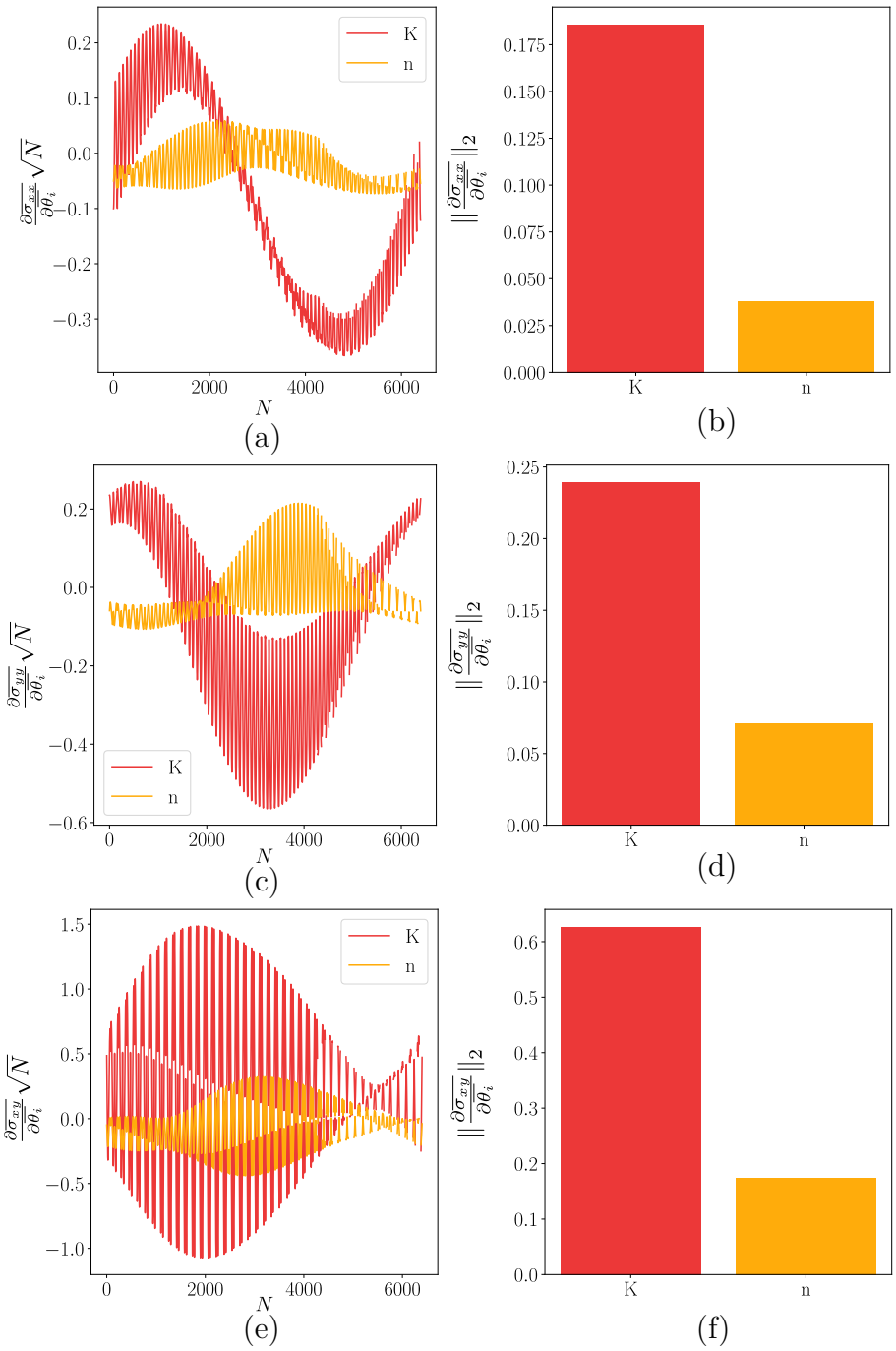

Figure 7.18 Sensitivity of the (a,b) σ_{xx}, (c,d) σ_{yy} and (e,f) σ_{xy} to a 15% variation of K and n for a shot along the [100] orientation at 40 m·s^{-1}. (a,c,e) Evolution of the sensitivity along the path represented in Figure 7.7. (b,d,f) L_2 norm of the sensitivity. For σ_{xx} and σ_{xy} only small variations of the sensitivity to n are observed along the path when compared to that of the sensitivity to K. All the components are more sensitive to a variation of K than to a variation of n.

improve the value of I as none of these components provide additional information on the influence of n.

Figure 7.18 (b,d,f) shows the value of the L_2 norm of the sensitivity for the three components of stress, respectively. All the components are at least three times more sensitive to K than to n, which further explains why different combinations of the stress components did not result in a better value of I.

Since impact along the [100] orientation and a single impact velocity seem to be sufficient to obtain the values of K and n, identifiability for different velocities and crystal orientations using the residual stress field was not investigated in this work.

7.4 Discussion

7.4.1 Identifiability using only the displacement curve

As shown in Figure 7.3, the effect of K and n can be distinguished respectively by changing the crystal orientation and the shot velocity. This results from the fact that K scales the stress. Its influence thus mainly depends on the stress value, which changes with the orientation. On the other hand, n acts mainly on the strain path. Its influence is therefore more related to the total absorbed energy.

Consequently, when combining two velocities along the same crystal orientation (conditions 1 and 2), only the total energy imposed to the material is varied. Therefore, combining those two tests only provides more information on the effect of n but not on the effect of K. Inversely, combining two different orientations with the same shot velocity only provides more information on the effect of K but not on the effect of n. Consequently, varying the two parameters simultaneously results in the best value of I (2.6) as the influence of both parameters is varied.

Also, combining two displacement curves did not result in an improvement of the value of I in every case. For instance, combining two tests at 40 m$\cdot s^{-1}$ along the [100] and [110] orientations resulted in a similar value of I as when using a single test at 40 m$\cdot s^{-1}$. This

Stress component	σ_{yy}	σ_{xy}
σ_{xx}	1.2	1.3
σ_{yy}		1.3

Table 7.5 Identifiability index values obtained for the different stress components combinations for large Hamming window radius.

reveals that no additional information is brought by adding the second test. Renner et al. [137] observed a similar phenomenon when combining two indentation imprint topographies for the identification of two parameters. In some cases, combining the two topographies resulted in a worst value of I than that obtained when using a single topography due to a dilution of the relevant information.

The value of I obtained in this work using only the displacement curve was still too high to assess the problem well-posedness. This might however be sufficient to obtain a first raw estimate of the value of (K, n) that could then be refined using another observation field, such as the residual stresses. This could be confirmed by performing identification on a virtual material using both the displacement curve and the residual stress field.

Also, combining the displacement curve with the residual stress field for the same test resulted in a lower value of I. The shot displacement is therefore an interesting complementary observation field to use for identification.

Finally, the hole space of crystal orientation and reachable shot velocity should be screened to find the most suitable conditions for identification. This will be performed in future works.

7.4.2 Identifiability using the residual stress field

Convergence of the sensitivity field in the vicinity of the dent was not achieved in this study, as shown in Figure 7.6. It is interesting to note that the noisy part of the sensitivity field corresponds to the zone where most plastic straining occurred. The more pronounced stress gradients are therefore also located in this zone. This explains the difficulty to obtain converged sensitivity values under the dent. Experimentally, large plastic strains also prevent stress estimations using HR-EBSD, as they induce noisier diffraction patterns. This zone would therefore also have to be masked on EBSD data and would therefore not be used for identification, even in the absence of numerical convergence issues.

The value of I provided in Tables 7.4 and 7.5 are those obtained by applying a low-pass filter with a large Hamming window radius on the residual stress field. Applying such filter does not add any information but removes the high frequency noise resulting from numerical uncertainties. However, it also removes parts of the field that should contain relevant information for identification as slight variation of the field could result from a variation of each parameters and not just from the quality of constitutive law integration. Such value of I should therefore be considered as a higher boundary of the identifiability index value.

Each of the three investigated components of the residual stress field contains sufficient information for identification of K and n with a single test in a single orientation with a

single shot velocity condition. Combining the different components only resulted in slight improvements of the identifiability index. This could result from the high Hamming windows radius used for filtering, which could remove parts of the specific relevant information of each field. It could also indicate that the two coefficients have a similar influence on the three components of the stress. Therefore there is no dilution of information when combining two components as each components contains relevant information for identification. However, it does not add any new information on the distinct influence of each parameter and therefore does not really improve the problem conditioning.

Also, using only the bottom of the field, the parts of the fields where the most pronounced effects occur is unused. To make better use of the whole residual stress field in future works, identification should not be performed by comparing the target and simulated field point-wise but by comparing well-chosen characteristics of the field.

The value of I found for identification of K and n using the residual stress field under the dent ranges from 1.2 to 1.4, depending on the stress component used. This is consistent with the value $I = 1.3$ found with the microcompression tests in Chapter 5. However, only a single simulation was required to achieve good values of I. As the residual stress field is a direct consequence of the plastic straining occurring during the impact event, it contains more information than a stress-strain curve which solely represents an average quantification of the material's behaviour. The value of I presented in Table 7.4 are therefore consistent with that of the literature.

The residual stress field under the impact dent therefore contains sufficient information to obtain the viscoplastic parameters with a single simulation. The resulting identification procedure would therefore be more efficient than that using micropillar compression tests as it would require less tests to be modeled. However, HR-EBSD residual stress analyses remain an experimental challenge. Indeed, it requires a perfect surface preparation with almost no subsurface residual polishing induced hardening, which could be tedious especially on ductile materials such as copper. Also, such analyses remain mainly applicable on large grains or single crystal samples as the elastic residual strain are obtained by comparing the deformed crystal volume with an undeformed reference volume inside the same grain. This study however reveals that the wealth of information provided by such residual stress fields worth the efforts spent in sample preparation.

7.5 Conclusion

The objective of this work was to investigate the possibility to obtain the viscoplastic parameters of the Meric-Cailletaud framework using outputs provided by a shot impact test. The main contributions are as follows:

- Identification of K and n using the shot displacement curve was shown to be an ill-posed problem.
- Combining two impacts along two different crystal orientations with two different shot velocities improved the problem well-posedness as it provided more information on the distinct influence of the two coefficients on the displacement, which resulted in a value of $I = 2.6$.
- A methodology to establish identifiability of the Meric-Cailletaud constitutive parameters using the residual stress field under the impact dent was established.
- Analysis of the stress sensitivity to a variation of K an n and the resulting values of $I = 1.2$ when combining two stress components revealed that the two coefficients could be identified using the residual stress induced by a single impact on a single crystal orientation.
- Combining the residual stress field with its corresponding displacement curve reduced the value of I from $I = 1.4$ when using only the residual stress field to $I = 1.1$. The two observations fields are therefore complementary.

Using the residual stress field induced by an impact could therefore provide a methodology for identification of material parameters at high strain rate as the strain rates involved by such impact could reach the order of 10^5 s^{-1}. Such parameters could then be used for modeling of processes involving such strain rates such as shot-peening.

However, the value of I presented in this study using the residual stress field are only higher boundary of the potential identifiability index. Therefore further analyses should be conducted by considering relevant descriptors of the residual stress field rather than using a point-wise comparison of the perturbed field with a reference one. This could for instance be performed by automatically extracting the field characteristic using image segmentation methods [205].

Also, identification on a virtual material with chosen coefficients will be conducted in future works to assess the convergence of classical optimization algorithm on the solution using

different starting points. This will effectively validate the identifiability analysis presented herein.

Finally the possibility to obtain the K and n parameters using only the shot displacement curve is very promising as it is very easy to obtain experimentally. The whole crystal orientation and reachable shot velocity space will therefore be screened to chose the experimental conditions that maximizes identifiability in future works.

CHAPTER 8

Conclusion

8.1 Summary

This work laid the first bricks toward the prediction of shot-peening induced intragranular residual stress. Each of the presented chapters contributed to one or several of the initial objectives:

- **New evidences of the relevance of modeling the process at the crystal scale were provided**: Chapter 3 revealed a strong influence of crystal orientation on the induced residual stress state at the grain scale. In particular, it revealed that spherical indentation in particular orientations could induce subsurface tensile residual stresses. Chapter 4 further emphasized the importance of accounting for microstructural evolution when modeling the process, especially for the treatment of complex geometries.
- **Methodologies were detailed for constitutive parameters identification at the local scale under process conditions**: in Chapter 5, a complete methodology for local parameter identification at high strain rate using micropillar compression was detailed. Since the methodology could not provide data for strain rates encountered in shot-peening, a shot-peening canon was developed as presented in Chapter 6 to perform controlled impact under various conditions. A methodology to retrieve the shot trajectory as accurately as possible was developed and its accuracy was thoroughly characterized. Chapter 7 confirmed that the propelled shot could generate sufficient

data for parameter identification. This chapter also confirmed the relevance of identifying the strain rate dependent parameters K and n as it revealed that the residual stress field was sensitive to their variation.

- **Tools for constitutive behavior validation were developed**: The comparison between residual stresses obtained by HR-EBSD estimations and CPFE simulations presented in Chapter 3 confirmed the possibility to compare numerically predicted stresses with HR-EBSD estimations for model validation. Also, various tools developed in the litterature for EBSD analysis such as dictionary indexing as presented in Chapter 4, or the NLPAR filter detailed in Chapter 2, could provide more accurate EBSD observations when large plastic deformations are present. The resulting rotation field or GND variations (using for instance the depth of the plastically deformed zone) could also be used for validation. Finally, the good correspondance between the displacement curves, the impact dent topography and the rotation field numerically predicted and obtained with the shot peening canon, as presented in Chapter 6, confirmed that it would be an excellent tool for model validation under process conditions. In particular, the position uncertainty provided by the reprojection error of the shot trajectory reconstruction procedure could allow to account for experimental uncertainty in the validation process.

Therefore, even though a complete methodology for intragranular stress prediction could not be developed in the frame of a single doctoral project, several contributions were brought to every aspects of the future methodology. Also, the many surprises encountered through the different sub-projects paved the way for future interesting researches in indirectly related domains.

8.2 Perspectives

The work presented herein faced several limitations that could represent interesting challenges for future researches.

First, the high strain rate micropillar experiments performed in this study were performed at the Ecole des Mines de Saint-Etienne for the first time. Given the preliminary results presented in Chapter 5, the following subjects could be investigated:

- Tests with different pillar size under different strain rate exhibited a dependence of the size effect with the strain rate. This dependency could be investigates by performing a more thorough study on a larger number of pillars under different strain rates

and crystal orientation with different pillar size. The induced dislocation structures could also be investigated using transmission electron microscopy (TEM) to identify the underlying deformation mechanisms.

- The stress/strain curves obtained under different strain rates for different orientations revealed an anisotropy of the strain rate dependency that could not be reproduced using the Meric-Cailletaud framework. Such anisotropy could be investigated on different materials by performing micropillar compression up to different strain amplitudes, strain rates, crystal orientations and analyzing the resulting load displacement curve, deformed pillar shapes and dislocation structure observed with a TEM.
- Finally, the highest reachable strain rate could be increased by positioning the load sensor under the tip, or using two smart tip sensor both for load sensing and actuation.

The shot peening test rig presented in Chapter 6 was also entirely developed during the project through an active collaboration with the Mëkanic company. The following improvements could however still be performed on the setup:

- The overall quality of the reconstructed shot trajectory could be improved by: improving the lighting, increasing the camera shooting frequency or by developing a more robust shot detection code based on feature extraction techniques. For that purpose, the shot reconstruction trajectory code was made fully open source and documented and is open for improvement.
- The impact dent geometry could be directly reconstructed by DIC using the stereomicroscope positioned on the setup. This would provide another observation field that could be used both for model validation or constitutive parameter identification. This could be investigated using a similar methodology as that provided in chapter 7.

Residual stress field induced by impacts could not effectively be used in this project for parameter identification or validation. However, Chapter 7 revealed that (i) the residual stress field was sensitive to the strain rate dependency parameters and (ii) those parameters had an uncorrelated influence on the residual stress field, which could make their identification possible. The following subject could therefore be investigated:

- Investigate the identifiability of all the Meric-Cailletaud constitutive parameters using the residual stress field.

- Develop a sample preparation methodology to perform HR-EBSD measurements on single crystal copper specimens or perform impact tests on alternative materials such as nickel single crystals.
- Perform identification of the strain rate dependent coefficients using the residual stress field induced under an impact for a virtual material and on experimental estimations using HR-EBSD to confirm the relevance of the good indentifiability index values obtained in the present work.
- Investigate the identifiability of the Meric-Cailletaud framework on the residual stress field obtained induced by an impact performed along every crystal orientation by mapping the indentifiability index on an inverse pole figure to obtain the optimal experimental conditions for identification.

APPENDIX A COMPARISON OF DESTRUCTIVE RESIDUAL STRESS ESTIMATION METHODS

	Ortner method	Micro-Laue diffraction	HR-EBSD
Spatial resolution	a few dozen μm to a few mm	hundreds of nm	hundreds of nm
Probed depth	a few dozen μm	a few dozen μm	a few dozen nm
Elastic strain uncertainty	-	$4.5\ 10^{-5}$ [98]	$1\ 10^{-4}$ [156, 206]
Stress estimation uncertainty	30 Mpa from experimental parameters measurements (diffraction angles...) 150 MPa from in depth stress gradient [95]	200 MPa on a dual phased alloy [96]	30 MPa relative stress if the PC is accurately know [207]
Drawbacks	• Requires around twenty non collinear diffraction conditions • Large probed depth inducing bias • Requires a reference state • Plane stress assumption	• Innacurate for severe plastic deformation (diffraction peaks asterisms) • Requires a synchrotron	• Requires perfect surface preparation • Plane stress assumption • Requires a reference point • Experimental parameters uncertainties (pattern center, tilt angle) • Pattern distortion [208] • Large acquisition time • Observation field limited to a few hundreds μm

APPENDIX B EFFECT OF CRYSTAL INDENTATION ON THE RESIDUAL STRESS FIELD

Convergence study

Global mesh convergence

This work mainly focused on spherical indentation-induced residual stress fields. Particular attention was given to the tensile residual stress quantity. Mesh size convergence was therefore based on the volume fraction of element with a positive first stress invariant, f_t.

Simulations were performed with eight different substrate mesh sizes. The total number of elements ranged from 20 277 to 280 277.

Figure B.1 shows the evolution of f_t with the total number of elements for an indentation in the crystal's [001] direction and with an angle $\beta = 0°$ (see Figure 5.3). The value of f_t stabilizes around 13 % for 66 517 elements. Evolution with the mesh density of the tensile stress volume fraction computed using the three axial stress components is shown in Figure B.2. It further confirms the residual stress field convergence for each stress components. Also the stress profile taken along z=0 at a depth of 40 μm is represented in Figure B.3 for different mesh densities. This results reveals that the stress variations seem only to converge around 114 518 elements. Simulations in this work were therefore performed with this mesh density. This corresponds to 28 μm sized elements in Zone A (Figure 5.3). Convergence found for these conditions was assumed to hold for any other crystal orientations.

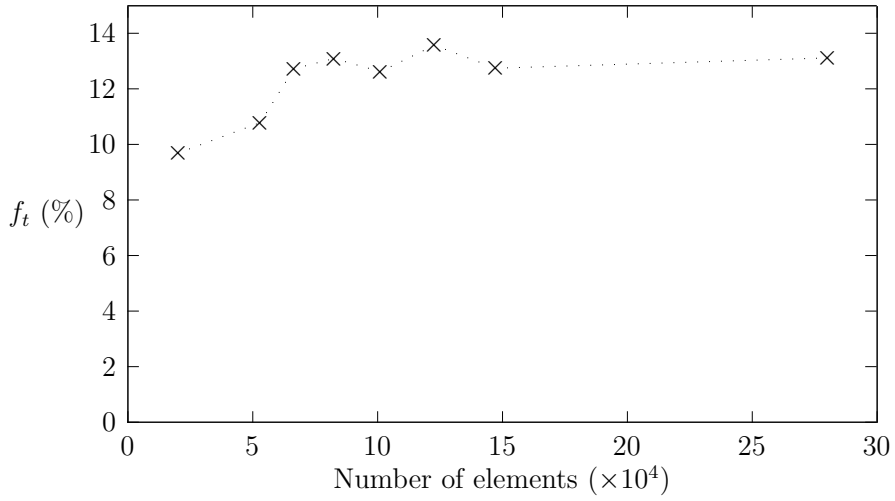

Figure B.1 Evolution of f_t with the number of elements. Indentation was performed in the crystal's [001] direction and with an angle $\beta = 0°$ (see Figure 5.3). Convergence found for these conditions was assumed to hold for any other crystal orientations. Convergence of f_t to a value of approximately 13 % is observed for a total of 66 517 elements.

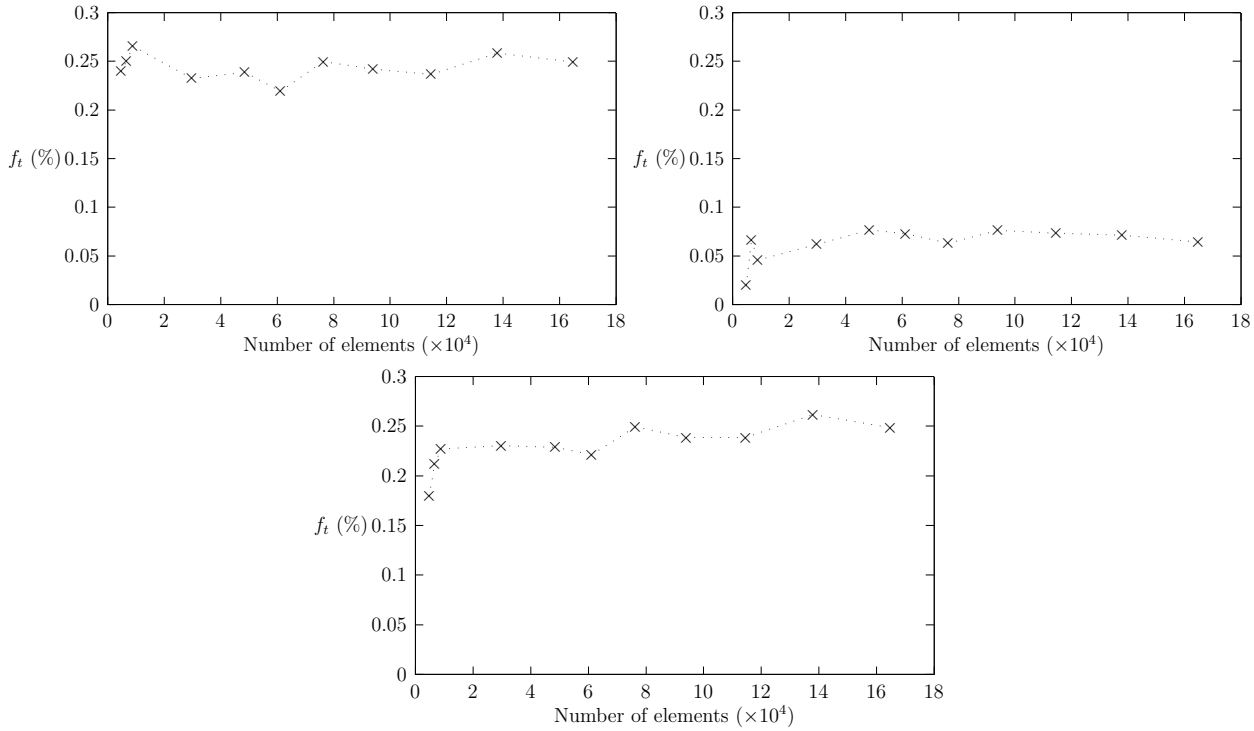

Figure B.2 Evolution of f_t, computed using (a) σ_{xx}, (b) σ_{yy} and (c) σ_{zz} with the number of elements. Indentation was performed in the crystal's [001] direction and with an angle $\beta = 0°$ (see Figure 5.3). Convergence found for these conditions was assumed to hold for any other crystal orientations. These figures confirms the previous converged element size for each stress components

Indenter mesh

A convergence study on the indenter mesh size was performed to remove the indenter mesh influence on the predicted residual stress and misorientation fields. The indenter being asymmetrically meshed (with respect to the sample symmetry axes), low indenter mesh density in the contact zone lead to asymmetric fields. Convergence was therefore assessed by characterizing the residual stress field symmetry in the (x,y) plane at z=0 at several depths y using an error criteria defined as:

$$\epsilon_y = \frac{2}{N_y} \sum_{i=0}^{N_y/2} \left(\frac{\sigma(x_i) - \sigma(x_{N-i})}{\underset{i}{max}(\sigma_i)} \right)^2 , \tag{B.1}$$

where N_y is the number of data point at depth y.

Evolution of ϵ_y with mesh density at different depths is presented in Figure B.4. It reveals that the indenter mesh has indeed an influence on the field symmetry for low mesh densities. The indenter was meshed with 15 040 elements to reduce this influence.

Border dimensions Border effects can induce local variations of the residual stress field,

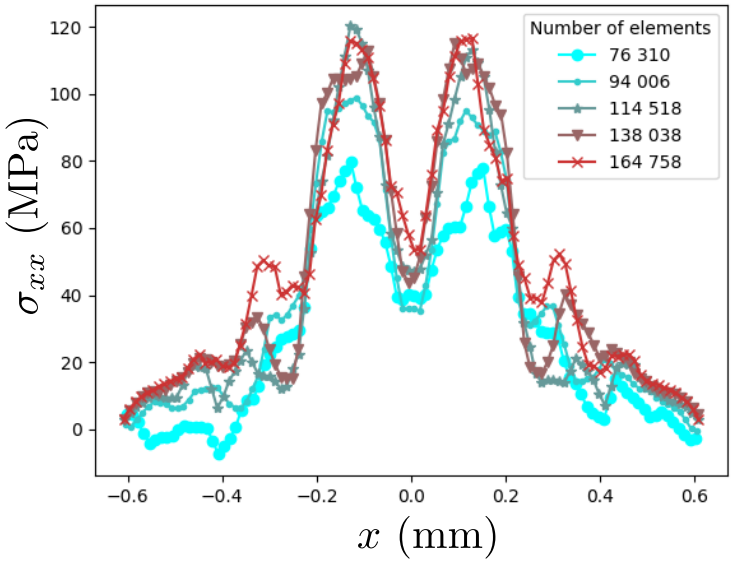

Figure B.3 Evolution of the stress profile along z=0 at a depth of 40μm with the mesh density. Convergence of the profile can qualitatively be observed for a similar mesh density as previously. This confirms the convergence of the residual stress field

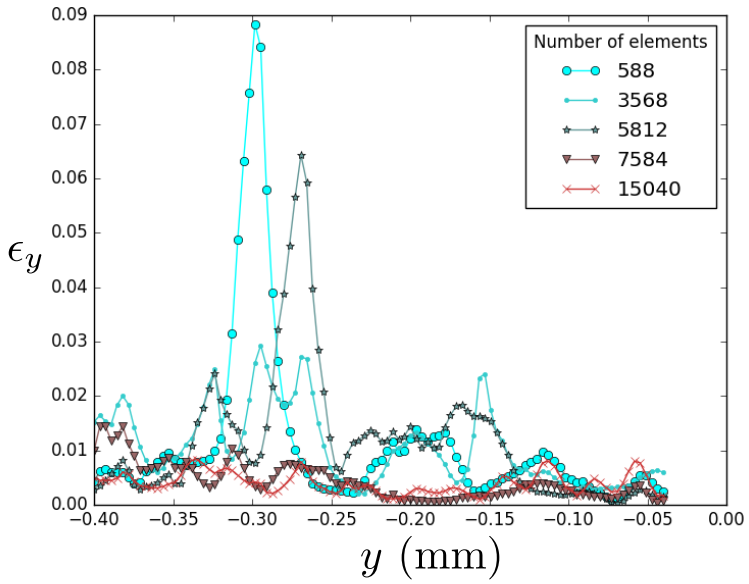

Figure B.4 Evolution of the residual stress field dissimetry ϵ_y with the indenter mesh density at several depth y. Indenter mesh density on the field symmetry can be observed for low mesh densities.

depending on Zone B (Figure 5.3) relative size to the contact radius. The value of f_t was therefore computed with three different border sizes b, corresponding respectively to 1, 2 or 3 times the Zone A dimension $\frac{R}{2}$.

Figure B.5 shows the evolution of f_t with Zone B to Zone A dimension ratio $\frac{2b}{R}$. Border influence on the value of f_t is observed for low Zone B dimension values. Convergence can however be observed for borders twice larger than the refined zone.

Results sensitivity to friction

Most CPFE studies on single crystal indentation modeled the contact as frictionless [145, 148, 209, 210]. However, according to Marteau et al. [211], friction coefficient influence has been observed in the litterature when modelling spherical indentation. According to their review, the friction coefficient can have an influence on the pile-up quantity and very locally, on strains and stresses distribution, for low indentation depths.

Friction coefficient influence on the value of f_t was therefore studied. Three simulations were performed using different friction coefficients ranging from 0 to 0.4.

Figure B.6 shows the evolution of f_t with the friction coefficient. A slight decrease is observed for higher friction (9% of the frictionless value). Contact was therefore modelled as frictionless in this study.

Inverse Pole Figure construction

Face-centered cubic crystal orientation can be described by three vectors, corresponding to the three rotated crystal axes. The orientation of one axis can be described by its spherical coordinate angles α and ϕ (as shown in Figure B.7(a)). One point on the IPF represents the projection of the crystal vertical axis y (aligned with the indentation direction) on the

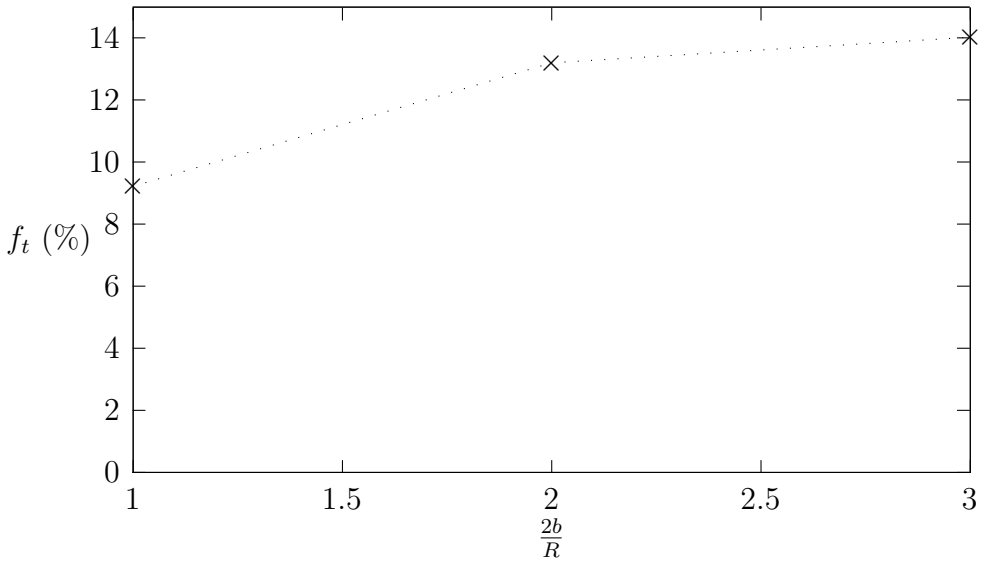

Figure B.5 Evolution of f_t with Zone B to Zone A dimension ratio $\frac{2b}{R}$. Stabilization of the value of f_t can be observed for borders twice larger than the refined zone.

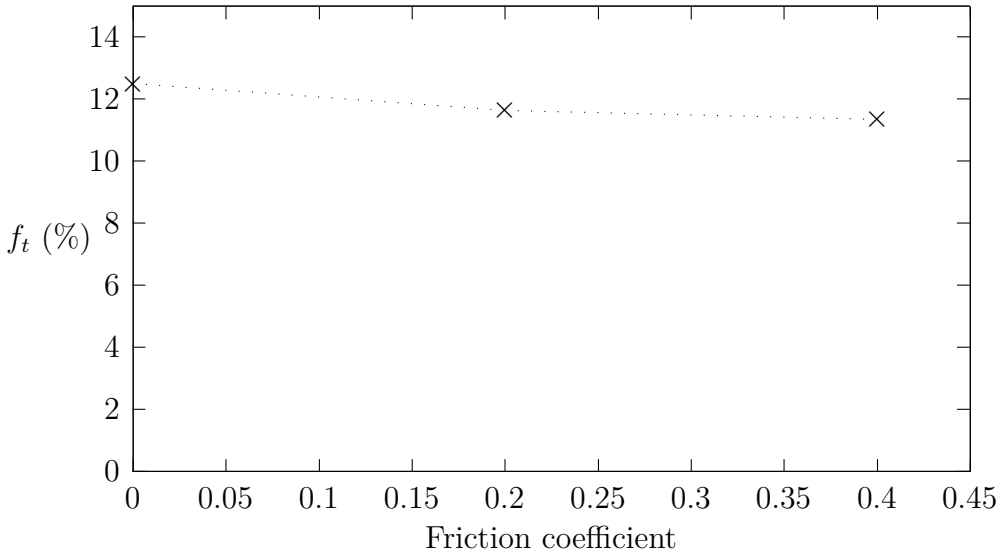

Figure B.6 Evolution of f_t with the static friction coefficient value. A slight decrease (9 % of the frictionless value) is observed for high friction coefficients. Variation of f_t with friction is therefore considered negligible.

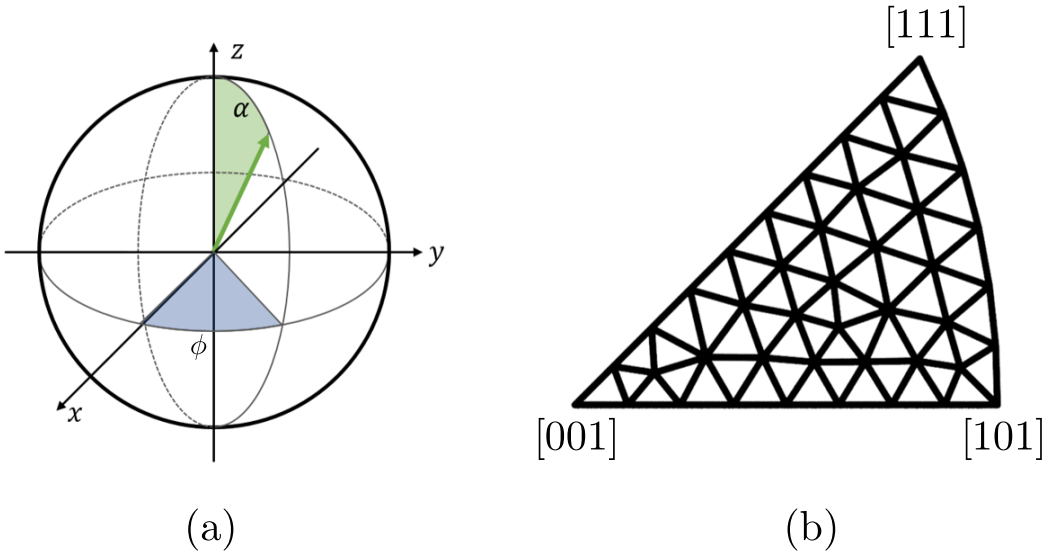

Figure B.7 (a) Representation of a vector's (green arrow) spherical coordinate angles α and ϕ. A point on an Inverse Pole Figure (IPF) corresponds to the projection of the green vector on the hemispherical plane. Its coordinates on the IPF can be expressed using α and ϕ. (b) Mesh used to generate the IPF. Each of the 43 nodes represents the crystal orientation axis aligned with the indentation axis.

hemispherical plane of the unit sphere. The second crystal axis x is chosen using spherical coordinates $\alpha_x = \alpha_y + \pi/2$ and $\phi_x = \phi_y$, so that the third vector always remains in the hemispherical plane.

Considering the face centered cubic crystal symmetry, covering the whole IPF therefore allows to describe all possible crystal orientations. Simulated orientations were chosen by meshing the IPF with tetrahedral elements, using gmsh software [212], so as to cover the whole domain as homogeneously as possible. The chosen mesh is represented on Figure B.7(b). Each node of the mesh represents a simulated indentation direction.

APPENDIX C HIGH STRAIN RATE MICRO-COMPRESSION FOR CRYSTAL PLASTICITY CONSTITUTIVE LAW PARAMETERS IDENTIFICATION

Model geometry convergence study

The substrate geometry dimensions h_{sub} and R_{sub} were chosen so that the influence of the boundary conditions on the stress-strain curve was negligible. Both dimensions of the substrate were therefore successively varied. The convergence criterion for the substrate geometry was chosen as:

$$\epsilon_{substrate}(h_{sub,i}, R_{sub,i}) = \frac{1}{T}\sum_{t=0}^{T}\left(\frac{\sigma_{conv}(\varepsilon(t)) - \sigma_{h_{sub,i},R_{sub,i}}(\varepsilon(t))}{max(\sigma_{conv})}\right)^2, \tag{C.1}$$

where σ_{conv} is the stress obtained using h_{sub}=20 μm and R_{sub}=20 μm and $\sigma_{h_{sub,i},R_{sub,i}}$ the stress obtained for $h_{sub,i}$ and $R_{sub,i}$ substrate dimensions.

Figure C.1 shows the evolution of ϵ with the variation of (a) the sample radius size and (b) the sample height. The substrate dimensions were chosen as h_{sub}=15 μm and R_{sub}=10 μm.

Mesh density convergence study

The pillar mesh size was varied to assure that the computed stress-strain curve was indepen-

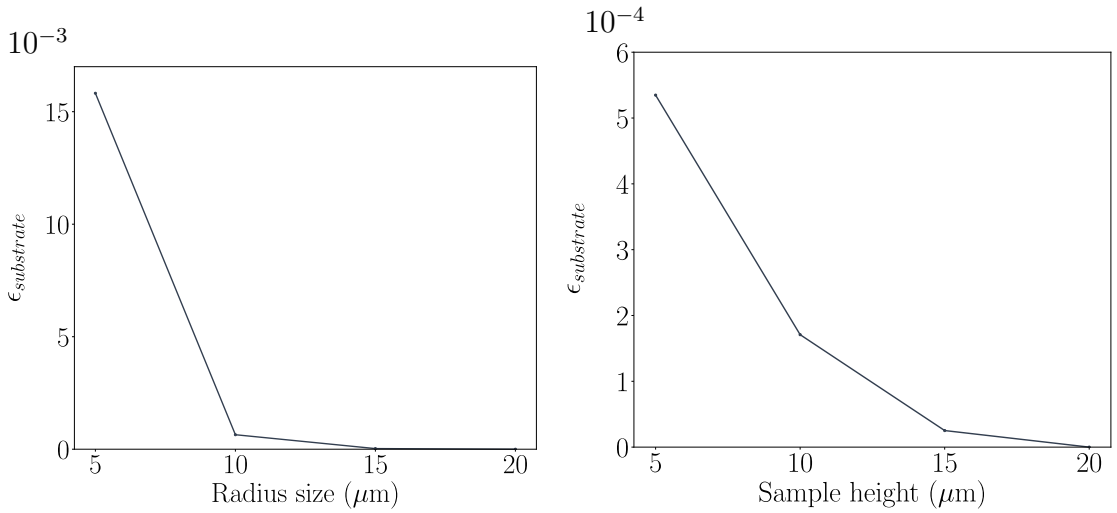

(a) (b)

Figure C.1 stress-strain curve error evolution with (a) the sample radius size and (b) the sample height. Negligible effect of the boundary conditions were found for h_{sub}=15 μm and R_{sub}=10 μm.

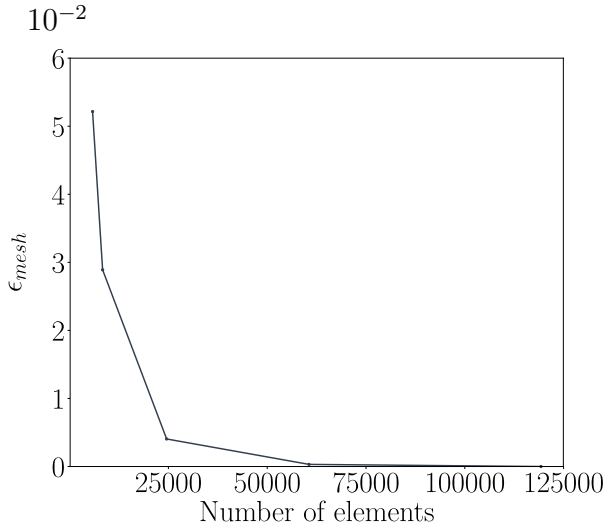

Figure C.2 Stress-strain curve sensitivity as a function of mesh size. Convergence can be observed for more than 25 000 elements.

dent of the number of elements. As previously, the convergence criteria was chosen as:

$$\epsilon_{mesh}(N_{el}) = \frac{1}{T}\sum_{t=0}^{T}\left(\frac{\sigma_{conv}(\varepsilon(t)) - \sigma_{N_{el}}(\varepsilon(t))}{max(\sigma_{conv})}\right)^2, \tag{C.2}$$

where N_{el} is the number of elements and σ_{conv} is the stress obtained for 119 264 elements. Convergence was considered attained for 24 556 elements.

Influence of friction

As the friction coefficient between the indenter and the pillar surface is very difficult to assess experimentally, a sensitivity analysis of the stress-strain curve to the friction coefficient was conducted. The stress-strain curve sensitivity to the friction coefficient was computed as:

$$\epsilon_{friction}(\mu_s) = \frac{1}{T}\sum_{t=0}^{T}\left(\frac{\sigma_{conv}(\varepsilon(t)) - \sigma_{\mu_s}(\varepsilon(t))}{max(\sigma_{conv})}\right)^2, \tag{C.3}$$

where σ_{conv} is the stress obtained a friction coefficient μ_s=0.3.

Figure C.3 shows the variation of ϵ with the friction coefficient. As reported in the literature [77, 81], the effect of the friction coefficient on the stress-strain curve is negligible. However, the absence of friction induces a very different behaviour as it generally leads to pillar buckling. In the present study the friction coefficient was therefore taken as μ_s=0.2, as pillar buckling is obtained numerically below this value and as no buckling was observed experimentally.

Size effects

Size effects were investigated to assure that the microcompression stress-strain curve obtained did not depend on the chosen pillar size. Pillars with three different diameters (3 μm, 6 μm

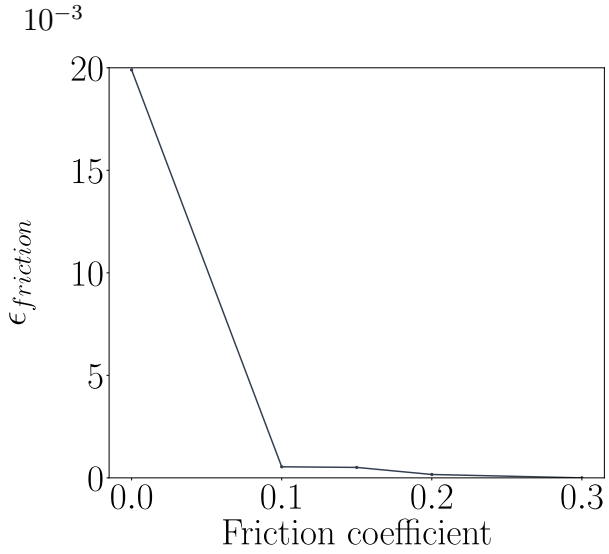

Figure C.3 Stress-strain curve sensitivity to the friction coefficient between the indenter and the pillar surface. Negligible influence of the coefficient value was found for values greater than 0.1.

and 8 μm) were compressed in the [110] orientation at low (10^{-2} s^{-1}) and high (10^{2} s^{-1}) strain rates to also investigate the compression rate influence on the potential size effects.

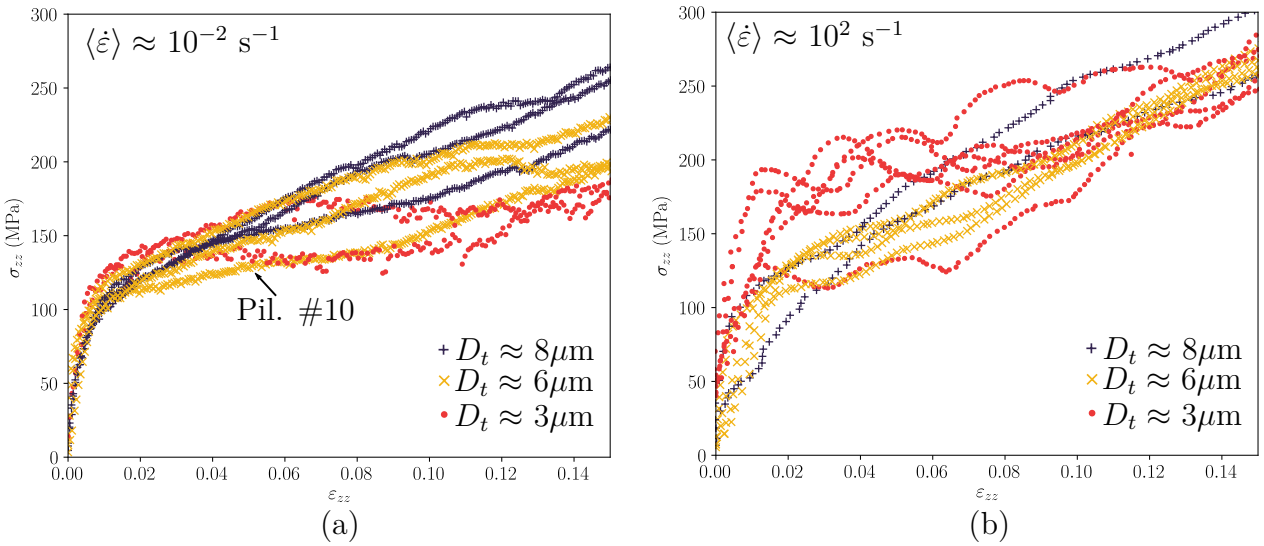

Figure C.4 Microcompression stress-strain curves for [110]-oriented pillars with 3,6 and 8 μm top diameters compressed at average strain-rates of (a) 10^{-2} s^{-1} and (b) 10^{2} s^{-1}. At low strain rate, smaller pillars presented an almost perfectly plastic behaviour. At high strain rates, a 'smaller is stronger' effect was observed in most cases.

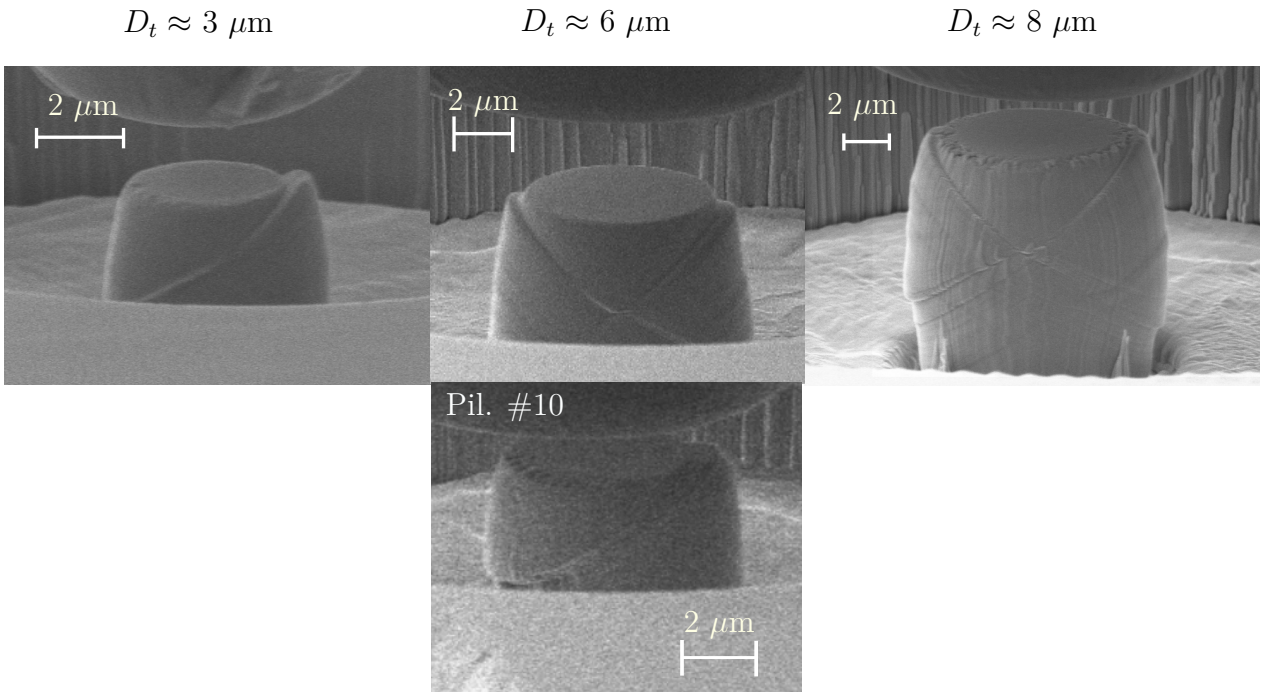

Figure C.5 3 μm, 6 μm and 8 μm diameter pillars deformed shape after quasi-static compression in the [110] crystal orientation. Every 3 μm pillars presented a single slip band pattern. The 6 μm and 8 μm pillars exhibited double slip patterns only, except for the 6 μm diameter pillar #10.

The [110] orientation was chosen as fewer slip systems are activated when compressing in this orientation as compared with [100] and [111]. It is therefore more prone to starvation size effects. Figure C.4 shows the stress-strain curved obtained.

At low strain rates, 3 μm pillars presented a much lower hardening at the onset of plasticity than the bigger pillars. In overall, the 6 μm and 8 μm pillars presented similar hardening behaviours (except for 6 μm pillar #10 at low strain-rates).

To better understand the differences in hardening behaviour, the deformed shape of the pillars were considered. Figure C.5 presents the pillars deformed shapes associated to each curves at low strain rates. Most 3 μm pillars experienced the formation of a single slip band. Inversely, 6 μm and 8 μm pillars presented a double-slip behaviour. One of the three 6 μm pillar presented a single slip band. It corresponds to the only 6 μm pillar which presented only little hardening at the onset of plasticity at low strain rate (see Figure C.4).

Such differences in strain localization behaviour was already observed, experimentally and numerically, for smaller pillars by Kiener et al. [82]. According to the authors, for smaller pillar sizes, the initial dislocation densities for each gliding systems are not evenly distributed. This results in strain localization in systems where dislocation density is the highest. This induces a reverse size effect on the stress-strain curve.

Interestingly, at high strain rates, 3 μm pillars presented an overall stiffer behaviour as the bigger pillars. This could be related to a change in plasticity mechanism as the strain rate

increases. Hu et al. [213] performed Discrete Dislocation Dynamics simulation of micropillar compression of submicronic copper pillars at different strain rates. According to the authors, at low strain rates, plasticity is driven by dislocation nucleation at sources. At higher strain rates, it is mainly driven by surface dislocation nucleation.However the strain rates amplitude used by the authors were higher and the pillar sizes were smaller than those used in this study. Also, validating such an assumption would require more tests to be conducted, owing to the statistical nature of dislocation distribution at this length scale. It is therefore beyond the scope of this study.

In the following, pillars presenting single slip in the studied orientation were not considered, as their strain mechanisms was not representative of the grain scale. Also, only 6 μm and 8 μm pillars were considered.

Single element simulation material parameter identification

To show the influence of the micropillar strain-rate enhancing structural effect developed in Section 5.3.1, the pillar was alternatively modeled as a single linear reduced hexaedric element (*e.g.* with a single integration point). Periodic boundary conditions were applied on the element faces. The experimental strain ε_{zz}, computed as:

$$\varepsilon_{zz} = \frac{u}{h_0}, \tag{C.4}$$

was imposed at the unique integration point. In Equation C.4, u and h_0 are respectively the experimental pillar displacement and the initial pillar height. This first approach was entirely modeled using the Z-set 8.6 software suite.

The inverse identification was performed on virtual data generated using the full pillar geometry model with $K = 7$ and $n = 4$. Figure C.6 shows the cost function Ψ_σ variations with coefficients K and n close to the virtual material solution. The figure reveals that the solution found by the identification procedure using a single element is very far from the chosen virtual material parameters. A factor two was found between the virtual material coefficients and the identified solution. Also, the cost function is stretched horizontally revealing a poor solution uniqueness.

To understand this bias induced by the identification procedure, single element simulations were performed with $K = 7$ and $n = 4$. Figure C.7 compares the numerical stress-strain curves obtained with the virtual material full-pillar geometry and the single-element simulations, using the [100] crystal orientation, at (a) $\langle\dot{\varepsilon}\rangle = 1$ s^{-1} and (b) $\langle\dot{\varepsilon}\rangle = 10^3$ s^{-1}.

The single element simulation did not capture the strain-rate sensitivity observed using the full-pillar geometry. When using this model for identification, it therefore resulted in a very different solution than that expected. Such differences in the strain-rate sensitivity can be explained by a structural effect, as a single element simulation cannot account for the high strain rate concentration in the shear bands evidenced in Section 5.3.1.

High strain rate internal heat generation

The potential influence of internal heat generation in the pillar during high strain rate plastic straining on the measured mechanical properties was investigated. Heat generation during plastic straining in a material could be estimated using the coupled mechanical heat conduc-

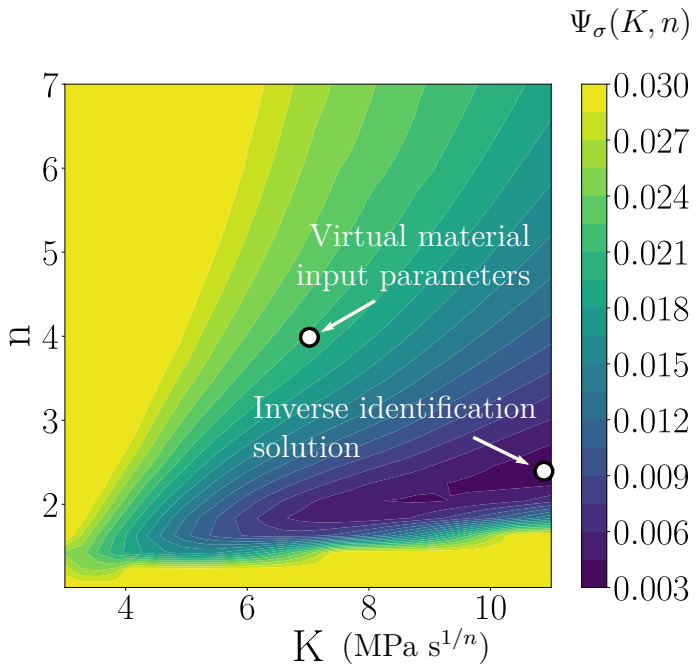

Figure C.6 Cost function Ψ_σ variation near the virtual material parameters, when performing identification of the K and n coefficients using the single element model. The identification solution was far from the virtual material parameters.

tion equation given as [44]:

$$\rho C_p \frac{\partial T}{\partial t} = div(k\nabla T) + \beta(\sigma : \dot{\varepsilon}^p), \tag{C.5}$$

where C_p is the specific heat taken as 386 10^6 mm^2 s^{-2} K^{-1}, ρ is the material's density chosen as 8.96 $10^{-6} kg\ mm^{-3}$ for copper, T is the temperature, k is the thermal conductivity coefficient, β is a material constant and $\dot{\varepsilon}^p$ is the plastic strain rate.

Assuming that all plastic straining is converted into heat ($\beta = 1$) [214] and that, in the worst case, no conduction occurs the expected temperature derivatives would be of the order of $10^4 K s^{-1}$ for $\dot{\varepsilon} = 10^2\ s^{-1}$. The quickest tests performed in the present study lasting at most 4.8 ms, the expected temperature raise in the pillar should not exceed 48 K. Internal heat generation should therefore not have any influence on the tested material mechanical properties for the investigated strain rates.

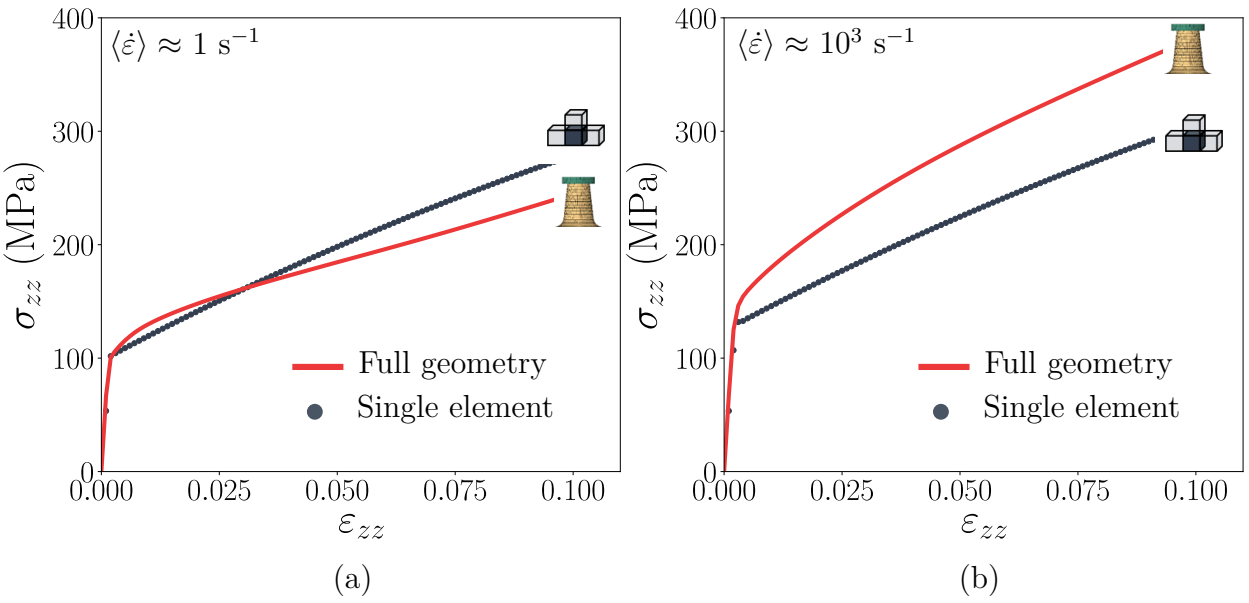

Figure C.7 Comparison of the numerical stress-strain curves obtained with the virtual material full-pillar geometry and the single-element simulations, using the [100] crystal orientation, at (a) $\langle\dot{\varepsilon}\rangle \approx 1\ \mathrm{s}^{-1}$ and (b) $\langle\dot{\varepsilon}\rangle \approx 10^3\ \mathrm{s}^{-1}$. The strain was computed using Equation C.4. The single element simulation presented a lower strain-rate sensitivity than when the whole pillar was modeled.

APPENDIX D VALIDATION OF THE SHOT TRAJECTORY ESTIMATION CODE

To validate the shot trajectory estimation code, the Blender open source 3D software [187] was used to model shot trajectories seen by two cameras. The benefit of using blender is that every experimental uncertainty can be accounted for:

- Cameras' relative position can be varied.
- Each camera's focal length and distortion parameters can be varied.
- The lighting and shot material can be chosen to account for the effect of light reflection on the shot on the detection algorithm.
- Everything can be controlled by a python code for automatic testing during the code implementation.

A script was implemented to generate chessboard calibration pictures for each camera and shot pictures with a given shot trajectory. The script can be found on github [215].

The two cameras were positioned within a distance similar to that of the experimental set-up, which was evaluated by manually measuring the distance in the laboratory. Two different trajectories were tested to assess the script performances: (i) A straight line along the Y direction and (ii) a linear variation of the three coordinates simultaneously. The first test is a basic test allowing to assess the code robustness when no perspective effects have to be accounted for. The second test assess the accuracy of the code when perspective is present.

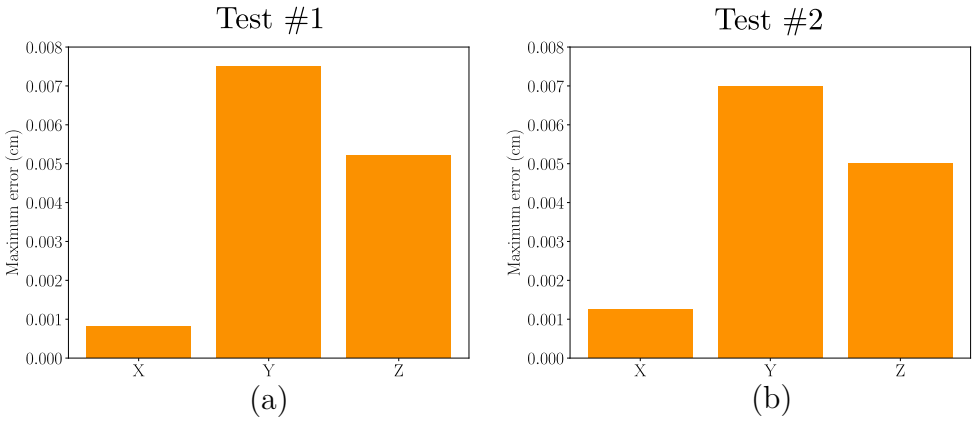

Figure D.1 Maximum error on each of the three shot coordinates using the calibration procedure detailed in Section 6.2.2 for (a) test #1 (variation of a single coordinate) and (b) test #2 (simultaneous variation of the three coordinates). In an ideal case the code can recover the shot 3D trajectory within a 70 μm accuracy. The error does not seem to vary with the amount of perspective.

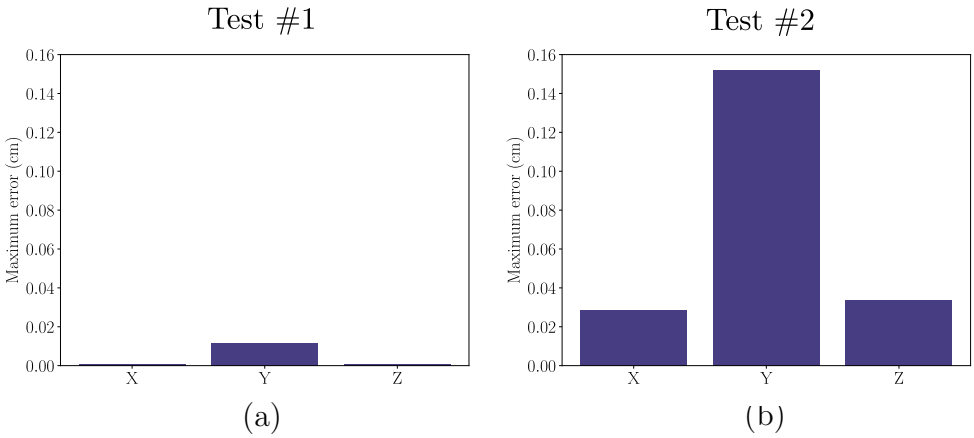

Figure D.2 Maximum error on each of the three shot coordinates by simply using the camera pixel to centimeter ratio without accounting for perspective for the (a) test #1 and (b) test #2 detailed previously. When the perspective effect is important, the error can reach up to 1.5 mm. The methodology detailed in Section 6.2.2 is therefore 22 times more accurate than this simpler approach.

Figure D.1 (a) and (b) show the maximum error made by the calibration procedure on test #1 and #2 respectively. The figure shows that the procedure can recover the shot position within a 70 μm accuracy in the ideal case set up in blender. More importantly, it reveals that the procedure is almost insensitive to perspective effects, which validates the code implementation.

To better assess the relevance of the proposed procedure, the test was also conducted using a simpler approach. This second approach consisted of recovering the shot trajectory by taking the shot position in pixel on the camera and multiplying it by a pixel to centimeter ratio obtained by taking a picture of a ruler positioned at the camera focal point. This second approach does therefore not account for any perspective.

Figure D.2 (a) and (b) show the maximum error obtained using this simplified approach on test #1 and #2 respectively.

It reveals that not accounting for perspective could lead to errors up to 1.5 mm even in an ideal case where the cameras are perfectly positioned.

In an ideal case, the calibration procedure detailed in Section 6.2.2 is therefore 22 times more accurate than if the perspective was not accounted for.

APPENDIX E SINGLE CRYSTAL COPPER PREPARATION FOR HR-EBSD OBSERVATIONS

Sample preparation for HR-EBSD observations is a critical task as such analysis requires a mirror-surface finish with as least polishing-induced hardening as possible. Indeed, the diffraction patterns should vary as little as possible to capture the small variations induced by local residual stresses. Also, the surface has to be mirror-finished with the smallest rugosity possible and no surface pollution to obtain sufficient diffracting conditions to get several orders of the diffraction bands. Indeed, the more detailed the pattern, the easier and the more accurate the cross-correlation will be.

Copper is a very ductile material. It is therefore very easy to scratch and often deforms when mechanically polished. Also, surface smearing could cover scratches induced by previous polishing steps. It is therefore difficult to assess whether the surface is well-polished or not using optical microscopy, as residual scratches can be hidden under the surface.

A very direct way to obtain satisfactory surface preparation of copper for EBSD is to use electropolishing as it does not require any mechanical action [141]. However, electropolishing induces surface topography. For HR-EBSD observations, the observed surface has to be completely flat to easily retrieve the sample to detector distance.

Alternative polishing method were therefore investigated in this study. Although those methods were not sufficient for residual stress estimation, they produced very satisfying results in terms of metallographic quality and are therefore detailed herein to serve as a strong basis for future copper sample preparation.

Two different methods were investigated during this work: (i) Mechanical polishing and (ii) Ion beam polishing.

Mechanical polishing

To reduce the sample deformations during polishing and get the most repeatable result, the samples were coated in an Methyl-Methacrylate Cold Mounting Resin 605 (Lamplan). Alternatively, Epoxy resins were also investigated as the 605 resins exhibited a pronounced shrinking during reticulation, leaving to much space between the sample's surface and the resin.

Since the objective of the study is to observe the microstructural evolution induced at the center of the impact induced dent, a methodology had to be detailed to measure the removed sample height through each polishing steps to reach the exact dent center at the end of the polishing. Before coating, the impact dents position on the sample was measured using a binocular to estimate the sample height that should be removed through grinding, as well as the dent position on the sample. After coating, the samples were then fixed on a special sample holder which can be mounted on a binocular table such that the sample is always observed at the same 3D position, as shown in Figure E.1. Before each polishing step, the focusing distance required to see the sample surface clearly is measured. The difference of focusing distance between each steps therefore gives a good estimate of the removed sample

height.

First, SiC paper P600 steps are performed with a 20 N load until only 300 μm are left to remove. The 150 μ are removed using P1200 paper with a 20 N load. Those first steps allows to get closer to the imprint but induces to much rugosity to observe its apparition as the imprints were not really deep. Therefore the sample is then polished using a MD-Largo composite disc with a 9 μm diamond suspension with a 20 N load until the distance to the imprint center is estimated to be less than 50 μm. Those first step are performed using an automatic polishing machine which head is equipped with an extensometer to estimate the polished height to ensure progressive polishing steps.

Note that there is not a unique relation between the papers abrasion rate and the polished material as it also depends on the paper wear rate and initial rugosity distribution. The observed abrasion rate are however given in Figure E.2 as an indication.

Finishing steps are then performed using 3 μm diamond suspension using an MD-MOL woven wool with a 20 N load then 1 μm diamond suspension using an MD-NAP fabric with a 10 N load ensuring to remove for each granulometry at least three times the height corresponding to the previous polishing step granulometry.

To reveal potential scratches induced by smearing, the sample is then successively chemically attacked using an $FeCl_3$ solution and repolished using a 1 μm diamond suspension until no residual scratches are observed. Finally residual hardening induced by the last polishing step is progressively removed using a vibromet with a half-diluted OP-S standard fumed silicat suspension. During this step, the sample has to be observed at least every 30 minutes as an oxydation reaction could happen inducing an "orange peel" aspect of the surface. The longer the vibromet step, the more likely this reaction could happen. However, the longer the step,

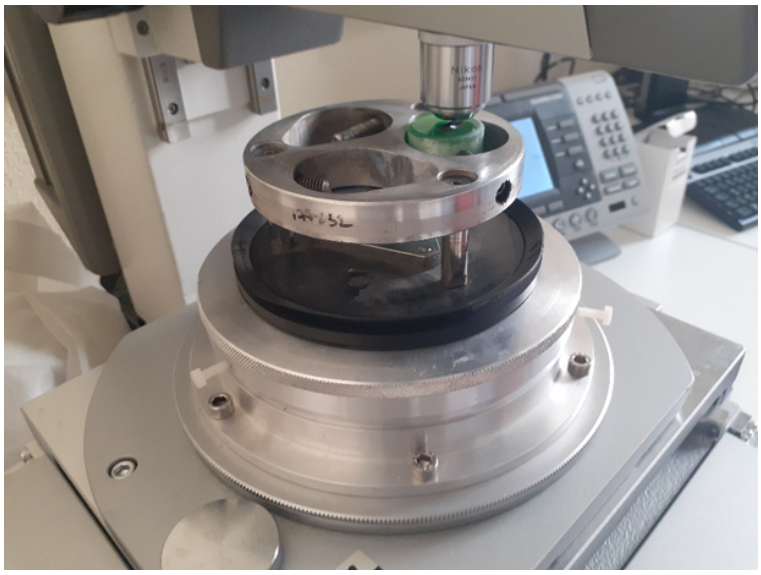

Figure E.1 Sample holder used for controlled abrasion of the samples. The holder can be placed at a fixed position on a microscope to follow the remove sample height by adjusting the focal distance between each polishing steps.

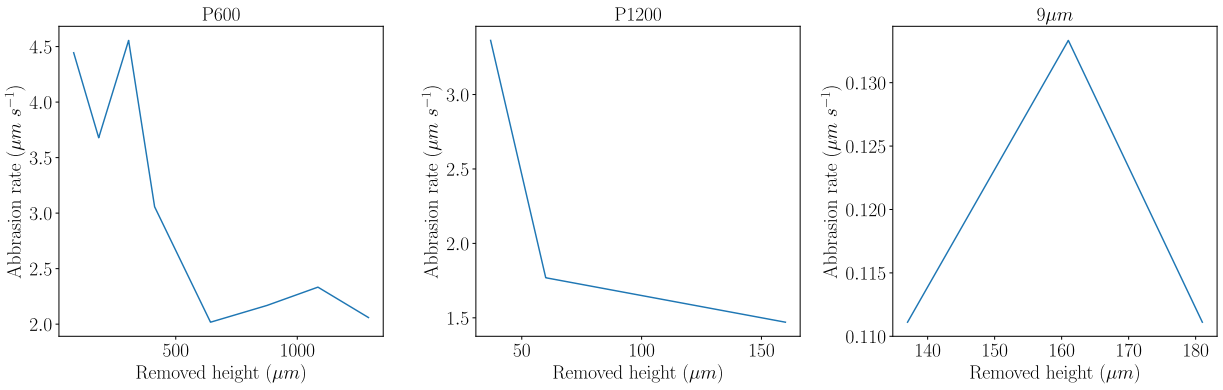

Figure E.2 Abbrasion rates as a function of removed sample height for the P600 and P1200 SiC grit paper and Largo composite disc with a 9 μm diamond suspension.

the less the observed surface hardening. A compromise therefore has to be found for each sample to get the best final surface state.

If the oxydation reaction starts, the damage can only be repaired by getting back to the 9 μm suspension step as fumed silicat particles tend to solidify in the space between the resin and the sample. Mechanical polishing steps tends to remove those solidified particle during polishing producing large but not deep scratches on the surface which are usually recognizable as they initiate at the sample border. The sample is then observed using EBSD to ensure a sufficient pattern quality before uncoating. If not, longer vibromet steps are performed to remove the remaining subsurface hardening. Otherwise, the sample is uncoated through a three-days acetone bath.

Unfortunately such careful procedure was still not sufficient to reduce the layer hardened by mechanical polishing to a sufficient depth for HR-EBSD observations.

Ion beam milling preparation

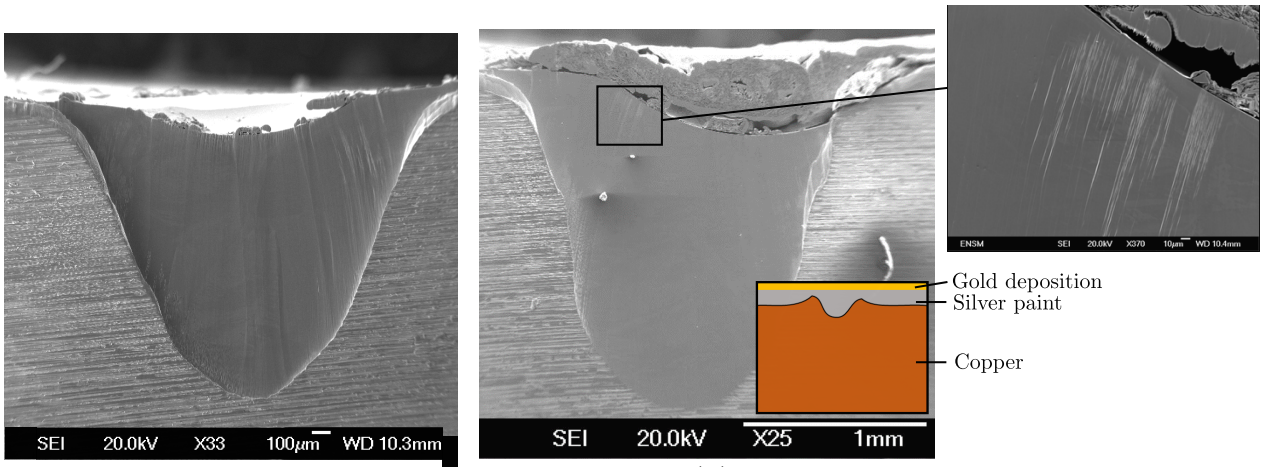

(a) (b)

Figure E.3 (a) Curtain effect induced by ion beam milling on a copper sample after a 5h milling at 6 kV followed by a 30min refining step at 4 kV. (b) Cross section surface obtained with the same milling conditions after filling the dent with silver paint. The curtain effect was greatly reduced but smaller residual curtains persists as shown in the close-up.

Alternatively, the samples were also polished using a Jeol Ion beam cross-section polisher. The sample cross-section is first cut using a diamond wire saw, so that less than a 100 μm thickness has to be removed by the polisher to reach the dent center. Then, the sample is positioned under a fixed argon beam and continuously rotated around the axis perpendicular to the cross section to ensure homogeneous milling. The benefits of this approach is that no mechanical steps are performed on the sample. No hardened layer is therefore produced by polishing.

However, the beam power and polishing duration have to be optimized to minimize curtains effects occurring when milling heterogeneous geometries as shown in Figure E.3 (a), which resulted from a 5h milling at 6 kV followed by a 30min refining step at 4 kV. To minimize the curtain produced by surface heterogeneities, the dent was filled with silver painting. A thin gold layer was electrodeposited on the silver painting to homogenize surface first seen by the beam. Figure E.3 (b) shows the resulting surface obtained with the same milling conditions, which reveals that filling the dent has greatly reduced the curtain effects. Unfortunately, smaller curtains were still present on the polished surface due to the silver painting heterogeneous distribution.

Unfortunately, the surface preparation methodologies detailed above were not sufficient for HR-EBSD analysis. Therefore only the misorientation data under the dent were analyzed in the following.

APPENDIX F SENSITIVITY OF CAMERA CALIBRATION ACCURACY TO THE CHECKER POSITIONING

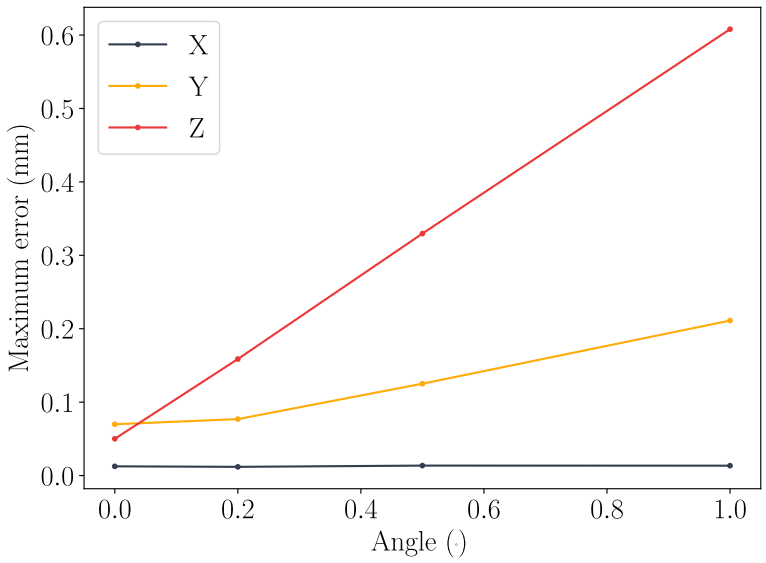

Figure F.1 Variation of the maximum error made by the trajectory reconstruction procedure as a function of the angle between the sample and the chessboard when positioning or transformation matrix determination.

In practice, the chessboard is not always positioned at exactly 90° from the sample when taking pictures for the estimation of the camera's transformation matrix, as it is manually positioned. The trajectory reconstructed by the procedure detailed in Section 6.2.2 is therefore not exactly given in the sample's coordinate system.

The influence of a variation of the angle between the sample and the chessboard was therefore estimated by computing the error made by the trajectory reconstruction procedure on a shot trajectory where the X, and Y and Z where simultaneously varied, using different calibration files.

Figure F.1 shows the variation of the maximum error made by the trajectory reconstruction procure when varying the angle between the sample and the chessboard during transformation matrix calibration. It reveals that for an error angle below 0.2° (which is achievable using the current chessboard holder), the maximum error made by the procedure is still below 200 μm.

APPENDIX G IMPACT MODEL MESH CONVERGENCE STUDY

A convergence study was first conducted to reduce the influence of numerical uncertainties on the identification procedure. Figure G.1 (a) and (b) respectively shows the displacement curves obtained for successively refined meshes and the evolution of the L_2 norm of the difference between the displacement curves obtained with two consecutive meshes. Convergence can be observed for simulations with 832000 elements which can be performed in 16h30 using 4 threads on an Intel Xeon Gold 6132, 2.6 GHz CPU with Abaqus 6.14 version.

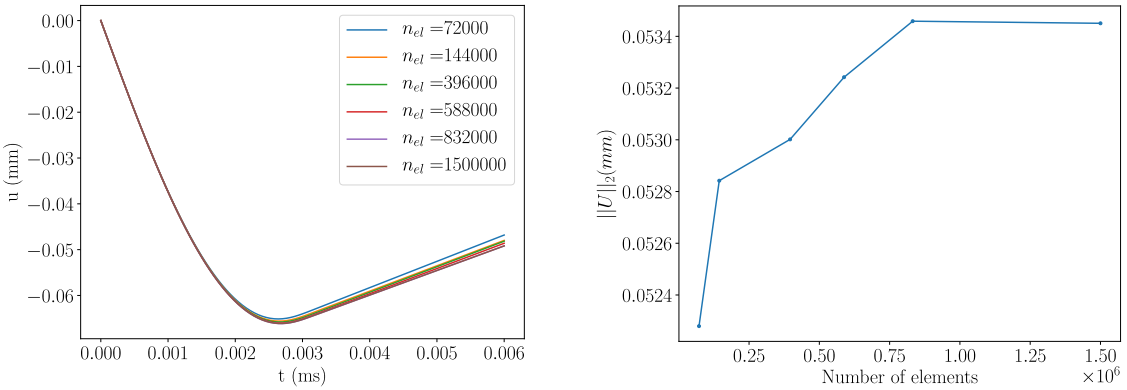

Figure G.1 (a) Impact displacement curves obtained for successively refined meshes. (b) Convergence of the L_2 norm of the difference between the displacement curves obtained with two successive meshes. Convergence is observed for simulations with 832000 elements.

Articles and codes

Published and submitted articles

S. Breumier, A. Villani, C. Maurice, M. Lévesque, and G. Kermouche, "Effect of crystal orientation on indentation-induced residual stress field: simulation and experimental validation", Materials & Design, 2018.

S. Breumier, S. Sao-Joao, A. Villani, M. Lévesque, and G. Kermouche, "High strain rate micro-compression for crystal plasticity constitutive law parameters identification", Materials & Design, vol. 193, p. 108789, 2020.

S. Breumier, F. Adamski, J. Badreddine, M. Lévesque, and G. Kermouche, "Microstructural and mechanical characterization of a shot peening induced rolled edge on direct aged inconel 718 alloy", Submitted in Materials Science and Engineering: A, 2020.

S. Breumier, F. Trudeau-Lalonde, T. Lafrance, A. Villani, G. Kermouche, and L. Martin, "A shot-peening test rig for controlled single and repeated impact testing in industrial conditions", Submitted in Strains, 2020.

S. Breumier, F. Richard, C.Maurice, A. Villani, G. Kermouche, and L. Martin, "Complementarity of impact shot displacements and induced residual stress fields for a reliable estimation of crystal viscoplasticity parameters", Submitted in Journal of Theoretical, Computational and Applied Mechanics, 2020.

Open source codes

Breumier, S. 3Deye, `https://doi.org/10.5281/zenodo.4043588` Zenodo, 2020

Breumier, S. Blender Shot lab, `https://github.com/simonBreumier/Blender_shot_lab` 2020

Breumier, S. Playing with I, `https://colab.research.google.com/github/simonBreumier/Play_with_I/blob/master/Playing%20with%20I.ipynb` 2020

Breumier, S. pyNLPAR, https://github.com/simonBreumier/pyNLPAR 2019

Open Database

Breumier, Simon, Villani, Aurélien, Maurice, Claire, Lévesque, Martin, and Kermouche, Guillaume. (2019, January 27). Effect of crystal orientation on indentation-induced residual stress field: simulation and experimental validation (Version 1). Zenodo. http://doi.org/10.5281/zenodo.2550820

Breumier, Simon, Sao-Joao, Sergio, Villani, Aurélien, Lévesque, Martin, and Kermouche, Guillaume. (2020). High strain rate micro-compression for crystal plasticity constitutive law parameters identification (Version 1.0) [Data set]. http://doi.org/10.1016/j.matdes.2020.108789

Breumier, Simon, Kermouche, Guillaume, and Lévesque, Martin. (2020). Shot peening test rig test database (Version 1.0) [Data set]. Zenodo. http://doi.org/10.5281/zenodo.4001762

References

[1] L. Méric, G. Cailletaud, and M. Gaspérini, "Finite element calculations of copper bicrystal specimens submitted to tension-compression tests," *Acta Metallurgica et Materialia*, vol. 42, no. 3, pp. 921 – 935, 1994. [Online]. Available: http://www.sciencedirect.com/science/article/pii/0956715194902879

[2] O. Casals and S. Forest, "Finite element crystal plasticity analysis of spherical indentation in bulk single crystals and coatings," *Computational Materials Science*, vol. 45, no. 3, pp. 774 – 782, 2009, proceedings of the 17th International Workshop on Computational Mechanics of Materials. [Online]. Available: http://www.sciencedirect.com/science/article/pii/S0927025608004497

[3] M. A. Jackson, E. Pascal, and M. De Graef, "Dictionary indexing of electron back-scatter diffraction patterns: a hands-on tutorial," *Integrating Materials and Manufacturing Innovation*, vol. 8, no. 2, pp. 226–246, Jun 2019. [Online]. Available: https://doi.org/10.1007/s40192-019-00137-4

[4] J. LU, "Traitements de surface mécaniques principes," *Techniques de l'ingénieur Traitements thermiques superficiels et thermochimiques*, vol. base documentaire : TIB501DUO., no. ref. article : m1190, 2006, fre. [Online]. Available: https://www.techniques-ingenieur.fr/base-documentaire/materiaux-th11/traitements-thermiques-superficiels-et-thermochimiques-42501210/traitements-de-surface-mecaniques-m1190/

[5] A. M. Eleiche, M. M. Megahed, and N. M. Abd-allah, "The shot-peening effect on the HCF behavior of high-strength martensitic steels," *Journal of Materials Processing Technology*, vol. 113, no. 1-3, pp. 502–508, 2001, 5th Asia-Pacific Conference on Materials Processing, Seoul, South Korea, 2001.

[6] D. Tumbajoy-Spinel, X. Maeder, G. Guillonneau, S. Sao-Joao, S. Descartes, J.-M. Bergheau, C. Langlade, J. Michler, and G. Kermouche, "Microstructural

and micromechanical investigations of surface strengthening mechanisms induced by repeated impacts on pure iron," *Materials & Design*, vol. 147, pp. 56 – 64, 2018. [Online]. Available: http://www.sciencedirect.com/science/article/pii/S0264127518301837

[7] T. Klotz, D. Delbergue, P. Bocher, M. Levesque, and M. Brochu, "Surface characteristics and fatigue behavior of shot peened inconel 718," *International Journal of Fatigue*, vol. 110, pp. 10–21, 2018.

[8] W. D. Musinski and D. L. McDowell, "On the eigenstrain application of shot-peened residual stresses within a crystal plasticity framework: Application to ni-base superalloy specimens," *International Journal of Mechanical Sciences*, vol. 100, no. Supplement C, pp. 195 – 208, 2015. [Online]. Available: http://www.sciencedirect.com/science/article/pii/S0020740315002313

[9] M. Gelineau, L. Barrallier, E. Rouhaud, R. Kubler, and Q. Puydt, "Residual stress field prediction in shot peened mechanical parts with complex geometries," in *Residual Stresses 2016: ICRS-10*, ser. Materials Research Proceedings, T. Holden, O. Muransky, and L. Edwards, Eds., vol. 2, 2017, Proceedings Paper, pp. 49–54.

[10] D. Gallitelli, V. Boyer, M. Gelineau, Y. Colaitis, E. Rouhaud, D. Retraint, R. Kubler, M. Desvignes, and L. Barrallier, "Simulation of shot peening: from process parameters to residual stress fields in a structure," *Comptes Rendus Mécanique*, vol. 344, no. 4, pp. 355 – 374, 2016, computational simulation of manufacturing processes. [Online]. Available: http://www.sciencedirect.com/science/article/pii/S1631072116000279

[11] A. Ghasemi, S. M. Hassani-Gangaraj, A. H. Mahmoudi, G. H. Farrahi, and M. Guagliano, "Shot peening coverage effect on residual stress profile by FE random impact analysis," *Surface Engineering*, vol. 32, no. 11, pp. 861–870, 2016.

[12] D. Hu, Y. Gao, F. Meng, J. Song, Y. Wang, M. Ren, and R. Wang, "A unifying approach in simulating the shot peening process using a 3d random representative volume finite element model," *Chinese Journal of Aeronautics*, vol. 30, no. 4, pp. 1592–1602, 2017. [Online]. Available: http://www.sciencedirect.com/science/article/pii/S1000936116302485

[13] F. Tu, D. Delbergue, H. Miao, T. Klotz, M. Brochu, P. Bocher, and M. Levesque, "A sequential dem-fem coupling method for shot peening simulation," *Surface and Coatings Technology*, vol. 319, no. Supplement C, pp. 200 – 212, 2017. [Online]. Available: http://www.sciencedirect.com/science/article/pii/S0257897217302748

[14] Z. Jiabin, L. Shihong, W. Tianrui, Z. Zhen, and Z. Wei, "An evaluation on SP surface property by means of combined FEM-DEM shot dynamics simulation," *Advances in Engineering Software*, vol. 115, pp. 283–296, JAN 2018.

[15] T. Zhang, J. Jiang, S. B.A., T. Britton, and D. F.P.E, "Slip localization and fatigue crack nucleation near a non-metallic inclusion in polycrystalline nickel-based superalloy," *Materials Science and Engineering: A*, vol. 641, pp. 328–339, 2015.

[16] J. Jiang, T. B. Britton, and A. J. Wilkinson, "Evolution of intragranular stresses and dislocation densities during cyclic deformation of polycrystalline copper," *Acta Materialia*, vol. 94, pp. 193 – 204, 2015. [Online]. Available: http://www.sciencedirect.com/science/article/pii/S1359645415002736

[17] H. Lieurade and A. Bignonnet, "Fundamental aspects of the effect of shot peening on the fatigue strength of metallic parts and structures," in *3rd International Conference on Shot Peening, Garmisch-Partenkirchen, Germany*, 1987, pp. 343–360.

[18] T. Rousseau, "Modélisation multi-échelle de la modification de structure d'un alliage à base de nickel soumis à de très fortes déformations plastiques en surface," Ph.D. dissertation, Ecole Centrale de Lyon, 2016. [Online]. Available: http://www.theses.fr/2016LYSEC016

[19] A. Castro Moreno, F. Tu, M. Lévesque, and P. Bocher, "Shot peening fem simulation: A novel approach based on crystal plasticity," in *ICSP-13*, 2017.

[20] S. Meguid, G. Sagals, and J. Stranart, "3D finite element analysis of peening of strain-rate sensitive materials using multiple impingement model," *International Journal of Impact Engineering*, vol. 27, pp. 119–134, 02 2002.

[21] S. Breumier, A. Villani, C. Maurice, M. Lévesque, and G. Kermouche, "Effect of crystal orientation on indentation-induced residual stress field: simulation and experimental validation," *Materials & Design*, 2018.

[22] S. Breumier, F. Adamski, J. Badreddine, M. Lévesque, and G. Kermouche, "Microstructural and mechanical characterization of a shot peening induced rolled edge on direct aged inconel 718 alloy," *submitted in Materials Science and Engineering: A*, 2020.

[23] S. Breumier, S. Sao-Joao, A. Villani, M. Lévesque, and G. Kermouche, "High strain rate micro-compression for crystal plasticity constitutive law parameters identification," *Materials & Design*, vol. 193, p. 108789, 2020. [Online]. Available: http://www.sciencedirect.com/science/article/pii/S0264127520303233

[24] S. Breumier, F. Trudeau-Lalonde, T. Lafrance, A. Villani, G. Kermouche, and L. Martin, "A shot-peening test rig for controlled single and repeated impact testing in industrial conditions," *submitted in Strains*, 2020.

[25] R. Guiheux, "Comportement d'aciers à transformation de phase austénite-martensite pour la simulation du grenaillage de précontrainte," Ph.D. dissertation, Arts et Métiers ParisTech, 2016.

[26] J. Badreddine, "Modélisation du grenaillage ultrason pour des pièces à géométrie complexe," Ph.D. dissertation, Université de Technologie de Troyes, 2014.

[27] R. Yang, X. Zhang, D. Mallipeddi, N. Angelou, H. L. Toftegaard, Y. Li, J. Ahlström, L. Lorentzen, G. Wu, and X. Huang, "Effect of shot peening on the residual stress and mechanical behaviour of low-temperature and high-temperature

annealed martensitic gear steel 18crnimo7-6," *IOP Conference Series: Materials Science and Engineering*, vol. 219, no. 1, p. 012046, 2017. [Online]. Available: http://stacks.iop.org/1757-899X/219/i=1/a=012046

[28] P. S. Prevey and J. T. Cammett, *The Effect of Shot Peening Coverage on Residual Stress, Cold Work and Fatigue in a Ni-Cr-Mo Low Alloy Steel*. Wiley-VCH Verlag GmbH & Co. KGaA, 2006, pp. 295–304. [Online]. Available: http://dx.doi.org/10.1002/3527606580.ch37

[29] M. Kobayashi, T. Matsui, and Y. Murakami, "Mechanism of creation of compressive residual stress by shot peening," *International Journal of Fatigue*, vol. 20, no. 5, pp. 351 – 357, 1998. [Online]. Available: http://www.sciencedirect.com/science/article/pii/S0142112398000024

[30] R. Haynes, "The influence of residual stress due to shot peening on the fatigue behaviour of silicon manganese spring steel," *Strain*, vol. 3, no. 4, pp. 3–11, 1967.

[31] M. Guagliano, "Relating almen intensity to residual stresses induced by shot peening: a numerical approach," *Journal of Materials Processing Technology*, vol. 110, no. 3, pp. 277 – 286, 2001. [Online]. Available: http://www.sciencedirect.com/science/article/pii/S0924013600008931

[32] M. Klemenz, V. Schulze, I. Rohr, and D. Löhe, "Application of the fem for the prediction of the surface layer characteristics after shot peening," *Journal of Materials Processing Technology*, vol. 209, no. 8, pp. 4093 – 4102, 2009. [Online]. Available: http://www.sciencedirect.com/science/article/pii/S0924013608007231

[33] K. Murugaratnam, S. Utili, and N. Petrinic, "A combined dem–fem numerical method for shot peening parameter optimisation," *Advances in Engineering Software*, vol. 79, pp. 13 – 26, 2015. [Online]. Available: http://www.sciencedirect.com/science/article/pii/S0965997814001446

[34] A. Mahmoudi, A. Ghasemi, G. Farrahi, and K. Sherafatnia, "A comprehensive experimental and numerical study on redistribution of residual stresses by shot peening," *Materials & Design*, vol. 90, no. Supplement C, pp. 478 – 487, 2016. [Online]. Available: http://www.sciencedirect.com/science/article/pii/S0264127515307401

[35] H. Wohlfahrt, "The influence of peening conditions on the resulting distribution of residual stress," *International Conference of Shot-Peening 2*, vol. p.316-331, 1984.

[36] C. Nouguier-lehon, M. Zarwel, C. Diviani, D. Hertz, H. Zahouani, and T. Hoc, "Surface impact analysis in shot peening process," *Wear*, vol. 302, no. 1-2, SI, pp. 1058–1063, 2013.

[37] V. B. Nguyen, H. J. Poh, and Y.-w. Zhang, "Predicting shot peening coverage using multiphase computational fluid dynamics simulations," *Powder Technology*, vol. 256, pp. 100–112, 2014.

[38] M. Zimmermann and M. Klemenz, "Literature review on shot peening simulation," *International Journal of Computanional Materials Science and Surface Engineering*, vol. 3, no. 4, 2010.

[39] S. Bagherifard, R. Ghelichi, and M. Guagliano, "Mesh sensitivity assessment of shot peening finite element simulation aimed at surface grain refinement," *Surface and Coatings Technology*, vol. 243, pp. 58 – 64, 2014, mechanical Behaviour of Treated Surfaces - selected papers from ICM-11. [Online]. Available: http://www.sciencedirect.com/science/article/pii/S0257897212002861

[40] K. Han, D. Peric, D. R. J. Owen, and J. Yu, "A combined finite/discrete element simulation of shot peening processes - part ii: 3D interaction laws," *Engineering Computations*, vol. 17, no. 6-7, pp. 680–702, 2000.

[41] S. Hu, C. Guo, D. Wang, Z. Wang, and C. Huang, "Finite element analysis of residual stress evolution with multiple impacts on one point in ultrasonic impact treatment process," *Proceedings of the Institution of Mechanical Engineers, Part B: Journal of Engineering Manufacture*, vol. 232, no. 7, pp. 1201–1211, 2018. [Online]. Available: https://doi.org/10.1177/0954405416666894

[42] S. M. Hassani-gangaraj, K. S. Cho, H. J. L. Voigt, M. Guagliano, and C. A. Schuh, "Experimental assessment and simulation of surface nanocrystallization by severe shot peening," *Acta Materialia*, vol. 97, pp. 105–115, 2015.

[43] P. Sanjurjo, C. Rodriguez, I. Penuelas, T. Eduardo Garcia, and F. Javier Belzunce, "Influence of the target material constitutive model on the numerical simulation of a shot peening process," *Surface & Coatings Technology*, vol. 258, pp. 822–831, 2014.

[44] E. Rouhaud, A. Ouakka, C. Ould, J. Chaboche, and M. François, "Finite elements model of shot peening, effects of constitutive laws of the material," in *Proceedings ICSP-9, Paris, France*, 01 2005.

[45] V. Boyer, "Modélisation du grenaillage d'un alliage de nickel avec prise en compte de l'écrouissage et de la microstructure," Ph.D. dissertation, Université de Technologie de Troyes, 2018.

[46] A. Gariépy, H. Miao, and M. Lévesque, "Simulation of the shot peening process with variable shot diameters and impacting velocities," *Advances in Engineering Software*, vol. 114, no. Supplement C, pp. 121 – 133, 2017. [Online]. Available: http://www.sciencedirect.com/science/article/pii/S0965997817300431

[47] A. Morançais, "Effet du grenaillage sur la durée de vie des aubes monocristallines de turbine," Ph.D. dissertation, Ecole doctorale Sciences pour l'Ingénieur (Troyes, Aube), 2016.

[48] R. W. Fonda and J. F. Bingert, "Texture variations in an aluminum friction stir weld," *Scripta Materialia*, vol. 57, no. 11, pp. 1052–1055, 2007. [Online]. Available: http://www.sciencedirect.com/science/article/pii/S1359646207004642

[49] M. Meo and R. Vignjevic, "Finite element analysis of residual stress induced by shot peening process," *Advances in Engineering Software*, vol. 34, no. 9, pp. 569 – 575, 2003. [Online]. Available: http://www.sciencedirect.com/science/article/pii/S0965997803000632

[50] E. Schmid and W. Boas, *Kristallplastizität*, Springer, Ed. Springer Verlag, 1935.

[51] E. Renner, "To the identification of a single crystal plasticity law by topographic analysis of Berkovich nanoindentation imprints," Theses, Université de Franche Comté, Jun. 2016. [Online]. Available: https://tel.archives-ouvertes.fr/tel-01412987

[52] J. P. Hirth, "On dislocation interactions in the fcc lattice," *Journal of Applied Physics*, vol. 32, no. 4, pp. 700–706, 1961. [Online]. Available: https://doi.org/10.1063/1.1736074

[53] P. Franciosi, M. Berveiller, and A. Zaoui, "Latent hardening in copper and aluminium single crystals," *Acta Metallurgica*, vol. 28, no. 3, pp. 273 – 283, 1980. [Online]. Available: http://www.sciencedirect.com/science/article/pii/0001616080901625

[54] F. Roters, P. Eisenlohr, L. Hantcherli, D. Tjahjanto, T. Bieler, and D. Raabe, "Overview of constitutive laws, kinematics, homogenization and multiscale methods in crystal plasticity finite-element modeling: Theory, experiments, applications," *Acta Materialia*, vol. 58, no. 4, pp. 1152 – 1211, 2010. [Online]. Available: http://www.sciencedirect.com/science/article/pii/S1359645409007617

[55] D. Peirce, R. Asaro, and A. Needleman, "An analysis of nonuniform and localized deformation in ductile single crystals," *Acta Metallurgica*, vol. 30, no. 6, pp. 1087 – 1119, 1982. [Online]. Available: http://www.sciencedirect.com/science/article/pii/0001616082900050

[56] E. P. Busso and G. Cailletaud, "On the selection of active slip systems in crystal plasticity," *International Journal of Plasticity*, vol. 21, no. 11, pp. 2212 – 2231, 2005, plasticity of Heterogeneous Materials. [Online]. Available: http://www.sciencedirect.com/science/article/pii/S0749641905000847

[57] M. Fivel and S. Forest, "Plasticité cristalline et transition d'échelle : cas du monocristal," *Techniques de l'ingénieur Étude des métaux et des alliages : état métallique*, vol. base documentaire : TIB345DUO., no. ref. article : m4016, 2004, fre. [Online]. Available: https://www.techniques-ingenieur.fr/base-documentaire/materiaux-th11/etude-des-metaux-et-des-alliages-etat-metallique-42345210/plasticite-cristalline-et-transition-d-echelle-cas-du-monocristal-m4016/

[58] B. Devincre, L. Kubin, and T. Hoc, "Physical analyses of crystal plasticity by DD simulations," *Scripta Materialia*, vol. 54, no. 5, pp. 741–746, 2006.

[59] P. S. Follansbee, G. Regazzoni, and U. F. Kocks, "The transition to drag-controlled deformation in copper at high-strain rates," *Institute of Physics Conference Series*, no. 70, pp. 71–80, 1984.

[60] R. W. Armstrong and S. M. Walley, "High strain rate properties of metals and alloys," *International Materials Reviews*, vol. 53, no. 3, pp. 105–128, 2008. [Online]. Available: https://doi.org/10.1179/174328008X277795

[61] F. C. Salvado, F. Teixeira-Dias, S. M. Walley, L. J. Lea, and J. B. Cardoso, "A review on the strain rate dependency of the dynamic viscoplastic response of fcc metals," *Progress in Materials Science*, vol. 88, pp. 186 – 231, 2017. [Online]. Available: http://www.sciencedirect.com/science/article/pii/S0079642517300397

[62] U. Kocks, A. Argon, and M. Ashby, "Thermodynamics and kinetics of slip," *Progress in Materials Science*, vol. 19, 1975.

[63] A. S. Khan, J. Liu, J. W. Yoon, and R. Nambori, "Strain rate effect of high purity aluminum single crystals: Experiments and simulations," *International Journal of Plasticity*, vol. 67, no. Supplement C, pp. 39 – 52, 2015. [Online]. Available: http://www.sciencedirect.com/science/article/pii/S074964191400196X

[64] U. Kocks and H. Mecking, "Physics and phenomenology of strain hardening: the fcc case," *Progress in Materials Science*, vol. 48, no. 3, pp. 171 – 273, 2003. [Online]. Available: http://www.sciencedirect.com/science/article/pii/S0079642502000038

[65] N. Djordjevic, R. Vignjevic, L. Kiely, S. Case, T. D. Vuyst], J. Campbell, and K. Hughes, "Modelling of shock waves in fcc and bcc metals using a combined continuum and dislocation kinetic approach," *International Journal of Plasticity*, vol. 105, pp. 211 – 224, 2018. [Online]. Available: http://www.sciencedirect.com/science/article/pii/S0749641917306186

[66] B. Gurrutxaga–Lerma, J. Verschueren, A. P. Sutton, and D. Dini, "The mechanics and physics of high-speed dislocations: a critical review," *International Materials Reviews*, vol. 0, no. 0, pp. 1–41, 2020. [Online]. Available: https://doi.org/10.1080/09506608.2020.1749781

[67] M. Kattoura and M. A. Shehadeh, "On the ultra-high-strain rate shock deformation in copper single crystals: multiscale dislocation dynamics simulations," *Philosophical Magazine Letters*, vol. 94, no. 7, pp. 415–423, 2014. [Online]. Available: https://doi.org/10.1080/09500839.2014.920540

[68] Z. Wang, I. Beyerlein, and R. LeSar, "Slip band formation and mobile dislocation density generation in high rate deformation of single fcc crystals," *Philosophical Magazine*, vol. 88, no. 9, pp. 1321–1343, 2008. [Online]. Available: https://doi.org/10.1080/14786430802129833

[69] M. M. Rahaman, B. Dhas, D. Roy, and J. Reddy, "A dynamic flow rule for viscoplasticity in polycrystalline solids under high strain rates," *International Journal of Non-Linear Mechanics*, vol. 95, no. Supplement C, pp. 10 – 18, 2017. [Online]. Available: http://www.sciencedirect.com/science/article/pii/S0020746217303013

[70] D. J. Luscher, M. A. Kenamond, A. Hunter, J. R. Mayeur, and H. M. Mourad, "Implementation of a dislocation-density based single-crystal model into a continuum shock hydrodynamics code," *AIP Conference Proceedings*, vol. 1979, no. 1, p. 180006, 2018. [Online]. Available: https://aip.scitation.org/doi/abs/10.1063/1.5045039

[71] M. A. Meyers, *Dynamic Behavior of Materials*. John Wiley & Sons, Inc., 1994.

[72] D. Luscher, J. Mayeur, H. Mourad, A. Hunter, and M. Kenamond, "Coupling continuum dislocation transport with crystal plasticity for application to shock loading conditions," *International Journal of Plasticity*, vol. 76, no. Supplement C, pp. 111 – 129, 2016. [Online]. Available: http://www.sciencedirect.com/science/article/pii/S0749641915001254

[73] A. E. Mayer, K. V. Khishchenko, P. R. Levashov, and P. N. Mayer, "Modeling of plasticity and fracture of metals at shock loading," *Journal of Applied Physics*, vol. 113, no. 19, p. 193508, 2013. [Online]. Available: https://doi.org/10.1063/1.4805713

[74] J. R. Mayeur, H. M. Mourad, D. J. Luscher, A. Hunter, and M. A. Kenamond, "Numerical implementation of a crystal plasticity model with dislocation transport for high strain rate applications," *Modelling and Simulation in Materials Science and Engineering*, vol. 24, no. 4, p. 045013, 2016. [Online]. Available: http://stacks.iop.org/0965-0393/24/i=4/a=045013

[75] A. Cruzado, B. Gan, H. Chang, K. Ostolaza, A. Linaza, S. Milenkovic, J. M. Molina-Aldareguia, J. Llorca, and J. Segurado, *Microtesting and Crystal Plasticity Modelling of IN718 Superalloy Grains*. John Wiley & Sons, Inc., 2014, pp. 897–907. [Online]. Available: http://dx.doi.org/10.1002/9781119016854.ch71

[76] K. Ekström, "Experimental investigation of the strain rate dependence of ss2506 gear steel," Master's thesis, KTH, Materials Science and Engineering, 2013.

[77] H. Zhang, B. Schuster, Q. Wei, and K. Ramesh, "The design of accurate micro-compression experiments," *Scripta Materialia*, vol. 54, no. 2, pp. 181 – 186, 2006. [Online]. Available: http://www.sciencedirect.com/science/article/pii/S1359646205005944

[78] Y. Xiao, J. Wehrs, H. Ma, T. Al-Samman, S. Korte-Kerzel, M. Göken, J. Michler, R. Spolenak, and J. Wheeler, "Investigation of the deformation behavior of aluminum micropillars produced by focused ion beam machining using ga and xe ions," *Scripta Materialia*, vol. 127, pp. 191 – 194, 2017. [Online]. Available: http://www.sciencedirect.com/science/article/pii/S1359646216304031

[79] J. R. Greer, W. C. Oliver, and W. D. Nix, "Size dependence of mechanical properties of gold at the micron scale in the absence of strain gradients," *Acta Materialia*, vol. 53, no. 6, pp. 1821 – 1830, 2005. [Online]. Available: http://www.sciencedirect.com/science/article/pii/S1359645404007670

[80] C. Frick, B. Clark, S. Orso, A. Schneider, and E. Arzt, "Size effect on strength and strain hardening of small-scale [111] nickel compression pillars," *Materials Science and Engineering: A*, vol. 489, no. 1, pp. 319 – 329, 2008. [Online]. Available: http://www.sciencedirect.com/science/article/pii/S092150930701996X

[81] D. Raabe, D. Ma, and F. Roters, "Effects of initial orientation, sample geometry and friction on anisotropy and crystallographic orientation changes in single crystal microcompression deformation: A crystal plasticity finite element study," *Acta Materialia*, vol. 55, no. 13, pp. 4567 – 4583, 2007. [Online]. Available: http://www.sciencedirect.com/science/article/pii/S1359645407002662

[82] D. Kiener, P. Guruprasad, S. Keralavarma, G. Dehm, and A. Benzerga, "Work hardening in micropillar compression: In situ experiments and modeling," *Acta Materialia*, vol. 59, no. 10, pp. 3825 – 3840, 2011. [Online]. Available: http://www.sciencedirect.com/science/article/pii/S1359645411001509

[83] J. Zhang, G. Liu, and J. Sun, "Strain rate effects on the mechanical response in multi- and single-crystalline cu micropillars: Grain boundary effects," *International Journal of Plasticity*, vol. 50, pp. 1 – 17, 2013. [Online]. Available: http://www.sciencedirect.com/science/article/pii/S074964191300079X

[84] D. T. Spinel, "Caractérisation du comportement mécanique de surfaces hyper-déformées par des phénomènes de contact," Ph.D. dissertation, Ecole des Mines de Saint-Etienne, 2016.

[85] R. Soler, J. M. Molina-aldareguia, J. Segurado, and J. Llorca, "Effect of misorientation on the compression of highly anisotropic single-crystal micropillars," *Advanced Engineering Materials*, vol. 14, no. 11, pp. 1004–1008, 2012.

[86] D. Singh, N. Chawla, G. Tang, and Y.-L. Shen, "Micropillar compression of al/sic nanolaminates," *Acta Materialia*, vol. 58, no. 20, pp. 6628 – 6636, 2010. [Online]. Available: http://www.sciencedirect.com/science/article/pii/S1359645410005392

[87] A. Cruzado, B. Gan, M. Jiménez, D. Barba, K. Ostolaza, A. Linaza, J. Molina-Aldareguia, J. Llorca, and J. Segurado, "Multiscale modeling of the mechanical behavior of in718 superalloy based on micropillar compression and computational homogenization," *Acta Materialia*, vol. 98, pp. 242 – 253, 2015. [Online]. Available: http://www.sciencedirect.com/science/article/pii/S1359645415004681

[88] F. D. Gioacchino and W. J. Clegg, "Mapping deformation in small-scale testing," *Acta Materialia*, vol. 78, pp. 103 – 113, 2014. [Online]. Available: http://www.sciencedirect.com/science/article/pii/S1359645414004534

[89] G. Guillonneau, M. Mieszala, J. Wehrs, J. Schwiedrzik, S. Grop, D. Frey, L. Philippe, J.-M. Breguet, J. Michler, and J. M. Wheeler, "Nanomechanical testing at high strain rates: New instrumentation for nanoindentation and microcompression," *Materials & Design*, vol. 148, pp. 39 – 48, 2018. [Online]. Available: http://www.sciencedirect.com/science/article/pii/S0264127518302351

[90] E. Nordin and B. Alfredsson, "Measuring shot peening media velocity by indent size comparison," *Journal of Materials Processing Technology*, vol. 235, pp. 143 – 148, 2016. [Online]. Available: http://www.sciencedirect.com/science/article/pii/S0924013616301029

[91] K. Murugaratnam, "A refined numerical modelling techniquefor shot peening," Ph.D. dissertation, University of Oxford, 2014.

[92] A. Sekkal, C. Langlade, and A. Vannes, "A micro/macro impact test at controlled energy for erosion and phase-transformation simulation," *Tribology Letters*, vol. 15, no. 3, pp. 265–274, Oct 2003. [Online]. Available: https://doi.org/10.1023/A:1024996621189

[93] H. Al Baida, G. Kermouche, and C. Langlade, "Development of an improved method for identifying material stress-strain curve using repeated micro-impact testing," *Mechanics of Materials*, vol. 86, pp. 11–20, JUL 2015.

[94] V. Hauk, *Structural and Residual Stress Analysis by Nondestructive Methods*. Elsevier, 1997.

[95] A. Morançais, M. Fèvre, M. François, N. Guel, S. Kruch, P. Kanouté, and A. Longuet, "Residual stress determination in a shot-peened nickel-based single-crystal superalloy using X-ray diffraction," *Journal of Applied Crystallography*, vol. 48, no. 6, pp. 1761–1776, Dec 2015. [Online]. Available: https://doi.org/10.1107/S1600576715017689

[96] G. Altinkurt, M. Fèvre, G. Geandier, M. Dehmas, O. Robach, and J. S. Micha, "Local strain redistribution in a coarse-grained nickel-based superalloy subjected to shot-peening, fatigue or thermal exposure investigated using synchrotron x-ray laue microdiffraction," *Journal of Materials Science*, vol. 53, pp. 8567–8589, 2018. [Online]. Available: https://hal.archives-ouvertes.fr/hal-01745299

[97] B. Hrishikesh, "Polychromatic micro x-ray beam strain analysis of aluminum sapphire composite," Master's thesis, Graduate College of the Oklahoma State University, 2002.

[98] J. Petit, M. Bornert, F. Hofmann, O. Robach, J. Micha, O. Ulrich, C. L. Bourlot], D. Faurie, A. Korsunsky, and O. Castelnau, "Combining laue microdiffraction and digital image correlation for improved measurements of the elastic strain field with micrometer spatial resolution," *Procedia IUTAM*, vol. 4, pp. 133 – 143, 2012, iUTAM Symposium on Full-field Measurements and Identification in Solid Mechanics. [Online]. Available: http://www.sciencedirect.com/science/article/pii/S2210983812000399

[99] T. Baudin, "Analyse EBSD- principe et cartographies d'orientations," *Techniques De L'ingenieur*, 2010.

[100] K. Z. Troost, P. Van Der Sluis, and D. J. Gravesteijn, "Microscale elastic-strain determination by backscatter kikuchi diffraction in the scanning electron microscope," *Applied Physics Letters*, vol. 62, no. 10, pp. 1110–1112, 1993.

[101] C. Maurice, J. H. Driver, and R. Fortunier, "On solving the orientation gradient dependency of high angular resolution ebsd," *Ultramicroscopy*, vol. 113, no. Supplement C, pp. 171 – 181, 2012. [Online]. Available: http://www.sciencedirect.com/science/article/pii/S0304399111002580

[102] A. Wilkinson, G. Meaden, and D. Dingley, "High-resolution elastic strain measurement from electron backscatter diffraction patterns: New levels of sensitivity," *Ultramicroscopy*, vol. 106, no. 4-5, pp. 307–313, 2006.

[103] T. Britton, C. Maurice, R. Fortunier, J. Driver, A. Day, G. Meaden, D. Dingley, K. Mingard, and A. Wilkinson, "Factors affecting the accuracy of high resolution electron backscatter diffraction when using simulated patterns," *Ultramicroscopy*, vol. 110, no. 12, pp. 1443 – 1453, 2010. [Online]. Available: http://www.sciencedirect.com/science/article/pii/S0304399110002214

[104] J. Alkorta, M. Marteleur, and P. J. Jacques, "Improved simulation based hr-ebsd procedure using image gradient based dic techniques," *Ultramicroscopy*, vol. 182, pp. 17 – 27, 2017. [Online]. Available: http://www.sciencedirect.com/science/article/pii/S0304399116301668

[105] T. Tanaka and A. J. Wilkinson, "Pattern matching analysis of electron backscatter diffraction patterns for pattern centre, crystal orientation and absolute elastic strain determination – accuracy and precision assessment," *Ultramicroscopy*, vol. 202, pp. 87 – 99, 2019. [Online]. Available: http://www.sciencedirect.com/science/article/pii/S0304399118302961

[106] T. J. Hardin, T. J. Ruggles, D. P. Koch, S. R. Niezgoda, D. T. Fullwood, and E. R. Homer, "Analysis of traction-free assumption in high-resolution ebsd measurements," *Journal of Microscopy*, vol. 260, no. 1, pp. 73–85, 2015.

[107] J. Nye, "Some geometrical relations in dislocated crystals," *Acta Metallurgica*, vol. 1, no. 2, pp. 153 – 162, 1953. [Online]. Available: http://www.sciencedirect.com/science/article/pii/0001616053900546

[108] S. Das, F. Hofmann, and E. Tarleton, "Consistent determination of geometrically necessary dislocation density from simulations and experiments," *International Journal of Plasticity*, vol. 109, pp. 18 – 42, 2018. [Online]. Available: http://www.sciencedirect.com/science/article/pii/S0749641918300068

[109] W. Pantleon, "Resolving the geometrically necessary dislocation content by conventional electron backscattering diffraction," *Scripta Materialia*, 2008.

[110] J. Kysar, Y. Saito, M. Oztop, D. Lee, and W. Huh, "Experimental lower bounds on geometrically necessary dislocation density," *International Journal of Plasticity*, vol. 26, no. 8, pp. 1097 – 1123, 2010, special Issue In Honor of Lallit Anand. [Online]. Available: http://www.sciencedirect.com/science/article/pii/S0749641910000574

[111] A. J. Wilkinson and D. Randman, "Determination of elastic strain fields and geometrically necessary dislocation distributions near nanoindents using electron back scatter diffraction," *Philosophical Magazine*, vol. 90, no. 9, pp. 1159–1177, 2010. [Online]. Available: https://doi.org/10.1080/14786430903304145

[112] A. Acharya and R. J. Knops, "An observation on the experimental measurement of dislocation density," *Journal of Elasticity*, vol. 114, no. 2, pp. 275–279, Feb. 2014. [Online]. Available: https://doi.org/10.1007/s10659-013-9437-2

[113] M. S. Mohamed, B. C. Larson, J. Z. Tischler, and A. El-Azab, "A statistical analysis of the elastic distortion and dislocation density fields in deformed crystals," *Journal of the Mechanics and Physics of Solids*, vol. 82, pp. 32 – 47, 2015. [Online]. Available: http://www.sciencedirect.com/science/article/pii/S0022509615001167

[114] E. Demir, D. Raabe, N. Zaafarani, and S. Zaefferer, "Investigation of the indentation size effect through the measurement of the geometrically necessary dislocations beneath small indents of different depths using ebsd tomography," *Acta Materialia*, vol. 57, no. 2, pp. 559 – 569, 2009. [Online]. Available: http://www.sciencedirect.com/science/article/pii/S1359645408007003

[115] A. Arsenlis and D. Parks, "Crystallographic aspects of geometrically-necessary and statistically-stored dislocation density," *Acta Materialia*, vol. 47, no. 5, pp. 1597 – 1611, 1999. [Online]. Available: http://www.sciencedirect.com/science/article/pii/S1359645499000208

[116] S. Wright, M. Nowell, S. Lindeman, P. Camus, M. De Graef, and M. Jackson, "Introduction and comparison of new ebsd post-processing methodologies." *Ultramicroscopy*, vol. 159, pp. 81–94, 2015.

[117] R. Hielscher, C. B. Silbermann, E. Schmidl, and J. Ihlemann, "Denoising of crystal orientation maps," *Journal of Applied Crystallography*, vol. 52, no. 5, pp. 984–996, Oct 2019. [Online]. Available: https://doi.org/10.1107/S1600576719009075

[118] A. Seret, C. Moussa, M. Bernacki, J. Signorelli, and N. Bozzolo, "Estimation of geometrically necessary dislocation density from filtered EBSD data by a local linear adaptation of smoothing splines," *Journal of Applied Crystallography*, vol. 52, no. 3, pp. 548–563, Jun 2019. [Online]. Available: https://doi.org/10.1107/S1600576719004035

[119] P. T. Brewick, S. I. Wright, and D. J. Rowenhorst, "Nlpar: Non-local smoothing for enhanced ebsd pattern indexing," *Ultramicroscopy*, vol. 200, pp. 50 – 61, 2019. [Online]. Available: http://www.sciencedirect.com/science/article/pii/S0304399118304248

[120] S. I. Wright and B. L. Adams, "Automatic analysis of electron backscatter diffraction patterns," *Metallurgical Transactions A*, vol. 23, no. 3, pp. 759–767, Mar. 1992. [Online]. Available: https://doi.org/10.1007/BF02675553

[121] S. Singh, Y. Guo, B. Winiarski, T. Burnett, P. Withers, and M. DeGraef, "High resolution low kv ebsd of heavily deformed and nanocrystalline aluminium by dictionary-based indexing," *Scientific Reports*, 2018.

[122] M. Burch, C. Fancher, S. Patala, M. De Graef, and E. Dickey, "Mapping 180° polar domains using electron backscatter diffraction and dynamical scattering simulations." *Ultramicroscopy*, vol. 173, pp. 47–51, 2017.

[123] M. De Graef, W. Lenthe, N. Schäfer, T. Rissom, and D. Abou-Ras, "Unambiguous determination of local orientations of polycrystalline cuinse$_2$ thin films via dictionary-based indexing." *Physica status solidi (RRL)–Rapid Research Letters*, p. 1900032, 2018.

[124] R. Hielscher, F. Bartel, and T. B. Britton, "Gazing at crystal balls – electron backscatter diffraction indexing and cross correlation on a sphere," *Microscopy and Microanalysis*, vol. 25, no. S2, p. 1954–1955, Aug 2019. [Online]. Available: http://dx.doi.org/10.1017/S143192761901050X

[125] W. Lenthe, S. Singh, and M. D. Graef, "A spherical harmonic transform approach to the indexing of electron back-scattered diffraction patterns," *Ultramicroscopy*, vol. 207, p. 112841, 2019. [Online]. Available: http://www.sciencedirect.com/science/article/pii/S0304399119301585

[126] C. Audet and J. J. E. Dennis, "Mesh adaptive direct search algorithms for constrained optimization," *SIAM Journal on Optimization*, vol. 17, no. 1, pp. 188–217, 2006. [Online]. Available: https://doi.org/10.1137/040603371

[127] F. Richard, "Towards a determination guided by the identifiability of the mechanical behaviour of materials by nanoindentation," Habilitation à diriger des recherches, COMUE Université Bourgogne Franche-Comté, Jun. 2017. [Online]. Available: https://hal.archives-ouvertes.fr/tel-01590429

[128] Y.-T. Cheng and C.-M. Cheng, "Can stress-strain relationships be obtained from indentation curves using conical and pyramidal indenters?" *Journal of Materials Research*, vol. 14, no. 9, pp. 3493–3496, 1999.

[129] Z. Ma, Y. Zhou, S. Long, X. Zhong, and C. Lu, "Characterization of stress-strain relationships of elastoplastic materials: An improved method with conical and pyramidal indenters," *Mechanics of Materials*, vol. 54, pp. 113 – 123, 2012. [Online]. Available: http://www.sciencedirect.com/science/article/pii/S0167663612001391

[130] F. Richard, M. Villars, and S. Thibaud, "Viscoelastic modeling and quantitative experimental characterization of normal and osteoarthritic human articular cartilage using indentation," *Journal of the Mechanical Behavior of Biomedical Materials*, vol. 24, pp. 41 – 52, 2013. [Online]. Available: http://www.sciencedirect.com/science/article/pii/S1751616113001355

[131] T. Klotz, M. Lévesque, and M. Brochu, "Effects of rolled edges on the fatigue life of shot peened inconel 718," *Journal of Materials Processing Technology*, 2018.

[132] R. Sun, Z. Che, Z. Cao, S. Zou, J. Wu, W. Guo, and Y. Zhu, "Fatigue behavior of Ti-17 titanium alloy subjected to different laser shock peened regions and its microstructural response," *Surface and Coatings Technology*, vol. 383, p. 125284, 2020. [Online]. Available: http://www.sciencedirect.com/science/article/pii/S0257897219312745

[133] C. You, M. Achintha, B. He, and P. Reed, "A numerical study of the effects of shot peening on the short crack growth behaviour in notched geometries under bending fatigue tests," *International Journal of Fatigue*, vol. 103, no. Supplement C, pp. 99 – 111, 2017. [Online]. Available: http://www.sciencedirect.com/science/article/pii/S0142112317302372

[134] B. He, K. Soady, B. Mellor, A. Morris, and P. Reed, "Effects of shot peening on short crack growth rate and resulting low cycle fatigue behaviour in low pressure turbine blade material," *Materials Science and Technology*, vol. 29, no. 7, pp. 788–796, 2013.

[135] C. Gérard, G. Cailletaud, and B. Bacroix, "Modeling of latent hardening produced by complex loading paths in fcc alloys," *International Journal of Plasticity*, vol. 42, no. Supplement C, pp. 194 – 212, 2013. [Online]. Available: http://www.sciencedirect.com/science/article/pii/S0749641912001635

[136] A. Guery, F. Hild, F. Latourte, and S. Roux, "Identification of crystal plasticity parameters using dic measurements and weighted femu," *Mechanics of Materials*, vol. 100, pp. 55 – 71, 2016. [Online]. Available: http://www.sciencedirect.com/science/article/pii/S0167663616300813

[137] E. Renner, A. Bourceret, Y. Gaillard, F. Amiot, P. Delobelle, and F. Richard, "Identifiability of single crystal plasticity parameters from residual topographies in berkovich nanoindentation on fcc nickel," *Journal of the Mechanics and Physics of Solids*, vol. 138, p. 103916, 2020. [Online]. Available: http://www.sciencedirect.com/science/article/pii/S0022509620301526

[138] T. Britton, J. Jiang, R. Clough, E. Tarleton, A. Kirkland, and A. Wilkinson, "Assessing the precision of strain measurements using electron backscatter diffraction – part 2: Experimental demonstration," *Ultramicroscopy*, vol. 135, pp. 136 – 141, 2013. [Online]. Available: http://www.sciencedirect.com/science/article/pii/S030439911300212X

[139] J. Ast, G. Mohanty, Y. Guo, J. Michler, and X. Maeder, "In situ micromechanical testing of tungsten micro-cantilevers using hr-ebsd for the assessment of deformation evolution," *Materials & Design*, vol. 117, pp. 265 – 266, 2017. [Online]. Available: http://www.sciencedirect.com/science/article/pii/S0264127516315787

[140] T. Rousseau, C. Nouguier-Lehon, P. Gilles, and T. Hoc, "Finite element multi-impact simulations using a crystal plasticity law based on dislocation dynamics," *International Journal of Plasticity*, pp. –, 2017. [Online]. Available: https://www.sciencedirect.com/science/article/pii/S0749641917303789

[141] P. Juran, P. J. Liotier, C. Maurice, F. Valiorgue, and G. Kermouche, "Investigation of indentation-, impact- and scratch-induced mechanically affected zones in a copper single crystal," in *Comptes Rendus Mecanique*, no. 343, 2014, pp. 344–353.

[142] M. Rester, C. Motz, and R. Pippan, "Indentation across size scales - a survey of indentation-induced plastic zones in copper {111} single crystals," *Scripta Materialia*, vol. 59, no. 7, pp. 742–745, OCT 2008.

[143] J. Alcalá, D. E. de los Ojos, and J. Očenášek, "Extracting uniaxial responses of single crystals from sharp and spherical hardness measurements," *Mechanics of Materials*, vol. 84, no. Supplement C, pp. 100 – 113, 2015. [Online]. Available: http://www.sciencedirect.com/science/article/pii/S0167663615000150

[144] E. Renner, Y. Gaillard, F. Richard, F. Amiot, and P. Delobelle, "Sensitivity of the residual topography to single crystal plasticity parameters in berkovich nanoindentation on fcc nickel," *International Journal of Plasticity*, vol. 77, no. Supplement C, pp. 118 – 140, 2016. [Online]. Available: http://www.sciencedirect.com/science/article/pii/S0749641915001680

[145] H. Petryk, S. Stupkiewicz, and S. Kucharski, "On direct estimation of hardening exponent in crystal plasticity from the spherical indentation test," *International Journal of solids and structures*, vol. 112, pp. 209–221, MAY 1 2017.

[146] J. Alcalá, A. Barone, and M. Anglada, "The influence of plastic hardening on surface deformation modes around vickers and spherical indents," *Acta Materialia*, vol. 48, no. 13, pp. 3451 – 3464, 2000. [Online]. Available: http://www.sciencedirect.com/science/article/pii/S1359645400001403

[147] M. Liu, K. A. Tieu, K. Zhou, and C.-T. Peng, "Indentation analysis of mechanical behaviour of torsion-processed single-crystal copper by crystal plasticity finite-element method modelling," *PHILOSOPHICAL MAGAZINE*, vol. 96, no. 3, pp. 261–273, JAN 22 2016.

[148] N. Zaafarani, D. Raabe, R. Singh, F. Roters, and S. Zaefferer, "Three-dimensional investigation of the texture and microstructure below a nanoindent in a cu single crystal using 3d ebsd and crystal plasticity finite element simulations," *Acta Materialia*, vol. 54, no. 7, pp. 1863 – 1876, 2006. [Online]. Available: http://www.sciencedirect.com/science/article/pii/S1359645406000292

[149] F. Han, B. Tang, X. Yan, Y. Peng, H. Kou, J. Li, Y. Deng, and Y. Feng, "Indentation Pileup Behavior of Ti-6Al-4V Alloy: Experiments and Nonlocal Crystal Plasticity Finite Element Simulations," *METALLURGICAL AND MATERIALS TRANSACTIONS A-PHYSICAL METALLURGY AND MATERIALS SCIENCE*, vol. 48A, no. 4, pp. 2051–2061, APR 2017.

[150] M. Liu, C. Lu, K. A. Tieu, and K. Zhou, "Crystal plasticity fem study of nanoindentation behaviors of cu bicrystals and cu–al bicrystals," *Journal of Materials Research*, vol. 30, no. 16, p. 2485–2499, 2015.

[151] Y. Su, C. Zambaldi, D. Mercier, P. Eisenlohr, T. Bieler, and M. Crimp, "Quantifying deformation processes near grain boundaries in alpha titanium using nanoindentation and crystal plasticity modeling," *International Journal of Plasticity*, vol. 86, pp. 170–186, 2016. [Online]. Available: http://www.sciencedirect.com/science/article/pii/S0749641916301498

[152] C. Dahlberg, Y. Saito, M. Öztop, and J. Kysar, "Geometrically necessary dislocation density measurements at a grain boundary due to wedge indentation into an aluminum bicrystal," *Journal of the Mechanics and Physics of Solids*, vol. 105, pp. 131 – 149, 2017. [Online]. Available: http://www.sciencedirect.com/science/article/pii/S0022509616307906

[153] K. Zeng, A. E. Giannakopoulos, D. Rowcliffe, and P. Meier, "Residual stress fields at the surface of sharp pyramid indentations," *Journal of the American Ceramic Society*, vol. 81, no. 3, pp. 689–694, 1998. [Online]. Available: http://dx.doi.org/10.1111/j.1151-2916.1998.tb02390.x

[154] B. Boyce, X. Chen, J. Hutchinson, and R. Ritchie, "The residual stress state due to a spherical hard-body impact," *Mechanics of Materials*, vol. 33, no. 8, pp. 441 – 454, 2001. [Online]. Available: http://www.sciencedirect.com/science/article/pii/S0167663601000643

[155] A. Giannakopoulos, P.-L. Larsson, and R. Vestergaard, "Analysis of vickers indentation," *International Journal of Solids and Structures*, vol. 31, no. 19, pp. 2679 – 2708, 1994. [Online]. Available: http://www.sciencedirect.com/science/article/pii/0020768394902259

[156] S. Villert, C. Maurice, C. Wyon, and R. Fortunier, "Accuracy assessment of elastic strain measurement by ebsd," *Journal of Microscopy*, vol. 233, no. 2, pp. 290–301, 2009.

[157] Y. H. Chen, C. H. Jiang, Z. Wang, and K. Zhan, "Influence of shot peening on surface-layer characteristics of a monocrystalline nickel-based superalloy," *Powder Diffraction*, vol. 25, no. 4, p. 355–358, 2010.

[158] C. You, M. Achintha, K. Soady, and P. Reed, "Low cycle fatigue life prediction in shot-peened components of different geometries – part ii: life prediction," *Fatigue and Fracture and Engineering Materials and Structures*, vol. 40, p. 749–760, 2016.

[159] F. Bachmann, R. Hielscher, and H. Schaeben, "Texture analysis with mtex – free and open source software toolbox," in *Texture and Anisotropy of Polycrystals III*, ser. Solid State Phenomena, vol. 160. Trans Tech Publications Ltd, 3 2010, pp. 63–68.

[160] W. Oliver and G. Pharr, "An improved technique for determining hardness and elastic modulus using load and displacement sensing indentation experiments," *Journal of Materials Research*, vol. 7, no. 6, p. 1564–1583, 1992.

[161] H. Mughrabi, "The alpha-factor in the taylor flow-stress law in monotonic, cyclic and quasi-stationary deformations: Dependence on slip mode, dislocation arrangement and density," *Current Opinion in Solid State and Materials Science*, vol. 20, no. 6, pp. 411 – 420, 2016, the COSSMS Twentieth Anniversary Issue. [Online]. Available: http://www.sciencedirect.com/science/article/pii/S1359028616300870

[162] V. M. Segal, "Equivalent and effective strains during severe plastic deformation (spd)," *Philosophical Magazine Letters*, vol. 98, no. 11, pp. 511–520, 2018.

[163] L. Mattei, D. Daniel, G. Guiglionda, H. Klöcker, and J. Driver, "Strain localization and damage mechanisms during bending of aa6016 sheet," *Materials Science and Engineering: A*, vol. 559, pp. 812 – 821, 2013. [Online]. Available: http://www.sciencedirect.com/science/article/pii/S0921509312013421

[164] T. Klotz, D. Delbergue, P. Bocher, M. Lévesque, and M. Brochu, "Surface characteristics and fatigue behavior of shot peened inconel 718," *International Journal of Fatigue*, vol. 110, pp. 10 – 21, 2018. [Online]. Available: http://www.sciencedirect.com/science/article/pii/S0142112318300069

[165] M. F. Naeini, M. H. Shariat, and M. Eizadjou, "On the chloride-induced pitting of ultra fine grains 5052 aluminum alloy produced by accumulative roll bonding process," *Journal of Alloys and Compounds*, vol. 509, no. 14, pp. 4696 – 4700, 2011. [Online]. Available: http://www.sciencedirect.com/science/article/pii/S0925838811001071

[166] R. Singh, "Influence of cold rolling on sensitization and intergranular stress corrosion cracking of aisi 304 aged at 500 degree c," *Journal of Materials Processing Technology*, vol. 206, no. 1, pp. 286 – 293, 2008. [Online]. Available: http://www.sciencedirect.com/science/article/pii/S0924013607013842

[167] M. Laleh and F. Kargar, "Effect of surface nanocrystallization on the microstructural and corrosion characteristics of az91d magnesium alloy," *Journal of Alloys and Compounds*, vol. 509, no. 37, pp. 9150 – 9156, 2011. [Online]. Available: http://www.sciencedirect.com/science/article/pii/S0925838811014071

[168] J. Zhang, S. Lu, T. Wu, Z. Zhou, and W. Zhang, "An evaluation on sp surface property by means of combined fem-dem shot dynamics simulation," *Advances in Engineering Software*, vol. 115, no. Supplement C, pp. 283 – 296, 2018. [Online]. Available: http://www.sciencedirect.com/science/article/pii/S0965997816305968

[169] A. Barnoush, P. Hosemann, J. Molina-Aldareguia, and J. M. Wheeler, "In situ small-scale mechanical testing under extreme environments," *MRS Bulletin*, vol. 44, no. 6, p. 471–477, 2019.

[170] Y. Tirupataiah and G. Sundararajan, "A dynamic indentation technique for the characterization of the high strain rate plastic flow behaviour of ductile metals and alloys," *Journal of the Mechanics and Physics of Solids*, vol. 39, no. 2, pp. 243 – 271, 1991. [Online]. Available: http://www.sciencedirect.com/science/article/pii/0022509691900059

[171] J. Lu, S. Suresh, and G. Ravichandran, "Dynamic indentation for determining the strain rate sensitivity of metals," *Journal of the Mechanics and Physics of Solids*, vol. 51, no. 11, pp. 1923 – 1938, 2003, proceedings of a Symposium on Dynamic Failure and Thin Film Mechanics, honoring Professor L.B. Freund. [Online]. Available: http://www.sciencedirect.com/science/article/pii/S0022509603001431

[172] Z. Zhang, T.-S. Jun, T. B. Britton, and F. P. Dunne, "Intrinsic anisotropy of strain rate sensitivity in single crystal alpha titanium," *Acta Materialia*, vol. 118, pp. 317

– 330, 2016. [Online]. Available: http://www.sciencedirect.com/science/article/pii/S1359645416305523

[173] Q. Shi, F. Latourte, F. Hild, and S. Roux, "Backtracking depth-resolved microstructures for crystal plasticity identification—part 2: Identification," *JOM*, vol. 69, no. 12, pp. 2803–2809, Dec 2017. [Online]. Available: https://doi.org/10.1007/s11837-017-2586-1

[174] M.-J. Pac, S. Giljean, C. Rousselot, F. Richard, and P. Delobelle, "Microstructural and elasto-plastic material parameters identification by inverse finite elements method of ti(1-x)alxn (0<x<1) sputtered thin films from berkovich nano-indentation experiments," *Thin Solid Films*, vol. 569, pp. 81 – 92, 2014. [Online]. Available: http://www.sciencedirect.com/science/article/pii/S0040609014007585

[175] J. A. El-Awady, M. Wen, and N. M. Ghoniem, "The role of the weakest-link mechanism in controlling the plasticity of micropillars," *Journal of the Mechanics and Physics of Solids*, vol. 57, no. 1, pp. 32 – 50, 2009. [Online]. Available: http://www.sciencedirect.com/science/article/pii/S0022509608001737

[176] B. Kondori, A. Needleman, and A. A. Benzerga, "Discrete dislocation simulations of compression of tapered micropillars," *Journal of the Mechanics and Physics of Solids*, vol. 101, pp. 223 – 234, 2017. [Online]. Available: http://www.sciencedirect.com/science/article/pii/S0022509616305373

[177] M. Horstemeyer, M. Baskes, A. Godfrey, and D. Hughes, "A large deformation atomistic study examining crystal orientation effects on the stress–strain relationship," *International Journal of Plasticity*, vol. 18, no. 2, pp. 203 – 229, 2002. [Online]. Available: http://www.sciencedirect.com/science/article/pii/S0749641900000760

[178] S. Rawat, S. Chandra, V. M. Chavan, S. Sharma, M. Warrier, S. Chaturvedi, and R. J. Patel, "Integrated experimental and computational studies of deformation of single crystal copper at high strain rates," *Journal of Applied Physics*, vol. 116, no. 21, p. 213507, 2014. [Online]. Available: https://doi.org/10.1063/1.4903734

[179] Z. Wang, I. Beyerlein, and R. LeSar, "Plastic anisotropy in fcc single crystals in high rate deformation," *International Journal of Plasticity*, vol. 25, no. 1, pp. 26 – 48, 2009. [Online]. Available: http://www.sciencedirect.com/science/article/pii/S0749641908000223

[180] E. Galindo-Nava, J. Sietsma, and P. R.-D. del Castillo, "Dislocation annihilation in plastic deformation: Ii. kocks–mecking analysis," *Acta Materialia*, vol. 60, no. 6, pp. 2615 – 2624, 2012. [Online]. Available: http://www.sciencedirect.com/science/article/pii/S1359645412000663

[181] R. Lacroix, V. Chomienne, G. Kermouche, J. Teisseire, E. Barthel, and S. Queste, "Micropillar testing of amorphous silica," *International Journal of Applied Glass Science*, vol. 3, no. 1, pp. 36–43, 2012.

[182] S. Breumier, "3deye, https://doi.org/10.5281/zenodo.4043588," Sep. 2020. [Online]. Available: https://doi.org/10.5281/zenodo.4043588

[183] G. Bradski and A. Kaehler, *Learning OpenCV*. O'Reilly Media, 2008.

[184] G. Bradski, "The OpenCV Library," *Dr. Dobb's Journal of Software Tools*, 2000.

[185] P. Virtanen, R. Gommers, T. E. Oliphant, M. Haberland, T. Reddy, D. Cournapeau, E. Burovski, P. Peterson, W. Weckesser, J. Bright, S. J. van der Walt, M. Brett, J. Wilson, K. J. Millman, N. Mayorov, A. R. J. Nelson, E. Jones, R. Kern, E. Larson, C. J. Carey, İ. Polat, Y. Feng, E. W. Moore, J. VanderPlas, D. Laxalde, J. Perktold, R. Cimrman, I. Henriksen, E. A. Quintero, C. R. Harris, A. M. Archibald, A. H. Ribeiro, F. Pedregosa, P. van Mulbregt, and SciPy 1.0 Contributors, "SciPy 1.0: Fundamental Algorithms for Scientific Computing in Python," *Nature Methods*, vol. 17, pp. 261–272, 2020.

[186] R. F. Kubler, R. Rotinat, J. Badreddine, and Q. Puydt, "Experimental analysis of the shot peening particle stream using particle tracking and digital image correlation techniques," *Experimental Mechanics*, vol. 60, no. 4, pp. 429–443, 2020. [Online]. Available: https://doi.org/10.1007/s11340-019-00574-4

[187] Blender Online Community, *Blender - a 3D modelling and rendering package*, Blender Foundation, Stichting Blender Foundation, Amsterdam, 2018. [Online]. Available: http://www.blender.org

[188] C. T. Rueden, J. Schindelin, M. C. Hiner, B. E. DeZonia, A. E. Walter, E. T. Arena, and K. W. Eliceiri, "Imagej2: Imagej for the next generation of scientific image data," *BMC Bioinformatics*, vol. 18, no. 1, p. 529, 2017. [Online]. Available: https://doi.org/10.1186/s12859-017-1934-z

[189] W. Johnson, G. ; Cook, "A constitutive model and data for metals subjected to large strains, high strain rates and high temperatures," in *7th International Symposium on Ballistics*, 1983, pp. 541–8.

[190] M. Ahmad, K. Ismail, and F. Mat, "Impact models and coefficient of restitution: A review," *ARPN Journal of Engineering and Applied Sciences*, 2015.

[191] T. Hong, J. Ooi, and B. Shaw, "A numerical simulation to relate the shot peening parameters to the induced residual stresses," *Engineering Failure Analysis*, vol. 15, no. 8, pp. 1097 – 1110, 2008. [Online]. Available: http://www.sciencedirect.com/science/article/pii/S1350630707001860

[192] B. Bhuvaraghan, S. M. Srinivasan, B. Maffeo, R. D. McCLain, Y. Potdar, and O. Prakash, "Shot peening simulation using discrete and finite element methods," *Advances in Engineering Software*, vol. 41, no. 12, pp. 1266 – 1276, 2010. [Online]. Available: http://www.sciencedirect.com/science/article/pii/S0965997810001183

[193] A. B. Edward, P. S. Heyns, and S. Kok, "A numerical investigation of a single-shot in a dem-fem approach to shot peening simulation," *Metals*, vol. 9, no. 11, 2019. [Online]. Available: https://www.mdpi.com/2075-4701/9/11/1183

[194] R. Fathallah, G. Inglebert, and L. Castex, "Determination of shot peening coefficient of restitution," *Surface Engineering*, vol. 19, no. 2, pp. 109–113, 2003. [Online]. Available: https://doi.org/10.1179/026708403225002559

[195] R. Seifried, W. Schiehlen, and P. Eberhard, "Numerical and experimental evaluation of the coefficient of restitution for repeated impacts," *International Journal of Impact Engineering*, vol. 32, no. 1, pp. 508 – 524, 2005, fifth International Symposium on Impact Engineering. [Online]. Available: http://www.sciencedirect.com/science/article/pii/S0734743X05000114

[196] C.-Y. Wu, C. Thornton, and L.-Y. Li, "A semi-analytical model for oblique impacts of elastoplastic spheres," *Proceedings of the Royal Scociety A*, 2008.

[197] W. Ludwig and P. Płuszka, "The analysis of the influence of the normal restitution coefficient model on calculated particles velocities by means of eulerian-lagrangian approach," *Powder Technology*, vol. 344, pp. 140 – 151, 2019. [Online]. Available: http://www.sciencedirect.com/science/article/pii/S0032591018310416

[198] W. Johnson, *Impact strength of materials*. Edward Arnold Publishers Limited, 1972.

[199] C. Thornton, "Coefficient of Restitution for Collinear Collisions of Elastic-Perfectly Plastic Spheres," *Journal of Applied Mechanics*, vol. 64, no. 2, pp. 383–386, 06 1997. [Online]. Available: https://doi.org/10.1115/1.2787319

[200] G. L. Sheldon, J. Maji, and C. T. Crowe, "Erosion of a Tube by Gas-Particle Flow," *Journal of Engineering Materials and Technology*, vol. 99, no. 2, pp. 138–142, 04 1977. [Online]. Available: https://doi.org/10.1115/1.3443423

[201] B. H, "Report on investigations on: Particle movement in straight horizontal tubes particle/wall collision erosion of tubes and tube bends," 1979.

[202] R. Cross, "Oblique impact of a steel ball," *Powder Technology*, vol. 351, pp. 282 – 290, 2019. [Online]. Available: http://www.sciencedirect.com/science/article/pii/S0032591019302839

[203] S. Breumier, F. Richard, A. Villani, G. Kermouche, and L. Martin, "Complementarity of impact shot displacements and induced residual stress fields for a reliable estimation of crystal viscoplasticity parameters," *submitted in Journal of Theoretical, Computational and Applied Mechanics*, 2020.

[204] R. B. Blackman and J. W. Tukey, "The measurement of power spectra from the point of view of communications engineering — part i," *Bell System Technical Journal*, vol. 37, no. 1, pp. 185–282, 1958. [Online]. Available: https://onlinelibrary.wiley.com/doi/abs/10.1002/j.1538-7305.1958.tb03874.x

[205] O. Ronneberger, P. Fischer, and T. Brox, "U-net: Convolutional networks for biomedical image segmentation," in *Medical Image Computing and Computer-Assisted Intervention – MICCAI 2015*, N. Navab, J. Hornegger, W. M. Wells, and A. F. Frangi, Eds. Cham: Springer International Publishing, 2015, pp. 234–241.

[206] E. Plancher, J. Petit, C. Maurice, V. Favier, L. Saintoyant, D. Loisnard, N. Rupin, J. B. Marijon, O. Ulrich, M. Bornert, J. S. Micha, O. Robach, and O. Castelnau, "On the accuracy of elastic strain field measurements by laue microdiffraction and high-resolution ebsd: A cross-validation experiment," *EXPERIMENTAL MECHANICS*, vol. 56, no. 3, pp. 483–492, MAR 2016.

[207] C. Zhu, K. Kaufmann, and K. S. Vecchio, "Novel remapping approach for hr-ebsd based on demons registration," *Ultramicroscopy*, vol. 208, p. 112851, Jan 2020. [Online]. Available: http://dx.doi.org/10.1016/j.ultramic.2019.112851

[208] G. Nolze, "Image distortions in sem and their influences on ebsd measurements," *Ultramicroscopy*, vol. 107, no. 2, pp. 172 – 183, 2007. [Online]. Available: http://www.sciencedirect.com/science/article/pii/S0304399106001483

[209] J. Alcalá and D. E. de los Ojos, "Reassessing spherical indentation: Contact regimes and mechanical property extractions," *International Journal of Solids and Structures*, vol. 47, no. 20, pp. 2714 – 2732, 2010. [Online]. Available: http://www.sciencedirect.com/science/article/pii/S0020768310002039

[210] O. Casals and J. Alcalá, "The duality in mechanical property extractions from vickers and berkovich instrumented indentation experiments," *Acta Materialia*, vol. 53, no. 13, pp. 3545 – 3561, 2005. [Online]. Available: http://www.sciencedirect.com/science/article/pii/S1359645405002181

[211] J. Marteau, S. Bouvier, and M. Bigerelle, "Review on numerical modeling of instrumented indentation tests for elastoplastic material behavior identification," *Archives of Computational Methods in Engineering*, vol. 22, no. 4, pp. 577–593, Nov 2015. [Online]. Available: https://doi.org/10.1007/s11831-014-9134-8

[212] C. Geuzaine and J. F. Remacle, "Gmsh: A three-dimensional finite element mesh generator with built-in pre- and post-processing facilities," *International Journal for Numerical Methods in Engineering*, 2009.

[213] J. Hu, Z. Liu, E. V. der Giessen, and Z. Zhuang, "Strain rate effects on the plastic flow in submicron copper pillars: Considering the influence of sample size and dislocation nucleation," *Extreme Mechanics Letters*, vol. 17, pp. 33 – 37, 2017. [Online]. Available: http://www.sciencedirect.com/science/article/pii/S2352431617301141

[214] R. Kapoor and S. Nemat-Nasser, "Determination of temperature rise during high strain rate deformation," *Mechanics of Materials*, vol. 27, no. 1, pp. 1 – 12, 1998. [Online]. Available: http://www.sciencedirect.com/science/article/pii/S0167663697000367

[215] S. Breumier, "Blender shot lab, https://github.com/simonBreumier/Blender_shot_lab," 2020.